Andreas Eich

Manipulation of Topological Edge States

How Stoichiometric Changes and Surface Manipulation
Influence the Dirac Cone of Topological Insulators

Cuvillier Verlag Göttingen
Internationaler wissenschaftlicher Fachverlag

Manipulation of Topological Edge States

Manipulation of Topological Edge States

How Stoichiometric Changes and Surface Manipulation
Influence the Dirac Cone of Topological Insulators

Dissertation zur Erlangung des Doktorgrades

am Fachbereich Physik der Universität Hamburg

vorgelegt von

Dipl.-Physiker Andreas Eich

aus Bonn

Hamburg

2014

Abstract

Topological insulators (TIs) are a recently discovered class of materials. Their topologically protected edge states (TES) promise break-throughs in the fields of spintronics and quantum computation. Before TIs can be utilized, it is necessary to understand the consequences of topological protection, analyze the interaction of TES with its environment and develop methods for customization. This thesis contributes to all three areas by investigating the TES behavior in presence of perturbations, targeted manipulation as well as disorder.

The presented samples were characterized in real space using scanning tunneling microscopy (STM). Properties of electron bands were investigated using scanning tunneling spectroscopy (STS), photoelectron spectroscopy and density functional theory. STM and STS were performed with a microscope built during the first part of my Ph.D.

On $TlBiSe_2$, the TES response to surface disorder is investigated. An incomplete recrystallized Tl layer terminating the crystal annihilates trivial surface states, while the TES survives by shifting into the bulk. This unique behavior is a direct consequence of the topological nature of the TES and provides proof of enhanced protection.

By characterizing $PbBi_4Te_7$ one possible method of customization is investigated. Here, the prototypical TI Bi_2Te_3 is modified by adding one layer of Pb and Te to every second quintuple layer. The resulting material remains a topological insulator and exhibits the predicted changes. The ratification of the theoretical predictions demonstrates that the implementation of group IV elements can be used to change shape and isolation of the TES of binary chalcogenides, such as Bi_2Te_3 and Bi_2Se_3.

Furthermore, a method for introducing magnetic moments to the vicinity of the TES is developed that avoids any secondary doping effects. Deposited Fe atoms are incorporated into a Bi_2Se_3 surface quintuple layer via annealing. The Fe atoms substitute atoms in the first and second Bi layer. The substitution type is controlled by the annealing temperature. The incorporation cancels the doping effect typical of *as deposited* material, while the magnetic moment of Fe atoms is preserved.

Finally, the TESs of the hybrid TI Bi-bilayer on Bi_2Se_3 are investigated. The system is fabricated by growing one Bi-bilayer on a Bi_2Se_3 bulk crystal. An analysis of Fourier transformed STS maps confirms the vertical shift of the Bi_2Se_3 TES towards the new surface. The interaction of the TES with Bi-bilayer states is revealed by mapping the scattering vectors (q-vectors). The linearity of the q-vector bands confirms the enhanched isolation of the TES from bulk states. Furthermore, the integrity of the bilayer states seems sufficiently preserved to host a 1D TES, which so far has only been predicted for freestanding bilayers.

Zusammenfassung

Der Begriff *topologischer Isolator* (TI) beschreibt eine kürzlich entdeckte, neue Material-klasse. TIs verfügen über spinpolarisierte, topologisch geschützte Randzustände (TRZ), die grundsätzlich in den Bereichen der Spintronik und der Quanteninformationsverarbeitung eine Anwendung finden könnten. Bevor TIs allerdings für Anwendungen genutzt werden können, müssen die Natur und die Konsequenzen des topologischen Schutzes der TRZ genauer verstanden werden, die Wechselwirkung der TRZ mit ihrer Umgebung muss untersucht werden, und es müssen Methoden entwickelt werden, die eine Anpassung der spezifischen Eigenschaften der TRZ an einen bestimmten Zweck ermöglichen. In der vorliegenden Doktorarbeit werden daher die Auswirkungen von Störungen bzw. von gezielten Manipulationen der Struktur von TIs auf die TRZ untersucht.

Die Topographie der verwendeten Proben wurde mittels Rastertunnelmikroskopie (RTM) untersucht. Die Eigenschaften der elektronischen Bänder wurden mit Rastertunnelspektroskopie (RTS), Photoelektronenspektroskopie (XPS und ARPES) und theoretischen Berechnungen basierend auf der Dichtefunktionaltheorie untersucht. Das Mikroskop, das für die RTM- und RTS-Messungen verwendet wurde, ist von mir in der ersten Hälfte meiner Doktorandenzeit gebaut worden.

Am Beispiel von $TlBiSe_2$ wurde die Reaktion der Randzustände auf eine Störung der Oberflächenstruktur untersucht. Bei der Präparation der Probe wird die oberste atomare Lage auseinandergerissen. Die zurückbleibenden Atome (Tl) rekristallisieren, ohne eine geschlossene Lage bilden zu können. Diese Störung der Oberflächensymmetrie zerstört die zu erwartenden trivialen Oberflächenzustände, während die TRZ überleben, indem sie unter der Oberfläche relokalisieren. Diese Verlagerung ist Beweis für den topologischen Schutz der Randzustände gegenüber Störungen.

Am Beispiel von $PbBi_4Te_7$ wurde eine mögliche Art der Manipulation des TRZ untersucht. $PbBi_4Te_7$ entspricht in seiner kristallinen Struktur größtenteils dem bekannten TI Bi_2Se_3. Allerdings ist jede zweite Quintuple-Lage um eine zusätzliche Pb und Te Lage ergänzt. Es wird gezeigt, dass trotz der Variation der kristallinen Struktur auch $PbBi_4Te_7$ ein TI ist. Die topologische Klasse sowie die weiteren untersuchten Eigenschaften des TRZ stimmen mit theoretischen Vorhersagen überein. Die Übereinstimmung von Theorie und Experiment lässt vermuten, dass auch bei Variation mit weiteren Elementen der 4. Hauptgruppe die topologische Natur von binären Chalcogeniden wie Bi_2Te_3 und Bi_2Se_3 erhalten bleibt, so wie es in der gleichen theoretischen Studie vorausgesagt wurde.

Des Weiteren wurde eine zusätzliche Manipulationsart entwickelt, die Atomen mit magnetischem Moment erlaubt, in der Nähe des TRZ zu lokalisieren, ohne die ursprüngliche elektronische Struktur des TIs durch weitere Dotierungseffekte zu beeinflussen.

Dazu wurden zuerst Fe Atome auf die Oberfäche von Bi_2Se_3 aufgedampft und dann durch Erhitzen in die erste Quintuple-Lage eingebaut. Die Fe Atome substituieren Atome der ersten und zweiten Bi Lage. Der Substitutionstyp kann durch die beim Erhitzen verwendete Temperatur beeinflusst werden. Durch das Einbauen der Fe Atome in das Substrat wird eine Elektronendotierung verhindert, wie sie typischerweise für aufgedampfte Atome auftritt.

Schließlich wurde der TRZ eines hybriden TI-Systems untersucht. Dazu wurde eine Bi-Doppellage auf Bi_2Se_3 gewachsen. Mithilfe Fourier-transformierter RTS-Bilder konnte nachgewiesen werden, dass der TRZ des Substrats an die neue Oberfläche des Hybridsystems wandert. Basierend auf diesen Bildern wurde auch die Streuung zwischen dem TRZ und anderen Oberflächenzuständen untersucht. Die lineare Dispersion der ausgelesenen Streuvektoren indiziert eine erhöhte Isolation des TRZ von den Volumenzuständen des Substrats. Des Weiteren konnte durch Berechnungen gezeigt werden, dass die elektronische Struktur der Doppellage trotz Hybridisierung mit dem Substrat soweit erhalten bleibt, dass an den Rändern der Doppellage ein 1D TRZ zu finden sein sollte.

Contents

List of Figures

List of Tables

1. Introduction

In the last 40 years the driving force of human progress was the so called *digital revolution*. The term describes the change from an analog to a digital technology initiated by the availability of digital computers and recording to a wider public. It is powered by a constant improvement of speed and complexity of its key technologies. Fundamental was the ability to downsize the basic building blocks, i.e. the transistor used for processing [1, 2] and magnetic areas used for recording [3]. Downsizing allowed to massively increase the number of basic blocks, while at the same time the absolute size of devices, their energy consumption and price remained constant (or even decreased). Because of this stability, it was possible to fully transfer the technological advancements to commercial products, e.g. the transistor count of microprocessors[1] doubled every two years from its invention in the year 1971 until today[2]. It was this dynamic development, that made computers affordable for every household and allowed the incorporation of microprocessors to almost any other existing technology, e.g. cars, telephones, even washing machines. Between 1986 and 2007 general purpose computational capacity grew by 58 % per year, from 0.06 million instructions per seconds and capita to 968 million. Storage capacity jumped from 539 MB to 44716 MB with a digital share of 0.8 % in 1986 and 94 % in 2007 [6].

The basic functionality of microprocessors and hard disk drives (HDD), the dominant recording device, did not change in that time. Microprocessors depend on the ability of transistors to switch and amplify electron currents. HDDs depend on the ability of domains of magnetic material to be stably magnetized in opposite directions and on read/write heads to access the stored information via magnetic fields. Downsizing was enough to keep the growth rate stable[3]. However, it is foreseeable that the used technologies reach their limits. Some of these limits are related to the technologies themselves, e.g. the switching rate of the used transistors or the usability of magnetic fields to access information of a HDD[4].

---

[1]A microprocessor contains the whole infrastructure needed to carry out a general computer program on one chip. It was this integration that allowed the simultaneous fabrication of the whole infrastructure independent of its complexity and is fundamental for the downsizing effect to deploy its full impact.

[2]The first microprocessor, the Intel 4004, had a transistor count of 2300 [4], the recently released Apple A8X has a count of more than three billion [5].

[3]It has to be mentioned though, that downsizing became only possible by the application of new materials and effects, e.g. the giant magnetoresistance effect for recording heads of HDDs [7, 8]

[4]When the size of a nanoparticle is decreased, its anisotropy constant per atom has to be increased to achieve a similar magnetic stability. Therefore, also the strength of the magnetic field has to be increased. But at smaller dimensions also the power available to create the field is reduced. At some point the saved data cannot be accessed anymore [9].

Other limits are more fundamental. The smallest connection between source and drain of a transistor is an atom [10]. When (and if) such a transistor is realized in commercial products, a further downsizing will not be possible.

Without downsizing more complex microprocessors and storage devices will grow in size, consume more energy and produce more heat (which again compromises the functionality). The production and running costs will increase. More powerful devices will be unaffordable for, at least, the consumer market. If no new driving forces can be found, i.e. new concepts of processing, the tremendous growth described before will come to an end.

But there are proposals on how traditional concepts can be replaced. The use of *spintronics* is maybe the most promising route. While the regular electronics described above utilizes charge transfer to carry and process information, in spintronics also the electron spin is utilized. Spin current based transistors may allow faster and more energy efficient information processing [11]. The spin-torque effect allows spin currents to switch magnetic domains and therefore makes HDD recording heads dispensable [12]. Furthermore, spintronics might allow the creation of qubits that would enable quantum computation [13, 14], a complete new concept of computation, which promises to be extremely fast.

The idea of spintronics has been discussed for quite some time now. In fact, a spin dependent field effect transistor was proposed already in 1990 [15], but most spintronic devices are far from being realized in commercial products[5]. One main issue of spintronics is the reliable creation of spin polarized currents. While these were already achieved and processed at low temperatures by several approaches [16–18], none of these are applicable for devices working at room temperature. Here, the new material class of topological insulator (TI)s [19–22], predicted in 2004 [23–26] and experimentally confirmed in 2007 [19, 27, 28], comes into play, which might solve the problem.

TIs are bulk insulators but with spin-polarized states, that close the band gap at the edge of the material. With a large enough gap, e.g. in Bi_2Se_3 [29], a 100 % spin-polarized current is carried at the surface by the edge states, also at room temperature. Moreover, the peculiar locking of spin and momentum predicted for these states results in complete quenching of direct backscattering.

The correct prediction of TIs is a great achievement of theoretical physics and has led to a new classification system of quantum phases for physical bodies: based on topology. The edge states are a result of a transition between two different topological classes, which is why they exhibit this increased stability concerning perturbations, called topological protection. Their unique properties, spin-polarization, topological protection and linear dispersion, may not only allow the reliable generation of spin currents, but the realization

---

[5]The only exception are spin valves based on the before mentioned giant magnetoresistance effect.

of new Quantum Hall Effects [30–32], a new type of magneto-electric-effect [33, 34] and the creation of magnetic monopoles [35] or qubits [36]. For this reason TIs are of tremendous interest. And research in this field exploded, especially since the first 3D TI got discovered in 2009[6] [28].

However, research on TIs just started and many questions need to be answered before TIs can be utilized for one of the given purposes. While TIs and the concept of topology are quite well described from a theoretical point of view, many predictions still have to be tested by experiment. Especially the consequences of topological protection have to be further investigated: To what degree are the edge states and their spin-polarization protected concerning different types of perturbations? Do they react? And if so, of what type of reaction is it? Answering these questions will not only sharpen the understanding of the topological concept but will help to find methods of manipulation to fit the properties of a given TI to a certain application. It is the aim of this thesis to contribute to both fields of interest.

The thesis is split in two parts, a theoretical and an experimental part. The theoretical part provides all the information needed to understand the results of the described experiments. It introduces the measurement techniques used, scanning probe methods (SPM) (chapter 2) and photoelectron spectroscopy (chapter 3). Here, the focus is on the scanning probe methods, as these were the main probes for the thesis. An overview on topological insulators is given (chapter 4), including an introduction on the concept of topology, a description of the origin of the edge states and the mechanism behind their protection. The theoretically predicted behavior of the topological edge states (TES) when exposed to perturbations is discussed and a closer look on applications is provided. Furthermore, the properties and the TES behavior of the prototypical TIs Bi_2Se_3 and Bi_2Te_3 are presented, as these are key samples used in this thesis.

The experimental part provides the setup of the scanning tunneling microscope (STM) used for this work (chapter 5) and the results of the conducted experiments. The STM was designed and constructed by myself during the first part of my thesis. It follows the variable temperature STM (VT-STM) design that allows a fast exchange of samples but is optimized concerning stability. Both properties, speed and stability, were crucial for the conducted experiments.

The first experiment (chapter 6) deals with the question how magnetic moments can be introduced to the vicinity of the TES by surface deposition without an extra doping effect, using the example of Fe atoms deposited on Bi_2Se_3. Due to the small density of electron

---

[6]TI related publications in 2008: 11, 2009: 56, 2013: 879 according to a Web of Science search on the key word "topological insulator" [37].

states around the Fermi level, TIs are very sensitive to surface doping, which induces a large band bending at the edge. This not only shifts the Fermi level, but introduces quantum well states that might interact with the TES and decrease the total spin-polarization of a given current. Here, the consequences of a diffusion of Fe atoms into the surface are investigated by scanning tunneling microscopy (STM), angle resolved photoemission spectroscopy (ARPES) and density functional theory (DFT) calculations.

The chapter concerning the characterization of $PbBi_4Te_7$ (chapter 7) explores the possibility to adjust the bulk band gap as well as the shape and location of the TES bands of binary chalcogenides, such as Bi_2Te_3 and Bi_2Se_3, by changing the crystal composition with group IV elements. Here, Bi_2Te_3 is modified by adding Pb, leading to extra Pb and Te layers within the original crystal structure. The sample is characterized in real and in k-space, using STM and ARPES, the results are compared to theoretical predictions.

On $TlBiSe_2$, the TES response to a heavily disturbed surface is investigated (chapter 8). $TlBiSe_2$ samples are cleaved, a process that rips apart the top layer of the new surface. The surface morphology is studied by STM and atomic force microscopy (AFM), the consequences for the electronic structure are investigated by x-ray photoemission spectroscopy (XPS) and ARPES.

In the final experimental chapter (chapter 9), the hybrid TI Bi-bilayer on Bi_2Se_3 is studied for two reasons. The TES of the substrate is supposed to vertically shift to the new surface, which isolates the edge state from Bi_2Se_3 bulk states. Moreover, the bilayer hosts intrinsic states that might interact with the bulk TES. This interaction as well as the bulk TES location is investigated.

The second reason is the topological nature of the bilayer itself. A freestanding Bi-bilayer is predicted to be a 2D TI with 1D TES, that are sharply localized at the edge [38, 39]. However, the hybridization with substrate states has so far closed the bilayer band gap for all used substrates [40, 41]. The relatively small lateral lattice constant of Bi_2Se_3 may lead to an increased van-der-Waals gap between bilayer and Bi_2Se_3 and therefore to a reduced hybridization. By investigating the final band structure, also the gap size of the bilayer should be unraveled. The first section of the chapter is concerned with a growth study to proof bilayer growth of Bi on Bi_2Se_3. Then the band structure is investigated by ARPES and DFT. In the third section the interaction of surface bands is investigated by an analysis of quasi-particle interference (QPI) patterns on the surface via Fourier transformed STS maps and a simulation of these maps based on the DFT-band structure. By a comparison of q-vectors from theory and experiment all present scattering channels (and therefore bands) at the surface are identified.

For every project presented in this thesis it was necessary to collaborate with different research groups, that provided their unique expertise to unravel all properties of each sample. Since each sample system can only be completely understood by the combination of all experimental and theoretical efforts, I chose to present not only the data measured by myself, but included the results of each part of the collaborations. In the beginning of each chapter I describe who contributed which result. The final conclusions of each experiment are a result of multiple discussions between all collaboration partners.

Part I.

Theoretical Basics of STM, PES and TIs

2. Scanning Tunneling Microscopy

The invention of STM by Binnig and Rohrer in 1982 [42] introduced a unique approach to investigate the surfaces of conductive materials. For the first time it was possible to map surfaces in real space with atomic resolution. In order to gain such a high resolution, a metallic probe is scanned over the sample close enough, that electrons can tunnel between probe and sample. The tunneling current (I) depends strongly on the probe-sample distance and on the local electronic density of states (LDOS) of the sample. By recording the variations of the tunneling current, a map of the surface is achieved, that, to first approximation, resembles the topography of the sample surface. Additionally, the dependency on the sample electron LDOS furthermore enables spectroscopic investigations of the surface electronic structure [43, 44].

The high lateral resolution, as well as the ability of atom manipulation [45] and the fact that the samples are typically not destroyed during measurement, makes scanning tunneling microscopes and derived devices a prime tool to create and characterize nano-structures [46, 47], molecules [48], atoms [49] and even biological systems [50, 51]. The characterization not only includes morphology and electronic structure, but magnetic structure [52], as well as environmental [53] and time dependencies [54, 55].

The intent of this chapter is to give an introduction to STM so far to understand the results of this thesis and the challenges to obtain those. A brief description on the basic STM setup is followed by a section on the fundamental effects and models used to describe the tunneling junction. Finally, the measurement techniques used for this work are described. For a wider overview the books of R. Wiesendanger [56], J. Chen [57] are recommended.

2.1. Basic STM-Setup

In order to measure clean, high resolution images of a sample surface, the sample has to be scanned by a small probe with extreme precision and in a stable environment. Fig 2.1 illustrates the basic setup for STM measurements. The probe is a sharpened metal wire called tip with an apex that is formed ideally by a single atom. It is attached to a scanner made out of a piezoelectric material. By applying a voltage, the scanner can be stretched, compressed or bent with sub-nanometer precision. For this, the scanner is covered with 5 electrodes, +x/-x, +y/-y and z.
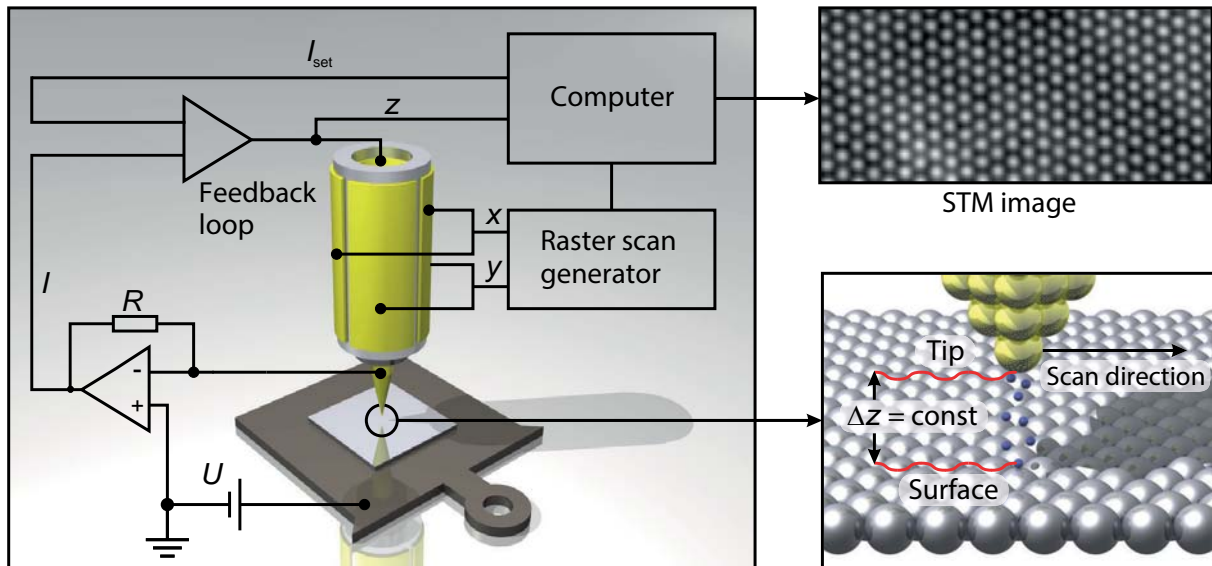
Figure 2.1.: Basic STM Setup A DC voltage U_B is applied between the sample and the tip of the microscope. Due to quantum-mechanical tunneling a current flows through the vacuum barrier (lower image on the right). The current is detected by an I/V-converter. The output signal is sent through a feedback loop to a computer. The tip is installed on a piezo tube. By applying a voltage to the electrodes on the tube, the tube is bent and stretched to scan the tip over the sample and to change the tip-sample distance. An STM image is obtained by the adjustments of the tip-sample distance via the feedback loop to keep I constant (constant current mode).

Tip and sample are integrated into an electric circuit. A net tunneling current I is established by applying a so called bias voltage (U_B) to the sample[1]. The resulting I is amplified by a pre-amplifier and then, depending on the measurement mode, directly processed by a computer to generate an STM image or fed into a feedback loop before. The feedback loop is used mainly to adjust the tip position to the topography of the sample. This will be further described in section 2.3.

The current across the tunneling junction is usually rather small, between 10 pA and several nA, and the tip-sample distance is around 5 Å. A change of 1 Å will already alter I by a factor of 10. Due to the strength and sensitivity of I, the STM is sensitive to pm changes in the sample topography. However, the measured signal is also prone to all kind of disturbances, e.g. mechanical vibrations and electrical noise.

To ensure the highest possible stability, STM measurements are typically conducted in protected environments, at ultra-high vacuum (UHV)-conditions[2] and at low temperatures,

---

[1]Applying U_B to the sample is the standard configuration. In principle, it can be applied to the tip, too.

[2]Besides an enhanced stability, UHV conditions are needed to guarantee a clean sample surface. Most investigated effects are extremely sensitive to surface contamination. Even the rather inert samples investigated for this thesis suffer from contact with residual gases, see section 4.8.

where either the microscope or the hole chamber is damped. Also the STM materials are chosen to reduce the transmission of vibrations and the used cables are isolated from all external and internal electronic perturbations. A closer look on this topic is given in chapter 5 where the experimental setup is described.

2.2. Theory

Fundamental to the understanding of the STM principle-of-operation is the quantum mechanical tunneling process. In this section a description of the process is given, starting with a simple one dimensional model, which is then adjusted to the peculiarities of STM.

1D Tunneling Effect

In Quantum Mechanics electrons of energy E can be described as waves [58]. When approaching a barrier with the potential strength $V_0 > E$, the electrons are either reflected by or tunnel through the barrier. Fig. 2.2 illustrates this process. Here, the black line represents the potential landscape and the blue line represents the electron wave. The momentum of the waves is indicated by arrows.

If the potential is constant in all three regions, the electrons can be described as quasi-free particles and the exact probability densities of the electron wave in either region can be calculated by the Schrödinger equation, leading to:

$$\psi(x) = \begin{cases} e^{ikx} + Ae^{-ikx} & ; \ x < 0 \\ Be^{i\kappa x} + Ce^{-i\kappa x} & ; \ 0 < x < s \\ De^{ikx} & ; \ x > s \end{cases} \tag{2.1}$$

where s is the barrier width, $k = \sqrt{2mE}/\hbar$ and $\kappa = \sqrt{2m(V_0 - E)}/\hbar$.

The electron wave runs towards the barrier in region I and interferes with that part of the wave that gets reflected at the barrier. Since the wave function and its derivative have to be continuous at every point of the system, it cannot drop to zero when it reaches the barrier. Instead it decreases exponentially within the barrier (region II), leading to a non-zero density probability of the electron wave behind the barrier (region III).
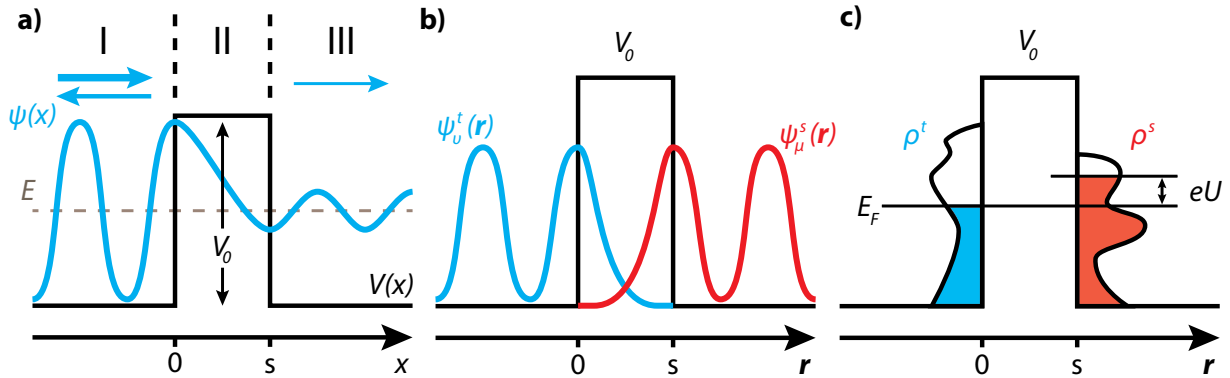
Figure 2.2.: 1D Tunneling Effect and Bardeen Ansatz a) Scheme of the 1D tunneling process at a rectangular barrier of width s and height V_0. An incident electron with energy $E < V_0$ is either reflected by or tunnels through the barrier. In region I and III the electron can be described by a plane wavefunction. Within region II the wavefunction can be described by an exponential decay. The probability density of the wavefunction in III depends on s and V_0. **b)** The Bardeen Ansatz considers two separate systems with known wavefunctions, e.g. ψ_ν^t of the tip and ψ_μ^s of the sample, that overlap in the barrier in between. **c)** I is a convolution of the LDOS of tip ρ^t and sample ρ^s.

Based on the solutions of Eq. 2.1 and the continuity of the wavefunction and its derivative, a transmission coefficient T can be calculated that gives the tunneling probability for the particles for this type of barrier:

$$T = \frac{1}{1 + (k^2 + \kappa^2)^2/(4k^2\kappa^2)\sinh(\kappa s)} \tag{2.2}$$

In case of a strongly attenuating barrier ($\kappa s >> 1$), which is typical for an STM tunnel junction, T can be approximated to:

$$T \approx \frac{16k^2\kappa^2}{(k^2 + \kappa^2)^2}e^{-2\kappa s} \tag{2.3}$$

Hence, T and therefore the tunneling current I, depend exponentially on the barrier width, which explains the high sensitivity to the tip-sample distance mentioned before. While this strong dependence explains the high vertical resolution of scanning tunneling microscopes, a real tunneling barrier is far more complicated than the simple example described here, e.g. the tip and sample exhibit an energy dependent electronic density of states (DOS) and have to be treated in three dimensions, not in 1D. Both aspects have a significant impact on the transmission probability and are considered by a model developed by Bardeen [59].

The Bardeen Ansatz

Bardeen's approach is based on time-dependent perturbation theory and was originally formulated in the 1960s for planar tunnel junctions with superconducting electrodes and insulating oxide layers [60, 61]. However, it can be adopted to calculate the tunneling current I of an STM junction. For this, tip and sample are treated as separate systems, but with an overlap of wave functions within the separating barrier, Fig. 2.2 (b). I is then calculated using Fermi's Golden Rule [58].

The transition rate $\omega_{\mu\nu}$ between an electron state of the tip ψ_ν^t at energy E_ν^t and an electron state of the sample ψ_μ^s at energy E_μ^s is given by

$$\omega_{\mu\nu} = \frac{2\pi}{\hbar} |M_{\mu\nu}|^2 \delta(E_\nu^t - E_\mu^s) \tag{2.4}$$

where the δ-function ensures conservation of energy. The associated tunneling matrix element $M_{\mu\nu}$ only depends on the wave functions ψ_ν^t and ψ_μ^s and is given, e.g., by [57] as

$$M_{\mu\nu} = \frac{\hbar^2}{2m} \int_{\mathbf{S}} (\psi_\nu^{t*} \nabla \psi_\mu^s - \psi_\mu^{s*} \nabla \psi_\nu^t) d\mathbf{S} \tag{2.5}$$

where $\mathbf{S}$ is an arbitrary separation surface between tip and sample.

Starting with the transition rate $\omega_{\mu\nu}$, one can calculate the tunneling current I:

$$I = \frac{4\pi e}{\hbar} \sum_{\mu\nu} [f(E_\nu^t - E_F^t) - f(E_\mu^s - E_F^s)] |M_{\mu\nu}|^2 \delta(E_\nu^t - E_\mu^s) \tag{2.6}$$

where $f(E) = 1/[1 + \exp(E/(k_B T))]$ is the Fermi distribution function. A net tunneling current only arises when a voltage is applied to either tip and sample. If one further replaces the summation over discrete states with the integration of the DOS, equation 2.6 can be written as

$$I(U) = \frac{4\pi e}{\hbar} \int d\epsilon [f(E_F^t - eU_B + \epsilon) - f(E_F^s + \epsilon)]$$
$$\times \rho^t(E_F^t - eU_B + \epsilon)\rho^s(E_F^s + \epsilon) \left|M(E_F^s + \epsilon, E_F^t - eU_B + \epsilon)\right|^2 \tag{2.7}$$

where ρ^t and ρ^s are the DOS of tip and sample given by

$$\rho_{t,s}(E) \equiv \frac{1}{\epsilon} \sum_{E_n = E - \epsilon}^{E} |\psi_{t,s,n}|^2 \tag{2.8}$$

13

Figure 2.3: Scheme based on the Tersoff-Hamann model. The tip apex is formed by a single atom at position $\mathbf{r}_0$ with a spherical potential well of radius R. The distance of nearest approach is d. The tip-sample distance is given by (R+d). $\mathbf{r}$ depicts the position of the sample surface below the tip. Dotted lines indicate s-wave tip states.
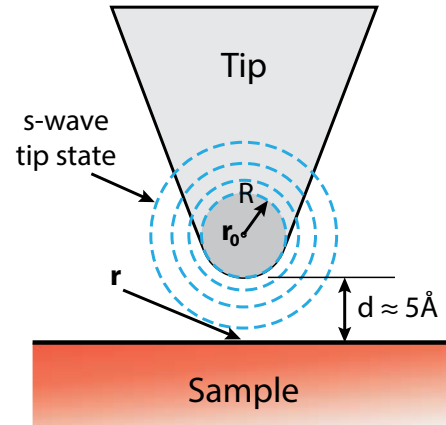
In the temperature limit $T \to 0$ the Fermi distribution becomes a step function and Eq. 2.7 simplifies to

$$I(U_B) = \frac{4\pi e}{\hbar} \int_0^{eU_B} d\epsilon \rho^t(E_F^t - eU_B + \epsilon)\rho^s(E_F^s - \epsilon) \left|M\right|^2 \tag{2.9}$$

With Bardeen's Ansatz it is theoretically possible to precisely calculate the tunnel current between tip and sample. However, to do so the exact DOS of the sample *and* the tip have to be known. But since the structure of the tip is typically unknown, the same is true for the tip density of states. The unknown tip density of states is not only a theoretical problem. The measured image depends on the DOS of sample and tip. When the influence of the tip is unknown, the origin of the measured features, tip or sample, cannot be identified.

Tersoff-Hamann Model

Fortunately, most experimental data can be reproduced by assuming a specific tip structure, which was introduced by J. Tersoff and D.R. Hamann [62, 63]. Here, the apex exhibits spherical symmetry and is described by s-type wave functions. These are typical of metal tips[3], see Fig. 2.3. Moreover, only small voltages and equal work functions of tip and sample are assumed and the tunneling contact is established at low temperatures.

---

[3]The model remains valid as long as higher orbital momenta ($l > 0$) have no significant influence on the tunneling current. This also depends on the size of the observed objects. E.g. for metals, Tersoff and Hamann showed that the objects have to be larger than ≈ 3 Å. Fortunately, the lattice constants of all samples measured in the framework of this thesis are much larger than 3 Å. Therefore, metal tips are sufficient to resolve even the smallest details and the Tersoff-Hamann model is adequate to describe the interaction.

14

With these assumptions the matrix element from Eq. 2.5 can be evaluated and the tunneling current has an extremely simple form. It is proportional to

$$I \propto \sum_{E_\mu^s = E_F - eU_B}^{E_F} \left| \psi_\mu^s(\mathbf{r}_0) \right|^2 = eU_B \rho^s(\mathbf{r}_0, E_F) \tag{2.10}$$

$\rho^s(\mathbf{r}_0, E_F)$ is nothing else but the local electronic density of states (LDOS) of the sample at the position of the tip. Hence, I does not depend on the DOS of the tip any more and the resulting STM image just depends on the tip-sample distance and the sample LDOS.

Model for Higher Bias Voltages

A more general model based on the Wentzel-Kramers-Brillouin (WKB) approximation [44, 64–67] includes also higher voltages. In the temperature limit $T \to 0$ the tunneling current is given by

$$I(U_B) \propto \int_{E_F}^{E_F + eU_B} \mathrm{d}E \rho^t(E - eU_B) \rho^s(\mathbf{r}, E) \mathcal{T}(E, eU_B, d) \tag{2.11}$$

with a transmission coefficient $\mathcal{T}$ described by

$$\mathcal{T}(E, eU_B, d) = \exp\left[-2d\sqrt{\frac{2m_e}{\hbar^2} \left(\frac{\Phi_s + \Phi_t}{2} + \frac{eU_B}{2} - E_\perp \right)} \right] \tag{2.12}$$

where $E_\perp = E - \hbar^2 k_\parallel^2 / 2m_e$ is the component of the electron energy normal to the sample surface, $k_\parallel$ the electron wave vector parallel to the surface and Φ_s and Φ_t are the work functions of sample and tip, respectively. Here, $\rho^s(\mathbf{r}, E)$ is the LDOS of the sample surface at position $\mathbf{r}$ just below the tip apex, see Fig. 2.3.

A closer look on $\mathcal{T}$ reveals two further properties of the tunneling current. Electrons closer to the vacuum level are more likely to tunnel. This is because their wave function decays less strongly within the barrier than tighter bound electrons (see Eq. 2.1). Furthermore, I is dominated by states around $\bar{\Gamma}$ of the surface Brillouin zone (SBZ) with $k_\parallel \to 0$.

a)

b)

c)
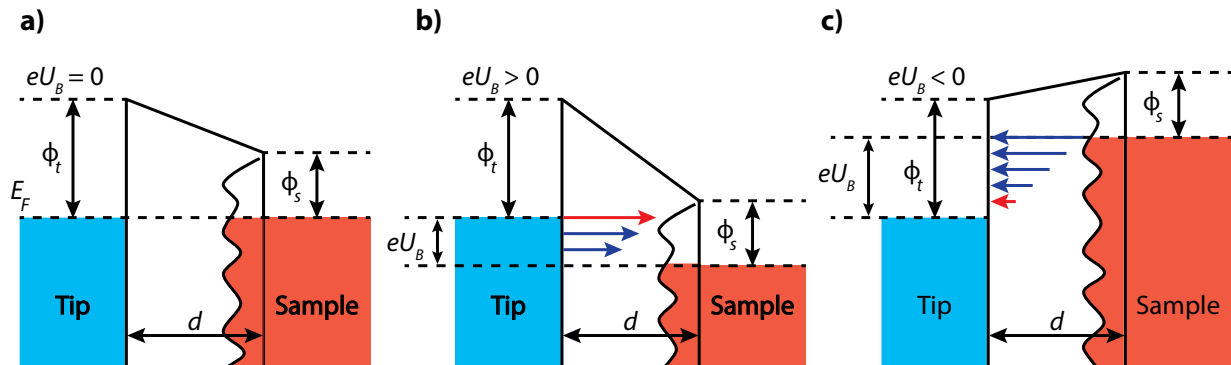
Figure 2.4.: Tunneling scheme for different bias voltages. a) No bias voltage is applied, the tip and the sample are in equilibrium. The rippled line represents the LDOS of the sample. According to Tersoff-Hamann the DOS of the tip is assumed to be constant. **b)** Positive bias voltage applied to the sample. Electrons tunnel from tip to sample and the LDOS of unoccupied states of the sample is probed. **c)** Negative bias is applied. Electrons tunnel from sample to tip. The LDOS of occupied states of the sample is probed. Red arrows mark channels used for spectroscopy measurements when a Lock-In amplifier is involved.

Summary

In conclusion, the following results can be pointed out: The tunneling current and its dependencies are very well understood. I depends exponentially on the tip-sample distance, is influenced by the energy of involved states with respect to the vacuum level and depends on the sample LDOS as well as the applied bias voltage. Due to the metallic nature of the tip, the tip's electronic structure is assumed to be constant and can be neglected. Fig. 2.4 shows schematics of the involved states for three different voltages. When no bias is applied, the net tunneling current is zero. With a positive bias applied to the sample, electrons tunnel from tip to sample. The unoccupied states of the sample and their LDOS are probed. Arrows indicate the relative probability for the electrons to tunnel, which is larger for less bound electrons. When a negative bias is applied, electrons tunnel from sample to tip and occupied sample states and their LDOS are probed.

2.3. Modes of Operation

An STM can be operated in different modes. These can be sorted into three main groups. Some modes focus on microscopy and are used to map the topography of a sample. Some focus on spectroscopy and are used to investigate the electronic (or magnetic) structure at specific spots of the sample surface. A third group combines microscopic and spectroscopic elements to map the surface electronic structure with lateral resolution.

2.3.1. Topography

For topography measurements two modes are utilized that focus on simplicity and speed on the one side and tip protection on the other side. An illustration is given in Fig. 2.5.

Constant-Height Mode

The simpler mode is the constant-height mode. Here the tip-sample distance is fixed at the beginning of the scan. An image of the sample surface is acquired by plotting the tunneling current for each spot of the scanned surface. The value of I is altered when the tip-sample distance is changed, due to variations of height or of the electronic structure of the sample surface. While in this mode the sample can be scanned very fast, chances are high that the tip crashes into the sample, when the surface exhibits a step or the temperature of the system changes. (This leads to an expansion of either tip or sample.)

Constant-Current Mode

This can be prevented by utilizing the constant-current mode. Here I is kept constant for the whole scan by a feedback loop added to the setup. The loop permanently compares the measured current with a preset value. When the measured current is not matching, the tip-sample distance is changed until both values agree again. Due to reduced tip crashes, the constant-current mode got established as the standard mode of topography scans and is used throughout this thesis.

17
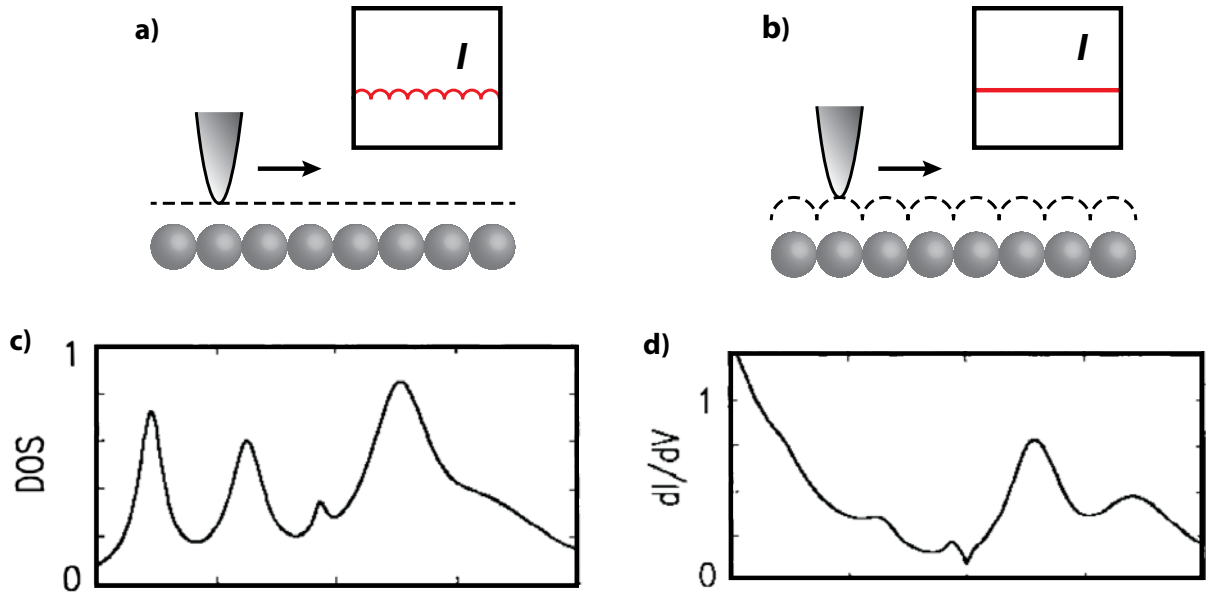
Figure 2.5.: STM modes of operation. Tip movement and measured current in **a)** constant-height and **b)** constant-current mode. **c)** and **d)** Artificial LDOS and derived $\mathrm{d}I/\mathrm{d}U$-curve expected from single-point spectroscopy, taken from [44].

2.3.2. Spectroscopy

As mentioned before, the tunneling current depends amongst others on the LDOS of the sample. The LDOS can be mapped against binding energy by calculating the differential conductance following Eq. 2.9[4]

$$\frac{\mathrm{d}I}{\mathrm{d}U_B} \propto \frac{4\pi e^2}{\hbar} \rho^t(E_F^T)\rho^s(E_F^s - eU_B)\left|M(E_F^s + eU_B, E_F^t)\right| \tag{2.13}$$

Considering the assumptions by Tersoff and Hamann, the differential conductance can be approximated by

$$\frac{\mathrm{d}I(\mathbf{r}, U_B)}{\mathrm{d}U_B} \propto \rho_{LDOS}^s(\mathbf{r}_0, E_F^s + eU_B) \tag{2.14}$$

Hence, to gain information about the LDOS from experiment only the change of the tunneling current ΔI has to be measured (or calculated) in response to a change in bias voltage. The experimental methods investigating energy dependent features are summarized under the term scanning tunneling spectroscopy (STS).

---

[4]Following the Bardeen Ansatz, this approximation of differential conductance is only valid for $eU << \Phi$, with Φ being the work function of the sample given by $\Phi = E_V - E_{\mathrm{F}}$.

2.3.3. Single-Point STS

In order to measure the LDOS distribution for a specific spot of the sample, the tip is fixed at a certain distance above the spot. For this the feedback loop is switched off. Starting at a preset bias voltage U_{stab} (and I_{stab}) the voltage is swept through the desired energy interval and I is recorded. The differential conduction can then be derived by numerical differentiation, or, more commonly, by the use of a Lock-In amplifier. Here, the bias voltage is modulated by a small AC voltage U_{mod}[5] with a typical frequency of $\nu_{mod} = 2 \dots 5$ kHz, an RMS amplitude of $0.5 - 20$ mV and a known phase. The resulting tunneling current is processed by a Lock-In amplifier. The Lock-In filters AC voltages of other frequencies than ν_{mod}, e.g. electronic 50 Hz or random noise, with an extremely narrow bandpass filter, via a cross-correlation with the initial U_{mod}, and gives the desired $\mathrm{d}I/\mathrm{d}U$ signal. At any measured energy the resulting signal is averaged over an energy interval around eU_B, determined by U_{mod}, see red arrows in Fig 2.4. Due to the filter, the resulting curve exhibits a much greater signal-to-noise ratio than the curves derived from a simple I/U curve.

The dominance of tunneling by electrons with highest energy demands a closer look at probing occupied and unoccupied states. For unoccupied states (applying a positive bias) the main contribution of the signal at the given bias stems from electrons tunneling at that energy, red arrow Fig. 2.4 (b), leading to a close resemblance of LDOS and $\mathrm{d}I/\mathrm{d}U$ curve. However, for occupied states, electrons tunneling at the applied bias exhibit the smallest tunneling probability of all involved states, red arrow in Fig. 2.4 (c). Therefore, the resemblance with the sample LDOS is weaker, as contributions from tunneling channels at other energies have a more considerable impact. Fig. 2.5 (c and d) compare an artificial LDOS with a derived $\mathrm{d}I/\mathrm{d}U$ curve expected from the experiment [44]. Indeed, at negative energy the peaks of the $\mathrm{d}I/\mathrm{d}U$ curve are less pronounced than the corresponding ones in the LDOS. Also, the resemblance decreases for higher total bias values. Again, this is due to larger contributions from other tunneling channels and the exponentially growing transmission coefficient (Eq. 2.12).

The energy resolution of STS is limited by the temperature of the system and the energy interval defined by the modulation voltage. For temperatures $T > 0$ the LDOS distribution is broadened by [68]:

$$\Delta E_{\mathrm{therm}} = 3.3 \, k_{\mathrm{B}} T \tag{2.15}$$

Hence, the lower the temperature, the higher the resolution. Tab. 2.1 gives the highest energy resolution achievable for typical temperatures.

The resolution limit resulting from averaging is determined by the amplitude of U_{mod} [69]:

$$\Delta E_{mod} = 2.5 \, eU_{mod} \tag{2.16}$$

---

[5]The value that is labeled U_{mod} is the RMS value A_{RMS} of the AC voltage. The waveform of the AC signal is usually a sine wave. Then the actual amplitude is $A = \sqrt{2} A_{RMS}$.

T	ΔE_{therm}	U_{mod}	ΔE_{mod}	ΔE_{tot}
0.3 K	0.09 meV	0.04 mV	0.10 meV	0.13 meV
4.2 K	1.19 meV	0.5 mV	1.23 meV	1.71 meV
30 K	8.53 meV	5 mV	12.3 meV	14.92 meV

Table 2.1.: STS energy resolution. T and ΔE_{therm} depict typical measurement temperatures and the resulting LDOS broadening when STS are measured at these temperatures [68]. U_{mod} depicts a typical RMS amplitude of modulation voltage used at the given temperature. ΔE_{mod} depicts the LDOS broadening due to the amplitude [69]. ΔE_{tot} gives the resulting total energy resolution.

The overall energy resolution is then described by

$$\Delta E_{tot} = \sqrt{(\Delta E_{\text{therm}})^2 + (\Delta E_{mod})^2} \tag{2.17}$$

Usually U_{mod} is chosen small enough to be negligible. Tab. 2.1 gives also usable modulation voltages for the before mentioned typical temperatures.

Simple STS has no resolution in momentum space as ARPES, but exclusively energy resolution. Therefore, it is a good tool to qualitatively prove the existence of states and investigate changes of LDOS or excitation channels, below and above the Fermi energy (E_F). While based on the same operation principle, spectroscopic experiments that specifically investigate excitations, e.g. vibronic modes, are called inelastic STS (I-STS) [70, 71]. Measurements utilizing a magnetic tip to unravel the spin-resolved LDOS distribution are called spin-polarized STS (SP-STS) [72].

2.4. Combining STM and STS

Several single-point spectra ordered in a grid in real space can be used to investigate spectroscopic changes within an area, e.g. in the presence of an adatom or close to a step edge. In principle, the grid mode can also be used to achieve a map or a set of maps of the LDOS intensity at certain energies. But measuring a grid usually takes several hours even if the lateral resolution is set to much lower values than usually used for real space images. Hence, this approach demands too high requirements concerning stability and holding time for most microscopes. However, single real space images at a particular energy can be measured much faster.

2.4.1. STS Maps

For this, the sample is scanned in one of the topography modes but with activated Lock-In. A so called dI/dU or STS image is measured simultaneously to topography, leading to a mapping of the LDOS at the given bias (Eq. 2.14). As in the case of simple topography, the mentioned scan modes exhibit some advantages and disadvantages. The constant-height mode shows more resemblance with single point STS as in both cases the tip height is fixed. While this mode is applicable for flat surfaces it shows the already known drawbacks on arbitrary surfaces, i.e. the tip either crashes into the sample or the tip-sample distance increases too much to preserve a tunneling junction. While the constant-current mode again lacks these problems, the adjustment to a set tunneling current can influence the resulting map. Imagine a flat surface with a varying LDOS and remember that I is proportional to the LDOS. The feedback loop will compensate the changes of I by adjusting the tip-sample distance. This effect can weaken the dI/dU signal. However, I depends on all tunneling channels, the dI/dU signal depends only on the channels at the applied bias. Changes at these energies only make a small contribution to the overall tunneling current as long as $U_B >> U_{mod}$. If so, the effect can be neglected. For $U_B \approx U_{mod}$, the effect can be compensated by recording $z(x,y)$ in parallel to dI/dU and measuring the $I(z)$-dependence of the tip at U_B [73]. These values are used to normalize the dI/dU signal and one obtains

$$\text{LDOS}(E,x,y) \propto \frac{dI/dU_B(U,x,y)}{I(U_B,z(x,y))} \tag{2.18}$$

It should be noted that the resulting signal contains additional noise due to the exponential $I(z)$ dependency. Hence, these adjustments should only be used when the activated feedback loop has a significant influence on the dI/dU signal, which was not the case for the experiments decribed here.

2.4.2. Analysis of Interacting Electron States

On certain sample surfaces a standing wave pattern can be observed in STS maps, see Fig. 2.6, with STS maps taken on a Cu(111) surface as an example. The waves represent a modulation of LDOS at that energy and stem from the interference of incoming and back-scattered surface electrons[6] at defects, such as point defects or step edges. Therefore the pattern is called quasi-particle interference (QPI). When the bias voltage is changed, the energy of probed states is altered and therefore the wavelength of the pattern is changed, too. In topography images the patterns are only barely visible, as in this case tunneling electrons of multiple energies are overlapping and the resulting wave patterns interfere destructively[7]. The pattern wavelength and its bias dependency provide information about the interaction of surface states and their dispersion.

For a better understanding imagine a 1D electron wave that is back-scattered by a potential barrier located at $x = 0$, see Fig. 2.6 (a). For simplicity, the height of the potential is set to infinity so the electron wave $\psi(x)$ has to vanish at $x = 0$. Then the overall wave function can be written as

$$\psi_E(x) = (e^{ik_x(E)\,x} - e^{-ik_x(E)\,x}) = 2i \sin\left[k_x(E)\,x\right] \tag{2.19}$$

The LDOS is given by the probability density of the state

$$\rho^s(\mathbf{r}, U_B) = |\psi_{E=eU_B}(\mathbf{r})|^2 = 2 - 2\cos\left[2k_x(E = eU_B)\,x\right] \tag{2.20}$$

Here, the term $2\cos\left[2k_x(E = eU - B)\,x\right]$ is responsible for the LDOS modulation and depends on $2k_x$. This is the wave vector k_{LDOS} of the modulation. It is connected to the wavelength of the pattern by

$$\lambda_{\mathrm{LDOS}} = \frac{2\pi}{k_{\mathrm{LDOS}}} = \frac{2\pi}{2k_x} \tag{2.21}$$

Hence, for the described example the wavelength of the modulation is half the wavelength of the electron wave. This relation is generally valid for backscattering.

More importantly, the wave vector k_{LDOS} is identical with the scattering vector $\mathbf{q}$ of the system. In general $\mathbf{q}$ can be written as

$$\mathbf{q} = \mathbf{k}_f - \mathbf{k}_i \tag{2.22}$$

where $\mathbf{k}_i$ and $\mathbf{k}_f$ denote the wave vectors of the incoming and final (reflected) electron.

---

[6]One requirement for a defined pattern is a limited number of scattering vectors. Projected bulk bands are usually quite broad in the SBZ, so many different scattering vectors are allowed.

[7]This changes for small bias voltages, when the number of states probed for topography and STS is similar

In case of backscattering $\mathbf{k}_f = -\mathbf{k}_i$, thus $|\mathbf{q}| = 2\mathbf{k}_i$, or for the given example $|\mathbf{q}| = 2k_x$. This identity connects the observed wavelength λ_{LDOS} with $\mathbf{q}$ by

$$|\mathbf{q}| = \frac{2\pi}{\lambda_{\mathrm{LDOS}}} \tag{2.23}$$

and allows conclusions on the $\mathbf{k}$-dependent band structure of surface states: which states interact and which states do not, as well as the (relative) dispersion and shape of the involved bands.

Mapping q-vectors via FFT

$\mathbf{q}$-vectors can be identified by a Fast Fourier transformation (FFT) of the measured STS image. Here, all involved wave vectors are drawn by mapping their strength (presence in the STS image) depending on $\mathbf{q}$. The resulting maps are called Fourier transformed scanning tunneling spectroscopy (FT-STS) images and the desired $\mathbf{q}$-vectors can be extracted easily, see Fig. 2.6 for an example. Here, STS images taken on the Cu(111) surface and one corresponding FT-STS map are shown. The circular shape in the FT-STS image is drawn by $\mathbf{q}$-vectors representing backscattering within the Cu surface state and is a direct result of the circular constant energy contour (CEC) of the surface state at the measured energy. The area within the ring is brighter than the area outside. This is due to smaller angle scattering of the surface state with smaller $\mathbf{q}$-vectors. Note that the intensity of these vectors is weaker than for backscattering vectors. The backscattering channel is the most likely scattering channel within the Cu(111) surface state. Longer $\mathbf{q}$-vectors are not possible, therefore the intensity outside the ring is within the noise floor.

Due to the fixed relation $\mathbf{q} = 2\mathbf{k}$, FFT pattern stemming from backscattering can be used to construct the band contour of the surface state at that energy. By taking STS maps at various energies the whole $\mathbf{k}$-dependent dispersion can be mapped, Fig 2.6 (i).

Obstacles of Interpreting FT-STS Maps

FFT maps have to be interpreted with care. They can contain features stemming from noise, artificial structures or are deformed due to temperature drift issues. Fig. 2.6 (g) exhibits some of these features. Mechanical or electronic noise leads to dots or vertical stripes (at $|y| \neq 0$) in the FFT image. The edge of the STS image is equivalent to a drastic drop in intensity. Due to this drop the FFT produces bright horizontal stripes (here seen as fringes left and right of the ring) and, in some maps, a vertical line without intensity is going through the image center.

A line of high intensity in the center of the image is due to slight height deviations along the slow scan direction. It can be caused by thermal drift or by atoms being temporally attached to the tip.

Additionally, drift deforms the FFT image as it stretches or compresses the wavelength of real space patterns along particular directions. Therefore, the drift and creep effects have to be reduced as much as possible during measurement in order to get reliable data.

The shape or presence of features also depends on the shape of the tip. A blunt tip might be too dull to resolve the periodicity of some features. These are then either missing in the FFT map, or when the tip is only expanded in certain directions, exhibit an anisotropy.

Finally, the relative intensity of features has to be handled with care. According to Eq. 2.12 the tunneling current is dominated by electrons close to the Γ-point of the SBZ. It furthermore depends on the expansion of surface states into vacuum. Therefore, a strong scattering channel might not be detected, because it involves states with a large $\mathbf{k}$ or states with a strong decay into vacuum. The latter case might be avoided by reducing the tip-sample distance.
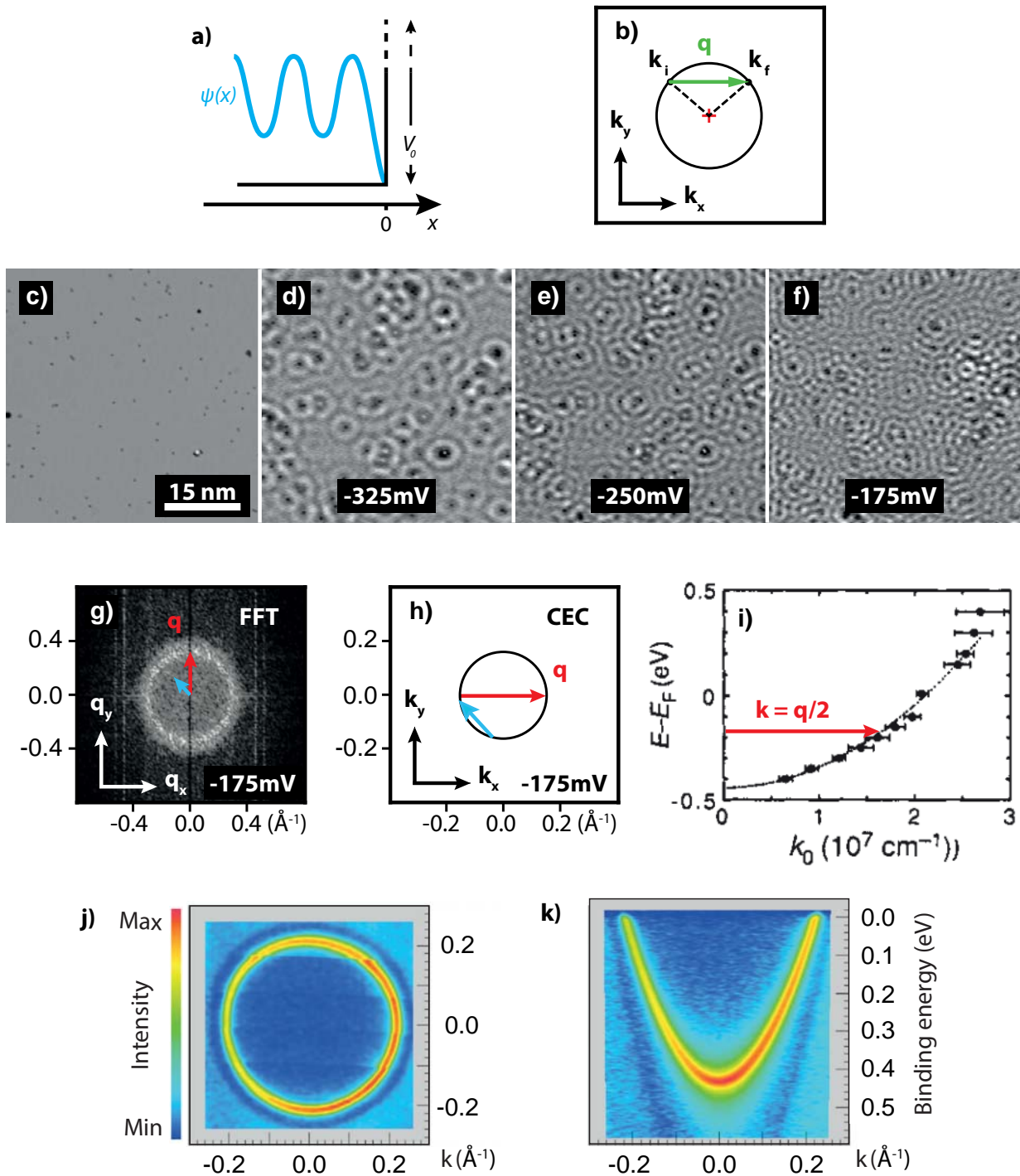
Figure 2.6.: From an STS image to a FT-STS map a) Wavefunction at a potential barrier with infinite height. **b)** Illustration of scattering in **k**-space with scattering vector **q**. **c-f)** Topography and STS images taken at given bias voltages on a Cu(111) surface. $I=4\,\mathrm{nA}$, $U_{mod}=10\,\mathrm{mV}$, **g)** FFT of STS map in (f). The bright ring stems from backscattering of the surface state (red arrow). The increased intensity within the ring originates from scattering channels with shorter **q**-vectors (e.g. blue arrow). **h)** Illustration of the CEC of the Cu surface state at $-175\,\mathrm{mV}$ (circle) with corresponding arrows indicating the same scattering channels as in (g). **i)** Dispersion of the Cu(111) surface state mapped by $\mathbf{k}=\mathbf{q}/2$-vectors taken from various STS maps [74]. **j)** CEC of the Cu(111) surface state measured by ARPES at E_F with the corresponding band dispersion shown in **k)** [75].

25

3. Photoemission Spectroscopy

All STM studies in this thesis are accompanied by photoemission spectroscopy (PES) experiments, namley x-ray photoemission spectroscopy (XPS) and angle resolved photoemission spectroscopy (ARPES). While STM has its strength in real space resolution, photon based techniques have advantages in investigating the electronic band structure. For this, photons of various energies are used to excite sample electrons into vacuum. These photoelectrons are then collected and analyzed by means of energy and propagation direction. XPS is mostly used to identify the chemical composition of a sample, ARPES directly maps the band structure at the surface. For a better understanding of the PES results, a brief description of XPS and ARPES are given in this chapter, following [76].

For both techniques photons of constant energy $h\nu$ are used to excite electrons of a sample with a certain binding energy E_B. Fig. 3.1 provides a scheme. Some electrons, particularly at the surface, are able to leave the sample directly. More general, electrons are excited to a final state E_f and propagate to the surface, incurring eventual scattering, before leaving the sample. The kinetic energy E_k of photoelectrons depends on the energy of the incident beam, E_B of the excited state and on Φ, the energy needed to leave the sample, which is called work function:

$$E_k = h\nu - E_B - \Phi \tag{3.1}$$

X-Ray Photoemission Spectroscopy

To obtain a XPS spectrum [77], the photoelectrons from core levels are collected by a spectrum analyzer and counted depending on their energy. E.g., when a hemispherical analyzer is used, the incoming electrons are discriminated by a circular electric field. An electron multiplier is used to enhance the flux before a detector counts the photoelectron-density. In the resulting spectrum intensity peaks occur at particular energies of probed electron states. The core level binding energies are unique for each element and can be used to identify the composition of a sample. The energy values can slightly change due to different atom environments. Hence, XPS provides information about changes of the sample structure, too.

Angle Resolved Photoemission Spectroscopy (ARPES)

For ARPES the electrons of bands close to the Fermi level are utilized. When leaving the sample, $k_\parallel$ of the electrons is conserved ($k_\perp$ is not conserved, due to the broken translational symmetry at the surface). This conversation can be used to directly map the band structure at the surface of the sample, i.e. resolving the photoelectrons depending on energy *and* $k_\parallel$ [78–80], see Fig. 3.1 (d). With a two-dimensional channel plate detector and a hemispherical analyzer it is possible to collect dispersion images with $I(\Psi, E_k)$, where I is the intensity, Ψ the acceptance angle of the analyzer and E_k, the kinetic energy of the electrons. The signal $I(\Psi, E_k)$ can be translated into an image with $I(k_x, E_k)$. By rotating the sample not only along Ψ but along a second angle Θ, a full map of the 2D surface band structure can be acquired. In a final step the signal $I(\Psi, \Theta, E_k)$ is translated into a dispersion map $I(k_x, k_y, E_k)$.

The mean free path of electrons within solids depends on their kinetic energy and therefore on the used photon energy. For energies typically used in ARPES ($15 - 150$ eV) it is in the range of a few Å. Hence, ARPES is only sensitive to electron states present at or close to the surface of a sample. By tuning the photon energy, the bulk sensitivity can be slightly changed. This is used to indirectly learn about the perpendicular component of the momentum $k_\perp$ as $h\nu \propto \mathbf{k}^2 \propto (\mathbf{k}_\parallel^2 + k_\perp^2)$. It enables to distinguish between surface and bulk states. Surface states have no perpendicular momentum. When the intensity of a band changes with photon energy, it must be a bulk band.

The intensity of an ARPES signal (a PES signal in general) is proportional to the density of states in k-space and photoemission matrix elements. In a single particle picture the lineshape of the spectrum is expected to be a single delta function around the binding energy. But, since the electron is interacting with its environment, its emission perturbs the system left behind, which increases the lifetime of the state and broadens the lineshape of its band. Such bands can be described by a spectral function $A(E, \mathbf{k})$ derived from the one electron Green's function of the system $G(E, \mathbf{k})$, where $A = -(1/\pi) \operatorname{Im} G(E, \mathbf{k})$. The spectral function takes all many-body effects into account and can be written as

$$A(E, \mathbf{k}) = \frac{|\Sigma''(E, \mathbf{k})|}{[E - \epsilon(\mathbf{k}) - \Sigma'(E, \mathbf{k})]^2 + \Sigma''(E, \mathbf{k})^2} \tag{3.2}$$

It exhibits a Lorentzian shape with a maximum at the band energy $\epsilon(\mathbf{k})$, that can be offset by the real part of the self energy $\Sigma''(E, \mathbf{k})$, which describes the quasi particle of the system. The broadening of the Lorentzian is given by the imaginary part of the self energy.
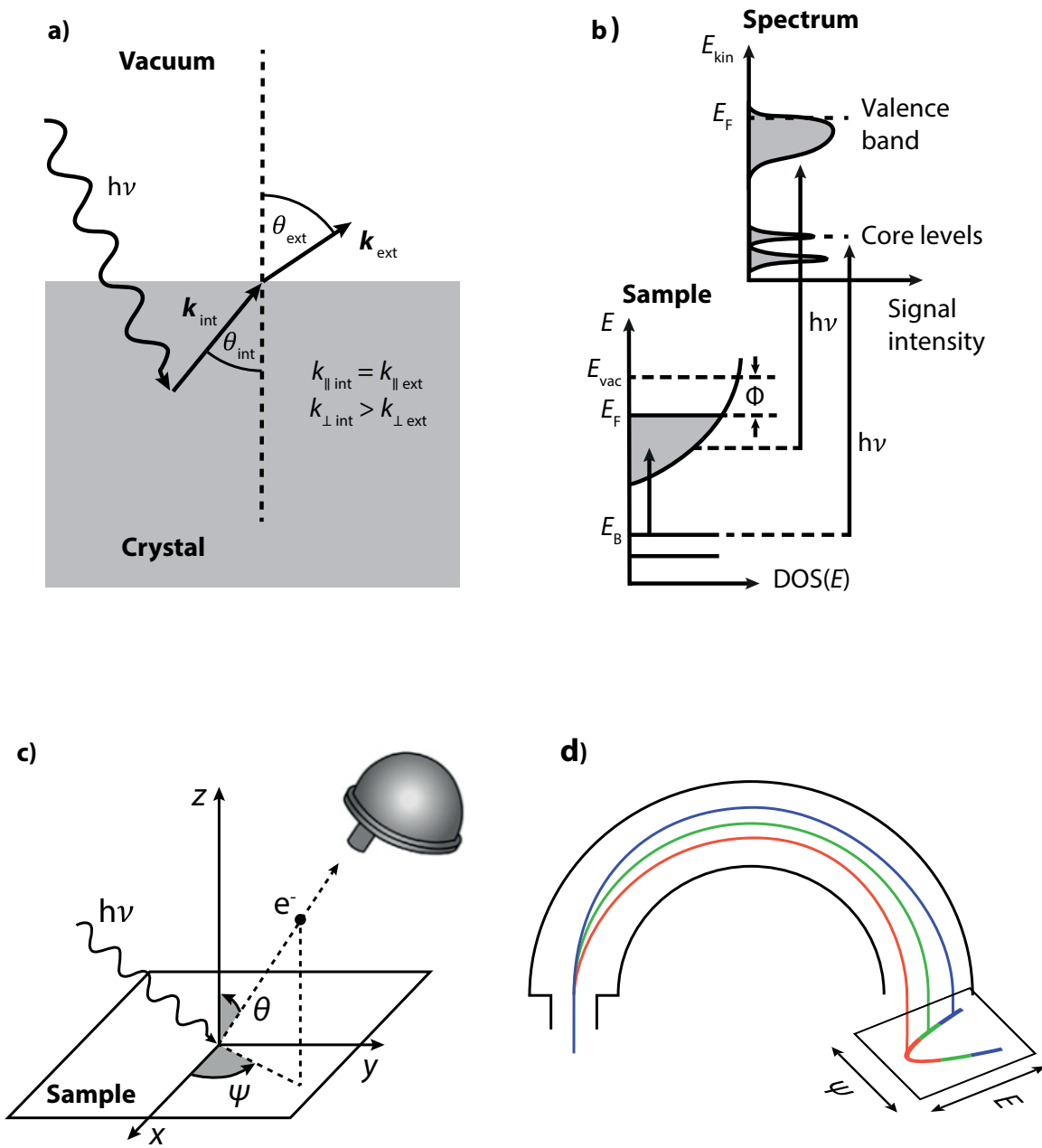
Figure 3.1.: Basic processes involved in XPS and ARPES. Illustration in real space **a)** and energy dependent **b)**. A photon excites a core level electron (XPS) or a valence band electron (ARPES). The electron propagates to the surface where it leaves the sample. Its kinetic energy is reduced by Φ, the work function of the material. $k_\parallel$ is conserved. **c)** Geometry of an ARPES setup with a hemispherical analyzer. **d)** Scheme of the hemispherical analyzer. Within the analyzer a circular electric field is applied that diffracts the electrons depending on their kinetic energy. This allows direct imaging of a part of the sample's band structure.

4. Topological Insulators

The discovery of the Quantum Hall effect (QHE) by Klaus v. Klitzing [81, 82] was one of the great achievements in the field of physics in the late 20th century. The exact quantization of the Hall conductance allowed a new definition of electronic resistance and determines the fine structure constant with extreme precision. Also, this new quantum phase of matter and its effects cannot be described by a spontaneous symmetry breaking [83, 84] as previously described classes, e.g. crystals (translation symmetry), magnets (rotation symmetry) or superconductors (gauge symmetry). A new classification system was needed depending on topological order [85, 86].

Even though an advanced Quantum Hall device would not only provide 1D transport but a net spin polarized transport of electrons, the QHE was never used in mass product microelectronic devices. This is due to the extreme conditions necessary to generate the effect: an ultra clean sample providing a 2D electron gas and a high external magnetic field of at least several Tesla. So it is not surprising, that in the years after its discovery the science community not only tried to find a deeper understanding of topological order, but was also looking for new classes of materials with similar effects that could much easier be achieved. Research, driven by these two motivations, led to the prediction and realization of TIs at the beginning of the 21st century[1].

TIs are insulating in the bulk, exhibit intrinsic metallic (gapless) edge states. The edge states are protected against small non-magnetic disturbances and are called topological edge states (TES). Their dispersion is Dirac-like[2], the bands are spin-polarized, while the spin is locked to the electron's momentum. Consequently, elastic backscattering is prohibited. These features (and the origin of the edge states) arise from an interplay of strong spin-orbit coupling and the time reversal character of the system.

The intrinsic spin-polarization of the edge states makes TIs most promising candidates for future spintronic devices [87]. Interaction with magnetic fields or ferromagnetic material may lead to new types of Quantum Hall Effects [30–32], a new type of magneto-electric-effect [33, 34] or the realization of a magnetic monopole [35]. Interaction with superconductors may create Majorana fermions, which may be utilized as qubits and allow the realization of quantum computers [36].

---

[1]2D TIs were predicted in 2003 [23, 24] and realized in 2007 [27]. 3D TIs were predicted in 2007 [25, 26] and realized in 2009 [28].

[2]Their dispersion is linear as the dispersion of massless particles close to the speed of light described by the Dirac-equation.

Figure 4.1: Schematic TES illustration of a 3D TI. In the 2D k-space the linear dispersion forms a so called Dirac cone. The singularity in the middle of the Dirac cone is named Dirac point (DP). The arrows represent the spin orientation of the electrons. The spins are orientated in-plane and perpendicular to the electron's momentum.
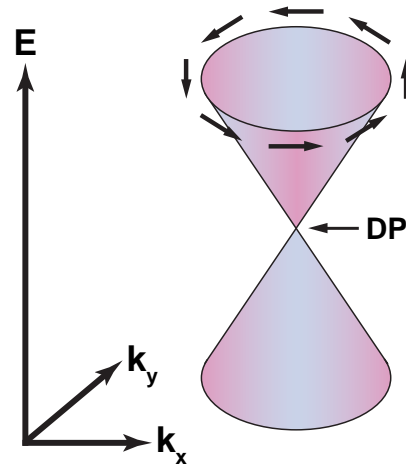
This chapter gives a general view over this most prominent material class. It will start with an introduction to the field of topology, identify the origin (spin-orbit coupling) of the edge states and mechanisms behind their robustness (time reversal symmetry). A method on how to identify TIs and different topological classes in general is given, as well as a method on how to lift the edge state's protection. Later on, a description of the most thoroughly studied TIs is provided: Bi_2Se_3 and Bi_2Te_3. Their features are not only closest to the ones of a perfect TI, they are the prototype samples for this thesis. The spectrum provided here will be sufficient to understand the basic concepts behind TIs and the results of this thesis. For an overall view and a deeper theoretical descrption, I recommend the reviews of Y. Ando [19], M. Hasan & C. Cane [20] and X. Qi & S. Zhang [21], as well as the textbook *Topological Insulators* by S. Shen [22]. If not mentioned otherwise, my introduction follows the recommended book and papers.

4.1. Introduction to Topology

Topology is a very general mathematical concept for the classification of objects and topological spaces. It uses different operations to define classes: Structures belong to the same class, if they can be transformed into each other via continuous deformations. If non-continuous deformations are needed, the structures belong to different classes.

See Fig 4.2 for an example: A ball and a rubber duck belong to the same class. They can be transformed into each other by continuous deformations: stretching and bending. A donut belongs to a different class, as it encloses a hole: To transform a ball into a donut, a hole has to be introduced so the surface. At one point of the transformation different sections of the surface have to be glued together (or torn apart when the donut is transformed to a ball). This is a non-continuous deformation. Classes can be defined by the number of non-continuous deformations needed for a transformation or by topological invariants. In this example by the number of holes:

class $0 := \{ball, rubber\,duck, ...\}$, class $1 := \{donut, ...\}$,...

Note that the classification indeed just depends on the shape of the objects.

Such a topological classification can as well be introduced for energetically gapped materials. Here materials with a different number of band inversions belong to different classes. At first sight these classes can be quite surprising, as they combine materials with very different chemical and physical properties: Atomic insulators, e.g. solid argon, crystalline insulators, e.g. sodium chloride, semiconductors, e.g. silicon, and vacuum[3]. All the men-
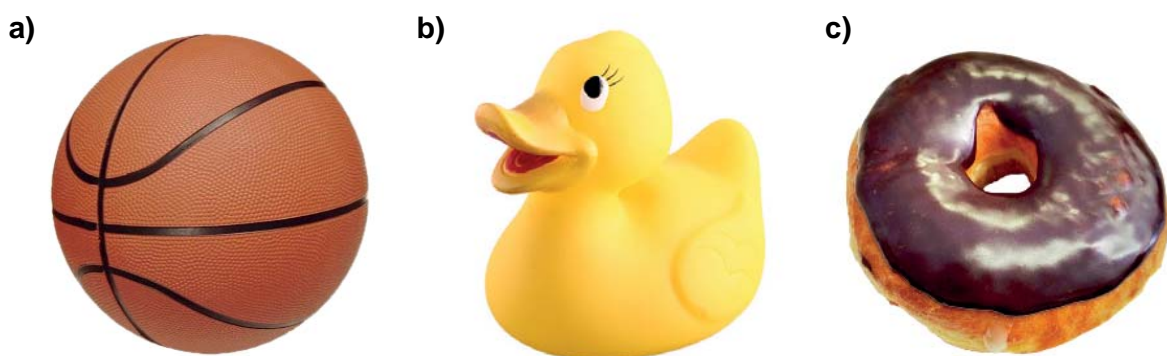
Figure 4.2.: Objects with different topology: A ball **a)** and a rubber duck **b)** have very differnt shapes but belong to the same topological class as both enclose no hole. A donut **c)** encloses a hole and so belongs to a different class. Images are adapted from [88], [89] and [90].

---

[3] In Dirac's relativistic quantum theory vacuum exhibits an energy gap (for pair production), where electron states form a conduction band and positron states form a valence band.

tioned materials do not host a band inversion and consequently they do belong to class 0. On the other hand, common long known insulators are now called TIs, as they host one band inversion and are identified as class 1 materials. Quantum Hall systems with different filling factors all belong to different topological classes[4].

The interface of materials with different topological classes, e.g. TIs and vacuum, is of special interest, as their band structures have to be transformed into each other[5]: The band inversion has to be lifted, the involved bands will cross the gap at the interface. The emerging states within the gap are called edge states.

The mechanisms behind the band inversions and the peculiarities of the edge state protection can be quite different. These differences are used to define different material classes: For Quantum Hall systems a magnetic field forms Landau levels and breaks time reversal symmetry, which is fundamentally needed for the effect. For TIs the band inversion is caused by spin-orbit-coupling. And the topological protection of the edge states depends on the preservation of time reversal symmetry.
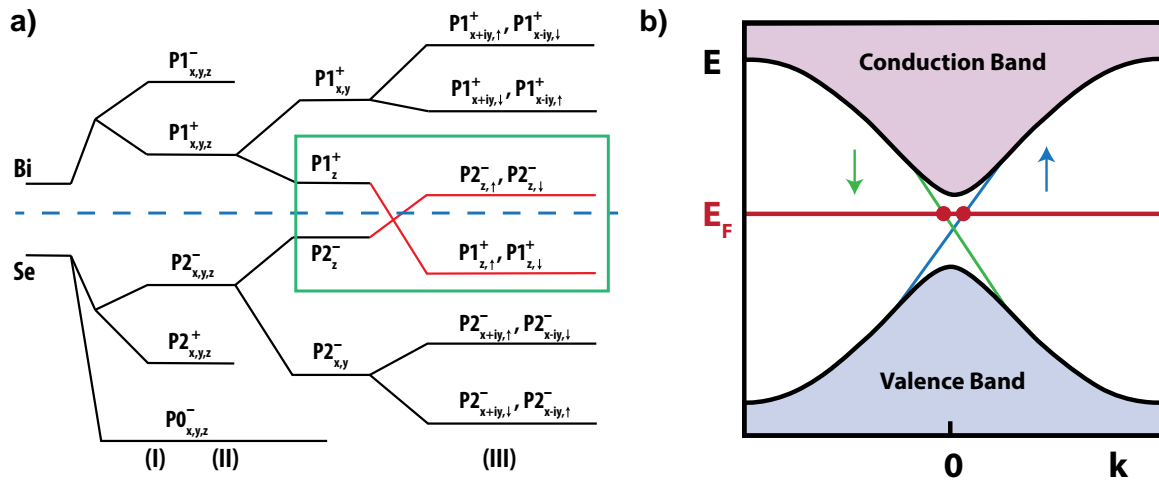
Figure 4.3.: Bi$_2$Se$_3$ band structure evolution, band inversion and edge states. a) Evolution from orbitals to bands for Bi and Se p$_{x,y,z}$ orbitals at Γ point. In three stages (I), (II) and (III) different effects are switched on: (I) chemical bonding, (II) crystal field splitting, (III) spin-orbit-coupling. The blue dashed line represents E_F. The bands inverting are plotted in red. Adapted from [91]. **b)** Illustration of the band structure at the edge of a TI. The TES is given by the green and blue lines. Adapted from [20].

---

[4] The QHE can be described as a gapped system, too. The Hall conductivity is quantized and is given by $\sigma_{xy} = Ne^2/h$. N gives the number of filled Landau levels and is the topological invariant of the system. When calculated via the Kubo formula [85], N is identical with the Chern number C, which will be introduced in Section 4.4. The exact quantization of the Hall conductivity is a manifestation of its topological nature.

[5] Such a transformation is a discontinuous transformation as described before.

4.2. Origin of Band Inversion: Spin-Orbit-Coupling

One key ingredient for TIs are heavy atoms with strong spin-orbit coupling (SOC): In an atom the nucleus holds a large number of (positively charged) protons and so generates a strong electric field or in the rest frame of the electrons: a strong magnetic field. The spin of the electrons orientates along this magnetic field (SOC), causing an energetic shift and splitting of the electron orbitals. In a crystal the electron states form bands that consequently show the same behavior in the presence of a magnetic field: The bands split and shift[6].

In a TI this effect is strong enough to invert the energetic positions of at least one pair of conduction and valence bands with different parity, see Fig. 4.3. In the bulk crystal this inversion has no significant consequences, the gap of the insulator is preserved. This changes at the edge of the system: e.g. the surface. Obviously right at the surface SOC is reduced, since only from one side of the edge a magnetic field is provided. As a last consequence the internal magnetic field drops to zero, resulting in a complete lifting of the band inversion. Or in other words: At the surface the inverted bands cross the band gap and new surface states are introduced.

Their origin is one of the causes for the edge state's robustness: Typical surface states (SS) are caused by breaking the translational symmetry (at the surface). If the symmetry of the surface is broken again, e.g. by dirt on the surface, impurities or a high number of step edges, regular SS can be annihilated. The TES described here are located at the surface, but their cause is the band inversion in the bulk of the crystal. To annihilate the edge states, the band inversion of the whole system has to be lifted.

---

[6]However, the splitting cannot be observed at every point of the crystal. Within the bulk, inversion symmetry forces the bands to be degenerate. At the edge, inversion symmetry is broken and the degeneracy is lifted.

4.3. Time Reversal Symmetry

SOC does not necessarily force the inverted bands to cross the whole gap, since they may avoid a band crossing, see Fig. 4.4 (a) and (b). In addition, it does not suppress the influence of small perturbations like electron localization at impurities. The protection of TES is a consequence of yet another fundamental feature of the hosting crystal: It obeys time reversal symmetry (TRS):

$$E(\mathbf{k}, \uparrow) = E(-\mathbf{k}, \downarrow) \tag{4.1}$$

Protection of TES

For TRS-materials Kramers theorem[7][92] demands electronic bands to be at least two-fold degenerate at the Brillouin zone's high symmetry points $(\Gamma_1, \Gamma_2, ...)$. These points are called Kramers points and the bands that degenerate at Kramers points are named Kramers pairs. This requirement ensures a completely closed bulk band gap.

Spin Locking and Orientation

In the presence of SOC the degeneracy of TES *in between* two Kramers points is lifted. As a consequence, the bands are not only degenerate but have to cross each other, as TRS demands different spin polarization on opposite sides of the Kramers points.

Hence, at all k of the SBZ the spin has to follow the electron's momentum, i.e. the spin is locked to the momentum. This behavior is called helical[8], see Fig. 4.4 (c).

Additionally to the locking, SOC reduces the spin degree of freedom even further. The spins are orientated in the same plane as the momentum as long as the band pair forms a circle on a constant energy contour as in Fig. 4.4 (c): The effective magnetic field is proportional to the cross product of their momentum and the gradient of the electrostatic potential. Since the potential gradient is normal to the edge and the momentum of the TES is in-plane (along the edge), the spin orientation is also in-plane but perpendicular to the electron's momentum.

---

[7]Kramers theorem is valid for quantum mechanical systems with a half-integer total spin.

[8]In this thesis I follow the definition of *Wu et al.* [93]: In TIs, edge electrons with opposite spin have to counter-propagate at a given edge. This behavior is called *helical*. This is in contrast to edge electrons of the QHE: In that case electrons with opposite spin propagate in the same direction (as there is only one direction and TRS is broken). This behavior is called *chiral*.
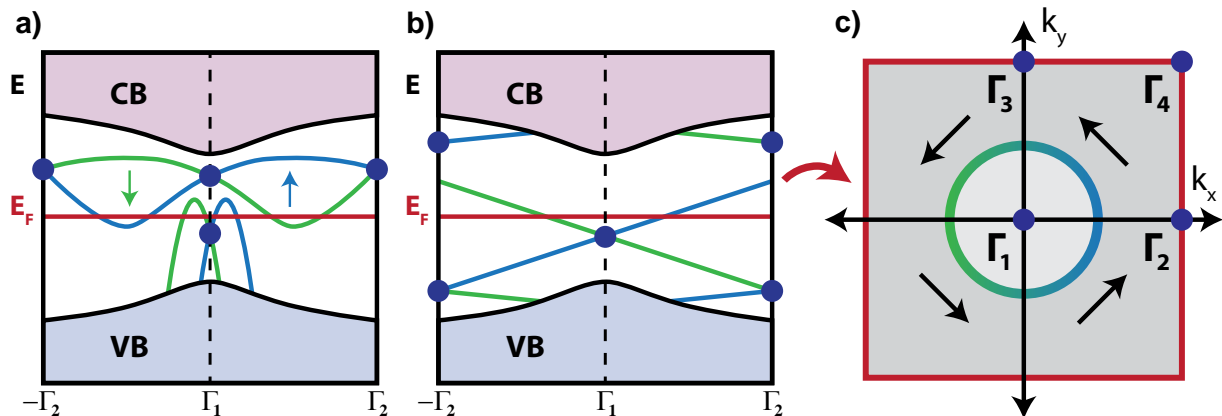
Figure 4.4.: Illustration of trivial and topologically protected (non trivial) edge states with SOC according to Kramers Theory: At Kramers points (filled dots) the bands are degenerate. Away from Kramers points the degeneracy is lifted. Different band colors mark opposite spin orientation. **a)** trivial states cross E_F an even number of times. **b)** Non-trivial states cross E_F an odd number of times. **c)** Constant energy contour of (b) at E_F. TRS demands spin locking for the edge states (non-trivial and trivial). SOC leads to an in-plane orientation of the spins.

Dirac Dispersion

When the non-degenerate bands cross at Kramers points, they exhibit a linear dispersion. A linear dispersion is usually known from relativistic, mass-less fermions described by the Dirac-equation. Hence, the electronic structure of TES around Kramers points is called Dirac cone (DC), as the states, depending on their dimensionality, either form two cones meeting at Kramers point (3D TIs) or a cross section of two connected cones (2D TIs). The meeting point of the cone is called Dirac point (DP), see Fig. 4.1. The linearity of the dispersion leads to an higher mobility of TES compared to regular surface states [19].

Other systems exhibit Dirac cones as well, e.g. graphene [94]. These systems always exhibit an even number of Dirac points as demanded for TR invariant systems by the fermion doubling theorem. However, TRS can circumvent this axiom by merging into the bulk bands. Via bulk bands they are connected with the Dirac cone on the opposite edge of the system, which technically leads to an even number of cones [93].

Suppressed Backscattering

In principle an electron spin can switch when the electron is scattered by an impurity. However, due to destructive interference of all possible scattering paths, elastic backscattering is forbidden for TIs as long TRS is preserved: The electron can either take a clockwise or a counter clockwise turn around the impurity. TRS determines the spin to rotate by an
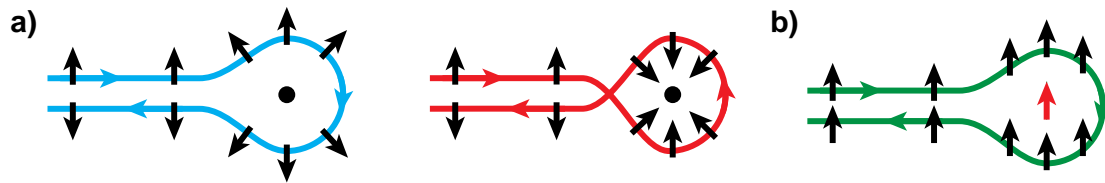
Figure 4.5.: Possible paths of backscattering: a) illustrates backscattering at a non-magnetic impurity. The electron can take a clockwise (left) or counter clockwise (right) turn around the impurity. In both cases the spin is locked to the momentum and rotates by an angle of π or $-\pi$ respectively, causing destructive interference between both paths, i.e. avoided backscattering. **b)** Illustrates backscattering at a magnetic impurity. The spin of the electron orientates itself with respect to the magnetic moment of the impurity. This is the case for all paths, leading to a non-destructive interference. Backscattering is allowed.

angle of π or $-\pi$, see Fig 4.5 (a). This 2π difference leads to a destructive interference of the wave functions of both paths [95]. Any other kind of scattering, including inelastic backscattering, is not suppressed by TRS. When TRS is lifted, e.g. at a magnetic impurity, Fig. 4.5 (c), the spin is not forced to rotate but orientates itself with respect to the magnetic moment of the impurity. The interference of all backscattering paths is non-destructive, i.e. backscattering is allowed.

Anti-Localization

The absence of backscattering causes another fundamental property of TES: weak anti-localization. In trivial systems the electronic conductivity decreases with decreasing temperature, due to Anderson localization. At low energy (temperature) the Coulomb potential of impurities is strong enough to pin electrons [96, 97]. The destructive interference of backscattering paths for TES quenches the probability of this localization [98]. Weak anti-localization is indicated by an odd multiple of π in the system's Berry phase. As can be seen in the next section, this property is also useful for identifying the topological nature of a system.

4.4. Identifying Topological Insulators

At E_F all present bands form Fermi surface pockets. Dirac cones form a pocket enclosing high symmetry points with the spin rotating along the curvature of the pocket, see Fig. 4.4 (c). Also the lower bands in (a) form two pockets enclosing Γ_1 at E_F. According to Berry [99], the full rotation of the spin along the curvature of the pocket will add a phase factor to the electron's wave function, the so called Berry phase:

$$\mathcal{A}_m = i \langle u_m(\mathbf{k})| \nabla_k |u_m(\mathbf{k})\rangle \qquad (4.2)$$

where $\mathcal{A}_m$ represents the Berry phase, and $|u_m(\mathbf{k})\rangle$ the Bloch wave functions of a specific band m of the SBZ.

The Berry phase for a full spin rotation is π. Pockets not enclosing a high symmetry point will not gain a Berry phase as they are formed by single bands, e.g. the ones formed by the upper bands in Fig. 4.4 (a), the spin is not rotating along the curvature of the pocket.

Pairs of trivial bands will always cross E_F an even number of times. Either they are degenerate with the same partner at all Kramers points, or both ends of the band are connected to the same bulk band and never fully cross the gap, see Fig. 4.4 (a). TES cross E_F an odd number of times as they switch partners at Kramers points and cross the gap, see Fig. 4.4 (b). Hence, the contribution of trivial states to the system's Berry phase is always an even multiple of π, while the contribution of TES is an odd multiple of π.

Chern Number

This marks a fundamental difference between trivial and non-trivial systems and can be used for defining topological invariants that identify the topology of the system.

Via the Berry flux

$$\mathcal{F}_m = \nabla \times \mathcal{A}_m \qquad (4.3)$$

the Chern number of the system can be calculated by taking all occupied bands into account with

$$C = \frac{1}{2\pi} \sum_{m=1}^{N} \int \mathcal{F}_m d^2\mathbf{k} \qquad (4.4)$$

Calculating the Chern number is a powerful tool to identify the topology of a system. Due to the integral, it is independent of peculiarities in the SBZ, like degeneracies of bands. This underlies the topological nature of the Chern number.

It does actually not depend on the presence of TRS and, with small changes, can be used for different classes like Quantum Hall systems, TIs, Topological Crystalline Insulators or Topological Superconductors. However, it is a rather complex method as all Bloch vectors of the SBZ have to be known.

$\mathbb{Z}_2$ **Topological Invariant**

In the special case of TIs, where TRS[9] is obeyed, a new topological invariant can be defined just depending on the parity eigenvalue of the occupied bands at given Kramers points of the system. Or in other words, the number of times E_F is crossed by Dirac cones [25]:

$$(-1)^\nu = \prod_i \delta_i \quad with \quad \delta_i = \prod_{m-1}^{N} \xi_{2m}(\Gamma_i) \tag{4.5}$$

Here, $\xi_{2m}(\Gamma_i)$ represents the parity eigenvalue of the 2mth occupied band at Γ_i and ν the new topological invariant. Since the parity eigenvalue is limited to ± 1, $\nu \in \mathbb{Z}_2$, i.e. its values are either 1 for an odd number of band pairs crossing E_F or 0 for an even number of band crossings.

---

[9]This method was developed for TIs obeying TRS *and* inversion symmetry, $E(-\mathbf{k}) = E(\mathbf{k})$. However, respecting inversion symmetry is not needed as long as the TI can be deformed into a system obeying inversion symmetry without closing the gap [25].

4.5. Disturbing the Topological Phase

The TI phase depends on the band inversion and time reversal symmetry. It is crucial to find and characterize effects that lift or disturb these requirements, either to avoid perturbations or use them specifically for manipulation.

Lifting TRS via Magnetic Perturbations

It has been shown that TRS is crucial for the protection of edge states. If TRS is lifted, the edge states will avoid a crossing at Kramers points, a gap opens and the insulating property is restored. The resulting cones become *massive* as, due to the avoided crossing, the dispersion is not linear anymore. Hence, the mobility of the electrons is lowered. Also backscattering is now allowed and Anderson localization takes place [19].

A magnetic structure or field naturally breaks TRS depending on its orientation. The behavior can be deduced from the surface Hamiltonian[101]:

$$\mathcal{H}_S = v_F \boldsymbol{\sigma} \cdot \mathbf{p} + g\mu_B \mathbf{B}\boldsymbol{\sigma} \tag{4.6}$$

where v_F denotes the Fermi velocity, g the effective Landé factor of the TES electrons, $\boldsymbol{\sigma}$ the vector containing the Pauli matrices σ_x, σ_y and σ_z acting on the electron's spin and $\mathbf{p}$ the electron's momentum. For a magnetic field with an out-of-plane component a gap opens at DP, with the size depending on the strength of the out-of-plane component: $\Delta E = 2g\mu_B B_z$. For an in-plane magnetic field the cone remains intact but is shifted in momentum space to $\mathbf{p}_{xy} = -g\mu_B \mathbf{B}_{xy}/v_F$. (See Fig. 4.6 for an illustration.)
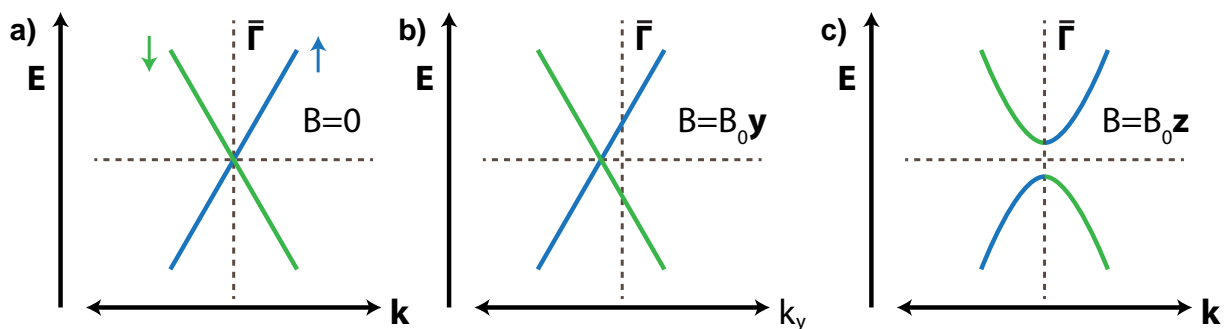
Figure 4.6.: Dirac cone with an applied magnetic field: a) no magnetic field, **b)** Magnetic field orientated in-plane to the spins of edge states. The cone shifts along the axis of the magnetic field. **c)** Magnetic field perpendicular to the spin orientation. A gap opens at the Dirac point. The dispersion is not linear, the electrons become massive. Adapted from [100].

Magnetic perturbations have different effects if they act on the edge locally, influence the whole edge or influence the whole crystal. A single magnetic impurity introduced to the edge of a TI will lift the protection against backscattering locally, see Fig. 4.5: The incoming electron will orientate its spin with respect to the impurities' magnetic moments. Different backscattering paths do not interfere destructively any more and Anderson localization is allowed.

If the number of magnetic impurities on the edge is increased, at some point TRS will break along the whole edge. A gap opens at DP with all its consequences. Fig. 4.6 illustrates this behavior. Additionally, the influence of a magnetic perturbation orientated in the same plane as the TES spins is shown. The Dirac cone shifts along the direction of the applied perturbation, but its structure is preserved: no gap opens, the linearity is preserved and backscattering remains suppressed.

Bulk doping [102] or the application of a magnetic field with a certain strength [20] can lead to the same behavior.

Changing the Crystal Structure

The TES robustness depends on an odd number of Dirac cones at a given edge. The oddness is only established by localizing two partner cones on opposite edges. The bulk prevents the two cones from interacting with each other. When the thickness of the system is lowered, at some point the cones will start to interact via quantum tunneling. This lifts the protection and the cones will hybridize[103][10]: a gap opens, backscattering and Anderson localization is allowed[105].

So far it was stated that impurities not breaking TRS have no influence on the topology of the system. This is only valid for small perturbations. TIs are crystals and so their features (and description) depend on the integrity of their crystalline structure. If the integrity of the system is destroyed globally, there will be no periodic potential, no band structure, no symmetries. Hence, the system is not a TI anymore.

The question arises: What happens when the topological interface (the edge) is disturbed in such a way? Will the edge state shift into the bulk to a region where the crystalline integrity is still sustained? Or will the TES remain in the perturbed region, but too delocalized to form a Dirac cone? In fact, both scenarios are predicted by theory and depend on the strength of the perturbation [106]. In chapters 7 and 8 the predictions are tested by experiment.

---

[10]This thickness limit is rather small. E.g. for Bi_2Se_3 a gap is only established for a thickness less than 6 quintuple layers (6 nm) [104].

4.6. Topological Insulators of Different Dimensionality

Topological insulators have been predicted and been proven to exist in two and three dimensions[11]. The dimensionality has no influence on the fundamental features (which is why it was not introduced so far), but reducing dimensionality reduces the degrees of freedom available to edge states and so influences their robustness.

2D Topological Insulators

2D TIs have 1D edge states. As mentioned before, edge states can be described as a cross section of two cones meeting at their tips. Due to their 1D nature at a given energy, only two states are possible at a given k. One is $k, (\uparrow)$ and one $-k(\downarrow)$. Since backscattering is suppressed and no other states exist, the electron transport is ballistic and (non-magnetic) impurities are circumvented, see Fig. 4.7. Due to the resemblance to quantum Hall systems (1D edge states and ballistic transport), 2D TIs are also called *Quantum Spin Hall* systems. However, the edge states of QHE systems show chiral rather then helical behavior.
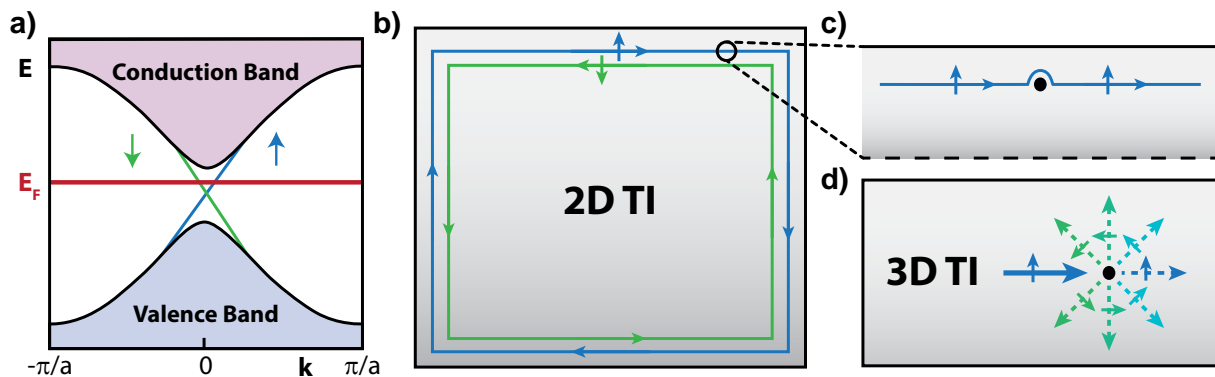
Figure 4.7.: 2D and 3D TIs: a) Edge state dispersion of a 2D TI. The bands form a cross section of two cones meeting at the tips. **b)** Each edge hosts two transport channels with opposite direction and spin. **c)** Due to suppressed backscattering, non-TRS breaking impurities are circumvented. **d)** For 3D TIs direct backscattering is forbidden, too. Other scattering directions are still allowed.

---

[11]2D TIs were predicted in 2003 [23, 24] and realized in 2007 [27]. 3D TIs were predicted in 2007 [25, 26] and realized in 2009 [28]. Also one-dimensional systems with a 0D edge state might have been identified, but this is still highly controversial[107–109].

3D Topological Insulators

3D TIs have 2D edge states, which form a Dirac cone in momentum space, see Fig. 4.1. Hence, there are several scattering channels available, which are not suppressed by TRS, Fig. 4.7 (d). Anti-localization is still observed, but electron transport is diffuse rather than ballistic. Along the already introduced $\mathbb{Z}_2$ topological invariant ν_0, for the description of 3D TIs three additional $\mathbb{Z}_2$ invariants have to be introduced [110, 111]: $\nu_1\nu_2\nu_3 \rightarrow (\nu_0; \nu_1\nu_2\nu_3)$. A crystal with $\nu_0 = 1$ is called a *strong TI* and exhibits all the features described so far. It depends on all Kramers points of the SBZ and hence describes the topology of the system. ν_1, ν_2 and ν_3 can be seen as Miller indices as they count Dirac points along high symmetry planes of the crystal. If $\nu_0 = 1$ and $\nu_i = 1$ for a particular $i = 1, 2, 3$, the system is called a *weak TI* . It exhibits edge states too, but these are not preserved by TRS as the number of enclosed Dirac points will always be even. Interestingly, a weak TI can be constructed by stacking 2D TIs[111]. For simplification, strong TIs are usually just referred to as TIs.

4.7. Applications and New Effects

It has been shown that TIs come with some unique features: Strong SOC leads to a band inversion in the bulk. At the edge to materials without strong SOC, the band inversion is lifted and the bulk band gap is crossed. The resulting Dirac cone is spin-polarized and protected by time reversal symmetry. Especially the natural spin-polarization of the TES makes TIs a highly interesting material class for future applications. The realization of spin-dependent electronics depends on devices that reliably generate highly spin-polarized currents[12][11, 87, 112]. These can be realized by sending a current through a TI. The spin-polarization can be changed by adjusting E_F, e.g. via a gate voltage, as the spin-polarization of the Dirac cone is inverted on opposite sides of the DP, see Fig 4.7 [113].

Besides the utilization of intrinsic properties of TIs, new effects can be created, when TIs are combined with other materials.

---

[12]Besides spin generation, a reliable spin-transport is fundamental for spintronic circuits. However, the applicability of TIs is limited for this purpose. In 3D TIs, electrons can be scattered into any direction. Due to the spin locking, the spin orientation has to change with every change of direction. For 2D TIs, spin locking protects electrons from scattering (for most perturbations), but so far no usable 2D TIs have been realized. However, graphene is a promising candidate for solving the transport issue [87].

Surface Half Integer QHE

As a 2D system, the TES of a 3D TI can exhibit Landau quantization in presence of a magnetic field. However, due to the linear, helical dispersion, the Landau levels show some peculiarities [32]. Quantization occurs according to:

$$E_\pm(N) = \pm\sqrt{(2e\hbar v_F^2 B/c)N} \tag{4.7}$$

i.e. Landau-level spacing is proportional to $\sqrt{N}$ when the Fermi level is changed. Moreover, a zeroth Landau level exists with $N = 0$ right at E_F. Other LLs are arranged symmetrically around the zeroth level[13]. This behavior of LL in TIs is similar to the behavior of LLs in graphene, as both systems exhibit (linear) Dirac cones. However, since the Dirac cone of a TI is spin-polarized, the Hall conductivity is half integer quantized[14]:

$$\sigma_{xy} = -\frac{e^2}{h}\left(N + \frac{1}{2}\right) \tag{4.8}$$

However, the half-integer quantization is impossible to measure via dc transport measurement setups. At the rim of a finite sample, where the leads are attached, opposite surfaces are connected, leading to a simultaneous use of edge states of both surfaces. This results in an integer quantization of the edge current. Still, the Landau levels can be probed via STS. By identifying the zeroth LL, the Dirac point can be determined and the linearity of the TES can be proven. The occurrence of Landau levels also provides an estimate of the purity of the sample, since LLs are suppressed, when the impurity distance is in the range of the magnetic length ($l_B \sim \sqrt{\hbar/eB}$)[32].

Anomalous QHE

An effect similar to the QHE, called *anomalous quantum Hall effect* can be archived when a thin ferromagnetic layer hosting a domain wall is introduced to the surface of a TI [30, 31]. If E_F is located in the gap of the now splitted Dirac cone, a half-integer Hall conductance is induced at the interface with $\sigma_{xy} = e^2/2h$, with opposite signs for opposite spin-polarized domains of the ferromagnet. At the domain wall, the Hall conductance jumps by a factor of e^2/h, leading to a chiral edge state along the wall with an integer quantization: $\sigma_H = e^2/h$.

---

[13]This holds, as long as the Landau levels are not suppressed due to the presence of bulk bands [32].

[14]In ordinary metals the LL spacing follows $\hbar\omega = e\hbar B/m_c c$, with m_c the cyclotron mass and is independent of E_F. There is no zeroth Landau level, the levels are equally spaced, the Hall conductance is in principle half-integer quantized. For an example see [114]

Topological Magnetoelectric Effect

A magnetoelectric effect is defined as a magnetization induced by an electric field or a charge polarization induced by a magnetic field. When an electric field $\vec{E}$ is applied parallel to the surface of a half-integer QHE system, the resulting magnetization is given by $\mathbf{M}\,\alpha\,E$ with $\alpha = e^2/2h$. Hence, the magnetization shows a fingerprint of the half-integer quantized Hall conductivity [33, 34]. The topological magnetoelectric effect would give rise to an image magnetic monopole, when an electric charge is brought into proximity of a 3D TI [35].

Superconducting Proximity Effect and Majorana Fermions

When a 3D TI is interfaced with a superconductor (SC), the latter one might induce Cooper pairs into the interface (proximity effect). Then, a superconducting energy gap is realized within the TES and the resulting 2D superconducting state exhibits properties typical of edge states: it is not spin-degenerate, has got only half the degrees of freedom of a normal metal and obeys TRS. Moreover, the creation of a Majorana fermion zero mode is predicted, which can be bound to a vortex (antidot) in the SC [36]. Majorana fermions [115][15] are their own anti-particles and therefore electrically neutral and cannot possess a magnetic moment. Since they are their own anti-particle, they represent a degenerate two level system which can be used as a qubit. Hence, Majorana fermions are proposed to be one of the possible basic modules for realizing a quantum computer [36].

---

[15]Ettore Majorana found a modification of the Dirac equation that only involves real numbers (instead of involving complex numbers, too). In his equation spin half particles can be their own anti-particles. These pairs are called Majorana Fermions. For decades, no Majorana fermions were identified in experiment. However, recently there is evidence that neutrinos are Majorana fermions [116]. While there is no experimental result so far proving the particle/anti-particle nature of neutrinos, a fingerprint of Majorana fermions might have been found for the topologically protected SC [117]. However, a final proof for Majorana Fermions has not been demonstrated yet (in general).

4.8. Prototypical Topological Insulators

So far TIs have been treated theoretically. The mechanisms leading to TES were explained, their properties described and possible applications as well as new effects presented. Based on this description, it is easy to define an ideal TI: A system with a well defined, large, direct energy gap hosting a single, linear Dirac cone stemming from band inversion. E_F is located at the DP in the middle of the gap, but can be tuned without further effects on the band structure. In general, an ideal material is easy to grow. Realizing an ideal system is rather complicated. In fact, the systems identified first as 2D and 3D TIs are far from being ideal TIs.

The first verified TI, HgTe/(Hg,Cd) Te quantum wells [27], depends on mercury as the key ingredient. But Mercury permanently contaminates molecular beam epitaxy (MBE) chambers, hence the number of research groups capable of growing these kind of samples is still very limited and no other significant paper has been published so far on systems containing Mercury. For the first realized 3D TI, $Bi_{0.9}Sb_{0.1}$, E_F is crossed five times by TES bands and the bulk band gap exhibits only a size of several 10 meV [118]. Additionally, alloys as $Bi_{0.9}Sb_{0.1}$ tend to induce impurity bands into the bulk gap, which might interact with the TES.

Most of these obstacles are avoided with the so-called second generation 3D TIs, Bi_2Se_3 and Bi_2Te_3. These samples are fairly easy to grow and host a single Dirac cone [29, 91, 119], see. Fig. 4.8. Bi_2Se_3 comes with a bulk band gap of 300 meV and exhibits an isolated Dirac point, located at E_F. The band gap of of Bi_2Te_3 is 150 meV. DP is located well below E_F, surrounded by bulk bands. In both cases the gap is much larger than the thermal energy at room temperature. The large gap as well as the single Dirac cone make Bi_2Se_3 and Bi_2Te_3 not only prime candidates for future applications, but ideal samples for experiments, e.g. for testing predicted intrinsic TES properties, or the behavior of the Dirac cone in response to perturbations. Bi_2Se_3, Bi_2Te_3 and related systems are the prototype samples investigated in this thesis. This section provides an overview of the crystal and electronic structure of Bi_2Se_3 and Bi_2Te_3 and gives examples of fundamental behavior of their TES in presence of perturbations.

Bi$_2$Se$_3$ and Bi$_2$Te$_3$ Crystal Structure

Bi$_2$Se$_3$ and Bi$_2$Te$_3$ grow in a rhombohedral crystal structure. The unit cell of Bi$_2$Se$_3$ is shown in Fig 4.8 (c) as an example (For Bi$_2$Te$_3$ the selenium atoms have to be replaced by tellurium atoms). The primitive cell is marked by black arrows and consists of five atoms. Along the z-axis the unit cell holds 3 quintuple layer (QL) (see (d) for greater detail), in which selenium and bismuth layers are alternating. Within a QL the atoms are covalently bonded, while coupling between QL is only established by van-der-Waals forces. The lattice constants are given in Tab. 4.1. Crystals can be grown by the Bridgman method [19] or epitaxially [120]. The growth is stoichiometric, which leads to a greater purity as compared to alloys such as Bi$_{0.9}$Sb$_{0.1}$. Especially epitaxially grown films exhibit a very low density of defects [32]. Due to the van-der-Waals bonding between QL, crystals can easily be cleaved with the scotch-tape method, see section 5.2.2, a simple approach to obtain clean surfaces.

A Closer Look on the Electronic Structure

The large band gap of Bi$_2$Se$_3$ protects the circular shape of the Dirac cone at constant energy. For Bi$_2$Te$_3$ the coexistence of bulk bands below E_F and hence the presence of a strong Coulomb potential, warp the cone. This leads first to a hexagonal-shaped, then to a star-shape contour at constant energy [122], Fig. 4.9. This warping also influences
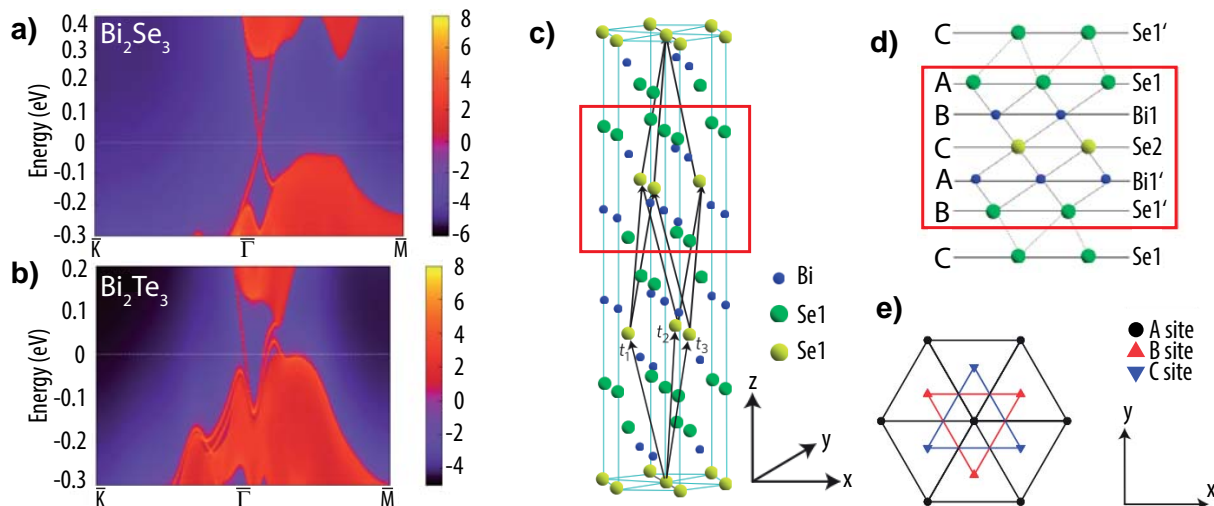
Figure 4.8.: Structure and band structure of Bi$_2$Se$_3$ and Bi$_2$Te$_3$ **a)** Surface band structure of Bi$_2$Se$_3$. **b)** Surface band structure of Bi$_2$Te$_3$. **c)** Crystal structure of Bi$_2$Se$_3$. The red square marks a QL. **d)** A QL in greater detail. **e)** Stacking sequence for sites A, B and C. Adapted from [91]. For a visualization of Bi$_2$Te$_3$ crystal, the Se atoms have to be replaced by Te atoms.
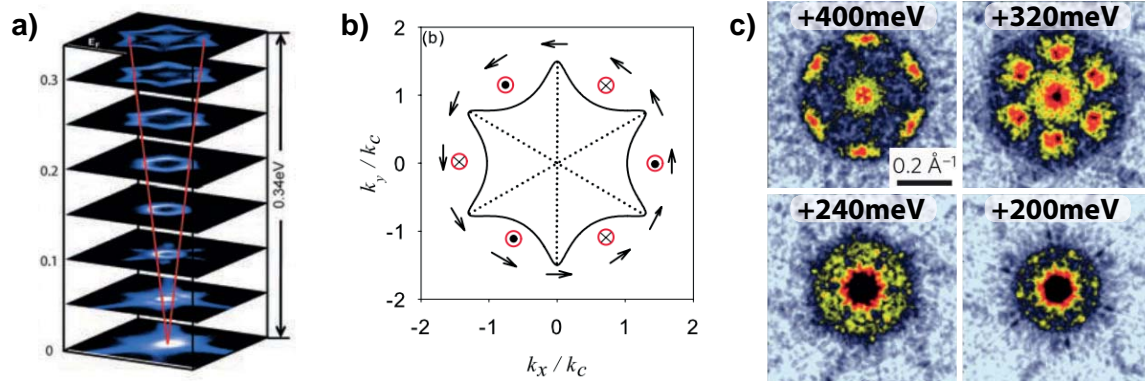
Figure 4.9.: Warping of the Bi_2Te_3 Dirac cone: a) ARPES measurements of the cone. Away from the Dirac point the contour gets more and more warped [122]. **b)** Spin orientation of a hexagonal contour. Only at the edges the spin remains in the xy plane. In the valleys the spin is pushed out-of-plane with alternating signs. Solid circles (crosses) refer to S_z being along $+\hat{z}(-\hat{z})$ [123]. **c)** Fourier transforms of QPI patterns at different energies from a Bi_2Te_3 sample [125].

the spin orientation. While the spins remain oriented in the xy-plane at the edges of the star, the spins are rotated out of the plane in between, with alternating directions for neighboring valleys [123]. This highly influences the scattering behavior of the TES, since the scattering between pockets with the same out-of-plane spin orientation is enhanced due to a large number of similar q-vectors. And scattering between pockets with opposite out-of-plane spin orientations is suppressed [124].

Due to its large direct band gap and hence less warped Dirac cone Bi_2Se_3 is a more ideal TI. However, Bi_2Te_3 enables an easier access for probing the system and for studying the topological state: For STM a large band gap is disadvantageous as it reduces the sample's conductivity around E_F. Moreover, warping leads to an increased signal in QPI maps. Hence, Bi_2Te_3 has been used first to prove the linearity and helical property of a TIs Dirac cone [124]. This established Bi_2Te_3 as the standard system for FT-STS measurements.

	Bi_2Se_3	Bi_2Te_3
a	4.14 Å	4.38 Å
c	28.64 Å	30.51 Å
$c_{1/3}$	9.55 Å	10.17 Å

Table 4.1.: Lattice constants of Bi_2Se_3 and Bi_2Te_3: a: lateral lattice constant, c: lattice constant along z-axis. $c_{1/3}$: height of a QL. [121]

49

Influence of Bulk Doping

The large band gap and the small density of edge states of Bi_2Se_3 and Bi_2Te_3 lead to a high sensitivity of the electronic structure towards electronic disturbances. All growth methods known so far exhibit more or less selenium (tellurium) vacancies [126–128], inducing a global downward shift of the band structure of up to several hundred meVs [29]. Additionally, the energetic position varies locally at the edge by a few 10 meV between patches with a size of some nm) [125]. Both features can be problematic. The large global shift might locate the DC at an energy far away from where it is desired (typically at E_F). The local variations limit the TES mobility, similar to Dirac electrons in graphene [129].

Increasing the growth quality is obviously the best way to handle this impurity problem. Nevertheless, it has been shown that the global shift can be handled by counter doping with calcium [28]. And doping in general offers an easy approach to manipulate the position of E_F . On the other hand, introducing more impurities to the surface gives rise to more local variations, thereby limiting TES mobility.

Influence of Surface Doping

Due to the sensitivity of the electronic structure, already small doping of the surface of Bi_2Se_3 leads to a notable band bending [130]. This not only leads to the effects known from bulk doping, but induces quantum well states in the engergy gap originating from the conduction band (CB) and valence band (VB). These states open new scattering channels for the Dirac cone. Moreover, the Coulomb potential induced by the surface dopants leads to a warping of the Dirac cone [130, 131]. This behavior was demonstrated for a great variety of atoms and molecules such as NO_2 (p-doping) [28], potassium [132], cobalt and rubidium [133], iron [100], gadolinium, caesium, nickel, copper [134] and HO_2 [135] (all n-doping). As a consequence of this great sensitivity to surface adatoms, Bi_2Se_3 suffers from an *aging effect*, when exposed to air or residual gases within vacuum chambers[130, 135]: The band structure will shift for several hours before the process is saturated.

The doping effect prevents tailoring of TIs. In most cases band bending shifts the Fermi level away from its desired position. Also, the presence of quantum well states is unwanted. Therefore, manipulation methods that are not accompanied by a doping effect have to be found. In chapter 6 a method is developed that allows the introduction of atoms carrying magnetic moments in the vicinity of TRS without causing band bending.

Part II.

Experimental Setup and Results

5. Experimental Setup

The present chapter gives a description of the tools and procedures needed to conduct the experiments and analyze the results. After explaining why a home-build-STM head is used, section 5.1 provides a description of the chamber system and the STM head itself, followed by general parameters of the setup. Section 5.2 deals with details of the particular experiments, i.e. preparation steps, used software and data analysis.

5.1. Experimental Setup

The experiments presented in this thesis are fundamental characterizations of new materials but also growth studies. In contrast to measurements on well-known systems, the sample preparation itself is part of the study and had to be carried out multiple times. STM in general demands high stability and profits from low temperatures (see chapter 2.1 on STM theory). However, loading a sample gets more complicated and time consuming, when these properties get optimized. In a mK environment [136] sample transport can already take $10 - 20$ min, loading a sample takes about 30 min (the STM has to be moved out of the cryostat), approaching the tip typically lasts $1 - 2$ h and, most important, cooling down the sample takes about 18 h. Using such a machine for growth studies would be extremely inefficient, since a first sample characterization does not require such low temperatures.

Therefore, an STM setup that allows a fast introduction of new samples was needed for the studies described in this thesis. This can be provided by a microscope class called variable temperature STM (VT-STM). Here, the STM head is connected to a flow cryostat instead of being operated in a bath cryostat. By a variation of He-flow or a change from liquid helium to nitrogen as a cooling agent, a VT-STM enables measurements in a wide temperature range.

However, the VT-STM design in general has some drawbacks, starting with a moderately low base temperature. In a bath cryostat the only heat introduced from room temperature parts stems from cables used to control the STM . These are cooled along the way. The base temperature of the sample is then ≤ 4.4 K. In case of a VT-STM, the base plate is directly connected to the chamber that is in thermal equilibrium with room temperature. The STM is also exposed to much stronger thermal radiation, again originating from the chamber. According to the Stefan-Bolzmann law the emissive power j of a body is proportional to the fourth power of its temperature T by $j \propto T^4$. A standard thermal radiation isolation of the VT-STM leads to a base temperature at the sample of ≈ 25 K [137].

The second drawback is an increased mechanical noise level induced by the helium stream within the flow cryostat. Especially, when one tries to reach low temperatures and the flow gets turbulent, due to a high helium consumption. Both, higher base temperature and enhanced noise level, reduce the stability of the system.

VT-STMs are commercially available from a variety of companies. Within these setups the STM *and* the chamber-system are optimized for fast accessibility. Furthermore, the design of the STM head is optimized for a large temperature window. E.g. the Omicron VT-STM can reach sample temperatures between $25 - 1500$ K [137]. However, such high temperatures are not needed for the described experiments and the focus on the larger temperature range reduces the general stability of the VT-STM setup even further. And the helium consumption of $1 \ \ell/h$ not only increases noise, but leads to a rather short holding time. Especially advanced spectroscopy techniques, as grid measurements or mapping of $\mathbf{q}$-vectors via FT-STS maps, highly depend on a long hold time and stable conditions. Hence, their usability is limited when working with a typical VT-STM.

For this reason, in the first part of my Ph.D. time, I designed and built a new VT-STM head that exhibits the same accessibility as other VT-STMs, but is optimized concerning stability and holding time to come closer to parameters of bath cryostat systems. The results presented later will prove that this VT-STM can be utilized for advanced spectroscopic techniques, such as FT-STS mapping, to characterize a sample. The general design follows the one developed by T. Eelbo, which is described in his diploma thesis "Construction of a new Ultra-High Vacuum Variable-Temperature Scanning Tunneling Microscope" [138]. The following description of the setup will focus on the basic construction and the ideas behind isolating the system. For details concerning tip exchange or the coarse approach mechanism, consult the mentioned thesis [138].

5.1.1. Chamber System

The used UHV-chambers are the standard chambers of the Omicron VT-STM, Fig. 5.1. It consists of three stainless steel chambers, a load-lock, a preparation chamber and an analysis chamber. The load-lock is used to insert new samples and tips. Via a valve it is connected to the preparation chamber. As the name indicates, the preparation chamber (prep chamber) is used to prepare the inserted samples and tips for the experiment. For this purpose, the chamber is equipped with a SPECS IQE 11/35 sputter gun, a home built e-beam heater and a manipulator stage, including a PBN[1]-heater. Next to the preparation chamber is the analysis chamber. This chamber hosts the STM head, an Omicron Spectra-low energy electron diffraction (LEED) unit, five Focus EFM-300 evaporators, as well as one WEZ 40 effusion cell from the company "MBE Komponenten" to deposit various materials onto tip and sample. Moreover, it contains a manipulator, again with a stage to

---

[1]PBN = phosphor-boron-nitride
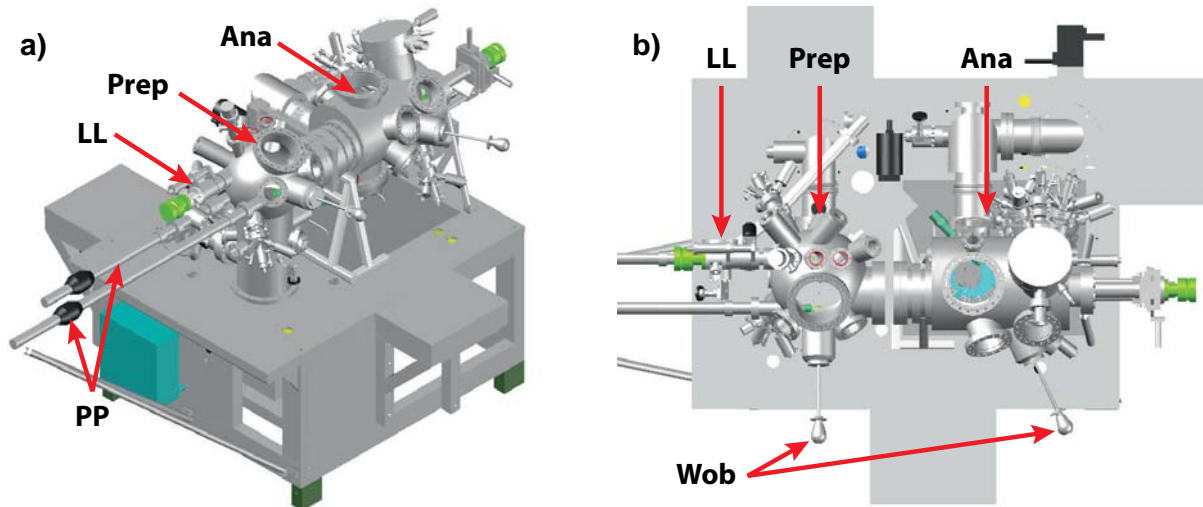
Figure 5.1.: 3D model of VT-STM chamber system a) 3D view **b)** top view. Ana: analysis chamber, Prep: preparation chamber, LL: load-lock, PP: power probes, Wob: wobble sticks.

heat samples by a PBN-heater and another stage that can be cooled via liquid nitrogen. Both stages can be oriented either towards the LEED unit or towards each evaporator. The sample can be heated during growth to ≈ 1000 K or cooled down to ≈ 100 K.

Within the preparation and analysis chambers the samples are moved via wobble sticks. For transport between chambers two UHV design power probes are used. Due to the hand moved probes, the direct connections and optimized exchange points between wobble sticks and power probes, a sample can be transported within a minute from the load-lock to the STM stage.

To establish UHV conditions within the system, several pumps are used optimized for different pressure regimes. A vacuumbrand MD4 NT membrane pump and a Pfeiffer TMU071 turbomolecular pump are connected in line with the preparation chamber. The membrane pump is used to establish a pressure of ≈ 0.1 mbar, the turbo pump lowers the pressure to $\approx 5\mathrm{x}10^{-9}$ mbar. The analysis chamber can only be turbo-pumped via the prep chamber, the load-lock can be pumped separately. To further lower the pressure, analysis and prep chamber are each equipped with a Varian VacIon Plus 150 ion-getter pump and a Varian ST22 TSP pump. With these pumps, the pressure in the analysis chamber can be lowered to $\approx 1\mathrm{x}10^{-11}$ mbar (prep chamber $\approx 5\mathrm{x}10^{-11}$ mbar). When UHV conditions are reached, the chambers can be sealed and the turbo as well as the membrane pump can be switched off. Ion-getter and TSP pumps alone are able to maintain the pressure. To speed up the pumping process after exposition to air, the chambers are baked for at least 48 h at 150 °C.

5.1.2. STM Head

Fig. 5.2 depicts a 3D model of the microscope, in cross-section and total views. The scanner unit, consisting of an oxygen free high conductivity (OFHC)-copper tip receptacle, a grounded radiation shield, the actual scanner, a piezo tube made of EBL #4, and a sapphire prism working as a host, is located in the center of the microscope body and fixed by a metal sheet pressing the unit into the body. The approach mechanism is based on the walker design [139]. Above the scanner unit, a block is glued into the body working as a sample receptacle. The glue, EPO-TEK H77, is not conductive. The sample receptacle is electronically detached from the body and the bias cable is not grounded. Both, body and sample receptacle, are made of phosphorus bronze. The material is a good compromise between high thermal conductivity and a sufficient hardness needed for drilling screw threads. Tab. 5.1 gives an overview on basic properties of the used materials.

Cooling and Isolation

An OFHC-copper block attached to the top of the STM-body works as a connector for two bundles of copper braids, which establish a thermal connection between microscope and a Cryovac Konti-Cryostat-UHV. This connection is the primary cooling cycle. For a faster cooling and a smaller temperature gradient within the body, a three part OFHC-copper shield is screwed on the body and the connector. Only the open side of the body, where tip and sample are exchanged, is not covered by this shield.

For thermal isolation, the STM head is not directly connected to its base plate but is located in a cylindrical metal box, called radiation shield. The cylinder bottom and top ring are made of phosphorous bronze, the cylinder itself is made of OFHC-copper. Three stainless steel tubes link the copper connector with the bottom piece of the cylinder. Stainless steel exhibits a very small thermal conductivity, even smaller than common ceramics, and is therefore used to minimize the thermal exchange between radiation shield and STM. The exchange is further minimized by using tubes with a wall thickness of only 1 mm. The shield is cooled to ≈ 215 K [138] by the cryostat via three copper braids connected to the top of the box, the so called secondary cooling cycle. This cycle is cooled by He, which was already used for the first cycle. So cooling the STM itself is not affected. A window in the cylinder enables access to the microscope. To cover the window during measurement, a second OFHC-copper cylinder is attached to the shield via a ball bearing. It can be rotated and thereby opens and closes the shield for tip and sample exchange. An extra copper plate is located at the part of the door that covers the open side of the body. The plate is thermally detached from the door by two short stainless steel tubes and is
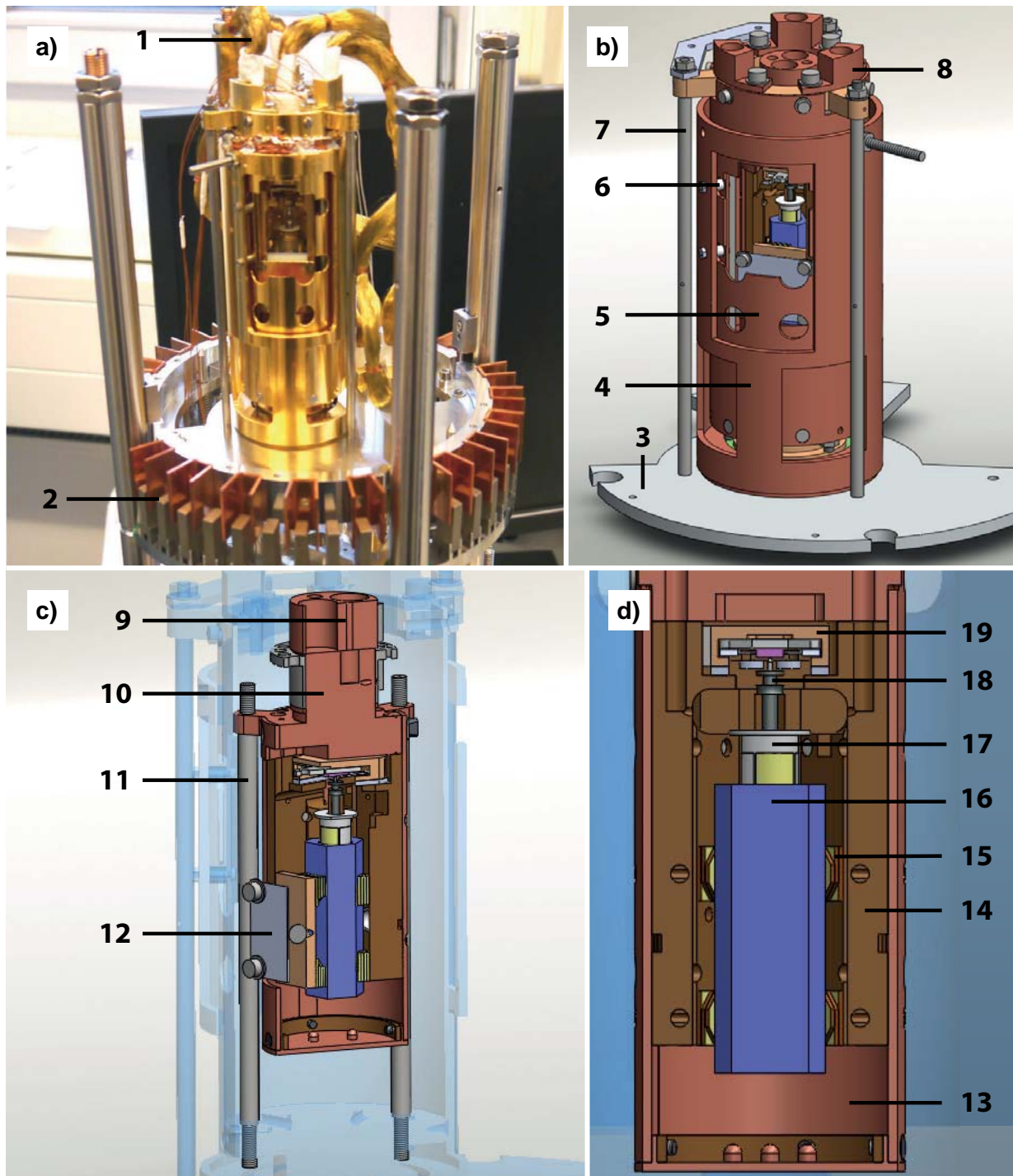
Figure 5.2.: VT-STM a) Photo of the VT-STM after finishing the assembly. **b)** 3D CAD model of STM and radiation shield. **c)** Cut through model. **d)** Detailed image of sapphire prism and scanner. (1) gold plated copper braids; (2) Omicron eddy current damping; (3) base plate; (4) radiation shield door; (5) radiation shield; (6) connection to inner copper plate; (7) tube connecting base plate and radiation shield; (8) Socked of copper braid (secondary cycle); (9) Socket of copper braid (primary cycle); (10) Cu block between braids and STM body; (11) tube connecting STM/Cu block and radiation shield; (12) Mo leaf spring fixing the scanner in the STM body; (13) Cu shield (14) STM body; (15) piezo stack, part of the coarse approach mechanism. Scanner unit: (16) sapphire prism; (17) piezo tube; (18) tip and tip holder; (19) sample receptacle with sample.

57

connected to the microscope body by a small bundle of copper braids. The extra plate is meant to compensate the missing plate of the inner shield in terms of thermal radiation. The top of the radiation shield is then connected to the base plate by another set of three stainless steel tubes. The base plate is mounted to an Omicron eddy current damping stage for vibration isolation.

In this configuration, thermal flux between the microscope body and the UHV-chamber is minimized by two sets of stainless steel tubes and the cooled radiation shield in between. Furthermore, all cables are cut in two lines to minimize their thermal flux to the sample (And for easier mounting of theSTM-head). One line running between the chamber (at room temperature) and a ring attached to the OFHC-copper block on top the STM body (at measurement temperature). And one line going from that ring into the microscope. The lines are connected by plugs. The cables going into the body are guided to the bottom of the body running between body and Cu shield for further cooling before they access the inner part.

Additionally, the STM head is only exposed to thermal radiation of the radiation shield, that is cooled to at least $\approx 50\,\mathrm{K}$. In order to further reduce the influence of thermal radiation, all parts of the microscope and radiation shield are gold plated. Tip and sample are double shielded and both connected to the primary cooling cycle. Hence, in contrast to commercial solutions, tip and sample can be assumed to exhibit the same temperature.

The temperature of the sample is measured by a Lakeshore type TG-120SD GaAlAs diode attached to the sample receptacle, and is monitored by a Lakeshore temperature controller model 332S. The controller is connected to a heater in the cryostat and can automatically adjust the sample temperature to a given value.

	Thermal conductivity $\left(\frac{\mathrm{W}}{\mathrm{m}\cdot\mathrm{K}}\right)$	Thermal expansion coefficient $\left(\frac{\mu\mathrm{m}}{\mathrm{m}\cdot\mathrm{K}}\right)$	Vickers hardness (GPa)	Emissivity
Gold	301	14	0.2	0.025
Cu-OFHC	390	17	0.36	0.05
Phosporus Bronze	84	18	0.4	0.06
Stainless Steel	16	17	0.4	0.5
Al$_2$O$_3$	46	0.6	13.3	0.1

Table 5.1.: Properties of the STM materials. Values are taken from [140]. The emissivity is normalized to the emission of a black body.

Other Components

In order to reduce electronic noise, all STM parts, except sample and tip receptacle, are connected to the same ground as the chamber. For I and U_B Elspec miniax Mk 5001 coaxial cables are used. For U_B the signal is transmitted by the cable core, which is glued[2] to the sample receptacle. The shield is grounded on the chamber side without an additional ground connection on the STM side. Also for I the signal is transmitted by the core. It is glued to the tip receptacle. The shield is again grounded only on the chamber side. On the STM side, it is connected to a Macor cap located between tip holder and piezo tube, that is covered with conductive glue to work as a radiation shield. It screens tip and sample from electromagnetic radiation stemming from the coarse approach and the piezo tube cabling. All parts of the U_B/I_T circuit are either directly shielded (cable cores) or located in the shadow of grounded components.

The measured signal is transmitted to a Femto DLPCA-200 pre-amplifier and then forwarded to the Nanonis SPM Control System of SPECS Zürich. To measure dI/dU signals, a SR830 DSP Lock-In amplifier from Stanford Research Systems is used.

5.1.3. System Parameters

Using the previously described setup, the STM can be cooled down to 18.2 K, see Tab. 5.2 . This leads to an overall temperature range of 18.2 K to $\approx$ 350 K. The upper limit is given by the used glues. Above 350 K the glues liquify [141] and the STM will fall apart. At a typical measurement temperature of about 30 K the helium consumption is 0.6 ℓ/h and an inserted sample reaches the desired temperature within $\approx$ 10 min. Also, a turbulent flow of the liquid helium in the cooling line is avoided at this temperature, resulting in a temperature variation in thermal equilibrium of less than 10 mK[3] even without using the Lakeshore temperature controller. Due to this thermal stability, the z-noise is not larger than 3 pm (minimum to maximum) and the drift is minimized to < 5 nm/hour after a 3 h waiting time. The drift can be further compensated by the drift correction function of the scan software.

The tip-sample approach takes about 15 min and therefore can be started while the sample is still cooling down. As mentioned before, the sample transfer within the chamber system takes about a minute. This means that samples that demand no further preparation steps, e.g. TIs with a freshly cleaved surface (see 5.2.2), can be measured already 30 min after leaving the load-lock. Tab. 5.3 compares the time frames of different STM setups.

---

[2]For glue spots that need to be conductive EPO-TEK H20E is used.

[3]To reach such stable conditions also the thermal conditions outside the UHV-chamber has to be held constant: Direct sun light has to be avoided and the lab temperature has to be kept constant via air conditioning.

Concerning sample transfer, the home-built VT-STM exhibits the same advantages as the commercial system. The time frame between inserting a sample into the STM chamber and starting a measurement is short enough to check several samples per day. Bath cryostat systems usually are only able to check one sample per day, mK-systems need a night in between to establish thermal equilibrium. On the other hand, bath cryostat systems are by far more stable. However, the home-built design comes with significant improvements compared to the commercial system. Z-noise and drift are reduced by a factor of 3 and 10, respectively. Due to the increased isolation, the base temperature is lowered from ≈ 25 K to ≈ 18 K. At first sight 7 K is not that much. However, a look at the He consumption suggests that here the limit for flow cryostat systems is reached. At 24 K only 0.8 ℓ/h are needed to hold that temperature. At 18.2K the maximum flow is needed which results in a consumption of 6 ℓ/h. For holding a temperature of 30 K, the He consumption drops to 0.6 ℓ/h. It turned out that 30 K is a good compromise between temperature, stability and holding time.

	Home-built VT-STM	Omicron VT-STM	Home-built mK-STM
Base temperature	18.2 K	25 K	0.3 K
Temperature range	$18.2 - 350$ K	$25 - 1500$ K	$0.3 - 100$ K
LHe consumption†	0.6 ℓ/h	1 ℓ/h	0.9 ℓ/h
Pressure	$< 10^{-10}$ mbar	$< 10^{-10}$ mbar	$< 10^{-10}$ mbar
Drift	< 5 nm/h	< 50 nm/h	< 30 pm/h
Noise (peak-peak)	< 3 pm	< 10 pm	< 1 pm

Table 5.2.: Basic VT-STM properties in comparison to an Omicron VT-STM and a home-built mK-STM described in [136]. † LHe consumption of the VT-systems at 30 K.

	Home-built VT-STM	Omicron VT-STM	Home-built mK-STM
Transfer	1 min	1 min	20 min
Loading	1 min	1 min	30 min
Approach	15 min	15 min	90 min
Cooling	0.3 h	0.3 h	18 h
Total	0.5 h	0.5 h	20 h

Table 5.3.: Duration of single sample transfer steps, in comparison with an Omicron VT-STM and a home-built mK-STM described in [136].

5.2. Measurement and Analysis

This section provides an overview of the preliminaries needed for measurements, i.e. STM calibration and sample preparation. It also introduces the analysis software used, describes processing steps and comments on the convention of displaying data in this thesis.

5.2.1. Calibration

Before each measurement session the scanner was calibrated at the temperature used for the experiment. In case of the four presented experiments here, the temperature was 30 K. For calibration, samples with well known features were measured. Then the prefactors in the Nanonis control software affecting the applied voltage to bend the scanner were adjusted until the measured values matched literature. For the x/y-direction the surface of highly oriented pyrolytic graphite (HOPG) was scanned with the lateral lattice constant as a calibration reference. For z-calibration, step edges on a W(110) surface was used. Fig. 5.3 gives an overview on calibration measurements. It also gives a typical line-profile from which the z-noise can be estimated.
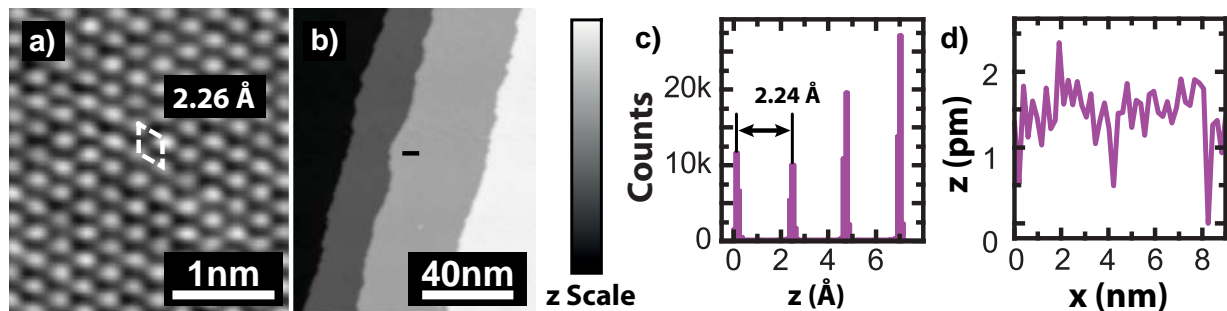
Figure 5.3.: VT-STM calibration. To calibrate the STM, samples with well known topographic features were measured. The voltage applied to bend the scanner was adjusted by pre-factors in the software till the measured values match literature. **a)** Surface of HOPG with atomic resolution. $U_B=$ 0.2 V, $I=$ 10 nA, 30 K. The hexagonal lattice should have a lattice constant of 2.456 Å [142]. **b)** Step edges on a W(110) crystal. $U_B=$ 1 V, $I=$ 20 pA, 30 K. **c)** Histogram of (b). Distance between peaks gave the step edge height, which should be 2.24 Å [143]. **d)** Line-profile along line in (b). The noise is smaller than 3 pm (peak to peak).

5.2.2. Sample and Tip Preparation

The samples measured for this thesis are rather easy to prepare. To achieve a fresh surface, Bi_2Se_3 and Bi_2Te_3 were cleaved by the scotch-tape method. For this, a stripe of scotch-tape was formed to a loop and glued to the sample according to Fig. 5.4. The sample was then put to a power probe parked in the open load-lock. The loose end of the tape was attached to the power probe. Then the load-lock was sealed and pumped. When the pressure as good enough, the valve between load-lock and prep chamber was opened and the power probe was moved into the prep chamber. The sample was grabbed by a wobble stick and pulled out the power probe. Since one end of the tape was fixed on the power probe, the loop rolled off the sample and cleaved it along a van-der-Waals gap, as the bonding between tape and sample surface is stronger than between quintuple layers.

Fresh $TlBiSe_2$ surfaces were also prepared by cleaving. But in this case the bonds between layers are always of ionic/covalent nature and therefore the scotch tape method does not work. Instead, a lever, e.g. a screw, was fixed to the sample surface using a sufficiently strong glue, e.g. EPO-TEK H20E (Fig. 5.4 (c)). Within the chamber the lever was then cranked, e.g. by a wobble stick, and the sample cleaved parallel to its layers.

As tips, electrochemically etched polycrystalline tungsten wires were used. Sharp tips were prepared by using the drop-off method [57]. Here, the tungsten wire is dipped into a two molar aqueous solution of NaOH. By applying an AC voltage of 5 V the lye is etching the wire at the interface between solution and air, which reduces the thickness of the wire. After several minutes the thickness is reduced enough, that the lower part of the wire
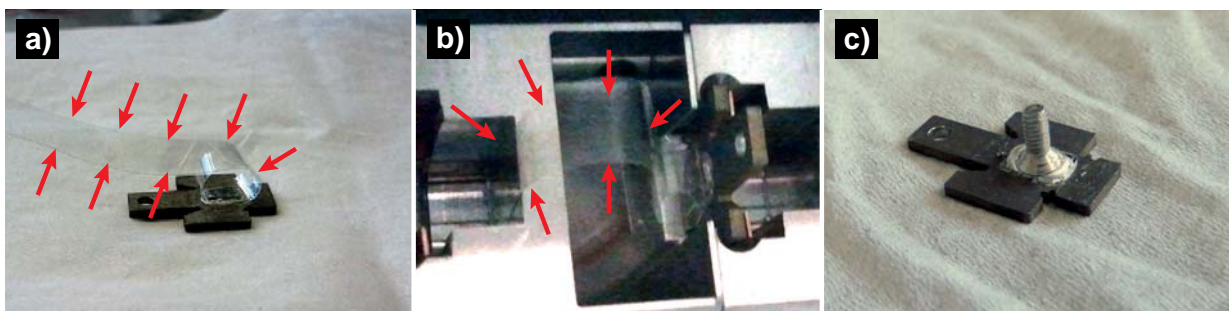
Figure 5.4.: Sample preparation. a) and b) For Bi_2Se_3, Bi_2Te_3 and $PbBi_4Te_7$ a fresh surface was prepared by cleaving the crystal *in situ* with scotch tape. One end of a scotch tape band is formed to a loop and glued to the sample (a). The red arrows are placed as a guide to the eye. The sample was then parked in a power probe and the loose end of the band is glued to the probe above the sample (b). After the load-lock was pumped, the power probe is moved to the prep chamber. There the sample was removed from the power probe. Thereby, the band rolls off and cleaves the sample. **c)** For $TlBiSe_2$ a lever was glued to the sample, which was then cranked using the wobble stick within the chamber system.

drops off and the etched part of the upper wire is used as an STM tip. The tip is then mounted to a tip holder and introduced to the chamber system via the load-lock. Coming from ambient conditions the tip exhibits a non-conductive oxidation layer at the surface. This layer was removed by annealing the tip to 1200 °C on the e-beam-station. At this temperature, the WO_3 reacts with the bulk tungsten to WO_2 which then desorbs, resulting in a clean conductive tip [57]. If a wire turned out to exhibit a blunt or double tip during an STM measurement, the tip apex was altered by voltage pulses until a sufficiently sharp tip was formed.

5.2.3. Data Analysis

The acquired images and spectroscopy curves were analyzed by several programs. For topography images and STS maps WSxM [144] was used. dI/dU-curves were processed by SPAM, an in-house developed analysis software. SPAM was also used to calculate the FT-STS maps from STS images. For figure preparation, line profiles, histograms and dI/dU-curves were further processed by the software OriginPro.

In order to avoid tampering of results, processing was kept to a minimum. Real-space data were only adjusted by a plane fit to remove z-drift. Other modifications were used to highlight certain features, including cutouts of original images or different color scales. The resulting dI/dU-curves were not processed, but were averaged over 10 curves already by the Nanonis software during data acquisition.

Processing of FT-STS Maps

FT-STS maps were calculated from STS images via Fast Fourier transformation (FFT) using the convention $q = 2\pi/\lambda$, where λ is the wavelength of periodical structures in the STS image. The FT-STS maps had to be symmetrized in order to increase visibility. For this, $n-1$ copies of the original FFT were created, where n denotes the rotational symmetry of the FT-STS map, which depends on the symmetry of the surface band structure. The copies were then rotated by the angle α, which depends on the number i of the copy and the symmetry n by

$$\alpha = \frac{360}{n} \cdot i \tag{5.1}$$

Due to the symmetry of the original FT-STS map, the features of the resulting images exhibit the same orientation. They only differ in intensity, due to random noise that shows a different symmetry.

63

A final image was then calculated by averaging over all intensities $I(x, y)$ at a given pixel

$$I_{final}(x, y) = \frac{1}{n} \cdot \left(I_{original}(x, y) + \sum_i I_i(x, y) \right), \tag{5.2}$$

which drastically improves the signal to noise ratio. Unfortunately, features not stemming from the sample electronic structure, i.e. artifacts or mechanical noise (see 2.4.2), can still be found in the final image now exhibiting the same symmetry as the surface band structure. A deformed FT-STS map as a result of drift might even produce new features.

Distinguishing between features stemming from the LDOS and features stemming from noise or drift is complicated by this symmetrization. However, artifacts related to the FFT can be avoided by adjustments to the original STS map, see Fig. 5.5. The bright horizontal lines stemming from the finite image size were minimized by a Gaussian drop of intensity towards the edge (window function). The bright vertical line, which stems from the z-modulation along the slow scan direction, was attenuated by a median filter applied along that direction. Fingerprints of noise or image deformation can only be reduced by minimizing these effects during measurement. In a final step the image was treated with a simple Gaussian filter, which increases the general visibility of features related to the sample LDOS.
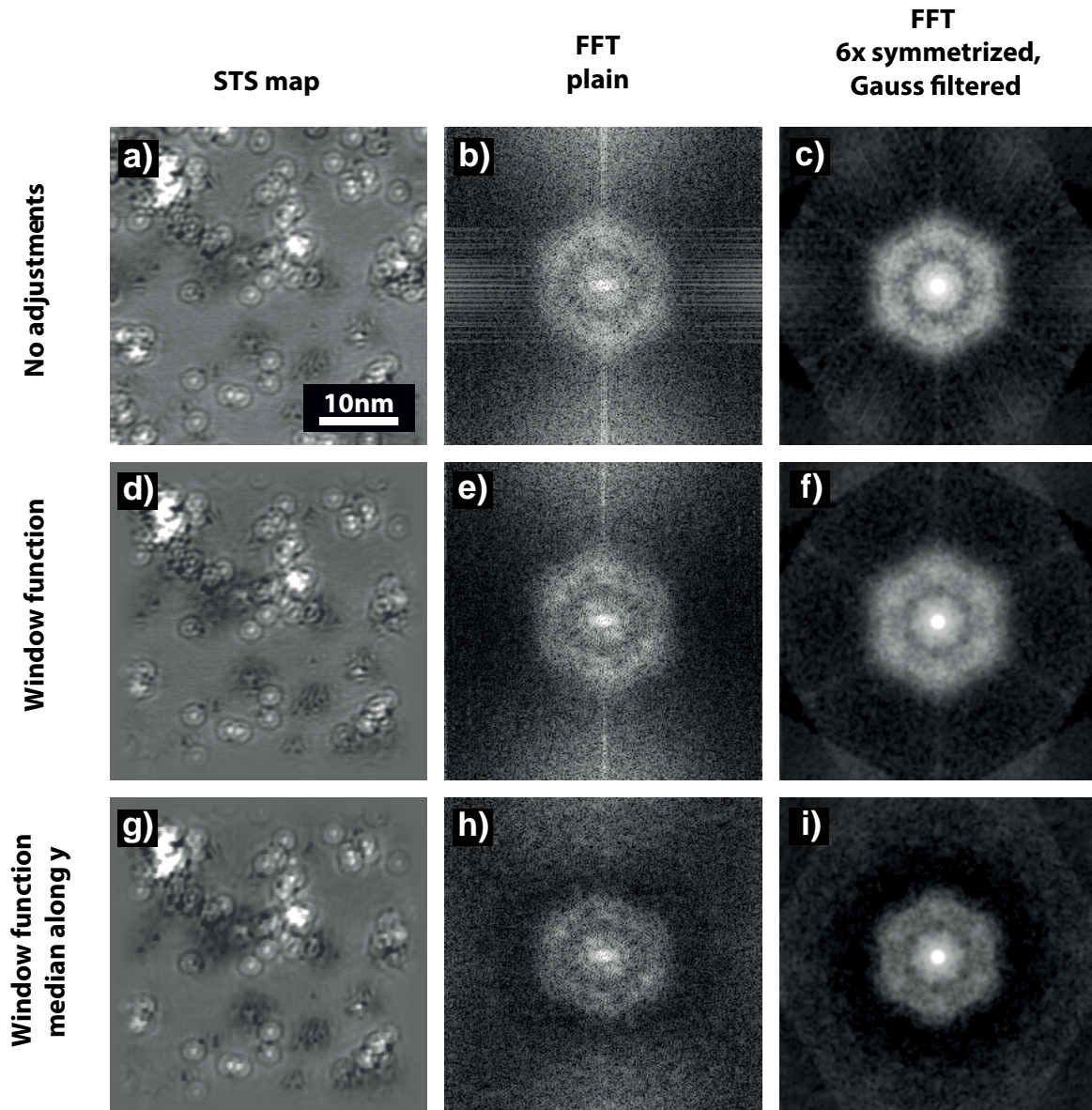
Figure 5.5.: FT-STS maps: noise reduction and symmetrization. Influence of individual processing steps illustrated for an STS map taken on Bi/Bi_2Se_3 , $U_B = -800\,\mathrm{mV}$, $I = 3\,\mathrm{nA}$. **a)-c)** From an STS to a symmetrized FT-STS map without adjustments. **d)-f)** With activated window function to smoothly decrease the intensity at the edge of the image. As a result, the horizontal stripes are eliminated from the FT-STS maps. **g)-i)** With activated window function and median along the slow scan direction. The median removes the bright vertical line in the center of the FT-STS map.

6. Reducing the Doping Effect of Fe atoms on Bi_2Se_3

The low density of states at the surface of an ideal TI leads to a high sensitivity of the band structure towards adatoms. Already a small amount of atoms working as donors or acceptors can induce a significant band bending at the surface, see section 4.8. While the ability to change the location of E_F within the bands is per se needed to customize a material for applications, other manipulations should be independent from this effect, e.g. contacting the TES or introducing magnetic moments. Not only might the DP shift too far away from its desired position (in most cases at E_F), the band bending might also induce the formation of quantum well states close to the DC establishing new scattering channels for the TES. Furthermore, on the research side, the identification and understanding of additional effects gets more complicated. One recent example is the influence of Fe adatoms on the Dirac cone of Bi_2Se_3. Due to partially filled 3d orbitals, free Fe atoms possess a magnetic moment. Introducing them to the surface of a TI opens a gap within the Dirac cone, if the magnetic moment is preserved and exhibits an out-of-plane orientation, see section 4.5. Wray *et al.* [100] presented an ARPES study on the influence of Fe on Bi_2Se_3 claiming to have found a DC gap opening after Fe deposition, see Fig. 6.1. However, the out-of-plane nature was not confirmed. In contrast Honolka *et al.* found an in-plane magnetization of the Fe adatoms by x-ray magnetic circular dichroism (XMCD) measurements [101] and other ARPES studies of the system did not find a gap within the DC, e.g. [145]. Most probably, the gap identified in the first study is one between the upper part of the Dirac cone and a quantum well state induced by band bending.
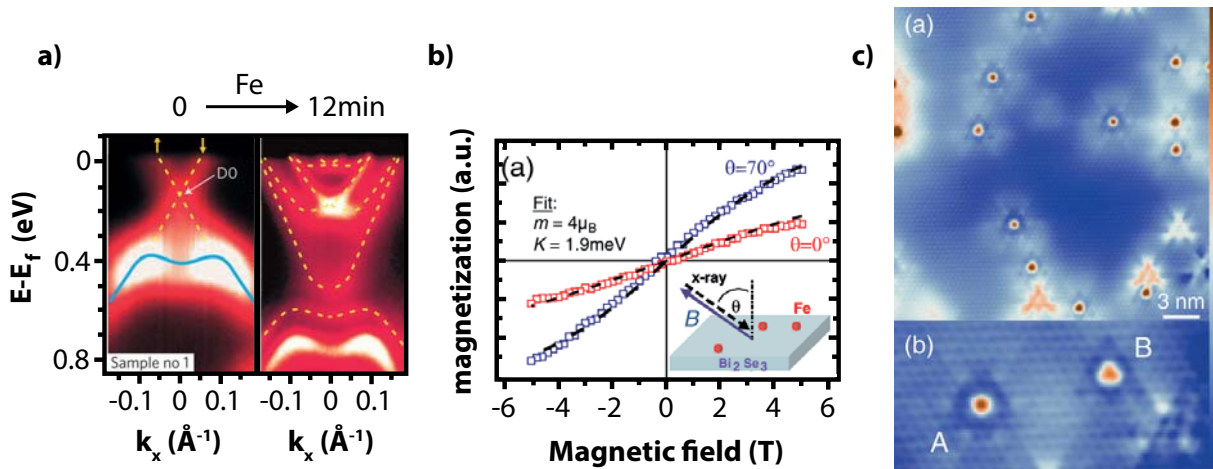
Figure 6.1.: Previous results for Fe deposited on Bi$_2$Se$_3$. a) ARPES spectra before and after cold deposition of Fe. The guides to the eye suggest a gap opening at the DP after deposition. Hence, it was concluded that the Fe atoms are magnetic with an out-of-plane easy axis [100]. **b)** Magnetization curves for 1 % ML Fe adatoms on Bi$_2$Se$_3$ measured by XMCD for different incident angles of the x-ray. The curve for $\theta = 70°$ exhibits smaller values than the $0°$ curve, pointing to an in-plane easy axis. The lack of hysteresis proofs the paramagnetic nature of the atoms. **c)** STM constant-current images of 1 % ML of Fe atoms absorbed on Bi$_2$Se$_3$. Top image: overview, bottom image: close up of atoms on two different binding sites A and B. (b) and (c) are taken from [101].

The question arises, how the band bending effect can be avoided. One possibility is counter doping the sample. However, this solution comes with other drawbacks: The over-all increased surface doping leads to local shifts of the band structure, thereby reducing the mobility of the TES [125]. The additional species of adatoms might interact with the magnetic adatoms, thereby quenching their magnetization. And finally, the surface might be disturbed strong enough to shift the TES away from the surface into the bulk. Therefore, any additional doping should be reduced to a minimum.

Another possibility would be to reduce the doping property of the initial adatoms, e.g. by incooperating them into the crystal structure. To this end, the atom of choice has to have a similar valency as the atom that gets substituted.

This opportunity is tested in the present chapter. The substrate is Bi$_2$Se$_3$, the adatoms are Fe atoms. One reason for the choice of Fe atoms is their metallic nature. Future TI devices have to interact with conventional materials, e.g. metallic conductors. So this interaction has to be further explored. Another reason is the Fe atom's magnetic moment. Is its magnitude lowered or increased? Is the magnetic anisotropy changing? Or is the disturbance strong enough to shift the TES?

The first section of this chapter provides a temperature dependent STM study on the growth and diffusion of iron atoms on Bi$_2$Se$_3$. The second part describes the behavior of

the Bi_2Se_3 band structure depending on the diffusion of the Fe atoms. In the third part the experimental results are compared to *ab initio* calculations. These will also reveal changes of the magnetic moment.

All experiments were conducted with pristine Bi_2Se_3 and with Ca-doped Bi_2Se_3 samples. Due to the higher purity, the pristine samples are the first choice for a proof-of-principle experiment. However, Ca-doped samples might be of greater interest in the long run, because E_F can be easily tuned by the amount of Ca. The ability to precisely tune E_F and simultaneously, but independently, introduce an additional component (here magnetic moments) to the edge of a TI is a fundamental requirement for transfers from basic research to applications for this material class.

The STM experiments were conducted by myself and Tobias Schlenk at Hamburg University. ARPES measurements were done by Tobias Schlenk and Marco Bianchi, member ofPhilip Hofmann's group at Aarhus University. The calculations were provided by Mohammad Koleini, Tim Wehling, Thomas Frauenheim from the Bremen Center for Computational Material Science and Alexander Balatsky from the Nordic Institute for Theoretical Physics. The crystal was provided by Jianli Mi and Bo Brummerstedt Iversen from Aarhus University. Some of these results have already been presented by Tobias Schlenk in his Ph.D. thesis: "Spin-Resolved and Inelastic Scanning Tunneling Spectroscopy of Magnetic Atoms and Clusters" [146]. Here, his focus is on magnetic properties of Fe atoms.

6.1. Diffusion of Fe Adatoms into Bi$_2$Se$_3$

STM experiments were conducted in the chamber system described in section 5.1. The base pressure was $< 10^{-10}$ mbar. Samples, grown according to [130, 147], were cleaved *in situ* at a pressure of $< 10^{-8}$ mbar with the scotch tape method described in section 5.2.2 and transferred to the manipulator-stage within 1 min. There, the samples were cooled to ≤ 150 K for 15 min. Subsequently, Fe was deposited with a Focus EFM 3 evaporator with a rate of 0.1 monolayer (ML) per minute on the cold sample to ensure single atom adsorption. Afterwards, the samples were moved to the STM in less than 5 min. During transfer, the samples were not cooled for a maximum time of 10 s. Surfaces were then checked for smoothness and coverage.

The samples were transferred back to the manipulator for annealing to a given temperature T_A. To ensure temperature equilibrium with the manipulator, samples were heated for 15 min. The changes of the sample surface were then investigated by STM. All measurements were performed at 30 K. The STM tip was an electrochemically etched polycrystalline W wire. STM topographs were taken in constant-current mode. Experiments were conducted with samples with and without Ca-doping. The report focusses on samples without Ca-doping to demonstrate the proof of principle. However, in each section differences and similarities of Ca-doped samples will be briefly commented.

Fig. 6.2 shows the surface of Bi$_2$Se$_3$ without[1] and with Fe atoms grown on top. The pristine surface exhibits two features. The visible clover-shaped features stem from Se vacancies within the first QL [148, 149]. The bright spots are residuals of the adjacent layer that has been removed by cleaving. The number of these spots depends on the quality of the cleave. With a good cleave no spots can be found. In contrast, the Se-vacancies are introduced during crystal growth and therefore can be found on every cleaved surface. After the deposition of Fe atoms, different types of Fe atoms are visible as bright spots on the surface with a height of 0.3 Å and 0.5 Å. The different heights reflect two different adsorption sites: fcc and hcp hollow sites [101]. The distribution of Fe atoms on the surface is random, see Fig. 6.2 (b). The outcome confirms previous results presented in [101], Fig. 6.1. The doping effect of the Fe atoms has a direct impact on the STM image quality. The greater LDOS at the surface stabilizes the tunneling junction, the system is less sensitive to tip changes or crashes, see Fig. A.1.

---

[1]The image of a freshly cleaved sample was measured by T. Eelbo with an STM cooled by a bath cryostat to 4.2 K. It was not possible to measure undisturbed images of the pristine surface with the VT-STM. The LDOS around E_F is too small to ensure a stable tunneling junction at the given temperature for the VT-STM. While the conductance is even further reduced in the bath cryostat system, the by far greater stability of such systems, see section 5.1.2, allows a reproducible measurement. A typical image of the pristine Bi$_2$Se$_3$ surface measured with the VT-STM can be found in the appendix in Fig. A.1.
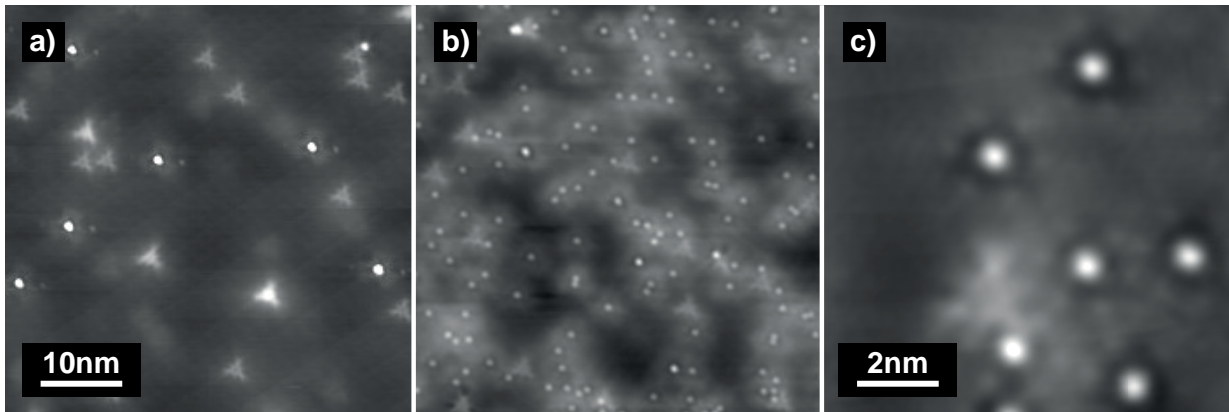
Figure 6.2.: Bi$_2$Se$_3$ before and after deposition. **a)** Bi_2Se_3 surface right after cleaving. Bright spots are residuals from the cleaving process, triangular protrusions are Se-vacancies at different depths below the surface. $U_B = 0.4$ V, $I = 400$ pA. **b)** Surface after cold Fe deposition. Fe adatoms are visible as bright spots surrounded by a halo of enhanced LDOS. $U_B = 0.25$ V, $I = 50$ pA. **c)** Detailed image of Fe adatoms. The appearance of the Fe atoms in STM topography confirms earlier results [101], see Fig. 6.1 (c). $U_B = -0.3$ V, $I = 5$ nA.

Temperature Dependency of Surface Features

Samples exhibiting an Fe covered surface were annealed to temperatures between 260 K and 470 K. Fig. 6.3 gives an overview of the induced changes. After annealing to 260 K the Fe adatoms are still the dominant feature on the surface, but their number is reduced and they are accompanied by triangular depressions (at a bias voltage of 250 mV) and clusters that appear slightly larger than the Fe atoms. At higher annealing temperatures, e.g. 370 K, the depressions dominating the surface and are accompanied by a few large clusters and some single Fe adatoms. Similar depressions can be found for Fe bulk doping of Bi_2Te_3 [150] and Bi_2Se_3 [151] and are identified as Fe atoms substituting Bi atoms within the first QL. The clusters on the surface are assumed to consist of Fe and/or Bi atoms.

A quantitative analysis of the numbers of adatoms, depressions and clusters reveals a sharp drop of Fe adatoms at ≈ 275 K, accompanied by an increase of triangular depressions. Both numbers stabilize between 290 and 370 K. The simultaneous change and stabilization of Fe adatoms and depressions strengthens the identification of the depressions as Fe atoms within the first QL. The overall reduced number of identified Fe-related features might have several causes: Some of the atoms form clusters on the surface. Other atoms might diffuse deeper into the bulk or are located on other sites within the first QL. In both cases the change of the crystal structure would be invisible to STM [152]. Finally, some atoms could have desorbed from the surface.
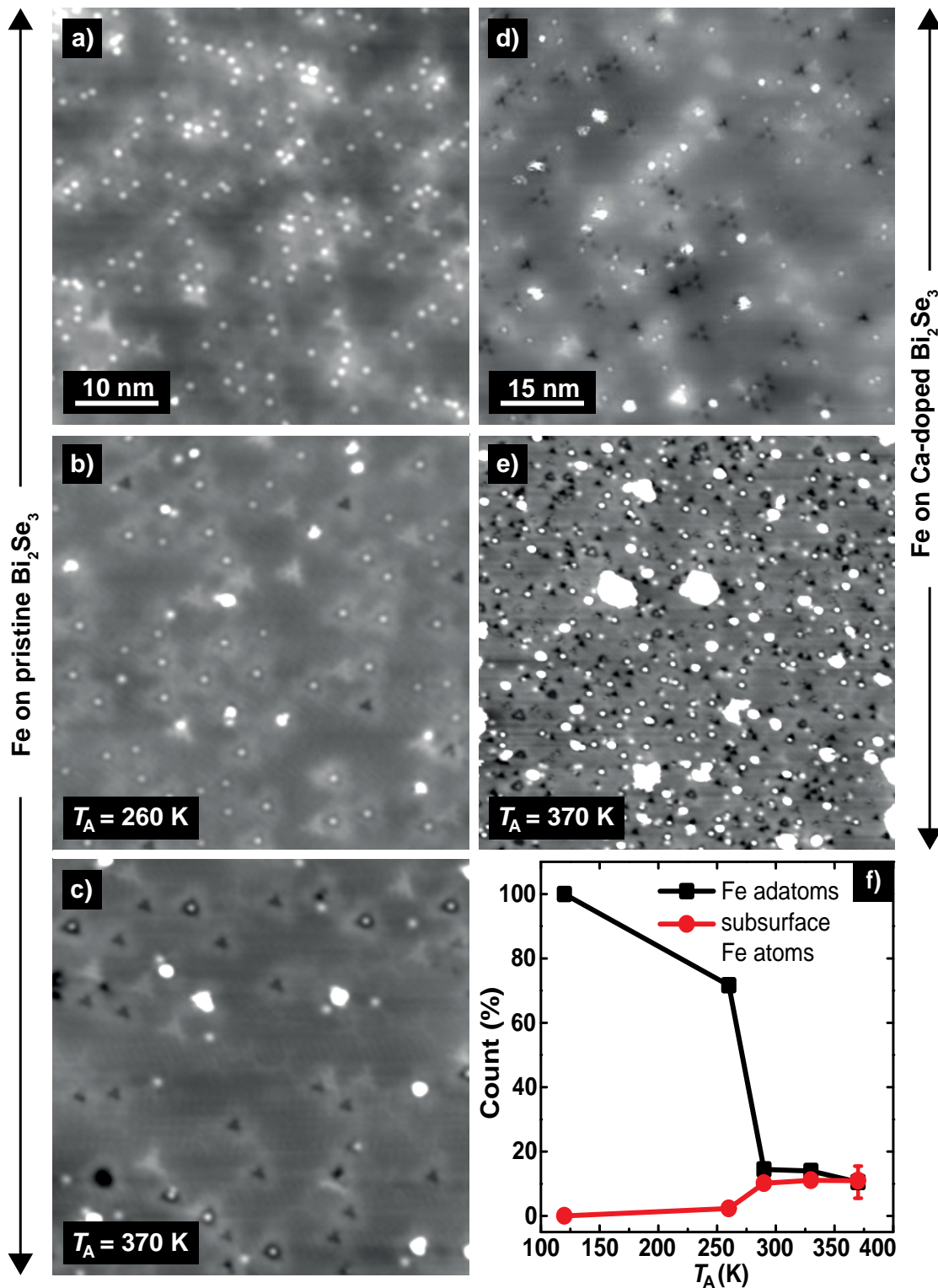
Figure 6.3.: Diffusion of Fe adatoms into subsurface sites a) $1\,\%$ of a ML Fe deposited on pristine Bi$_2$Se$_3$ at $\leq 150\,$K. **b)** and **c)** same preparation as in (a) but with subsequent annealing to $260\,$K (b) and $370\,$K (c). **d)** $0.5\,\%$ Fe deposited on Ca-doped Bi$_2$Se$_3$ at $\leq 150\,$K. **e)** Same preparation as in (d) but with $6\,\%$ deposition and subsequent annealing to $370\,$K. **f)** Number of Fe adatoms and subsurface Fe atoms relative to the initial number of Fe depending on the annealing temperature T_A.

At temperatures above 370 K the number of adatoms and triangular depressions is reduced. This is accompanied by an increased instability of the STM tip during scanning, pointing to a reduced surface doping. Due to this imaging instability above 370 K, a quantitative analysis of surface features was not possible. Images from samples annealed to temperatures higher than 370 K can be found in the appendix in section A.

The growth study was repeated with Ca-doped samples. Except for an additional feature due to the Ca atoms in the first QL, the observed features and their behavior were the same, see Fig. 6.3. Here, an image with a higher Fe coverage is shown as well (6 % of a monolayer). The fact that still many single Fe adatoms with a similar distribution as before are visible, gives rise to a number of conclusions: First, the applied annealing temperature is not high enough for the Fe atoms to move on the surface (by itself, see next section). Second, the clusters are rather formed by Bi atoms that got exchanged, than by Fe atoms.

A Closer Look on Subsurface Fe Defects

At a closer look, two different subsurface Fe defects, called type A and type B, can be found, see Fig. 6.4. These differ by appearance and by measured depth. Type A exhibits an apparent depth of 17.2 ± 1.6 pm at a bias of 250 mV, type B of 34.7 ± 3.7 pm. For the type A defect the bias dependency is shown in Fig. 6.4 (e-j). The different depressions have alreaddy been identified on bulk doped samples as Fe atoms substituting atoms in the first (type A) or second Bi layer (type B) of the surface QL [150–152].

As an analysis of the depth distribution of type A and B defects reveals, Fig. 6.4 (c and d), a higher annealing temperature is needed in order to induce the Fe substitutionals in the second Bi layer: While at 330 K both depression types can be found, at 260 K only type A depressions are present at the surface. Thus, since the annealing temperature can be chosen precisely, not only the surface doping itself, but the type of surface doping can be controlled.

Finally, the fact that type B depressions, which are farther away from the surface than type A, exhibit a greater depth, points towards a large impact of the type B defects on the surface electronic structure. This conclusion is supported by the of the residual Fe adatoms' behavior. On samples treated with high annealing temperatures, where Fe adatoms start to diffuse, many of these can be found on top of type B depressions, none can be found on top of type A impurities. This means that type B substitutional Fe atoms induce a charge in the surface DOSwhich is attractive for other Fe adatoms.

73
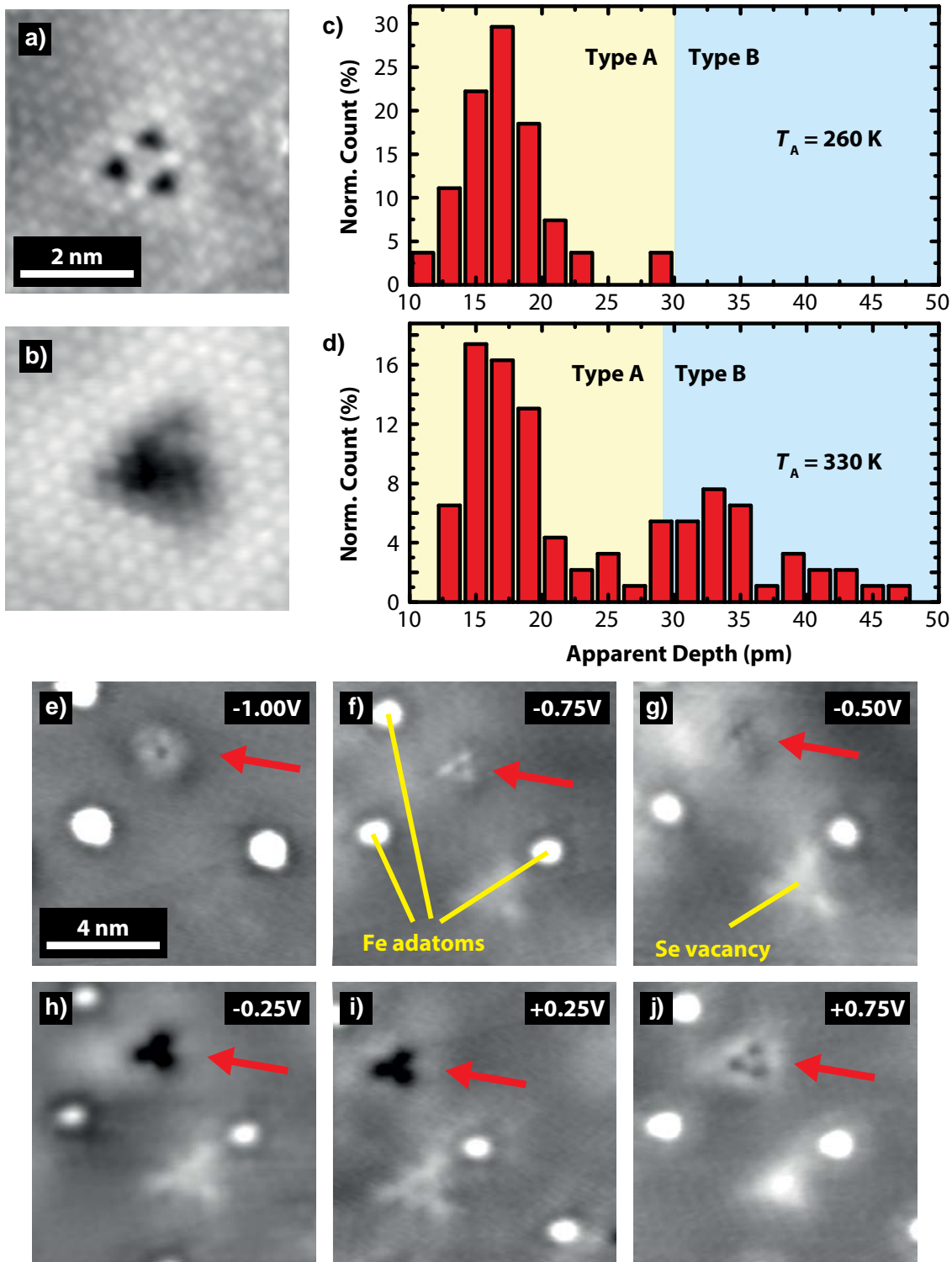
Figure 6.4.: A closer look to different subsurface Fe defects: **a)** Type A defect, average depth: 17.2 ± 1.6 pm. $U_B = 1$ V, $I = 50$ pA. **b)** Type B defect, average depth: $34, 7 \pm 3.5$ pm. $U_B = 0.25$ V, $I = 50$ pA. Distribution of apparent defect depths for a sample annealed to 260 K (c) and 370 K (d) measured with a bias voltage of 0.25 V. Type A defects are marked with a yellow background, type B defects with a blue background. No type B defects can be found after annealing to 260 K. **e)-j)** Appearance of type A defects at different bias voltages. The defect is marked with a red arrow. Other features are labeled in yellow. $I = 100$ pA, $\Delta z = 35$ pm.

74

Fe Deposition Without Cooling the Sample

So far, samples were cooled down for Fe deposition to less than 150 K before the substitution was triggered by annealing. This two step process was needed the ensure and document the presence (and amount) of single Fe atoms at the Bi_2Se_3 surface. However, the preparation could be simplified, if the annealing temperature can be already applied during deposition. This is not trivially the case. With the low temperature deposition Fe atoms arriving at the surface are immediately cooled down and reduced in mobility. The probability to interact with other Fe atoms to form clusters is dramatically reduced. (Compare with images in Fig A.1. The greater the annealing temperature and hence the mobility of the adatoms, the larger are the clusters at the surface.) Atoms that are already bound in clusters have a much lower probability to diffuse into the surface.

In order to check on this the experiment was repeated with Fe deposition at room temperature, see Fig. 6.5. No qualitative difference was found. Even annealing to 370 K did not change the morphology, underlining the stability of the subsurface substituted Fe atoms in this temperature range, as already found by the quantitative analysis in Fig. 6.3 (f).
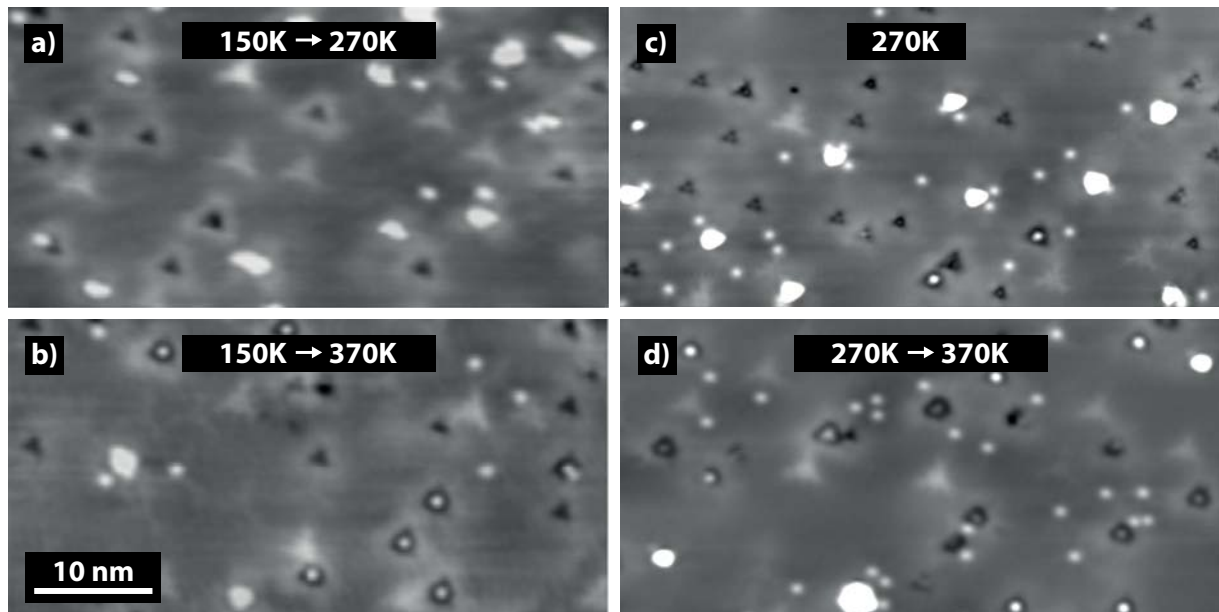
Figure 6.5.: Comparison of preparations with and without cooling the sample for Fe deposition. a) and **b)** Bi_2Se_3 samples cooled to ≤ 150 K, followed by Fe deposition, then annealed to 270 K (a) and 370 K (b). **c)** Deposition at 270 K. **d)** Sample annealed to 370 K after deposition at 270 K. There are no substantial differences of morphology between samples where Fe was deposited at ≤ 150 K and at 270 K before annealing to 370 K. For all images: $U_B = 0.25$ V, $I = 200$ pA.

Open Questions

The experiments applied so far have successfully proven that Bi atoms of the first QL can be substituted by Fe adatoms in a controlled manner. However, STM cannot answer the question if Fe atoms actually diffuse into other sites of the first QL, as this would not provide features visible to STM [152]. Since such a diffusion could be the reason for the great decrease of adatoms, unveiling that diffusion and the doping by these atoms is of great interest. These questions will be answered within the next sections, together with the other open question: Do the subsurface atoms still exhibit a magnetic moment?

6.2. Changing the Doping Effect

The ARPES measurements for investigating the doping effect were carried out at the SGM3 beamline at the ASTRID synchrotron in Aarhus with a SPECS Phoibos 150 hemisperical analyzer [153], at a sample temperature of 60 K. The energy and angular resolutions were better than 15 meV and 0.13°, respectively. Images were acquired along the $\bar{K} - \bar{\Gamma} - \bar{K}$ direction with a photon energy of 19.2 eV. The base pressure of the system was $< 10^{-9}$ mbar. Samples were cut from the same crystal used for the STM study. The preparation followed the procedure developed during the STM study.

On each sample Fe was deposited several times with increasing coverage for each deposition: 1 % of a ML, 2.5 %, 5 % and 10 %. After each deposition the samples were annealed to 370 K with a holding time of 1 min. To study the influence of deposition and annealing, samples were measured by ARPES right after cleaving and after every preparation step.

The ARPES data is summarized in Fig. 6.6 for both types of substrates, pristine (a to e) and Ca-doped Bi_2Se_3(f to j). The position of the DP determined from the measured band structure is marked with a green line (red for Ca-doped samples). After each deposition (b, d, g, i) the whole band structure shows a shift to larger binding energies expected from the surface doping with Fe adatoms [101] and the formation of quantum well states (QWS) (red arrows). At higher coverages, also a Rashba splitting of the CB QWS can be observed [131, 133–135, 147, 154], e.g. green arrows Fig. 6.6 (d). Most notably, annealing the samples (c, e, h, j) almost reverses the band bending and destroys the QWS completely.

In order to exclude that the band bending and its reduction is induced by the adsorption (and desorption) of residual gases in the chamber [130] the experiment was repeated with a running but closed evaporator. Hence, due to the evaporator heat the same amount of residual gases should be present but no Fe atoms can reach the sample. A comparison of ARPES images taken before and after the virtual deposition reveals no shift of the band structure. The DP shifts observed in the main experiment can therefore be clearly attributed to the presence and diffusion of Fe adatoms.

With this certainty, the shifts can be analyzed closer. Fig 6.6 (k) plots the DP position against the number of preparation steps taken for a pristine Bi_2Se_3 substrate and two Ca-doped substrates. All uneven numbered preparation steps are depositions, all even ones are annealing processes. After every deposition the DP drops to a larger binding energy and after every annealing the DP shifts back to an energy close to its location before deposition. While it never reaches that energy, the differences get smaller for each iteration.
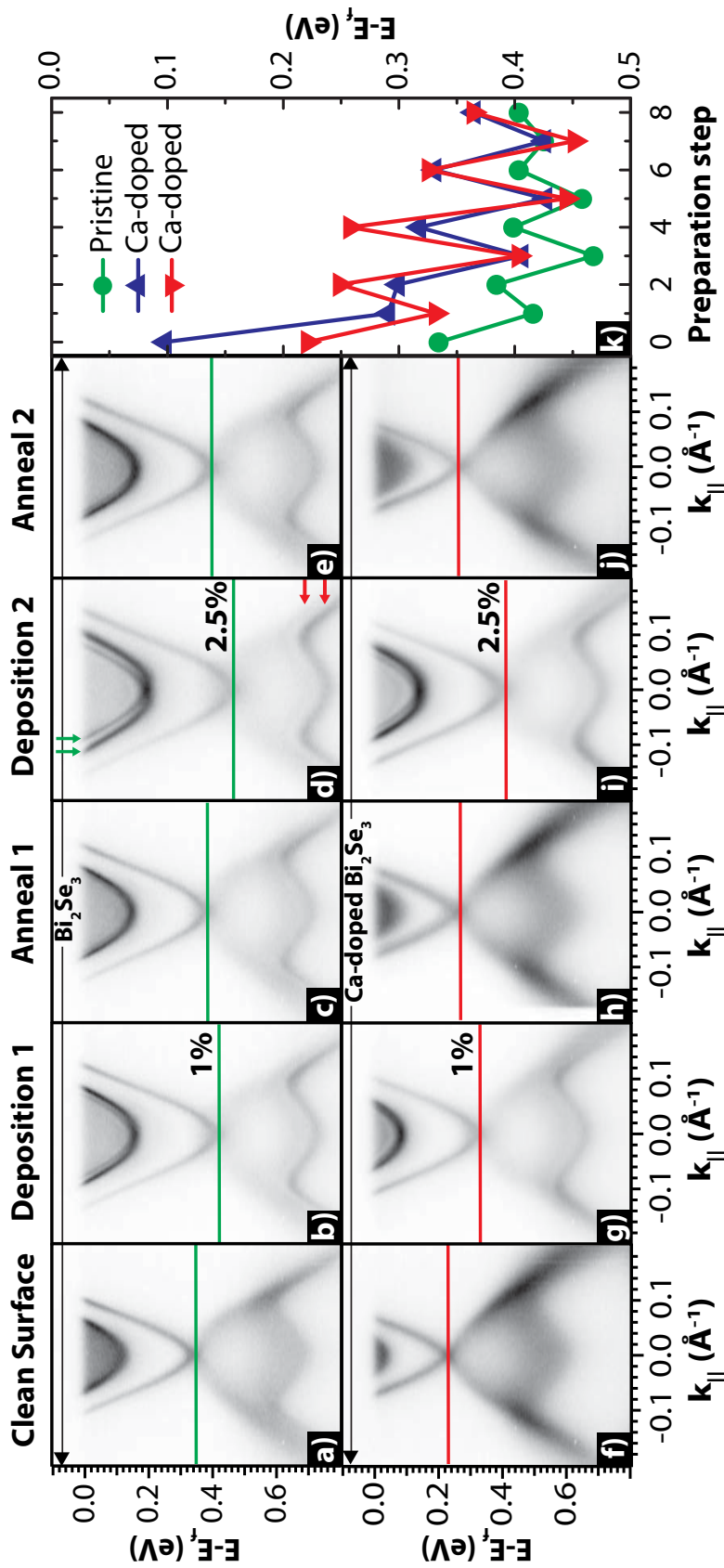
Figure 6.6.: Band structure shift of Bi₂Se₃ depending on Fe deposition and annealing measured by ARPES. Two series of ARPES measurements for pristine (a-e) and Ca-doped (f-j) Bi₂Se₃ substrates. **a)**, **f)** Initial spectra after *in situ* cleaving. Subsequent cycles of deposition of Fe at ≈ 150 K, in % ML Fe as indicated and subsequent annealing to T_A ≈ 370 K. The DP energy extracted from the spectra is marked by a red or green horizontal line. Arrows in (d) mark QWS induced by band bending [154], red: VB QWS, green: CB QWS. **k)** Resulting binding energy plotted in dependence of preparation steps for a pristine (dots) and two differently Ca-doped samples (up and down triangles). Preparation step number 0 indicates a freshly cleaved substrate without Fe. Steps 1 (1 %), 3 (2.5 %), 5 (5 %), 7 (10 %) indicate depositions; steps 2, 4, 6, 8 subsequent annealing steps.

Taking into account the surface defect analysis based on STM images in section 6.1, the upward shift after annealing can be explained as follows: The number of Fe adatoms on the surface is reduced, because Fe diffuses below the surface. This reduces the number of donors on the surface. If the Fe that diffused below the surface mainly sits on Bi substitutional sites and is neutral, the band bending will consequently be reduced.

The small drops of the DPs energetic position after each iteration may have several causes: A growing number of residual Fe adatoms that do not diffuse or desorb, the presence of diffused Fe atoms (if there is any doping effect) and the typical aging effect observed for such an environment. Indeed, the shift caused by aging is typically in the same range as the observed shift between steps 0 and 8 of 100 meV. However, annealing should reduce this effect by removing adsorbed residual gases from the surface [130]. Therefore, both, aging effect and residual Fe adatoms, most likely contribute to the overall downward shift of the DP. However, since one cannot estimate their share qualitatively, a possible doping effect of the diffused Fe atoms cannot be excluded. To solve this open question and to gain information about the changes of the Fe atoms' magnetic moments, diffused Fe atoms were simulated by DFT calculations. These results are presented in the next section.

6.3. Simulation of the Diffusion Process

DFT calculations were carried out, using the VASP code [155, 156] with the GGA-PBE approximation for the exchange and correlation functional [157] and utilizing plane-wave basis sets with a kinetic energy cutoff of 20 Ry in combination with projector augmented-wave (PAW) pseudopotentials [158, 159]. A 3x3 supercell with a slab consisting of two QL was employed, where atoms were relaxed until the maximum force component of each atom was below 0.02 eV. For the calculation of the DOS a (6x6) k-point grid was used.

Doping Effect of Fe atoms on Different Sites

To investigate the doping effect and the magnetic moment six different sites were considered for the Fe atoms, see Fig. 6.7: The positions of adatoms at the fcc (T$_1$) and hcp (T$_2$) hollow sites of the surface, visualized in (a) and (b), as Fe substitutions of Bi atoms in the first (Bi$_1$, c) and second (Bi$_2$, d) bismuth layer and Fe on two different interstitial sites I$_1$ (e) and I$_1$ (f) within the first QL. The calculated DOS for each case, together with the DOS of pristine Bi$_2$Se$_3$, is given in Fig. 6.7 (g). For the pristine crystal the onset of the VB is just below E_F and the onset of the CB is at an energy of 0.75 eV. Within the bulk gap a small DOS can be found with a minimum at $\approx E_F$ and a gradual increase above. This can be attributed to the TES of the system.

The DOS for Fe adatoms (green, yellow) as well as for the atoms on interstitial sites (cyan, purple) exhibit a significant shift of 0.5 eV to higher binding energies, as expected for electron donors. For Fe atoms on Bi substitutional sites the DOS shows no shift, indicating a neutral doping behavior. This is supposed to change when the sample is heavily n-doped, e.g. by a large number of Se vacancies or Fe adatoms, and E_F is shifted into the bulk CB of the crystal. Then the Fe atoms replacing Bi might act as electron acceptors.

In both cases DFT calculations are in line with the observations of STM and ARPES and clarify some of the open questions. The decrease of band bending after annealing can be amongst others attributed to the diffusion of adatoms into the bulk. Here, Fe most probably substitutes Bi atoms and switches from an electron donor to a neutral behavior. Fe seems not to diffuse into interstitial sites, as here the doping effect would be similar to Fe adatoms and the residual band bending is too small to leave room for such a behavior[2]. The residual band bending in contrast can be explained by the remaining adatoms and the natural aging effect of the surface.

---

[2]A small amount of Fe atoms on interstitial sites cannot be excluded, but the possible number seems to be small enough to be neglected
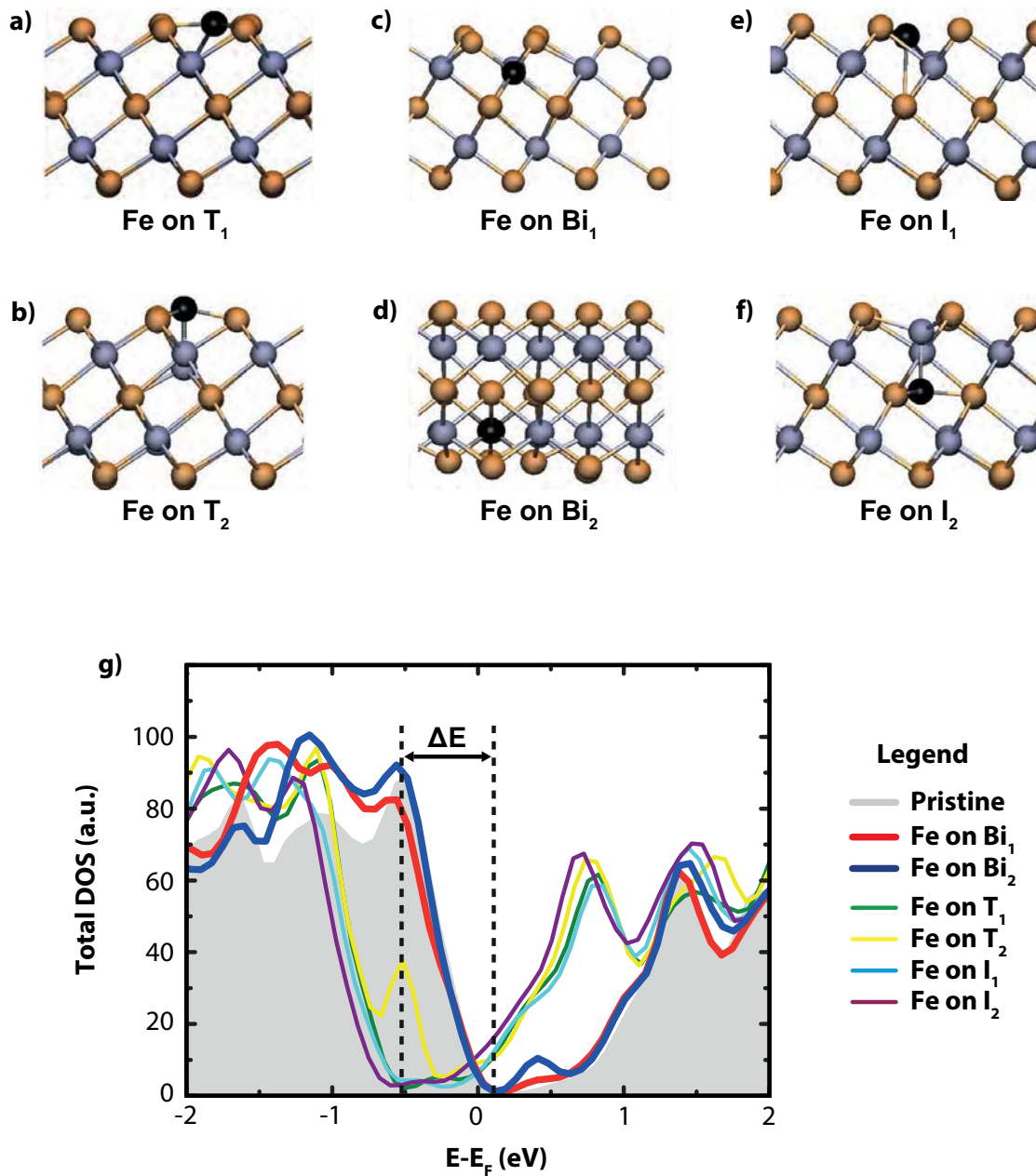
Figure 6.7.: DFT calculations of total DOS for Fe doped into different sites of a surface Bi$_2$Se$_3$ QL a)-f) Ball and sticks models of considered geometries. Fe colored black, Bi grey and Se orange. (a) and (b) depict Fe adatoms on fcc (T_1) and hcp (T_2) sites. (c) and (d) show Fe atoms substituting Bi atoms of the first (Bi$_1$) and second (Bi$_2$) bismuth layer. (e) and (f) illustrate Fe atoms on two interstitial sites (I$_1$, I$_2$). **g)** Calculated total DOS for pristine Bi$_2$Se$_3$ (grey background) and all six configurations described in (a) to (f). ΔE indicates the energy shift for all configurations, where Fe is not in a $(+3)$ oxidation state: T_1, T_2, I_1, I_2. Fe atoms on Bi sites do no lead to band-shifts.

	T$_1$	T$_2$	Bi$_1$	Bi$_2$	I$_1$	I$_2$
m$_{Fe}$	2.8	2.8	3.5	3.4	2.7	3.3
m$_{tot}$	3.0	3.2	5.0	4.9	3.1	2.4

Table 6.1.: 3d and total magnetic spin moments of Fe atoms on different Bi$_2$Se$_3$ sites according to Fig. 6.7. m$_{Fe}$ and m$_{tot}$ denote the Fe 3d spin moments and the total spin moment of the whole super cell. Values are given in units of μ_B

Magnetic Moments of Bulk-Diffused Fe Atoms

DFT also provides the magnetic spin moments m$_{Fe}$ for every considered site, see Tab. 6.1. All Fe atoms exhibit a strong spin moment in the range of 2.7 μ_B to 3.5 μ_B, originating from the 3d shell of the atom. Fe atoms on Bi sites exhibit the strongest moments with 3.4 μ_B and 3.5 μ_B. The stronger magnetic moment, as well as the reduced doping, might be explained by the (+3) oxidation state of these atoms, while adatoms and interstitial atoms naturally exhibit a smaller oxidation state.

Since coupling of the Fe magnetic moment to the substrate is crucial for magnetism induced modifications of the TES, also the total spin moment m$_{tot}$ of the simulated supercell was calculated. Typically, the Bi atoms couple anti-ferromagnetically, while the Se atoms couple ferromagnetically to the Fe atoms. Hence, for Fe atoms on Bi sites m$_{tot}$ is increased (by 1.5 μ_B), as they are surrounded by Se atoms. For adatoms and interstital site I$_1$ m$_{tot}$ is still slightly enhanced, by 0.2 to 0.4 μ_B. Only for I$_2$, m$_{tot}$ is reduced compared to m$_{Fe}$ by 0.9 μ_B. Here, the presence of an Fe atom on I$_2$ is accompanied by a coordination change of the Bi atom above, creating a Bi dominated neighborhood for the Fe atom.

6.4. Summary

The study presents a method to controllably diffuse Fe atoms below the surface of Bi_2Se_3. With a precise presetting of the annealing temperature, not only the process itself can be triggered, but different types of diffusion sites can be favored. Combining the results from STM, ARPES and DFT calculations the type of diffusion sites were identified, the doping capabilities of the diffused atoms analyzed and their magnetic moments determined.

Diffusion into the surface was observed for a temperature interval between 260 K and 430 K, with a stable number of adatoms and diffused atoms between 290 K and 370 K. At the lower end of the interval (below ≈ 300 K) only one type of defect induced by the diffused Fe atoms is detectable. Here, Fe atoms substitute atoms of the first Bi layer of the surface QL. Above ≈ 300 K a second type of defect can be observed, where the diffused Fe atoms substitute atoms of the second Bi layer of the surface QL. Other sites can be excluded.

Fe atoms on Bi sites are in a (+3) oxidation state and are neutral concerning doping of the host crystal. This is in sharp contrast to Fe adatoms on Bi_2Se_3, which significantly n-dope the Bi_2Se_3 surface [100]. Also the diffused atoms retain a magnetic moment. This couples ferromagnetically with the moment of neighboring Se atoms leading to an increased total magnetic moment of the crystal.

A study published by Ye *et al.* [160] reveals the magnetic anisotropy of Fe atoms grown on Bi_2Se_3 at room temperature, i.e. Fe atoms on Bi substitutional sites, via XMCD measurements. The anisotropy is revealed to have an out-of-plane easy axis. Hence, with a sufficiently large density of diffused Fe atoms TRS should be broken and a gap should be observed by ARPES [3].

For a proof-of-principle this study focuses on pristine Bi_2Se_3 crystals as a substrate. The same diffusion behavior was found for Ca-doped Bi_2Se_3 substrates, Fig. 6.3 (d and e). This proves the usability of the technique for future applications: Fe atoms can be used to introduce an out-of-plane magnetic moment to the edge of a TI without shifting the Fermi level out of the gap. If E_F is not at the location needed for the aspired application, the band structure can be shifted by calcium doping into its optimal position without interfering effects introduced by Fe.

While the temperature dependent diffusion process has been proven to work successfully for Fe on Bi_2Se_3, the method should be applicable for the whole Bi_2X_3-family and a wide range of adatoms. Indeed, indications for a similar behavior were already found for Al on Bi_2Se_3 and Mn as well as Ni adatoms on Bi_2Te_3, see appendix A.

---

[3]However, this result should be taken with care. The study by Ye *et al.* provides no STM image of the surface so the state of Fe atoms for this experiment is not known. In principle, the diffusion mechanism described in this chapter should work with any Bi_2Se_3-sample. However, so far not all grown Bi_2Se_3 crystals show the same high quality and reproducibility of results as crystals used here [145].

7. Characterization of PbBi$_4$Te$_7$

The results of this chapter are an excerpt of findings published in

This chapter deals with stoichiometric manipulations of 3D TIs in order to investigate the influences of the changes of the general electronic structure on the topological edge state. Manipulation of the bulk electron structure is ambitious. Specific crystal structure and material composition are fundamental for the topological nature of the system and too severe changes might reverse the band inversion. But when the inversion is conserved, bulk manipulation can be a powerful tool to tailor the band gap of TIs . Its size can be increased and its nature (direct or indirect) can be changed.

Based on its properties, Bi$_2$Te$_3$ would be a good candidate to test bulk band structure manipulation. Its gap is indirect and compared to Bi$_2$Se$_3$ rather small. Small changes of the bulk band structure might lead to a direct band gap with increased size. Fortunately, the stoichiometry of Bi$_2$Te$_3$ (and Bi$_2$Se$_3$) can be changed easily with only small adjustments to the crystal structure.

Both, Bi$_2$Te$_3$ and Bi$_2$Se$_3$, belong to the pseudobinary family of material systems. These are composed of defined elements of the IV, V and VI main group of the periodic table, where the material composition follows the formula A^{IV}B^{VI}−A$_2^V$B$_3^{VI}$, with A^{IV} = Ge, Sn, Pb; A^V = Bi, Sb and B^{VI} = Te, Se. The crystal structure of these systems exhibits a homologous series of nA^{IV}B^{VI} · mA$_2^V$B$_3^{VI}$ layered compounds [161–163]. For Bi$_2$Te$_3$ (and Bi$_2$Se$_3$) this means adding Ge, Sn or Pb to the crystal does not change the layered nature of the parent system, but introduces new layers within its the unit cell.
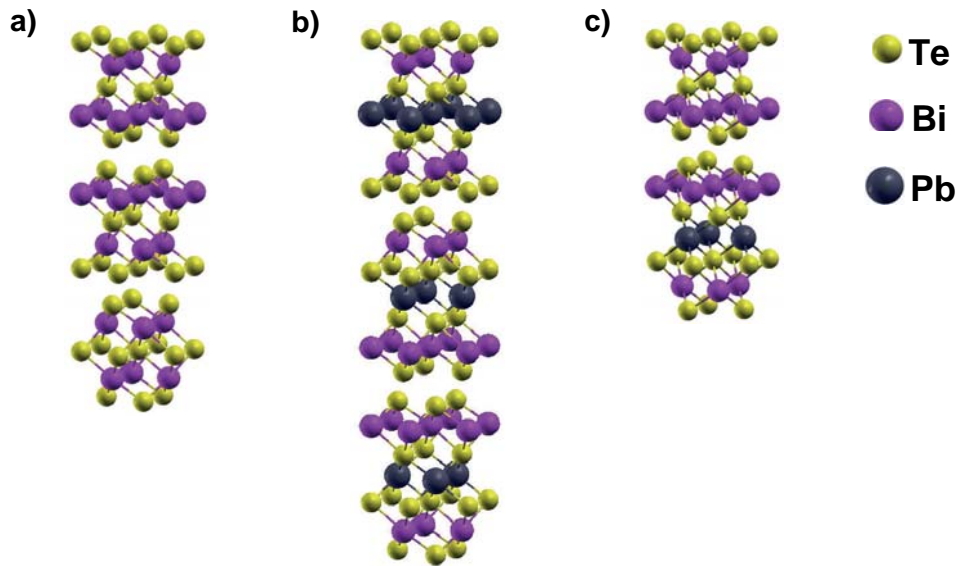
Figure 7.1.: Atomic structure of Bi$_2$Te$_3$ and Pb-based ternary compounds. a) Three quintuple layers of Bi$_2$Te$_3$. **b)** Three septuple layers of PbBi$_2$Te$_4$. **c)** Quintuple and septuple layer sequence typical for PbBi$_4$Te$_7$.

Fig. 7.1 gives the atomic structures of Bi$_2$Te$_3$ and two different Pb-based ternary compounds. Adding Pb introduces septuple layers to the crystal. The original quintuple layer (QL) is complemented by one Pb- and one additional Te-layer, leading to a stacking sequence of Te-Bi-Te-Pb-Te-Bi-Te. The septuple layers (SL) exhibit a height of ≈ 14 Å instead of the ≈ 10 Å, which can be found for quintuple layers [163, 164]. The occurrence of the SL depends on the stoichiometry of the system, e.g. in PbBi$_2$Te$_4$ every QL is replaced by a SL, in PbBi$_4$Te$_7$ only every second QL is replaced.

Since the original crystal structure is only slightly changed by the presence of Pb, the topological nature of the parent system might be conserved. Indeed, DFT calculations using a method developed by Fu *et al.* [25] predict all these variations to be TIs. The variation of Pb concentration not only influences the bulk band gap (and hence the shape of the Dirac cone), but can influence the *localization* of the cone as well.

PbBi$_2$Te$_4$ exhibits the smallest changes compared to its parent compound concerning the electronic structure, see Fig. 7.2. The bulk gap exhibits the same width, but is now indirect and the dispersion of the cone below the DP is more linear. The TES is localized in the topmost SL.

In PbBi$_4$Te$_7$ QLs and SLs are alternating. Hence, two terminations are possible: a QL termination or a SL termination. In both cases the gap is indirect and its size is practically conserved. The dispersion of the cones below the DP is more linear again.

However, the two terminations differ concerning the localization of the TES. For the SL termination, the TES is located in the topmost slab, just as in the case of Bi_2Te_3 and $PbBi_2Te_4$. In case of the QL termination, the TES is *not* located in the slab at the edge, but in the first SL underneath. This is the first TES that is predicted to be localized significantly away from the edge of the system. The QL on top works as a ≈ 1 nm buffer to the edge and will protect the TES from perturbations at the surface.
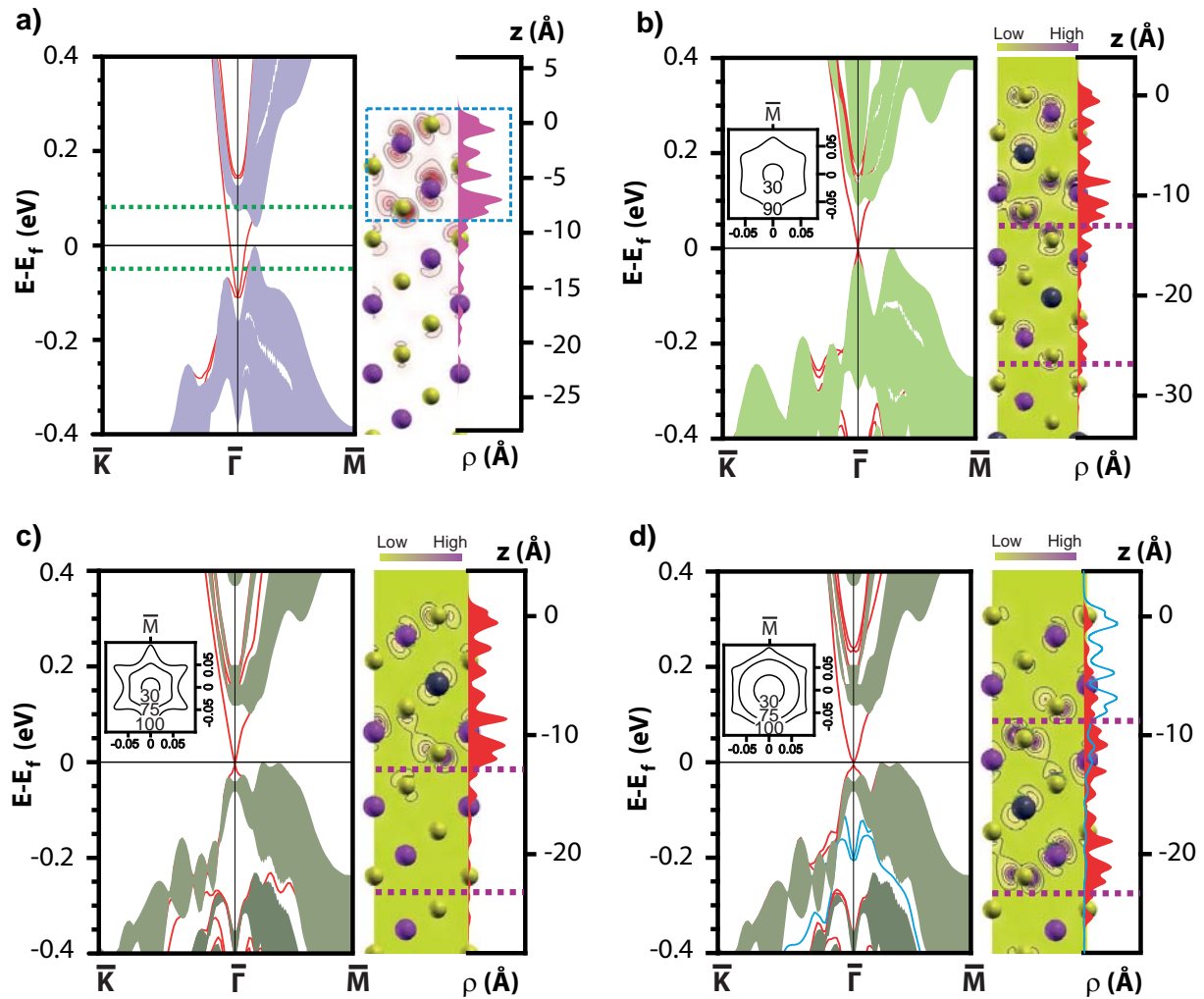
Figure 7.2.: Surface electronic structure of Bi_2Te_3, $PbBi_2Te_4$ and $PbBi_4Te_7$. Left side of each panel: the calculated surface band structure of each system. Insets show iso-energy contours of the Dirac cone at various energies. Right side of each panel: spatial distribution of the charge density of the TES at $\bar{\Gamma}$ in the $(11\bar{2}0)$ plane and the charge density $\rho(z)$ (red) of this state integrated over the x-y-plane; z = 0 corresponds to the surface atomic layer. Horizontal dashed lines show boundaries between building blocks. **a)** Bi_2Te_3. **b)** $PbBi_2Te_4$. **c)** $PbBi_4Te_7$ with SL termination. **d)** $PbBi_4Te_7$ with QL termination. Additional trivial surface state localized in the topmost QL is shown in blue.

Additionally, the buried Dirac cone exhibits a much smaller warping than in the case of a SL termination, see Fig. 7.2 (c) and (d). Hence, interaction within the cone is reduced.

The peculiarity of this Dirac cone is underlined by the presence of another set of surface states (blue lines). These are localized in the edge QL slab. In the parent system (Bi$_2$Te$_3$) these states would form the TES. In PbBi$_4$Te$_7$ their dispersion is almost identical to the Dirac cone in Bi$_2$Te$_3$, but their location is below the gap and their topological nature is trivial. In order to test the theoretical predictions, PbBi$_4$Te$_7$ samples were fully characterized by ARPES and STM measurements.

In the first section, an analysis of ARPES data will verify the topological nature of the system and the predicted buried Dirac cone. The shape of the cone will suggest a dominant QL termination of the surface. This will be falsified in the STM section where the surface morphology of PbBi$_4$Te$_7$ is investigated. The results will be summarized in a third section. Several solutions for the discrepancies will be given, including a shift of the Dirac cone corresponding to the SL termination into the bulk of the crystal.

ARPES measurements were carried out by Gabriel Landolt, Bartosz Slomski, Luc Patthey and Jan Hugo Dil from the Physik-Institut of Zürich University, Switzerland. STM measurements were conducted by myself with the assistance of Julian Hagemeister at Hamburg University. Julian Hagemeister wrote his Bachelor thesis about some aspects of the STM characterization of PbBi$_4$Te$_7$. The title of his thesis is "Strukturelle Charakterisierung des Topologischen Isolators PbBi$_4$Te$_7$ mit einem temperaturvariablen Rastertunnelmikroskop".

The DFT calculations presented in this section were provided by Sergey V. Eremeev, Tatiana V. Menshchikova, Yuri M. Koroteev, Pedro M. Echenique, Stepan S. Tsirkin and Evgueni V. Chulkov from the Donostia International Physics Center at San Sebastian, Spain as well as Jürgen Henk and Arthur Ernst from the Max-Planck-Institut für Mikrostrukturphysik at Halle, Germany.

7.1. Probing the Electronic Structure of PbBi$_4$Te$_7$

ARPES experiments were performed at the Surface and Interface Spectroscopy beamline at the Swiss Light Source of the Paul-Scherrer Institute. A photon energy of 20 eV was used. Data were collected with a Scienta R4000 hemispherical analyzer, with a total energy and angular resolution of 12 meV and 0.1°, respectively. The PbBi$_4$Te$_7$ crystals were grown from the melt by the vertical Bridgman-Stockbarger method. Further details are described in [165]. Fresh surfaces were prepared by cleaving the samples *in situ* with the scotch-tape method, see section 5.2.2. Samples were cooled down for experiments to 10 K.

ARPES images of the PbBi$_4$Te$_7$ sample show a pronounced Dirac cone, confirming the topological nature of the system, see Fig. 7.3 (a - c). The whole band structure exhibits a downward energy shift of ≈ 500 meV compared to DFT calculations, which can be taken as a first hint for defects. The bulk band gap stretches between a binding energy of ≈ 0.3 eV and ≈ 0.5 eV. Below 0.5 eV the Dirac cone remains separated from bulk bands along $\bar{\Gamma}\bar{K}$, but crosses along $\bar{\Gamma}\bar{K}$.

A comparison of measured CECs with calculated iso-energy contours, Fig. 7.3 (d) and (e), shows a great resemblance of the measured data with the Dirac cone for QL termination, pointing to a dominance of QL termination at the surface. However, a signature of the theoretically predicted trivial surface state (Fig. 7.2 (d) cannot be found. Surface defects might be a possible explanation for the absence of this band. The presence of surface defects is indeed indicated by a further analysis of the measured Dirac cone bandwidth and the charge density distribution of the TES provided by theory. At larger $\bar{K}$-values the states of the Dirac cone are localized primarily in the topmost QL, while close to $\bar{M}$ the DC states are localized in the first SL below the surface, Fig. 7.3 (g). For the states at large $\bar{K}$, the bandwidth is increased in the measured Dirac cone, see the region marked with arrows in Fig. 7.3 (a). This is a phenomenon typical of scattering at defects.

The characterization by ARPES confirms the topological nature of PbBi$_4$Te$_7$. The shape of the Dirac cone and the observed bandwidth change can be seen as a first proof of a *buried* Dirac cone. The measured spectra indicate a termination dominated by QLs and the presence of defects at the surface (and the bulk) of the crystal. Especially, the preference of a QL termination is surprising, as, due to the symmetry of alternating quintuple and septuple layers, van-der-Waals forces should be similarly strong between each slab. However, the layers might be organized differently within the crystal, leading to the dominating QL termination. Another possibility is, that the crystal cleaves not only between, but also through the slabs, leading to greater perturbations of the Dirac cone. To answer these questions, the crystal has also been characterized by STM measurements, which are presented in the next section.
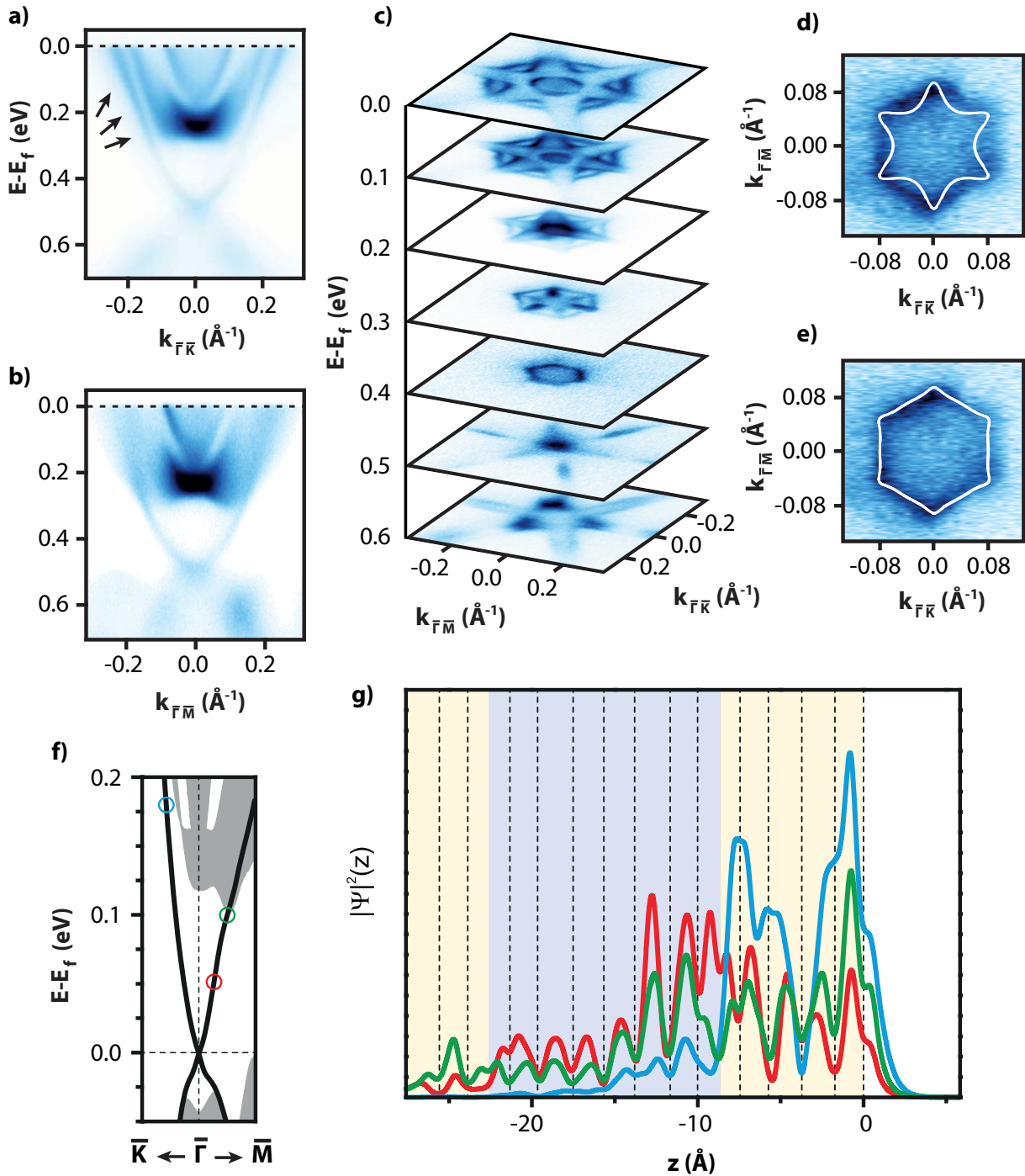
Figure 7.3.: ARPES and charge density distribution for PbBi$_4$Te$_7$. a) Band structure measured by ARPES along $\bar{\Gamma}\bar{K}$ and **b)** $\bar{\Gamma}\bar{M}$ directions. Arrows mark a region with increased bandwidth. **c)** Measured energy dependence of CECs at $h\nu = 20$ meV. **d)** Comparison of CEC at 100 eV above DP with a correspondingly calculated iso-energy contour for SL termination and **e)** a calculated contour for QL termination. **f)** Scheme of the PbBi$_4$Te$_7$ QL terminated band structure around E_F with markers pointing to states where the charge density distribution was calculated for in **g)**. Vertical dashed lines indicate the position of atom cores, colors in the background identify the slab; yellow: quintuple layer, blue: septuple layer.

7.2. Surface Characterization

STM experiments were conducted in the chamber system described in section 5.1. The base pressure was $< 10^{-10}$ mbar. The investigated samples were cut from the same region of the same crystal that was used for ARPES. Samples were cleaved *in situ* at a pressure of $< 10^{-8}$ mbar with the scotch-tape method described in 5.2.2 and got transferred to the VT-STM within one minute. All measurements were performed at 30 K. The STM tip was an electrochemically etched polycrystalline W wire. STM topographs were taken in constant-current mode.

Fig. 7.4 (a) shows an overview scan typical of the samples investigated. The surface is covered with large slabs of alternating heights of 10.3 ± 0.3 Å and 14.1 ± 0.3 Å. The resulting height of the crystal's unit cell, 24.4 ± 0.4 Å, is very well in agreement with values found in literature, compare Tab. 7.1. The alternating heights prove the QL-SL slab periodicity of the crystal. Together with the absolute heights of individual slabsand the smoothness of the surface, STM measurements prove that the crystal cleaves dominantly along the van-der-Waals gap.

A quantitative analysis of surface termination including 18 images from different cleaves with a total area of 212.7 μm^2 reveals a coverage of about 53 % with septuple slabs and of 47 % with quintuple slabs. Hence, no type of slab is dominating the termination.

Images with atomic resolution, Fig. 7.4 (c), reveal a hexagonal lattice structure with a lateral lattice constant of 4.5 ± 0.2 Å; again very well in agreement with literature (see Tab. 7.1). A comparison with images taken from Bi_2Te_3, depicts a rather high density of sub-surface defects for $PbBi_4Te_7$, see Fig. 7.4 (c) and (d). Moreover, there is a large scale apparent height modulation, where the slabs do not appear flat but are covered with ditches, e.g. red arrow in Fig. 7.4 (a). Since the crystal seems to cleave easily along the van-der-Waals gap, these disturbances seem more likely to be a bulk property of the crystal, though it cannot be excluded that the cleaving process introduces defects.

	STM	Literature
a	4.5 ± 0.2 Å	4.426 Å
c	24.4 ± 0.4 Å	23.892 Å

Table 7.1.: Lattice constants of PbBi$_4$Te$_7$ a: lateral lattice constant, c: lattice constant along z-axis, see Fig. 7.1, including a QL and SL slab. STM values are measurements of the present work, literature values are measured by X-ray diffraction [163]

91
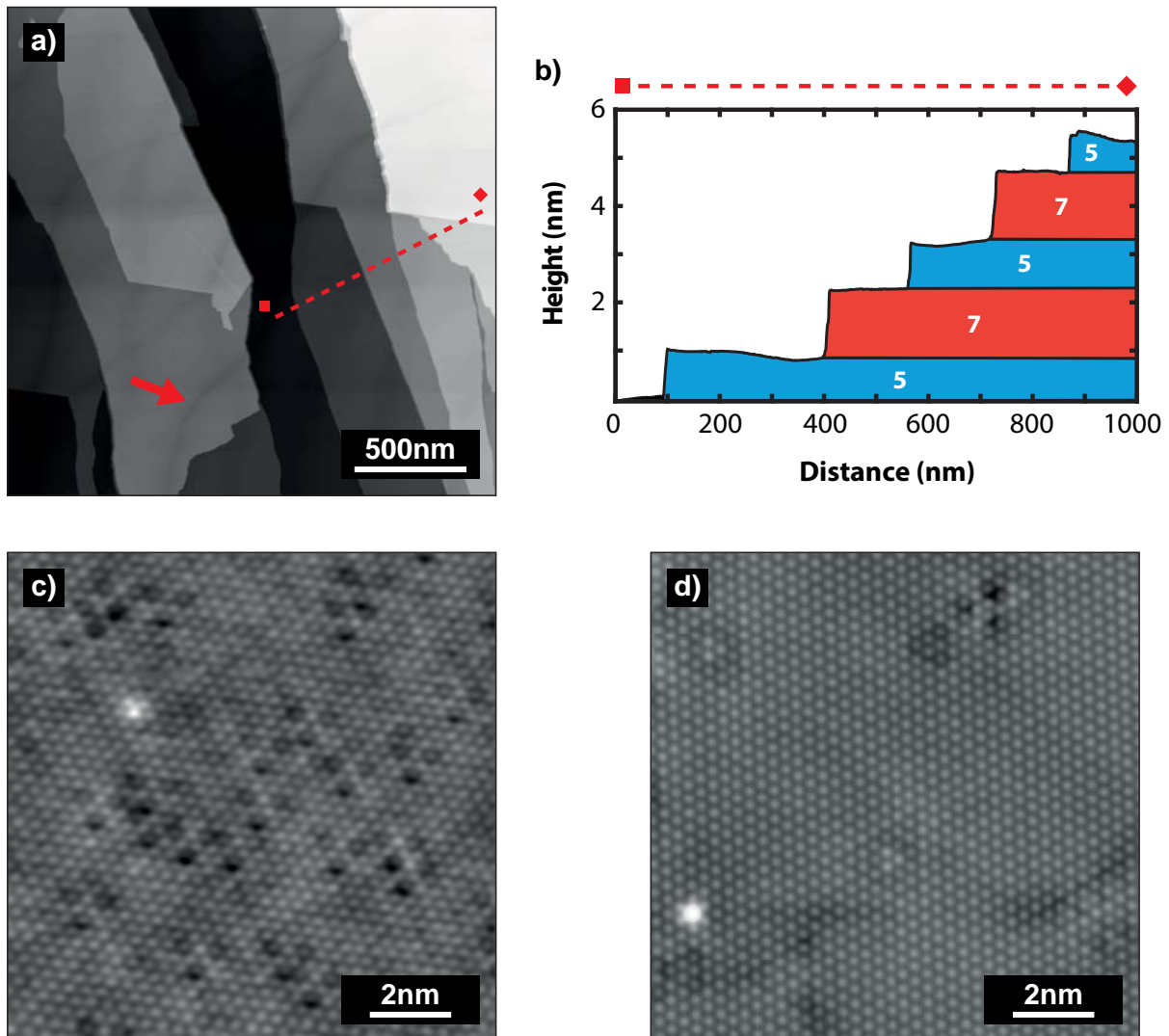
Figure 7.4.: Overview and atomic resolution images of PbBi$_4$Te$_7$. **a)** Overview image of PbBi$_4$Te$_7$. The surface is built by large terraces and covered with ditches, e.g. red arrow U_B: 0.5 V, I: 250 pA. **b)** Line section along dashed red line in (a). Colors and numbers identify slab type. red: SL, blue: QL. Note the height variation of the QLs in particular. **c)** Topographic image with atomic resolution of the PbBi$_4$Te$_7$ surface, here of a spot with SL termination. QL terminated surfaces exhibit the same defect density. U_B: 0.4 V, I: 50 nA. **d)** For a comparison an image of the Bi$_2$Te$_3$ surface is shown. U_B: 0.4 V, I: 2.1 nA. The PbBi$_4$Te$_7$ surface exhibits a much larger number of defects and a greater variation of the local density of states.

7.3. Discussion and Summary

At first sight, the results of the STM investigation concerning surface termination seem to be in conflict with the conclusions drawn from ARPES. The lack of warping of the measured Dirac cone cannot be explained by a dominance of QL termination, as the surface is formed by both terminations equally. One possible explanation is that the prediction of a warped Dirac cone for SL terminated surfaces is wrong. However, this seems unlikely, because other predictions from DFT calculations have been confirmed quite precisely: the topological nature of the material, the shape of the Dirac cone corresponding to QL termination, its buried localization as well as the location of single states of the cone within the slab[1].

Hence, the measured Dirac cone should per se come with a warped component. The lack of this component indicates a mechanism that suppresses the formation of a Dirac cone at the SL terminated surface. This mechanism might originate from the high number of defects observed by STM. Both, STM and the increased bandwidth of the Dirac cone for states closer to the surface (Fig. 7.3), point to the surface nature of these defects. This is also supported by ARPES measurements on Bi_2Se_3, which show that the Dirac cone vanishes, when the number of surface defects is increased by mild sputtering [166]. This proves that such defects can influence the TES.

For surface disturbances Schubert *et al.* [106] predicted the behavior of TES with respect to the disturbance strength, as illustrated in Fig. 7.5. If not disturbed or for small perturbations, the cone is unchanged, due to its topological protection. If the disturbance is in the order of the band gap, the TES is still present at the surface, but is too much localized in real space to form a defined cone in $\vec{k}$-space (scenario A). The surface of the TI can be described as a diffuse metal. For disturbances much larger than the gap, the surface layer transforms to a topologically trivial Anderson Insulator (AI) and a Dirac cone can be found again at the Anderson insulator (AI)/TI-interface (Scenario B).

In case of $PbBi_4Te_7$ with its slab nature, the Dirac cone would shift most likely to the next SL for such a strong perturbation. Localized more than 24 Å below the surface, this cone is no longer accessible by ARPES and cannot contribute to the measured spectra. Hence, both scenarios can explain the lack of warping of the measured Dirac cone. The high number of surface defects are likely to cause this effect. However, both scenarios cannot be verified or falsified, neither on a theoretical ground, as the actual strength of the disturbance is unknown, nor on an experimental ground, as a possible shifted Dirac cone cannot be probed anymore. The exact mechanism remains an open question.

---

[1]Only the position of E_F is shifted by 0.5 eV to higher binding energies. This is a typical discrepancy between measured band structures and DFT calculations that is caused by the doping of real crystals.

It is worth mentioning that a shift as described in scenario B would be unique to TES and has not been confirmed experimentally so far. Its observation would be a clear proof for the robustness of the TES. A more conclusive experiment showing this effect is described in chapter 8, where the topological insulator TlBiSe$_2$ is characterized by STM, AFM and photoemission experiments.

Apart from the unsolved question of the behavior of the TES, the combined ARPES and STM study confirms the topological non-trivial nature of PbBi$_4$Te$_7$. By a comparison with the calculated band structure, the observed Dirac cone is identified as a TES localized more than 10 nm below the surface. The study presented is the first having identified such a buried Dirac cone. The localization of the TES below the surface is already a property that cannot be found for trivial surface states. The buried nature, as well as the greater brilliance of the cone, reduced warping and increased isolation from bulk bands, make (at least) QL terminated PbBi$_4$Te$_7$ a promising candidate for future applications. The protection from surface perturbations is a key requirement whenever a UHV environment cannot be guaranteed.

The agreement between ARPES measurements and calculated band structure proves the reliability of the theoretical method, not only for determining the topological class of a material, but also for the prediction of the exact surface band structure. Applying this method to other systems of the pseudobinary family confirms most systems to be non-trivial TIs indeed, see Tab. 7.2. Hence, the described stoichiometric manipulation of the prototypical TIs Bi$_2$Te$_3$ and Bi$_2$Se$_3$ with group IV elements such as Ge, Sn and Pb is a promising path to tailor TIs for various demands.

Bi$_2$Te$_3$	ν_0	Bi$_2$Se$_3$	ν_0
GeBi$_2$Te$_4$	1		
SnBi$_2$Te$_4$	1	SnBi$_2$Te$_4$	0
PbBi$_2$Te$_4$	1	PbBi$_2$Te$_4$	1
GeBi$_4$Te$_7$	1		
SnBi$_4$Te$_7$	1		
PbBi$_4$Te$_7$	1	PbBi$_4$Te$_7$	1
GeBi$_6$Te$_1$0	1		
SnBi$_6$Te$_1$0	1		
PbBi$_6$Te$_1$0	1		

Table 7.2.: Topological nature of systems belonging to the pseudobinary family. Bi$_2$Te$_3$ and Bi$_2$Se$_3$ denote the parent system. ν_0 denotes the topological number. For $\nu_0 = 1$ the system is a TI. For $\nu_0 = 1$ the system is trivial [165].
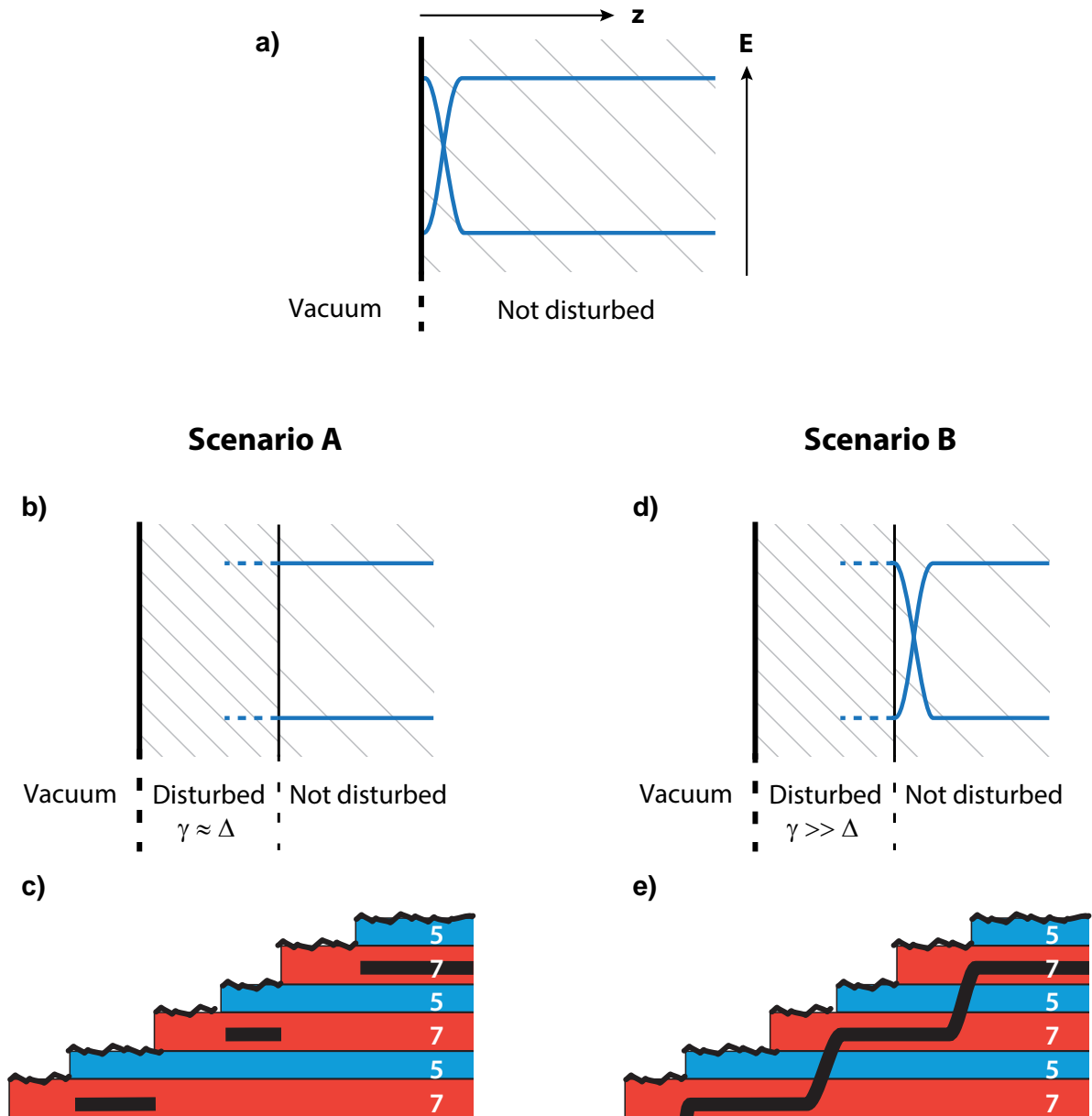
Figure 7.5.: Scenarios for TES-behavior at SL terminated PbBi$_4$Te$_7$ according to Schubert et al [106] **a)** Scheme for an undisturbed surface. The band inversion happens to be lifted close to the surface. **b) Scenario A** Sample with moderate surface disorder. Disturbance γ is of the order of the surface gap: $\gamma \approx \Delta$, the TES are present at the surface but localized, therefore no Dirac cone can form in $\vec{k}$-space. **c)** As a result, a Dirac cone (grey bands) can be found in areas with QL termination only. **d) Scenario B** Sample with heavy surface disorder, where $\gamma \gg \Delta$. The surface region is transformed to an Anderson insulator. A Dirac cone is established at the edge between the TI and the topologically trivial AI. Consequently, as shown in **e)**, the Dirac cone can be found for all terminations of PbBi$_4$Te$_7$, but is buried with different spacings to the surface.

8. TES Shift in TlBiSe$_2$

The results of this chapter are published in

F. Pielmeier, G. Landolt, B. Slomski, S. Muff, J. Berwanger, A. Eich,
A.A. Khajetoorians, J. Wiebe, Z.S. Aliev, M.B. Babanly, R. Wiesendanger,
J. Osterwalder, E.V. Chulkov, F.J. Giessibl, and J.H. Dil

Response of the topological surface state to surface disorder in TlBiSe$_2$

New Journal of Physics, **17**, 023067 (2015)

This chapter deals with the behavior of the TES in case of a heavily disturbed surface. Two mechanisms are described by theory depending on the strength of the perturbation [106]. For a potential disorder with the strength in the order of the band gap, the TES is present at the edge, but, due to a strong localization in real space, a Dirac cone cannot be formed in k-space. For a potential disorder much stronger than the size of the gap, the affected volume is turned into a topologically trivial Anderson insulator. The quantum phase transition between the trivial and nontrivial phases shifts from the surface of the sample to the interface between Anderson and topological insulator. Here, the Dirac cone is established again, see Fig. 7.5.

Finding evidence for a shift of the TES into the bulk in the presence of disorder would be a significant discovery. It would prove the unique topological nature of the TES. Trivial surface states originate from the particular environment at the surface (symmetry breaking, presence of a quantum well) and vanish when the surface is altered (breaking of the surface symmetry, band flattening, destroying the surface band structure). A shift of the TES in the presence of disorder would not only prove the difference in origin of these states, namely the inversion of bulk bands, but would strengthen the concept of different topological classes of crystalline matter.

Both mechanisms were already discussed in chapter 7 to explain the differences between the theoretically predicted and the measured Dirac cones. However, the discussion was highly speculative, since there was no direct evidence for a particular type of behavior. For slab-structured materials like PbBi$_4$Te$_7$ and other pseudobinary calchogenides the TES is bound to a specific slab. If this slab is disturbed, the TES most likely shifts to the next possible slab , i.e. too deep into the bulk to be investigated. To prove such a shift, materials without the described slab structure have to be used.

One promising system is TlBiSe$_2$, which was already predicted and confirmed as a TI with a single Dirac cone around Γ and a bulk band gap larger than ≈ 0.3 eV [167–169]. The atoms are organized in layers along the [0001]-direction of the hexagonal lattice structure, but avoid a slab structure as the bondings are either ionic between Tl and Se atoms or mixed ionic/covalent between Se and Bi atoms [167, 170, 171]. Fig. 8.1 (a) illustrates the hexagonal unit cell together with the rhombohedral primitive unit cell of the system. The order of the atomic layers is ...-Tl-Se-Bi-Se-... . Due to the comparable strength of the bonds, none of the atomic layers can *a priori* be predicted as the typical termination layer. However, all three possible terminations (Tl, Se, Bi) are predicted to exhibit a Dirac cone, but with different positions of the DP and additional trivial surface states of different dispersion[1], see Fig. 8.1 (c).

The TES is primarily formed by the p_z orbitals of Se and Bi atoms. Its localization is not as defined as in the case of Bi$_2$Se$_3$ or Bi$_2$Te$_3$, where the TES is bound to the topmost slab. For TlBiSe$_2$, the TES reaches deep into the bulk, but with decreasing charge density for layers further away from the edge[2], see Fig 8.1 (b).

A typical method for preparing a fresh surface is to cleave the crystal similar to the method used for Bi$_2$Se$_3$ and Bi$_2$Te$_3$. Due to the similar strength of the bonding forces between the layers, a clean cleave along layers cannot be expected. In case of a cleave *through* the layers, the surface might be sufficiently disturbed to influence the TES, e.g. to induce a shift away from the surface. This makes TlBiSe$_2$ a prime candidate for studying the behavior of the TES in presence of surface perturbations: If the Dirac cone shifts only a few layers, it should still be detectable by ARPES.

Here, this hypothesis is tested by characterizing the surface morphology of cleaved TlBiSe$_2$ crystals with scanning probe methods and by investigating the resulting surface band structure by ARPES. STM and LEED measuremnts were carried out by myself at Hamburg University. Photoemission studies were conducted by Gabriel Landolt, Bartosz Slomski, Jürgen Osterwalder and Jan Hugo Dil from the Physik-Institut of Zürich University, Switzerland. AFM experiments were done by Florian Pielmeier, Julian Berwanger and Franz Josef Giessibl from the Institute of Experimental and Applied Physics at Regensburg University, Germany.

---

[1] Unlike the other crystals formed by slabs of covalently bonded layers connected by van-der-Waals forces, atoms forming the TlBiSe$_2$ surface exhibit unpaired electrons, that form additional trivial surface bands

[2] The highest charge density of the TES in TlBiSe$_2$ is found close to the fourth (Tl) and fifth (Se) layers below the surface Tl layer. This is due to a "leakage" of charge to the vacuum for the topmost layers.
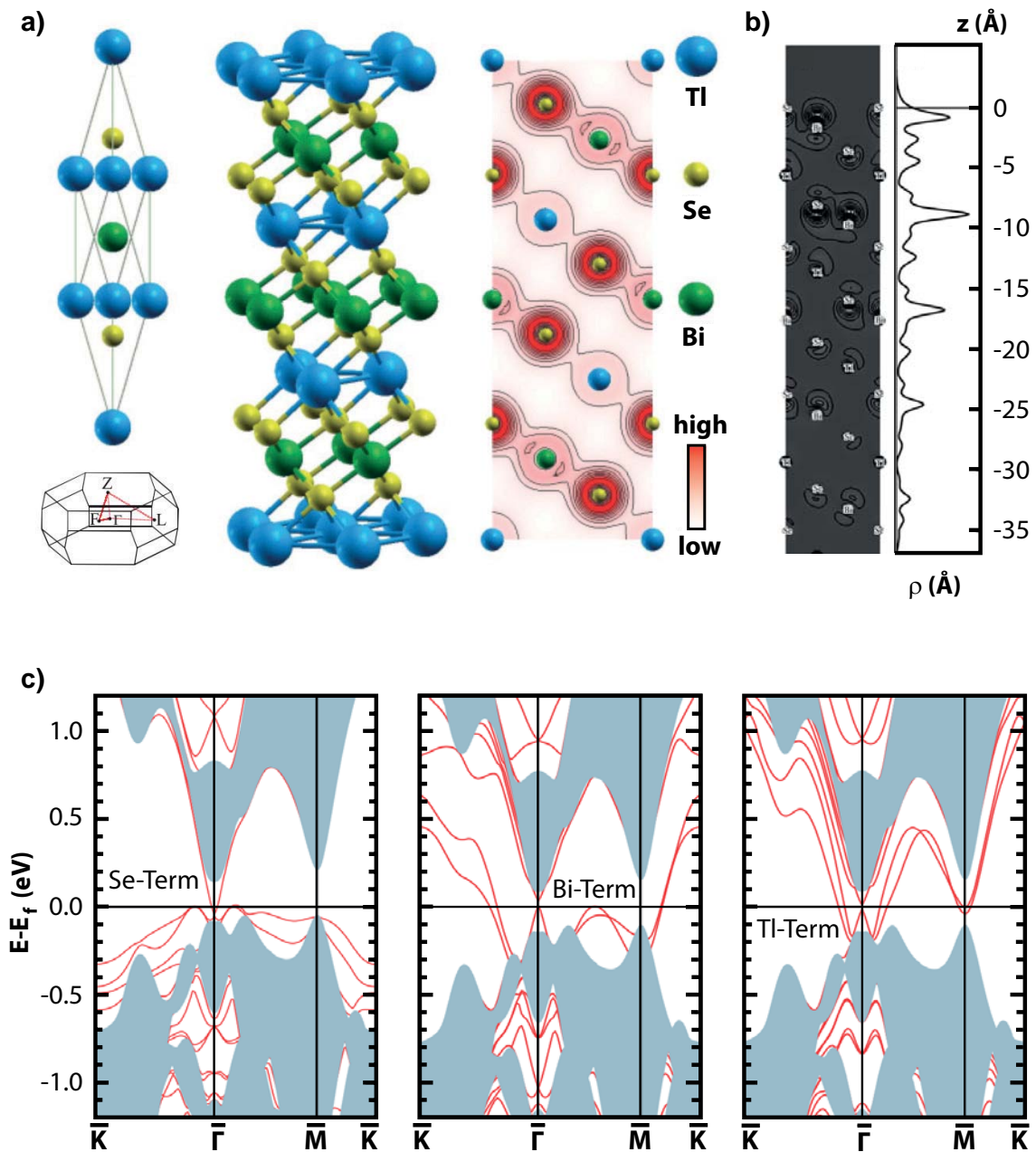
Figure 8.1.: TlBiSe$_2$: lattice and electronic structure a) Atomic structure in rhombohedral (left) and hexagonal bases (middle) and the charge-density distribution in the (11$\bar{2}$0) plane of the hexagonal cell (right). The Brillouin zone for the rhombohedral cell is shown in the lower left corner. **b)** Spatial distribution of the TES at Γ in the (11$\bar{2}$0) plane (left) and its charge density along z (right). **c)** Calculated surface band structure for Se-termination (left), Bi-termination (middle) and Tl-termination (right). The surface states are indicated as red lines, projected bulk bands as blue areas. Figures (a) and (c) are adopted from [172], figure (b) from [167].

99

8.1. Experimental Results

Photoemission experiments were performed at the COPHEE end station at the Swiss Light Source [173], using linear (p) polarized light. The sample temperature was 20 K and a base pressure was $2 \cdot 10^{-10}$ mbar. Samples were cleaved at 20 K, 60 K and at room temperature (RT) with the method described in section 5.2.2.

Low temperature STM experiments were performed with the system described in section 5.1. The base pressure was $< 10^{-10}$ mbar. All STM measurements were taken at 30 K. The STM tip was an electrochemically etched polycrystalline W wire. STM topographs were taken in constant-current mode. The samples were cleaved at ≈ 150 K and RT. LEED images were taken with an Omicron SPECTRALEED optics on samples characterized and investigated before by STM in the same chamber system.

AFM experiments were performed with a combined STM/AFM Omicron low temperature system operated in UHV at a temperature of 4.4 K. The microscope is equipped with a qPlus sensor [174]; again W was used as tip material. The bias voltage was applied to the sample. For AFM operation, the frequency modulation mode was utilized [175]. Here, the oscillation amplitude A (typically A = 50 pm) is kept constant and the frequency shift Δf of the cantilever, which is a measure of the force gradient between tip and sample, is monitored. Samples were cleaved at RT. The RT STM measurements were carried out in a home-built STM/AFM-system in UHV at a pressure of $2 \cdot 10^{-10}$ mbar. QPlus sensors with W tips were used. The bias voltage was applied to the tip. Samples were cleaved at RT.

Photoemission Spectroscopy

XPS measurements assured the chemical purity of the system and ARPES confirmed the TI nature of the sample, see Fig. 8.2. In the XPS spectrum core levels of Se and Bi atoms exhibit a single peak structure, while for Tl a double peak structure can be found. This indicates two different environments for Tl atoms, which should not be the case. According to ARPES, the sample exhibits an isolated Dirac cone at $\bar{\Gamma}$ with a DP at -0.4 eV, about 0.1 eV above the bulk VB. For a perfect crystal the DP is expected to be located at E_F. Here, the whole band structure is shifted by about ≈ 0.4 eV to higher binding energies, indicating an n-doping of the sample. Above the DP no bulk CB states are visible. Hence, this sample exhibits a band gap of at least 0.5 eV, about 0.2 eV larger than the gap of Bi$_2$Se$_3$. The trivial surface states predicted by theory, see Fig. 8.1, are not visible in the spectrum. This indicates a disturbed surface, which will be confirmed by scanning probe measurements in the next section.
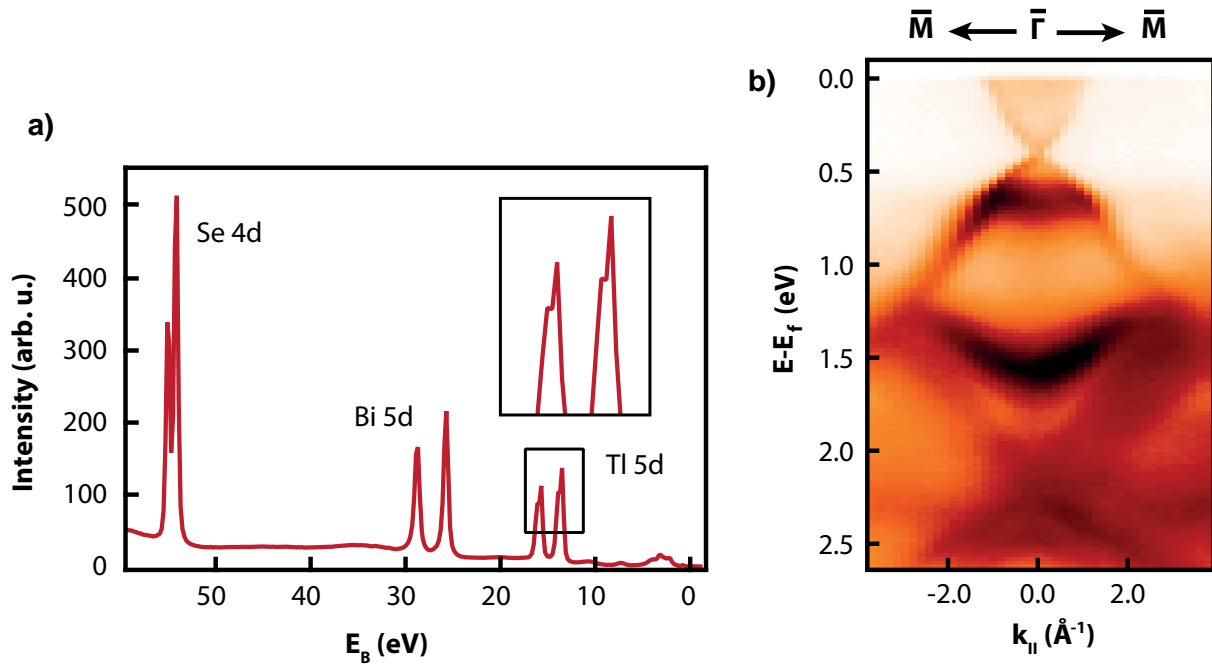
Figure 8.2.: TlBiSe$_2$ investigated via photoemission spectroscopy a) Core level XPS obtained at normal emission with a photon energy of 120 eV. Both Tl 5d excitations exhibit a double peak. **b)** ARPES map of the TlBiSe$_2$ band structure along $\bar{\Gamma}\bar{M}$ measured with a photon energy of 20 eV.

STM and LEED

An overview scan of the surface by STM confirms the general crystal integrity of the sample, Fig. 8.3 (a). The vertical distance between terraces is 7.3 ± 0.3 Å for each slab, which is about 1/3 of the expansion of the hexagonal unit cell along c and corresponds to the height of one Se-Bi-Se-Tl-block, see Tab. 8.1. This constant height indicates a dominant cleavage plane. The slight double peak of the Tl 5d core levels in the XPS spectrum suggests that the top layer is a Tl layer.

The step edges of the terraces are sharp and exhibit two principal orientations rotated by 60° with respect to each other. This implies a good overall in-plane crystallinity. However, on images with higher spatial resolution the surface does not appear flat, but exhibits a worm-like superstructure, Fig. 8.3 (c) and (d). While the individual features cannot be resolved on the atomic scale by STM, an FFT analysis reveals that the superstructure as a whole exhibits a hexagonal symmetry, with an average next nearest neighbor distance of 2.3 ± 0.3 nm, Fig. 8.3 (e). The superstructure was found on all terraces on all surfaces of all crystals, regardless of the temperature of the cleave or the tip condition. The spacing is independent of the applied bias voltages, in topography and in STS images, Fig. 8.3 (f-i). Only the contrast and shape of the features vary minimally, the lateral size is unchanged.
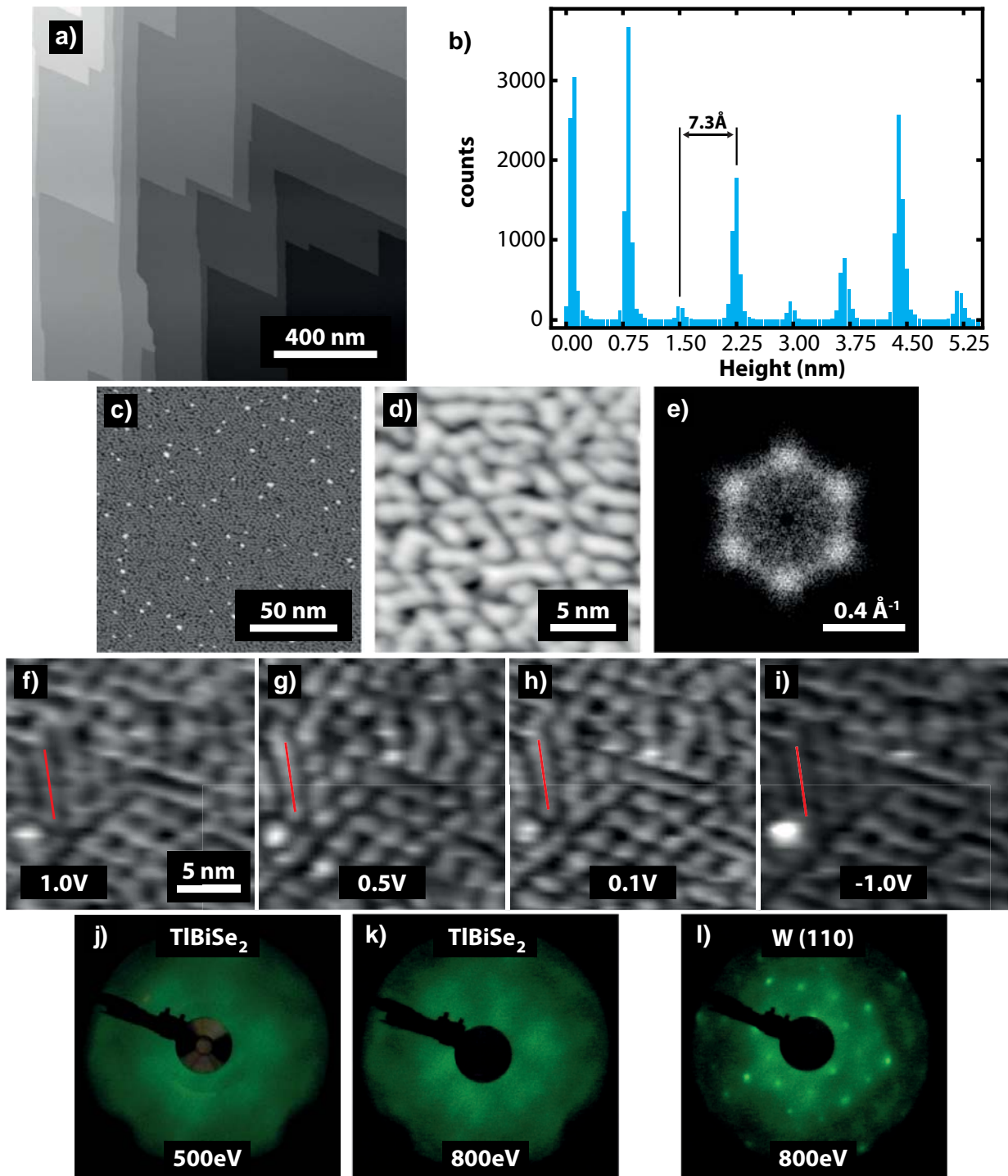
Figure 8.3.: STM and LEED images of TlBiSe₂. a) Topography overview. For all topography images shown: U_B: 0.5 V, I: 100 pA. **b)** Distances of the terraces in (a). **c)** Overview and **d)** detailed scan of a single terrace. **e)** FFT of (c), the worm-like structure produces a hexagonal pattern. The image was created with the method described in 5.2.3. **f)-i)** STS maps taken at given sample biases (I: 1 nA). The color range covers the following conductances: (f) $0.05\,\mathrm{nS}$ to $0.1\,\mathrm{nS}$, (g) $0.07\,\mathrm{nS}$ to $0.16\,\mathrm{nS}$, (h) $0.21\,\mathrm{nS}$ to $0.46\,\mathrm{nS}$ and (i) $0.05\,\mathrm{nS}$ to $0.22\,\mathrm{nS}$. The red line marks the same structure in each image. The visible pattern does not change in periodicity. **j)** and **k)** LEED images of TlBiSe₂ taken at given beam energies. **l)** LEED image of a W(110) crystal for comparison.

This indicates that the worms pattern is closely related to the structure of the surface. However, LEED measurements (j-l) of the surface do not exhibit any diffraction spots, neither originating from an atomic lattice, nor from any superstructures. Just by itself, this would indicate a total disordering of the surface.

To resolve these contradictory results and to finally unravel the surface structure, $TlBiSe_2$ samples were investigated by AFM. AFM is sensitive to the *forces* between tip and sample and provides access to the total charge density distribution on surfaces [176].

AFM

For a better comparison with previous STM results, AFM and STM images were measured with the same setup. The STM image, taken in constant-current mode, shows the same surface structures as observed before, Fig. 8.4 (a). The simultaneously measured AFM image exhibits the same features (not shown). Starting with a tip-sample distance given by the setpoint and bias typically used for constant-current STM, the sample is subsequently scanned by AFM in constant-height mode with decreasing tip height. After approaching the sample by 230 pm relative to the original tip-sample distance, the atomic structure of the surface can be resolved, Fig. 8.4 (b). An FFT analysis of the image confirms that the atoms are ordered in a hexagonal lattice with the same orientation and lateral lattice constant a for all atoms, see Fig. 8.4 (c) and red lines in (b). a is measured to
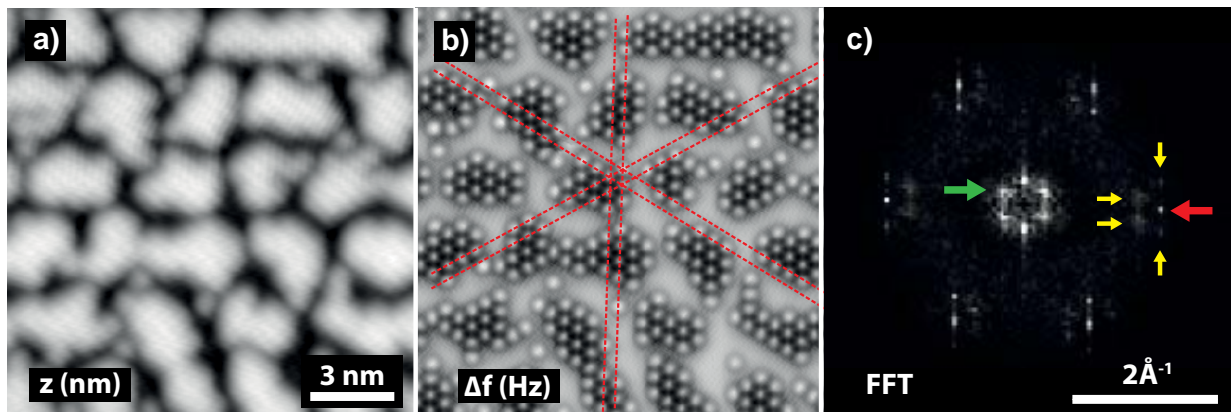
Figure 8.4.: $TlBiSe_2$ investigated by AFM. a) Constant-current STM topography of a specific area. $U_B = 0.2$ V, $I = 130$ pA. **b)** Same area measured by AFM in constant-height mode, 230 pm closer to the surface than in (a), quality factor $Q = 28140$, stiffness $k = 1800$ N/m, resonance frequency $f_0 = 26.666$ Hz, red dashed lines highlight the order of the surface layer. **c)** FFT of (b) The inner hexagon (green arrow) originates from the superstructure and is already known from STM images, see Fig. 8.3 (e). The spots with the highest intensity of the outer hexagon (red arrow) originate from the atomic lattice. Satellite spots (yellow arrows) forming a hexagon around the high intensity spots stem from the superstructure.

	STM/AFM	Literature
a	4.45 ± 0.1 Å†	4.24 Å
a_{IS}	23 ± 3 Å	-
$c_{1/3}$	7.3 ± 0.3 Å	7.44 Å

Table 8.1.: Lattice parameters of TlBiSe$_2$ a: lateral lattice constant of the atomic lattice, †: Measured on recrystallized Tl islands. a_{IS} average distance of TL islands. $c_{1/3}$: height of one Se-Bi-Se-Tl-block. STM and AFM values were measured, literature values are taken from [170].

be 4.45 ± 0.1 Å, i.e. less than 5 % larger than the bulk lattice constant and thus fits the literature value [170], Tab. 8.1. The superstructure hexagon is rotated by 30° relative to the hexagon originating from the atomic lattice. All these findings suggest that the surface Tl atoms are located on Tl bulk lattice sites and the crystal layers underneath are intact.

The overall Tl atom density at the surface is 51 % of the bulk layer density. The missing 49 % are most likely sticking to the part of the crystal that got cleaved away. Hence, the cleave does not occur between layers, but results in partially destroyed Tl layers at the nano-scale. Most of the Tl islands present at the surface appear with similar shape and size and are typically well separated. Only a small minority of islands is connected. Assuming the surface of the crystal piece that got cleaved away was exactly the negative of the measured surface, one would expect that the Tl on that surface forms a network of interconnected narrow islands. Since both parts of the cleaved crystal are similar, about 50 % of the Tl atoms stick on each side, one would expect half of the investigated surfaces exhibit the well separated islands and the other half exhibits the connected narrow islands. But the narrow islands do not occur on any investigated surface. Hence, the Tl atoms must have been provided with enough energy during the cleaving process to rearrange and form the observed islands.

8.2. Conclusion

The experiments affirmed the assumption made in the introduction that the cleaved $TlBiSe_2$ should reveal a rough surface. Double peaks of the Tl 5d core levels measured by XPS indicate two different environments for Tl atoms, one in the bulk, one at the surface. The absence of double peaks for other elements, as well as the constant step height measured by STM, suggest that $TlBiSe_2$ typically cleaves at a Tl layer. An analysis of the surface atom density reveals that only half of the atoms of the original bulk layer are present. The other half must stick to the piece of the crystal that got cleaved away. During the cleaving process the majority of remaining atoms form well ordered islands, all with the same orientation and lattice constants. These are identical with bulk values. The uniform ordering of the Tl islands, as well as the defined step edges and the single peak structures of the Bi and Se core levels in XPS measurements, indicate that only the topmost Tl layer is affected by the cleaving process.

The investigation of the band structure by ARPES reveals the topological nature of the system. The cleaved $TlBiSe_2$ exhibits a single Dirac cone, well isolated from bulk states, located at $\bar{\Gamma}$. The observed bulk band gap of at least 0.4 eV is the largest of all experimentally investigated TIs so far. The position of the DP close to the bulk VB is similar to the predicted position of the Dirac cone of Se-terminated $TlBiSe_2$, compare Figs. 8.1 and 8.2. For Tl and Bi terminated surfaces, the DP is located closer to the bulk CB. The great resemblance suggests that the cone is not directly located at the sample surface, which is expected for an unperturbed termination, but is shifted to the first intact layer underneath, i.e. the Se layer. The absence of the TES in the Tl island layer can also be deduced from the bandwidth and integrity of the cone. As seen in chapter 7 the bandwidth of the cone increases with the magnitude of the surface perturbation. While already the small disturbances at the $PbBi_4Te_7$ surface lead to a significant broadening of the cone, the $TlBiSe_2$ Dirac cone is surprisingly narrow, if one considers the much stronger degree of disorder at the $TlBiSe_2$ surface. The Tl islands form a network of equal size and structure, similar to particular molecules on crystalline solids, e.g. DPDI-molecules on Cu(111) [177]. In this example, the presence of the molecules changes the band dispersion and opens a gap within the trivial surface state of Cu(111). In contrast, the integrity of the $TlBiSe_2$ Dirac cone is not affected.

The existence and brilliance of the cone alone is yet another example of the enhanced protection of the TES compared to trivial surface states. The observed shift of the cone away from the surface, indicated by its integrity and shape, is the first confirmation of a TES protection in presence of a heavily disturbed surface. It directly proves the connection between TES and the topological nature of the bulk crystal.

The confirmation of the topological nature of $TlBiSe_2$ introduces a new class of topological insulators with exciting properties. $TlBiSe_2$ belongs to the thallium-based chalcogenide material family that, similar to pseudobinary chalcogenides, shares the same lattice structure and a similar stoichiometric composition, $Tl-V-VI_2$ with V: Bi, Sb and VI: Se, Te. Also the electronic properties are similar, e.g. all members of the family are predicted to be TIs with a single Dirac cone and a band gap at $\bar{\Gamma}$, with at least the size of Bi_2Se_3 [172]. In the mean time the topological nature of $TlBiSe_2$ and related systems has been confirmed by several groups world wide [113, 168, 169, 178–180]. The brilliance of the TES , its isolation from bulk bands, the shown self-protection and the minor shift away from the surface in case of perturbations, makes $TlBiSe_2$ a promising candidate for testing the usability of TIs in applications.

9. QPI Mapping of Bi/Bi$_2$Se$_3$

The results of this chapter are published in

A. Eich, M. Michiardi, G. Bihlmayer, X.-G. Zhu, J.L. Mi, Bo B. Iversen,
R. Wiesendanger, Ph. Hofmann, A. A. Khajetoorians and J. Wiebe

*Intra- and interband electron scattering in a hybrid topological insulator:
Bismuth bilayer on Bi$_2$Se$_3$*

Physical Review B, **90**, 155414 (2014)

The purpose of this chapter is threefold. The first aim is to find a sample system providing a 2D TI with a reasonably large band gap. The second is to investigate the isolation of a 3D TES shifted *away* from the bulk states of its host material. The third is to establish Fourier-Transformed STS maps as a method to determine the dispersion of complex surface band structures and as a method to identify interactions between these bands.

Isolation of a 3D TES from bulk bands

In the previous chapter, the structure of the surface was disturbed such, that the TES moved into the bulk. While this behavior proved the robustness of the TES on the one hand, it can be disadvantageous on the other hand for two reasons: 1. Only at the surface of crystals the electronic states can be accessed and contacted by electrodes. 2. The interaction between bulk states and the TES is enhanced. As a result, the scattering probability between bulk and TES states is increased. Also the cone warping is enhanced, due to the stronger impact of the crystal Coulomb potential in the bulk. This gives rise to the following question: Is it possible to isolate the TES from bulk states by moving it further away from the bulk into the vacuum?

Hirahara *et al.* [181] presented a study where a bismuth bilayer (BL) was grown on top of Bi$_2$Te$_3$. DFT calculations suggest that the Dirac cone is localized at the surface of the bilayer, even extending into vacuum, while on bare Bi$_2$Te$_3$ the TES is located within the first QL. ARPES supports the calculations by showing a more linear Dirac cone for the Bi-bilayer on Bi$_2$Te$_3$ system (Bi/Bi$_2$Te$_3$).

However, the 2D TES of the 3D system is accompanied by bands of the Bi-bilayer. Neither ARPES nor calculations can give an estimation of the interaction between TES and bilayer states. On the other hand, due to the strong localization at the surface of the bilayer (and reaching into the vacuum), the analysis of QPI patterns by FT-STS might be a useful tool to investigate that interaction.

Mapping of QPI Patterns

So far QPI mapping was utilized to investigate the dispersion of simple surface states, e.g. on Cu-(111) [74] or the Dirac cone of Bi$_2$Te$_3$[182]. Here, the band dispersion can be directly determined by the FT-STS pattern, as only **q**-vectors from scattering within an individual band, the surface state, are contributing. The experiment proposed here deals with potentially far more complex FT-STS maps. There are at least two bands present, the bilayer band(s) and the Dirac cone. In this case, features originating from *intra-band* scattering can be expected, as well as features generated by *inter-band scattering*. Also, the original features might superimpose and form new features. Hence, the identification of features is not a trivial task. The complexity might be a reason why this technique was not used so far to investigate dispersion or scattering behavior of more complex surface band structures.

In the present study the identification of FT-STS features is supported by a simulation of FT-STS maps based on a joint electronic density of states (JDOS) approach and a band structure calculated by DFT. In the simulation single bands can be switched on and off. as a result, the presence of bands can be directly linked to FT-STS features. If successful, this work might establish the techniques applied as a general tool to investigate complex 2D band structures and their interactions.

For the presented experiment the substrate is changed from Bi$_2$Te$_3$ to Bi$_2$Se$_3$. One reason for this choice is the greater extent of isolation of the Dirac cone within Bi$_2$Se$_3$, due to the larger band gap. Another reason is the interaction between substrate and bilayer and its consequences for a fundamental property of the bilayer itself: It is predicted to be an almost ideal 2D TI [183].

The Bismuth-bilayer, a 2D Topological Insulator

A confirmation of the topological nature of Bi-bilayers would be of great interest, since an ideal 2D TI has not been found so far. While already 21 materials have been proven to be 3D topological insulators (until April 2013 [19]), only two systems have been experimentally confirmed to be 2D TIs: CdTe/HgTe/CdTe [118] and AlSb/InAs/GaSb/AlSb [184], both being quantum well systems and exhibiting rather bad properties.

The band gaps are small, < 10 mV for CdTe/HgTe/CdTe and ~ 4 mV (!) for AlSb/InAs/-GaSb/AlSb. Moreover, the TES in CdTe/HgTe/CdTe has a large penetration depth into the film of about 50 nm from the edges [185]. Therefore, the 1D TES mixes easily with other states [39].

At first sight, the small number of 2D TI materials is surprising. 2D TIs were confirmed earlier and their general properties are more promising for applications (ballistic transport due to complete suppression of scattering). However, the obstacles for growing 2D TIs are greater as well. The key element of the first 2D TI, mercury, cannot be used as the key element for a general 2D TI material class. One needs a very specialized MBE technique to deal with Hg[1] and only a few number of research groups are equipped with such chambers [118]. In addition, mercury is highly poisonous and degassing at room temperature.

Another obstacle for identifying 2D TES systems is the necessity for an appropriate substrate. The substrate will more or less influence the band structure of the 2D system. The bands might shift or invert or may hybridize with bulk bands.

With single Bi-bilayers, the ideal system might have been found. In contrast to mercury, bismuth is easy to handle and does not need a quantum well structure to act as a TI. One valence band and one conduction band of the free standing bilayer are inverted at $\bar{\Gamma}$ with a calculated band gap of 200 mV [38], Fig. 9.1 (c) and (d). Theory predicts the gap to host edge states [39]. These are supposed to stretch almost along the complete SBZ and therefore might be localized within a few lattice constants at the bilayer edge in real space.

Bi-bilayers can be found in bismuth crystals. These exhibit bilayers along the [111]-direction. A bilayer consists of two layers with a hexagonal lattice structure, which together form a distorted honeycomb lattice, similar to graphite [186], Fig 9.1 (a) and (b). The atoms are bonded covalently with their neighbors, which are located in the same bilayer. The bonding between the bilayers is established by van-der-Waals forces.

For bulk bilayers the lateral lattice constant of each layer is 4.54 Å. The intralayer distance is 1.59 Å, the van-der-Waals gap (interlayer distance) is 2.33 Å. Altogether the spacial expansion of a bilayer is 3.94 Å [187].

As shown by Hirahara et $al.$, smooth bilayers can be grown by MBE on Bi_2Te_3. Here, the bilayer grows pseudomorphic, i.e. the in-plane lattice constant of the film is reduced to 4.38 Å, the lattice constant of Bi_2Te_3 [188]. To reduce the strain within the film the van-der-Waals gap between bilayer and substrate is increased to 2.42 Å. The overall height of the bilayer is then 4.06 Å [40]. Unfortunately, the presence of the Bi_2Te_3 substrate closes the bilayer band gap, no TES is expected. (The band inversion remains, though.) Therefore, a substrate with a reduced influence on the electronic structure of the bilayer has to be found.

---

[1] Also, Hg poisons UHV chamber systems. All other grown samples will suffer Hg-doping.
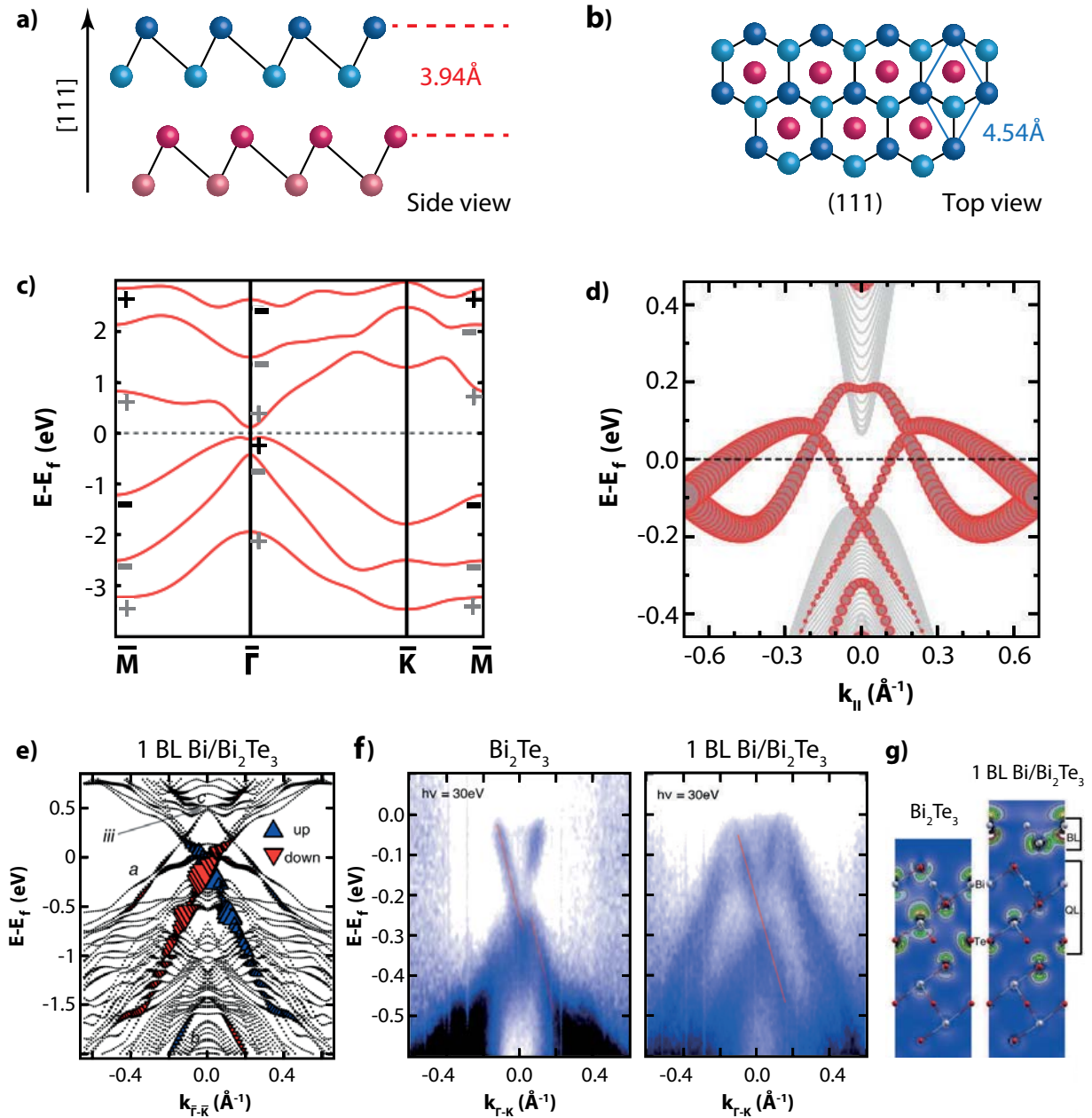
Figure 9.1.: Properties of a bismuth bilayer with and without a Bi$_2$Te$_3$-substrate: Crystal structure in **a)** side view and **b)** top view. **c)** Parity values at Kramers points for a bulk Bi(111)-bilayer. The parity at $\bar{\text{M}}$ is inverted with respect to $\bar{\Gamma}$. Relevant parities are marked in black (+,-). **d)** Calculated dispersion of the 1D TES (red). Symbol size corresponds to the weight of the states at the edge atoms. **e)** Band structure for one Bi BL on Bi$_2$Te$_3$. Point size reflects localization on the surface. The spin-polarization of the Dirac cone is color coded. iii highlights the closed gap between the bilayer VB and CB. **f)** ARPES measurement of Bi$_2$Te$_3$ without and with a Bi-bilayer termination. Lines visualize the enhanced linearity of the Dirac cone. **g)** Spatial distribution of the charge density of the 2D TES at the Dirac point for bare Bi$_2$Te$_3$ and with a bilayer terminated surface. (c) and (d) adapted from [39], (e-g) from [181].

Bi_2Se_3 exhibits the same hexagonal lattice structure as Bi_2Te_3, but with a smaller in-plane lattice constant of 4.18 Å. Hence, a bilayer grown on Bi_2Se_3 should be compressed even further and as a consequence the van-der-Waals gap should increase to a greater extend. The interaction with the substrate will be reduced and the gap may open again. However, the Bi_2Se_3 lattice constant might be too small for growing epitaxial bilayers. On Si(111), with an in-plane lattice constant of 3.84 Å [189], Bi-bilayers can only be established after the growth of a wetting layer and three {012}-phase doublelayers [190]. Hence, in a first step Bi-bilayer growth on Bi_2Se_3 has to be proven.

The first section of this chapter presents a growth study of bismuth on Bi_2Se_3. One of the observed structures will be identified as a Bi-bilayer. In the next section, the band structure of the Bi BL on Bi_2Se_3 system is investigated by ARPES and DFT calculations. The calculations predict that the Bi_2Se_3 Dirac cone is shifted towards the surface of the bilayer and the bilayer band gap remains open, hence the 1D TES should still be present.

In the third section the interaction of states present at the surface, including the Dirac cone, is investigated experimentally via FT-STS and by a simulation of FT-STS maps The simulation is based on the bands of the DFT calculation. The experimental maps have been indeed the most complex maps analyzed so far. By a comparison of experimental and simulated maps all measured features will be identified and forbidden scattering channels will be unraveled. In addition, the relocalization and greater isolation of the Bi_2Se_3 Dirac cone from the Bi_2Se_3 bulk states will be confirmed.

The growth of bismuth on Bi_2Se_3 turned out to be quite complex. While the main chapter provides an overview of all found structures, the analysis focuses on the film that is identified as a bilayer. Other structures, also at higher coverages, are analyzed in Appendix B, including the first identification of Bismuth monolayers.

The STM experiments, growth study and FT-STS measurements, were conducted by myself in Prof. Wiesendanger's group at Hamburg University. During the first part of the growth study I was accompanied by Cornelius Eder, who wrote his Bachelor thesis on a first characterization of the bismuth films: "Strukturelle Charakterisierung von epitaktisch gewachsenem Bismut auf Bismutselenid mittels Rastertunnelmikroskopie" [191]. The Bi_2Se_3 crystals were grown by J.L. Mi and Bo. B. Iversen from Aarhus University.

For ARPES experiments, I joined Prof. Philip Hofmann's group at Aarhus, Aarhus, Denmark. Measurements were performed together with Matteo Michiardi, Lucas Barreto, Wendell Silva, Xie-Gang Zhu and Marco Bianchi. DFT calculations were contributed by Gustav Bihlmayer from the Institute of Advanced Simulation and the Peter Grünberg Institut at the Forschungszentrum Jülich. The simulation of FT-STS maps were carried out by Matteo Michiardi from the Aarhus group.

9.1. **Growth and Identification of the Bi-Bilayer on Bi$_2$Se$_3$**

The experiments were conducted in the chamber system described in section 5.1. The base pressure was $< 10^{-10}$ mbar. The samples were taken from the same crystal that was already used in previous experiments [101, 130, 192]. The samples were cleaved *in situ* at a pressure of $< 10^{-8}$ mbar with the scotch-tape method described in 5.2.2 and transferred to the manipulator-stage within 1 min. There, samples were cooled down/annealed to the target temperature for 15 min before deposition. Bi was grown with a Focus EFM 3 evaporator at a rate of 5 bilayers per minute. After deposition, the samples were moved to the STM in less than 5 min. All measurements were taken at 30 K. The STM tip was an electrochemically etched polycrystalline W wire. STM topographs were taken in constant-current mode.

Growth

On Bi$_2$Te$_3$, Bi-bilayers are typically grown at room temperature (300 K). The films exhibit layer-by-layer growth and the islands exhibit a triangular shape. The island surface is smooth and its height is 4.7 Å[2], see Fig. 9.2 (a) and (e).

On Bi$_2$Se$_3$, the growth at 300 K leads to rough islands as shown in Fig. 9.2 (c) and (g). The height of the layer, ~ 4.5 Å, is in the range one would expect for compressed bilayers, but it is smaller than for bilayers grown on Bi$_2$Te$_3$, as measured by STM. With further deposition the height of the first layer changes to ~ 3.4 Å, Fig 9.2 (j) and (n). Also, the first layer does not form a closed film at any stage of the preparation procedure. Both observations might indicate that the layer needs a certain amount of additional energy (and time) to find a stable and ordered configuration. The second layer exhibits the same roughness and a slightly larger height: ~ 3.7 Å. Both heights (first and second layer) are smaller than the height of bulk Bi-bilayers and much smaller than expected. Overall, the as-grown layers seem to be rather unstable (change of layer height) and rough. The first guess was that additional energy might help to find a stable layer configuration, ideally with closed and smooth films. Hence, the sample temperature was increased step by step in subsequent preparations.

---

[2]4.7 Å is the height measured by STM. With LEED the height is measured to 4.1 Å [40]. STM systematically seems to overestimate the bilayer height on Bi$_2$X-systems, a fact important for finding the right band structure later on.
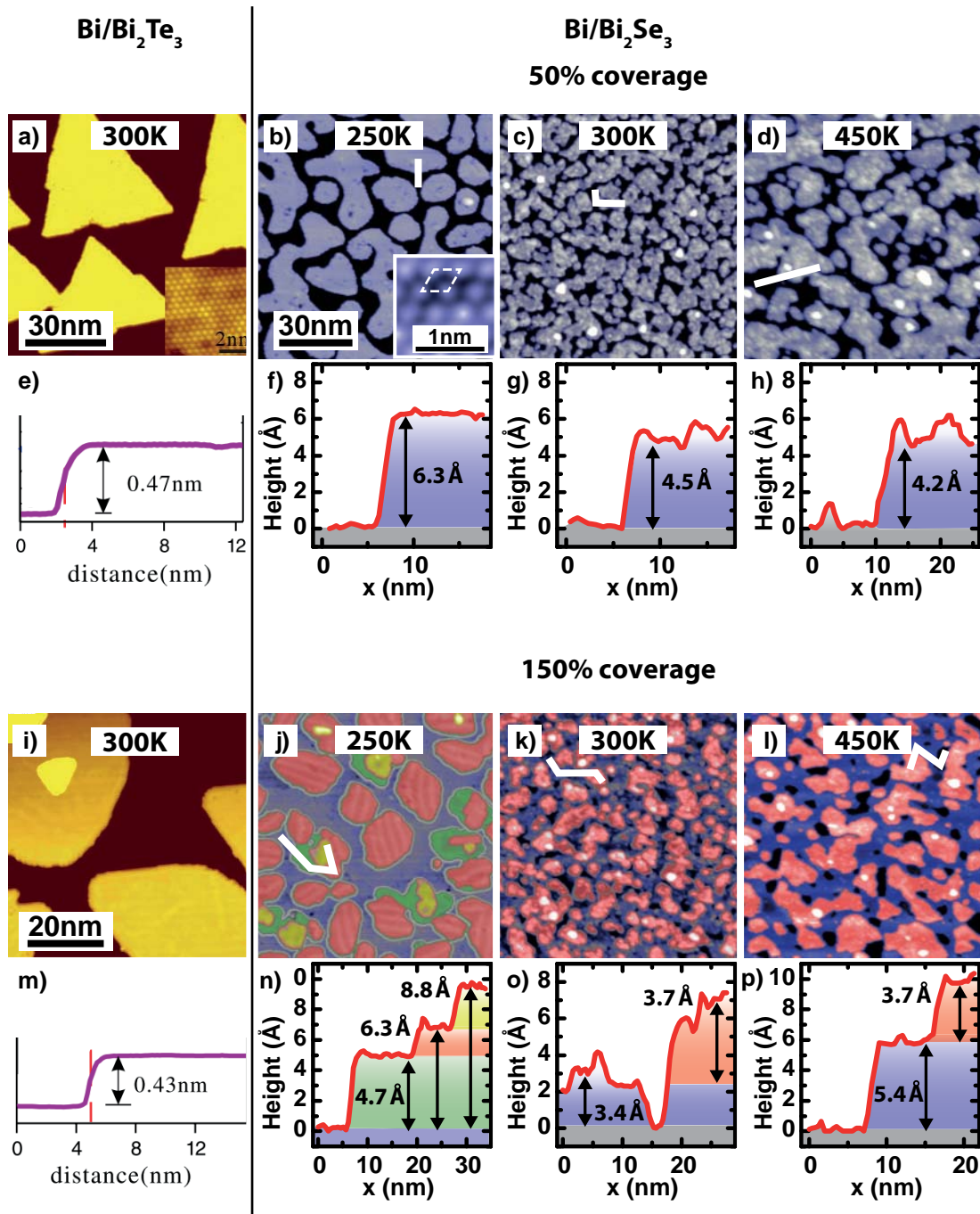
Figure 9.2.: **Temperature dependent growth of 50% and 150% bismuth BL on Bi_2Te_3 (left) and Bi_2Se_3 (right). a)-d)** Samples with $\sim 50\%$ bilayer coverage grown at given temperatures. **e)-h)** Corresponding line cuts **i)-l)** Samples with $\sim 150\%$ bilayer coverage grown at given temperatures. **m)-p)** Corresponding line cuts. The inset in (b) shows the hexagonal lattice structure of the Bi layer grown at 250 K. Bi/Bi_2Te_3 images (a) and (h) are taken from [193]. Layers are color coded: Bi_2Se_3: black, 1st Bi layer: blue, 2nd Bi layer: green, 3rd Bi layer: red, 4th Bi layer: yellow. Dark shades of color represent lower altitude, bright shades higher altitude. For all overview images: $U_B = 1$ V, $I = 20$ pA. For the inset image: $U_B = -0.1$ V, $I = 5$ nA.

At 450 K[3] and $\sim 50\,\%$, the grown islands turned out to be larger but exhibit the same rough surface and about the same height as islands grown at 300 K ($\sim 50\,\%$), Fig. 9.2 (d) and (h). Again at $\sim 150\,\%$ the height of the first layer changes, but it gets larger not smaller, Fig 9.2 (k) and (o). The second layer has about the same height as for 300 K. The surface appears less rough. The holes in the film are larger than at $\sim 50\,\%$ coverage or for preparations at 300 K. Thus, increasing the temperature leads to a different configuration of the layers. Now, the layers exhibit a smoother but not yet flat and fully closed surface with unexpected layer heights. A higher temperature than 450 K was not used. Previous experiments showed that higher temperatures damage the substrate.

Other growth experiments showed that under certain circumstances smooth layers can also be achieved by growth at lower temperatures [194]. Therefore, we also tried to grow Bi-bilayer films at temperatures below 300 K. Indeed, at 250 K the layer configuration changes drastically, Fig. 9.2 (b) and (d). As in the case of bilayer growth on Bi$_2$Te$_3$, the films get smooth and close completely during growth. However, in contrast to Bi$_2$Te$_3$, the islands on Bi$_2$Se$_3$ are rather round than triangular and the height of the first layer, 6.3 ± 0.1 Å (at 1 V), is surprisingly high, Fig 9.2 (b) and (f).

On top of the first layer, the grown structures get more complex, Fig. 9.2 (i) and (m). At $\sim 150\,\%$ coverage, islands with various heights can be identified. The surface is dominated by islands exhibiting the same height as the first layer (6.3 ± 0.1 Å) but showing a stripe pattern on top (red islands). Other islands exhibit a height of 4.7 ± 0.1 Å (green) or 8.8 ± 0.1 Å (yellow), respectively.

A detailed analysis of the second layer islands is to be found in appendix B together with an analysis of higher coverages. The results can be summarized as follows: The red islands belong to the *second* Bi-bilayer on the surface. The stripe pattern on their surface is a structural feature. It is present at all measured bias voltages and exhibits a wavelength of 4.4 ± 0.4 Å. A dominant orientation of the stripe pattern cannot be found.

Identifying the Bilayer

At first glance, the exceptionally large height of the first layer rather points to a Bi growth in the {012}-phase, than to bilayer growth, see Tab. 9.1. However, in that case the surface unit cell should be square like, a wetting layer is expected and all layer heights must be multiples of the height of the double layer height in the {012}-phase. But the presented experiment falsifies all indications for {012}-phase double layer growth.

---

[3]The parameters of the grown films change smoothly with increasing the annealing temperature. Only the results for the highest annealing temperature are described here. For overview images taken at other temperatures see Appendix B.

- The growth of a wetting layer can be excluded by a comparison of area coverage with the amount of deposited material. Reducing the amount of deposited material to 30 or 50 % of the material needed for the completion of the first layer lead to islands covering 30 and 50 % of the substrate. Hence, there is no indication for additional material that is consumed by the growth of a wetting layer.

- The islands with the stripe-shaped surface reconstruction exhibit the same height as the first layer, which would fit to the {012}-doublelayer-growth. However, the lowest and highest islands of the second layer do not fit to this model as their heights (4.7 and 8.8 Å) deviate from multiples of {012}-interlayer-spacing.

- The surface atoms are ordered in a hexagonal lattice with a lattice constant of 4.18 ± 0.1 Å, see Fig. 9.4, in very good agreement with the hexagonal unit cell and lateral lattice constant of Bi$_2$Se$_3$ [188]. The film is therefore grown pseudomorphically on the substrate.

- Additionally, bilayers were grown on Bi$_2$Te$_3$ for a coverage calibration. The lateral atom density of Bi$_2$Se$_3$ is about 10 % larger than that of Bi$_2$Te$_3$. Hence, Bi(111)-bilayers grown with the same amount of material will cover 9 % less of a Bi$_2$Se$_3$ substrate than of Bi$_2$Te$_3$, while {012}-doublelayers would cover almost 45 % less. The coverage difference found by experiment is 9 %, exactly the expected value for bilayers.

- And finally, as will be shown later, that the electronic structure measured by ARPES is in agreement with the electronic structure calculated for a Bi(111)-bilayer grown on Bi$_2$Se$_3$.

The results lead to the conclusion, that the first Bi layer on Bi$_2$Se$_3$ is indeed a (111)-bilayer. It grows pseudomorphically on the substrate and exhibits an extraordinarily large height. As opposed to the bilayer on Bi$_2$Te$_3$, the bilayer islands exhibit a rather round, not triangular shape. This indicates a smaller interaction with the substrate. These islands have greater freedom to reduce the surface energy: shorter edges, due to the round shape;

	Bulk	On Bi$_2$Te$_3$[†]	On Bi$_2$Te$_3$[‡]	On Bi$_2$Se$_3$ [‡]	{012}-doublelayer-phase
a	4.54 Å	4.39 ± 0.05 Å	4.38 Å	4.18 ± 0.1 Å	4.54x4.75 Å
c	3.94 Å	4.06 ± 0.08 Å	4.7 Å	6.3 ± 0.1 Å	6.56 Å

Table 9.1.: Lattice constants of the first grown bismuth layer, depending on the substrate: a: lateral lattice constant, c: lattice constant along z-axis. Bulk values are taken from [187]. †: measured by LEED . ‡: measured by STM . Bi$_2$Te$_3$[†] values are taken from [40] . Bi$_2$Te$_3$[‡] values are taken from [193]. Bi$_2$Se$_3$ values are own measurements. {012}-phase values are taken from [190].
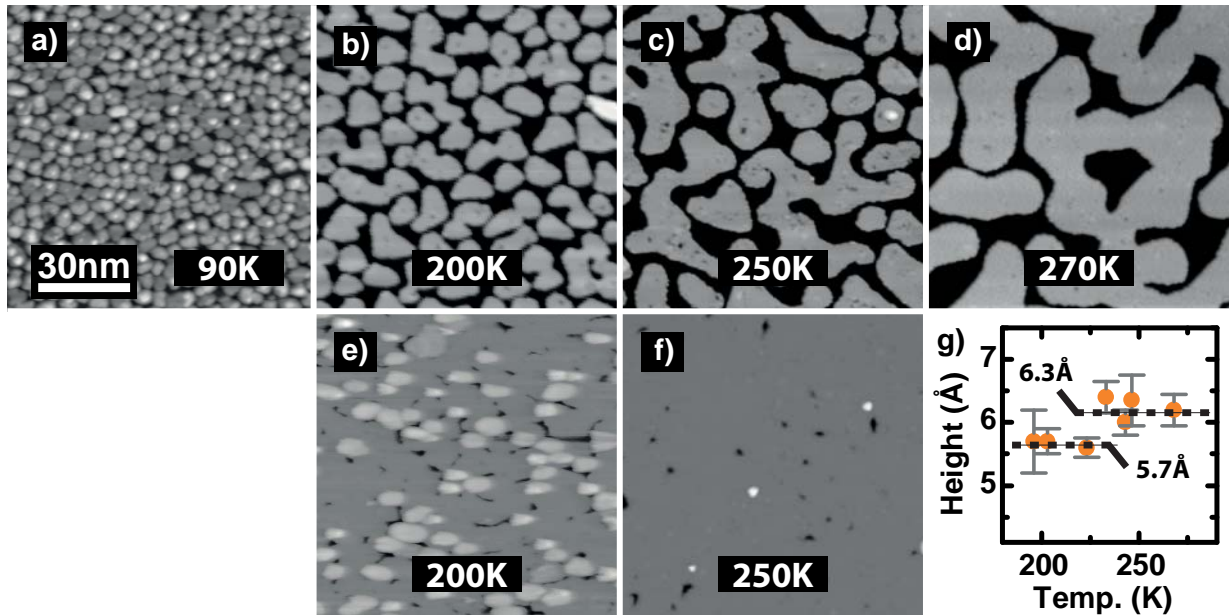
Figure 9.3.: Bilayer film morphology depending on growth temperature. a)-d) 50 % of a bilayer. **e)-f)** 100 % coverage. The films are grown at the given temperature. All images are measured with U_B= 1 V, I= 20 pA. **g)** temperature dependent layer height at 50 % coverage. Dotted lines mark average height.

instead of being shaped according to the substrates' lattice structure: triangular, due to the hexagonal lattice. Most likely an extension of the van-der-Waals gap is responsible for the reduced interaction described. This is supported by a height analysis of the additional layers, see appendix B. For the second bilayer it is possible to investigate the distances between the substrate and the bilayer as well as within the bilayer. The van-der-Waals gap has increased by 100 %, while the interlayer distance has only increased by 6.9 %. Due to the greater distance between substrate and bilayer, the bilayer electronic states should be more isolated from bulk states than on Bi$_2$Te$_3$.

Optimizing the Bi Growth for STM

To provide the highest quality of samples for subsequent FT-STS measurements, the bilayer growth had to be optimized. Especially the study of the interaction of electron bands with FT-STS depends on large areas of closed bilayers: The signal-to-noise-ratio of the FFT image increases when the algorithm integrates over a larger number of wave-fronts. Moreover, scanning the bare Bi$_2$Se$_3$ substrate in between the bilayer often alters the tip due to the low conductivity of the substrate, Fig A.1 (h).
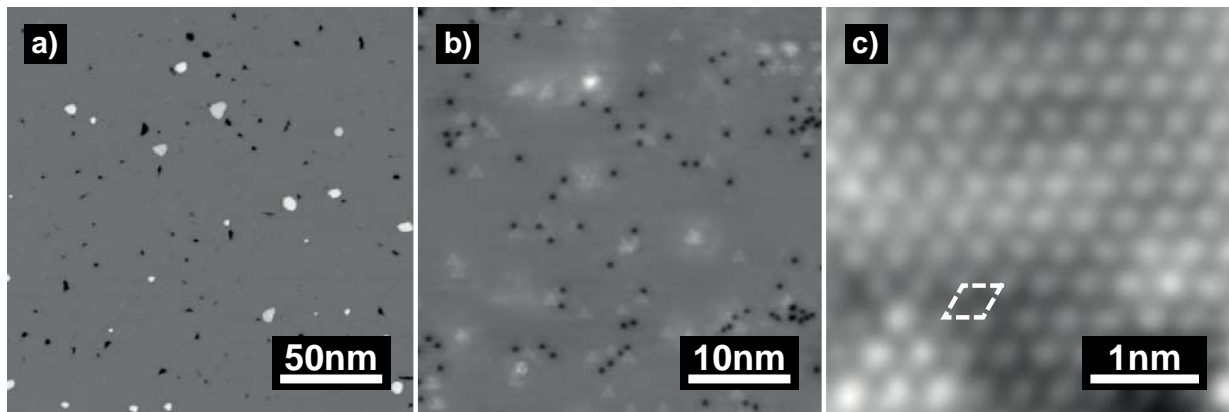
Figure 9.4.: Optimized bilayer growth. Summary of the optimized Bi/Bi_2Se_3-surface grown at 250 K: **a)** Overview topography. The surface exhibits large, smooth areas with few vacancy islands and Bi excess clusters. $U_B = 1$ V, $I = 20$ pA. **b)** Zoom in an area without vacancy islands and clusters. Black dots are atomic defects, bright triangular protrusions are defects of the substrate underneath. $U_B = -550$ mV, $I = 3$ nA **c)** Atomically resolved topography. The lattice constant of the bilayer is 4.18 ± 0.1 Å. $U_B = -100$ mV, $I = 5$ nA.

Additional temperature dependent studies revealed an interval of ~ 200 K to ~ 270 K for the growth of smooth bilayer films. Below this temperature range the thermal energy is not sufficient for the material to form a smooth film. Instead, the material forms clusters of homogeneous shape, see Fig. 9.3 (a). Above ~ 270 K, films with very rough surfaces are obtained as described before (Fig. 9.2). Within the interval of $200 - 270$ K, the bilayer morphology changes slightly as a function of T.

At higher temperatures within the interval, the islands tend to get larger and rounder, Fig. 9.3 (b-d). Moreover, different layer heights can be found, Fig. 9.3 (g). Below 230 K the bilayers exhibit an average height of 5.7 ± 0.1 Å. Above 230 K, the average height is $(6.3 \pm 0.1$ Å). However, films grown below 230 K relax to a height of 6.3 Å, when they get stored at room temperature for several hours. Hence, 6.3 Å must be the equilibrium height of the Bi(111)-bilayer on Bi_2Se_3.

Additionally for coverages around 100 %, the films grown at higher temperatures exhibit a smaller number of vacancy islands or excess Bi islands on top, Fig. 9.3 (e) and (f).

Fig. 9.4 illustrates the results of a sample grown at 250 K. The areas without large scale defects are about 50 nm x 50 nm in size (a). This is large enough to perform high resolution FT-STS images. Still the areas contain enough atomic scale defects, which are needed to induce the desired QPI (b). As a consequence, a growth temperature of 250 K was chosen for further experiments.

Summary

The growth of bismuth bilayers on Bi_2Se_3 is complex and surprising. Smooth (111)-bilayers can be grown in a temperature range of ~ 200 K and ~ 270 K. Below ~ 200 K the adatoms are not provided with enough energy to form a film with a smooth surface. Between ~ 200 K and 230 K the adatoms are sufficiently mobile to form smooth (111)-bilayer islands, but the substrate forces the islands into a more triangular shape with a reduced height of 5.7 ± 0.1 Å. The surface energy is at a local minimum, but not at a global minimum. Above 230 K the film is provided with enough energy to reach the global minimum of surface energy by overcoming the influence of the substrate. The bilayer can relax into its equilibrium height of 6.3 ± 0.1 Å and the islands exhibit a rounder shape to reduce the edge-to-area ratio.

If the temperature during growth is larger than ~ 270 K, the resulting islands exhibit a rough surface. The structure of these films is unknown (For an analysis attempt see B). While for a growth temperature below 230 K the influence of the substrate is too strong to grow fully relaxed films, above ~ 270 K its influence seems to be too small to form a well-ordered bismuth layer. However, once grown bilayers are not destroyed by annealing to temperatures above ~ 270 K (see B). The film only reduces its surface energy by forming larger islands and relaxes to its equilibrium height of 6.3 Å (if this was not reached before).

The equilibrium height is surprisingly high. Together with the complexity of the growth, the unusual bilayer height points to a large stress within the bilayer. On a substrate with an even smaller lateral lattice the Bi-bilayer might not grow anymore.

The unusually large height of the Bi-bilayer should lead to a stronger decoupling of the bilayer electronic states from the electronic states of the substrate. Also, the degree of isolation of the TES with respect to the bulk bands should be increased, if the TES is relocated to the new surface.

9.2. Unraveling the Electronic Structure

In this section the band structure of Bi/Bi_2Se_3 is studied by ARPES and DFT calculations. While ARPES measurements only map the dispersion of occupied bands, DFT can provide band dispersions below and above E_F. However, a comparison with measured data is needed to ensure the correctness of the calculation. Especially for the given system a comparison of DFT and ARPES is needed. As mentioned in the previous section, STM seems to overestimate the bilayer height on Bi_2X systems and so cannot provide the correct input for DFT. Therefore, the band structure was calculated several times with varying layer heights. Each calculation was then compared with ARPES-derived band dispersions.

ARPES

Measurements were carried out at the SGM3 beamline at the ASTRID synchrotron in Aarhus with a SPECS Phoibos 150 hemispherical analyzer [153]. For all measurements, a photon energy of $E_{Ph} = 18$ eV and a path energy of $E_{Ph} = 10$ eV were used. The energy resolution was ≤ 20 meV, the angle resolution was better than 0.2 deg. The sample temperature during measurements was 60 K. The base pressure of the system was $< 10^{-8}$ mbar during annealing and $< 10^{-9}$ mbar during measurements. The bilayers were grown by MBE with a commercial SPECS EBE-4 evaporator.

Fresh Bi_2Se_3 surfaces were achieved by cleaving the samples in the chamber at room temperature. For bismuth growth, the samples were cooled down to 250 K. To ensure large bilayer patches, the samples were annealed afterwards to 450 K for 5 min[4].

The bismuth coverage was estimated based on angle integrated XPS core level spectra of the Bi 5d and Se 3d orbitals, Fig. 9.5 (b). The double peak at $E_B = 50$ eV originates from the Se in the substrate. Its intensity simply decreases with Bi deposition. The double peak at $E_B = 20$ eV, which results from the substrate Bi, also decreases with Bi deposition. After Bi deposition, an additional side peak can be found for each peak of the substrate Bi. These new features are attributed to the 5d core levels of the Bi-bilayer. Using the relative intensities of the bilayer and substrate Bi 5d(3/2) peaks, the mean free path of

---

[4]The preparation for ARPES differs in this point from the preparation for STM. It was not possible to control the growth procedure as precisely as during the the STM experiment. The ARPES signal would be weakened, if not a coverage close to 100% is reached. Below 100%, the substrate is covered with (small) bilayer islands. Above 100%, the bilayer is covered with Bi excess clusters. In both cases the structure size reduces the signal-to-noise-ratio. Annealing the system after growth increases the size of the islands and therefore leads to clearer ARPES images. The integrity of the bilayer, after exhibiting the bilayer to such high annealing temperature, was verified by STM. The surface is only covered with more dirt. The extra annealing step is not optimal for STM experiments but optimal for ARPES. The influence of annealing on the ARPES signal anf the surface integrity is described in appendix B.
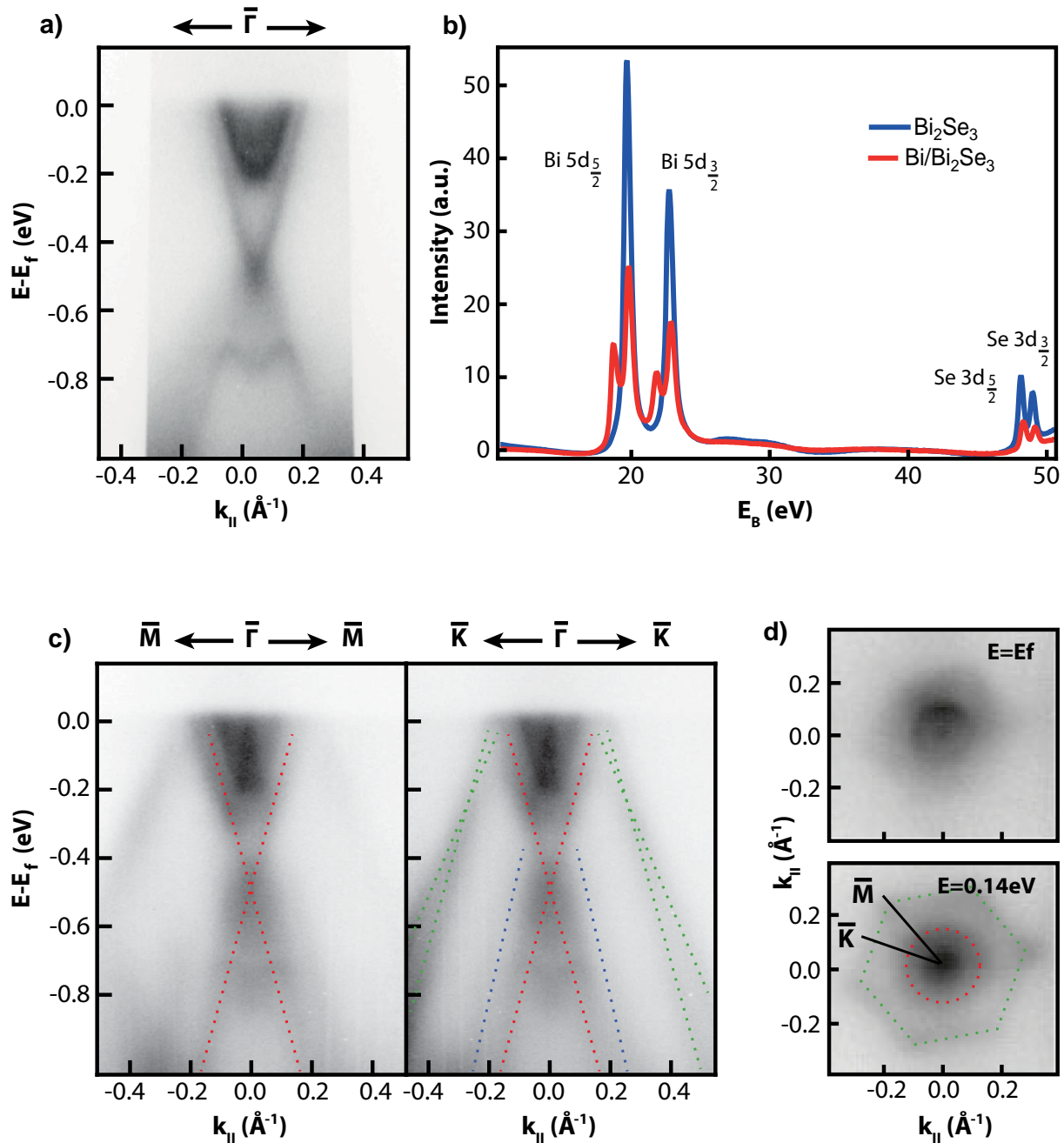
Figure 9.5.: ARPES and core level photoemission of Bi₂Se₃ and Bi/Bi₂Se₃. a) Photoemission intensity of Bi₂Se₃ around $\bar{\Gamma}$ **b)** Core level photoemission of Bi₂Se₃ (blue) and Bi/Bi₂Se₃ (red) as a function of the binding energy. **c)** Photoemission intensity of Bi/Bi₂Se₃ along $\bar{\Gamma}\bar{M}$ and along $\bar{\Gamma}\bar{K}$. **d)** CECs of (c) at the Fermi energy and at a binding energy of 0.14 V.

the emitted electrons $\lambda = 4.5$ Å and the known bilayer height, the coverage is calculated to 20 %. ARPES shows no differences in the surface band structure for coverages between 20 % and 160 %. see Fig. B.5 (d). In the following, the band structure of the 20 % covered sample is analyzed as an example for bilayer covered surfaces.

The bare Bi_2Se_3 surface provides a clear ARPES signal with the expected features, Fig.9.5 (a): The Dirac cone is located at $\bar{\Gamma}$ with the Dirac point at an energy of $E_B = 0.49 \pm 0.04$ eV. The m-shaped state at $E_B = 0.7$ eV is the bulk valence band. From the Fermi level down to 0.21 eV a 2D electron gas can be identified within the Dirac cone. This indicates a slight contamination of the bare substrate by adsorbates[5] [130].

After the preparation of the bilayer two new bands occur, Fig. 9.5 (c) green dashed lines. CECs reveal a strongly hexagonal shape of the new bands, with a warping along $\bar{\Gamma}\bar{K}$, Fig. 9.5 (d). The position and the slope of these bands are clearly visible and can be used to find the correct DFT band structure (see next section).

A Dirac cone is visible at the original position, but blurred as the whole band structure. The preserved location of this Dirac cone, as well as the fact that not the hole surface is covered with the bilayer, indicate that this is the Dirac cone of the uncovered Bi_2Se_3 surface. If this is correct, a second Dirac cone should be found, stemming from areas with bilayer coverage. Its position should be shifted in energy, due to the expected charge transfer between the bilayer and the substrate.

Indeed, another weak band can be found, marked with blue dashed lines in Fig. 9.6 (c). This band could be the DC of the Bi/Bi_2Se_3 system. However, the intensity of this band is too small to verify a possible Dirac cone. A Dirac point is not visible. When the visible parts of the band are extrapolated, the DP can be expected around $E_B = 0.05$ eV). We turn to ab-initio calculations of the band structure in order to identify this band.

DFT

The DFT calculations were performed using the full-potential linearized augmented plane wave method as implemented in the FLEUR code [195]. DFT is employed in the generalized gradient approximation as given by Ref. [157], including spin-orbit coupling self-consistently. Using the Bi_2Se_3 lattice parameters, the epitaxial Bi-bilayer was assumed to be located on one side of a slab of six Bi_2Se_3 quintuple-layers. The in-plane lattice of the bilayer has been set to that of Bi_2Se_3, consistent with the pseudomorphic growth observed by STM. The atomic positions of the bilayer and the first substrate layers were relaxed. To match the dispersion of Bi-bilayer bands found by ARPES, the van-der-Waals gap was

---

[5]The aging effect of Bi_2Se_3 mentioned before. The adsorbates originates from residual gas within the chamber.

then varied, while the intralayer distance of the bilayer was kept constant, see Fig. 9.6 (a). A good agreement was found for a bilayer height of 4.93 Å, Fig. 9.6 (b). This height is much smaller than the height observed by STM. However, the overestimation of Bi-bilayers on Bi$_2$Se$_3$ and Bi$_2$Te$_3$ by STM does not seem to be unusual, see Tab. 9.2. However, the optimized height is 0.8 Å larger than the height calculated by relaxation of the structure and is much larger than for the Bi-bilayer on Bi$_2$Te$_3$.

The optimized DFT-calculated band structure reveals four principal bands that dominate the surface, marked in light and dark green, red, light and dark blue in Fig 9.6 (c). The green bands can be identified as the Bi-bilayer VB (dark green) and the Bi-bilayer CB (light green). These are energetically shifted upwards by about 0.6 eV with respect to a free standing bilayer (compare with Fig. 9.1 (d). This can be explained by a charge donation to the substrate. The subsequent electric field between bilayer and substrate shifts the bands upwards[6]. Different for bilayers on Bi$_2$Te$_3$, the gap between the VB and CB of the bilayer is not closed. In addition, the band inversion is conserved. Hence, the 1D TES can be expected at about +0.6 eV.

Furthermore, the band bending induced by the charge transfer establishes a quantum well. This hosts 2D electron states originating from the Bi$_2$Se$_3$ valence and conduction band (light and dark blue), which reveal a similar shape as the respective bands of the pristine Bi$_2$Se$_3$ covered with adsorbates [130, 135, 145, 154, 198]. The Bi$_2$Se$_3$ CB states can even be found below E_F, due to the band bending.

The electric field also causes a Rashba-type spin-splitting of the Bi VB and Bi$_2$Se$_3$ CB. While in the bulk crystal inversion symmetry and TRS preserve spin degeneracy of the bands [$E(|\mathbf{k},\uparrow\rangle) = E(|\mathbf{-k},\uparrow\rangle), E(|\mathbf{k},\uparrow\rangle) = E(|\mathbf{-k},\downarrow\rangle)$], the surface breaks inversion symmetry, so that $E(|\mathbf{k},\uparrow\rangle) = E(|\mathbf{-k},\uparrow\rangle)$ has not to be fulfilled anymore. Therefore, the electric field splits the previously spin-degenerate bands.

	On Bi$_2$Te$_3$	On Bi$_2$Se$_3$
STM	4.7 Å	6.3 Å
Other	4.19 Å	4.94 Å

Table 9.2.: Comparison of Bi-bilayer heights measured by STM and other techniques. For Bi on Bi$_2$Te$_3$, the STM value is from literature [193]. The other value is measured by LEED [196]. For Bi on Bi$_2$Se$_3$, the STM value is derived from own measurements. The other value is found by the comparison of ARPES and DFT

---

[6]A similar charge transfer effect was already proposed for Bi-bilayers on Bi$_2$Te$_3$ and attributed to the difference in work function between film and substrate [197].
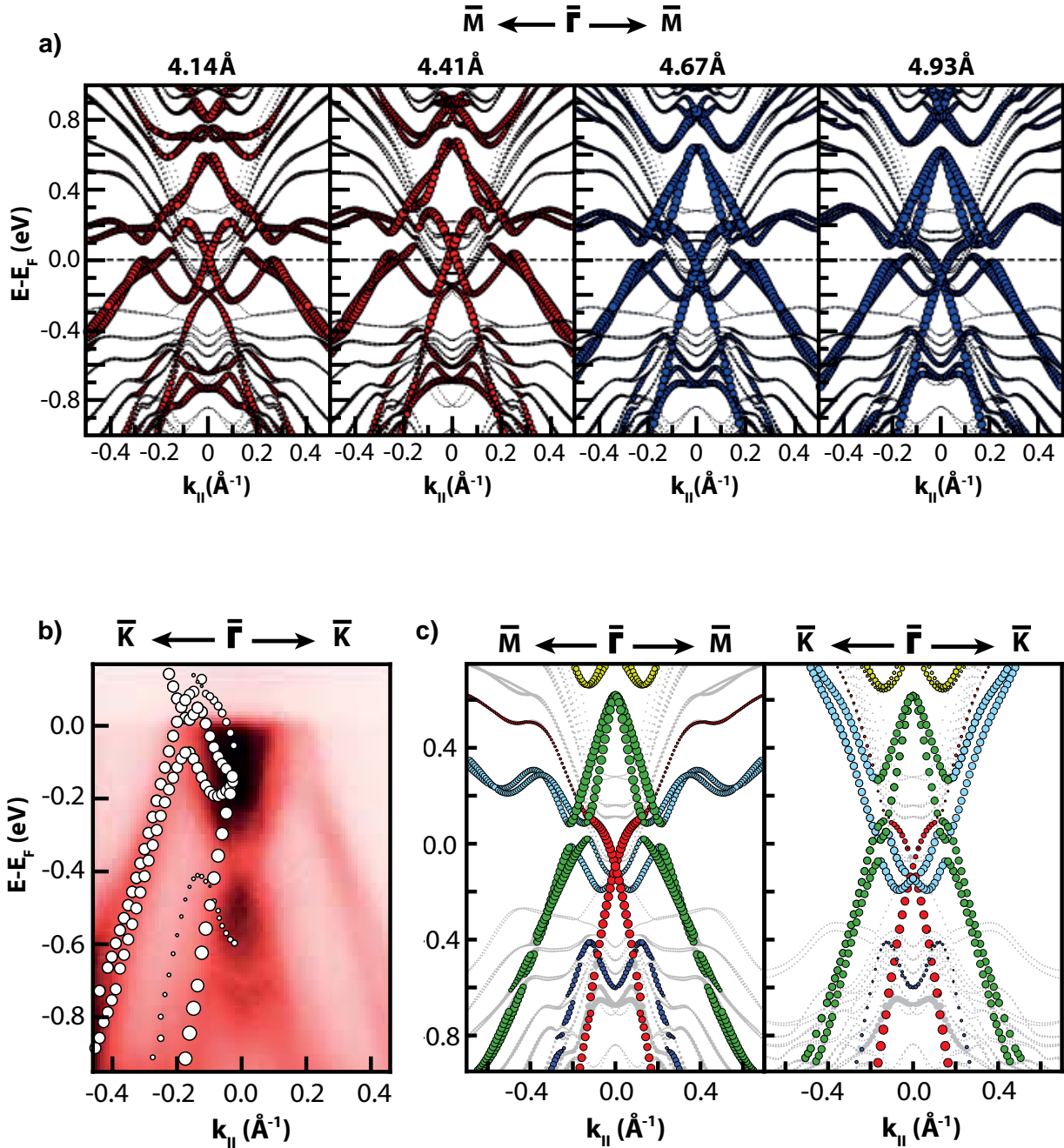
Figure 9.6.: Band structure of Bi/Bi$_2$Se$_3$ calculated by DFT. a) Band structure depending on the size of the van-der-Waals gap. (Distance of the topmost layer of the bilayer and the topmost Se layer of the substrate is indicated.) The circle size is proportional to the localization of the corresponding electronic state at the surface of the bilayer. **b)** Comparison of the band structure derived from ARPES and DFT, calculated with a bilayer height of 4.94 Å. The new bands found by ARPES fit the simulation. **c)** DFT along $\bar{\Gamma}\bar{M}$ and $\bar{\Gamma}\bar{K}$ for a bilayer height of 4.94 Å. Colors denote the dominant origin of the bands: dark green: Bi-bilayer VB, light green: Bi-bilayer CB, red: Dirac cone, dark blue: Bi$_2$Se$_3$ VB, light blue: Bi$_2$Se$_3$ CB, grey: Bands with a weak localization on the surface.

The two sets of the Rashba split bands hybridize and a gap opens along $\bar{\Gamma}\bar{M}$ at $E = \sim 50$ meV above E_F. A similar hybridization gap opens for a single Bi-bilayer on Bi$_2$Te$_2$Se [41]. Here, the original bilayer gap closes and the hybridization gap is the only gap of the system. It was argued that this gap hosts the 1D TES. For two reasons this cannot be the case for Bi-bilayers on Bi$_2$Se$_3$. Most important, the original gap of the Bi-bilayer bands remains open. And to host the 1D TES, a gap has to be open in every direction. While this is the case for the original gap, the hybridization gap is closed along $\bar{\Gamma}\bar{K}$. (In fact, also the hybridization gaps of Bi/Bi$_2$Te$_2$Se and Bi/Bi$_2$Te$_3$ are closed along the $\bar{\Gamma}\bar{K}$ direction. These systems should not exhibit any 1D TES at all.)

The two spin split Bi$_2$Se$_3$ CB states cross at $\bar{\Gamma}$, ~ 0.1 eV below E_F and form a Dirac cone like structure. While Miao *et al.* [199] identify the crossing point as the Dirac point of the substrate, its origin is clearly the Rashba splitting of the 2DES. Therefore, it does not exhibit a topological protection.

The actual Bi/Bi$_2$Se$_3$ 2D TES (red) shows the same behavior as in the case of Bi/Bi$_2$Te$_3$: It originates from the topological nature of the substrate, but is relocated to the bilayer surface. Therefore, it is energetically shifted upwards as the original bilayer bands. The corresponding Dirac point is located at -0.1 eV. This is about 0.4 eV closer to E_F than the original DP.

However, the relocated Dirac cone was not identified in the ARPES data. The band marked by blue dashed lines in the ARPES image (Fig. 9.5 c), which was thought to be the DC of the Bi/Bi$_2$Se$_3$ system, is in fact the Bi$_2$Se$_3$ VB. The actual DC is overlapping with other bands and is not visible, see Fig. 9.6 (b). Therefore, the experimental verification of the TES has to be done by FT-STS as shown in the next section.

DFT calculations together with a comparison with ARPES confirm the unusual large bilayer height of the Bi/Bi$_2$Se$_3$ system. Like the TES of Bi/Bi$_2$Te$_3$, theory predicts a relocation to the surface of the bilayer. However, this cannot be clearly verified by ARPES and needs a confirmation by FT-STS. DFT also predicts a preserved gap between the bilayer's VB and CB. Since this gap closes when Bi$_2$Te$_3$[181] or Bi$_2$Te$_2$Se[41] are used as a substrate, the Bi/Bi$_2$Se$_3$ system is the prime candidate for searching the 1D TES of the Bi-bilayer.

9.3. Identifying Interactions

This section investigates the interaction of the bulk and surface states of Bi/Bi$_2$Se$_3$. In the first part the interactions are visualized by FT-STS maps. In order to identify the origin of the measured features, a method to simulate FT-STS maps is developed in the second part. Measured and simulated maps are compared with each other in the third section.

9.3.1. Accessing q-Vectors by FT-STS

STS images that are used to calculate FT-STS maps were taken with bias voltages between -1000 mV and $+400$ mV in constant-current mode. The feedback loop was activated and the Lock-In amplifier modulated the bias voltage with a modulation voltage of 10 mV. The sensitivity of the Lock-In was optimized for each bias voltage and is given in the caption of the figures. Samples were prepared using the optimized procedure found during the growth study and measured with the same UHV-STM system at equal conditions.

To gain high quality FT-STS maps, the original images were worked on according to the method described in section 5.2.3, follwed by a symmetrization of the FFT images:

1. The STS maps were flattened, to increase the overall intensity of the resulting FT-STS maps.

2. A median over 5 pixels was taken along the slow scan direction in order to reduce the intensity of FFT artifacts induced by jumps between scanned lines.

3. A window function was used to damp the STS image intensity for the 40 pixels closest to the image edges.

4. The FFTs were taken with the convention of $|\mathbf{q}| = 2\pi/\lambda$.

5. In order to damp the intensity in the center of the FFT, which results mainly from long range potential disorder, the intensity of the FT-STS maps were multiplied with the factor $x^2 + y^2 + 1000$.

6. The resulting FFT images were 6-fold symmetrized following the pseudo sixfold symmetry of the underlying band structure.

7. Finally, the images were smoothened with a Gauss filter and plotted in a logarithmic scale to further enhance visibility.

STS images have been taken with a size of 40 nm $\times$ 40 nm on an area of the bilayer without any vacancy islands or excess Bi. Still there are many defects visible in the topography
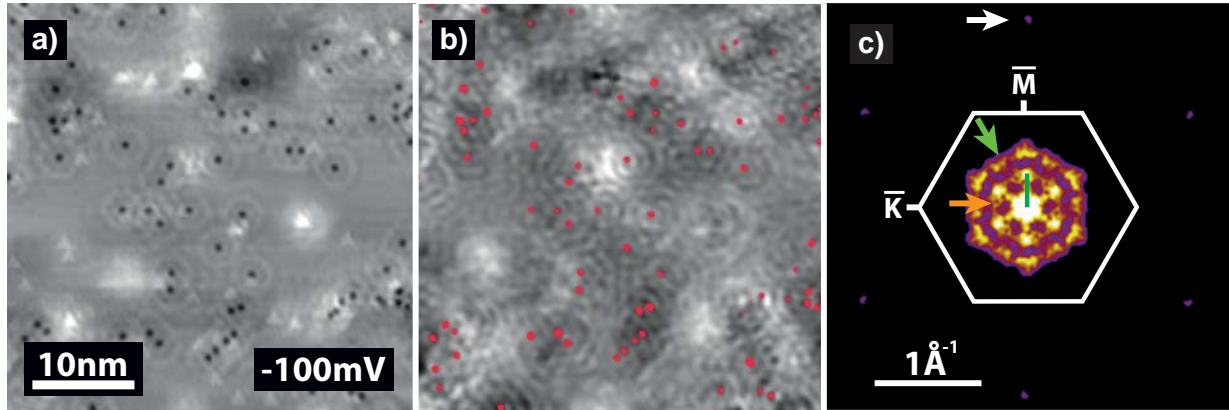
Figure 9.7.: Topography, STS and FT-STS map of Bi/Bi$_2$Se$_3$. a) Topography, **b)** STS and **c)** FT-STS maps of Bi/Bi$_2$Se$_3$ at $U_B = -100$ mV. $I = 3$ nA, $U_{\mathrm{mod}} = 10$ mV. the conductance range of the STS map is 0.7 to 1.3 nS. Red spots in (b) mark the point defects on the bilayer surface extracted from (a). **c)** The six spots in the outer part of the image (white arrow) originate from the atomic lattice. With these spots, the size and orientation of the Brillouin zone can be determined (white hexagon). Furthermore, an are an outer hexagon (bright green arrow), an inner hexagon (orange arrow) and a star (dark green line, only one arm is marked) are visible. These features originate from the interaction within the electronic structure.

image, see Fig. 9.7 (a): Atom sized depressions, due to atom vacancies at the surface; triangular shaped protrusions, due to defects of the Bi$_2$Se$_3$ substrate, most likely within the first quintuple layer; and a large scale contrast with a length scale of 10 nm. Already in the topography image the atom vacancies are surrounded by several oscillations of the dI/dU signal. This is the first indication of a QPI. the pattern gets more obvious in the corresponding STS map, Fig 9.7 (b). Here, the QPI-pattern originating from atom vacancies covers the whole surface. It is superimposed on a background modulation of larger length scale, where the regions of highest intensity are located around the substrate defects while areas exhibiting the weakest intensity are located around groups of vacancies.

The corresponding FT-STS map (Fig. 9.7 (c) shows six spots at large wave vectors at the edge of the image. These are the signature of the surface atomic lattice and are used to determine the orientation and size of the SBZ. Besides the spots, at least three features can be identified around $\bar{\Gamma}$: A strong outer hexagon with the flat side along $\bar{\Gamma}\bar{M}$ (bright green arrow), a weaker inner hexagon with the same orientation (orange arrow) and a star with six arms along $\bar{\Gamma}\bar{M}$ (one arm marked by a dark green line). At the intersection of the inner hexagon and the star the FT-STS intensity is increased. The high intensity spot in the middle is induced by the long range modulation of the STS image. The large number of features already indicates that several bands are contributing to the QPI.

The situation gets even more complex when the energy dependence of FT-STS is taken into account. Fig. 9.8 gives a good view over STS and FT-STS maps at energies between -700 and 250 mV. The STS images reveal that the wavelength and intensity of the QPI
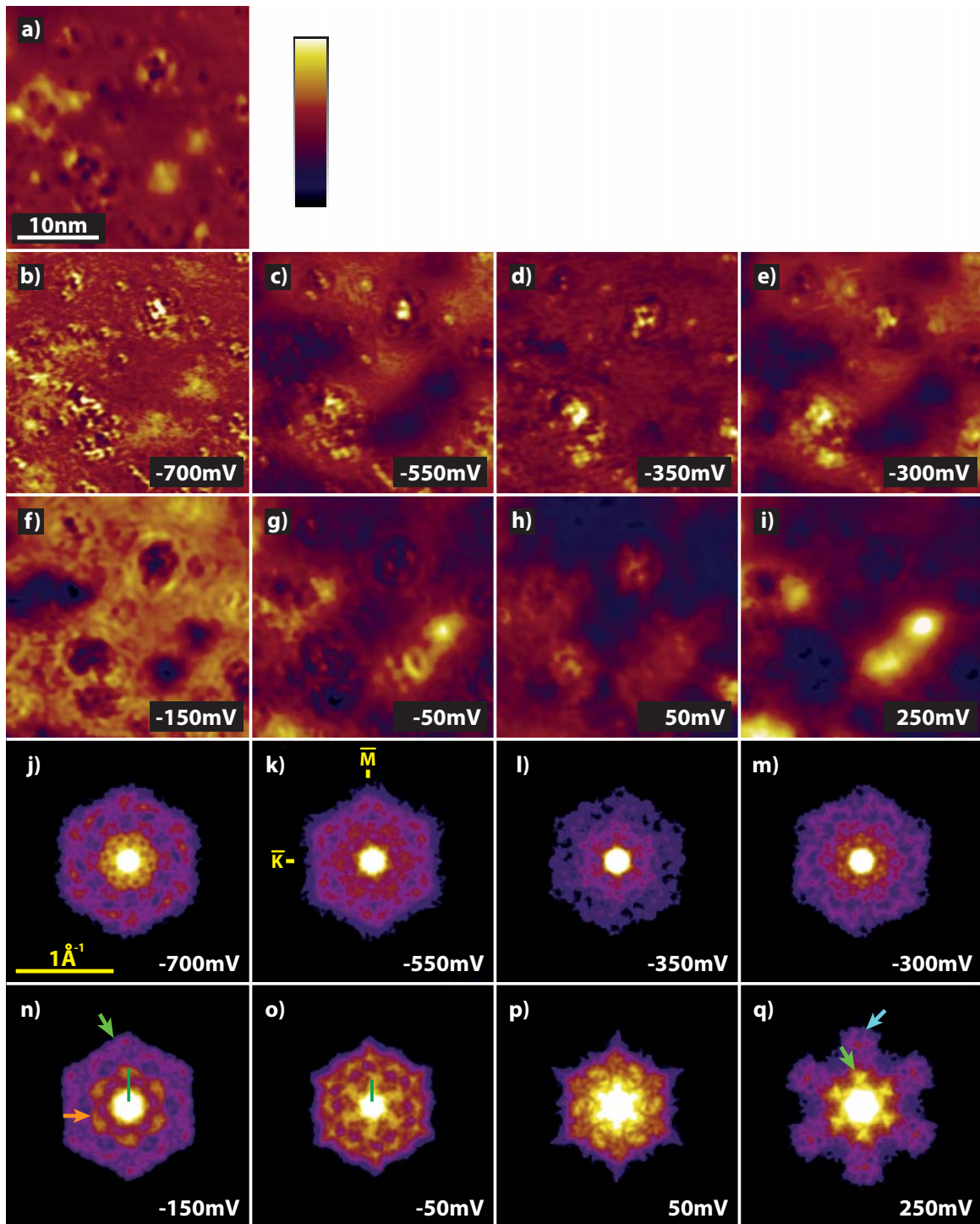
Figure 9.8.: Overview of STS and FT-STS maps taken on Bi/Bi$_2$Se$_3$. a) STM topograph of the investigated region ($U_B = -50\,\text{mV}$, $I = 3\,\text{nA}$, scale bar from 0 to 80 pm). **b)-i)** STS images measured at the indicated sample biases ($I = 3\,\text{nA}$). The color range covers the following conductance intervals: (b) $0.09\,\text{nS}$ to $0.13\,\text{nS}$, (c) $0.09\,\text{nS}$ to $0.17\,\text{nS}$, (d) $0.17\,\text{nS}$ to $0.29\,\text{nS}$, (e) $0.23\,\text{nS}$ to $0.4\,\text{nS}$, (f) $0.4\,\text{nS}$ to $0.7\,\text{nS}$, (g) $1.2\,\text{nS}$ to $2\,\text{nS}$, (h) $0.46\,\text{nS}$ to $1.8\,\text{nS}$, (i) $0.23\,\text{nS}$ to $0.79\,\text{nS}$. **j)-q)** FT-STS images resulting from the Fourier transformation of (b-i) and image processing as described in the main text. The highlighted features are: outer hexagon (bright green arrow), inner hexagon (orange arrow), star (dark green line, only one arm is marked) and another star above E_F (blue arrow).

pattern change with bias voltage. Moreover, the contrast of the long range modulation inverts several times, i.e. between -700 mV and -500 mV, and again between -150 mV and -50 mV, but its wavelength does not change. Due to this behavior, bias dependent contrast change with a conserved wavelength and fixed contrast extrema located at the position of dopants (surface vacancies and subsurface defects), it is reasonable to conclude that the background modulation originates from potential disorder induced by the dopants.

In the following the QPI is investigated using the bias dependent FT-STS maps calculated from the measured STS images. These are illustrated in Fig. 9.8 (j-q). Further FT-STS maps can be found in the appendix, section B.6. While Fig. 9.8 already displays all relevant features, the figure in the appendix may allow a greater traceability of changes.

The FT-STS maps show complex features that change in size and shape with energy. Below E_F, the maps are dominated by an outer hexagon already identified in Fig. 9.7 (green arrow) that exhibits a negative dispersion. Other features are only dominant at some energy intervals, e.g. the inner hexagon and the star between E_F and about -200 mV (orange arrow and green line).

Above E_F, the outer hexagon gets gradually warped with increased intensity at the edges and reduced intensity in between. At 250 mV the hexagon is reduced to six single points along $\bar{\Gamma}\bar{M}$. Within this energy range the hexagon is accompanied by another prominent feature at larger $|\mathbf{q}|$, which exhibits a positive dispersion. Starting as a hexagon around 100 mV, it gets gradually warped at higher energies and finally transforms into a star-like shape with six arms along $\bar{\Gamma}\bar{M}$ at 250 mV (blue arrow). Above 400 mVn no feature can be identified anymore, see Fig. B.6.

Due to the complexity of the maps (large number of features, with changing forms and intensity, different dispersions and superpositions), it is a nontrivial task to identify all original features. However, only with a distinct identification, the correct $\mathbf{q}$-vectors can be extracted and the interaction between bands can be unveiled. Therefore, we developed a method to simulate FT-STS maps from the band structure $E(\mathbf{k})$ of the system, which was determined by ARPES and DFT.

9.3.2. JDOS Simulation of FT-STS Maps

For a simulation of FT-STS maps all possible scattering events between bands at a certain energy must be known. A first step could be the calculation of an FT-STS map by plotting all scattering vectors present in $\mathbf{k}$-space between the bands ($\mathbf{q}$-vectors) in a new map, with all vectors starting at the the center of the map. The intensity of a certain point in the map depends on the number of $\mathbf{q}$-vectors that reach this point. For a more realistic simulation,

the density of states and the broadening and eventual spin-polarization of the bands have to be taken into account, too. Therefore, a model of the band structure is needed that provides all these parameters and an algorithm that calculates the feature intensity with respect to these parameters. The first part of this section deals with the question how a proper model of the band structure can be acquired; the second part describes the method used to calculate an FT-STS map.

Determining the Spectral Function

A map of the band structure containing all the information needed can principally be obtained quite easily by probing the material with (spin-resolved) ARPES. However, this approach exhibits two major drawbacks, a general one and a specific one of the given system. In general, ARPES can only access occupied states, the bands above E_F remain unknown. Moreover, as shown in section 9.2, the ARPES images are of low quality. The images exhibit a rather bad signal-to-noise ratio and, due to the surface morphology, bands are further broadened.

As mentioned in chapter 3, the band structure measured by ARPES including all electron-electron correlations, can be described by a spectral function. Thus, also a spectral function can be used as an input for the FT-STS map simulation. Due to the restrictions of the system, the spectral function cannot be derived from the given ARPES images. In an alternative approach, we modeled the spectral function from the band structure calculated by DFT[7], see section 9.2.

DFT provides the band structure along three different directions: $\bar{\Gamma}\bar{M}$, $\bar{\Gamma}\bar{B}$[8] and $\bar{\Gamma}\bar{K}$ in a $0.7\,\mathring{A}^{-1}$ range from the center of the surface Brillouin zone. The relevant eigenvalues $E(\mathbf{k})$ for each band were isolated and symmetrized in k-space according to the pseudo-sixfold symmetry of the system. This resulted in a description of the band structure along 12 different directions. A three-dimensional interpolation, based on a voronoi-natural-neighbors approach [201], was utilized to obtain a full profile of the single electron bare energy. In this case, the interpolation method is more precise and simpler to handle than fitting the data by functions, the band dispersion is far from being free-electron like. The interpolated data points were used as the bare-energy term $\epsilon(\mathbf{k})$ in the spectral function.

---

[7]A spectral function to simulate FT-STS maps has been modeled before using a tight binding Hamiltonian [200]. However, this was a rather simple simulation. e.g. no occupied states were included.

[8]$\bar{B}$ is defined as a point along the perimeter of the Brillouin zone exactly between $\bar{M}$ and $\bar{K}$.

Finally, the full 3D spectral function was calculated by

$$A(E, \mathbf{k}) = \frac{|\Sigma''(E, \mathbf{k})|}{[E - \epsilon_\mathbf{k} - \Sigma'(E, \mathbf{k})]^2 + \Sigma''(E, \mathbf{k})^2} * W(E, \mathbf{k}) \qquad (9.1)$$

Here, the real and imaginary part of the self energy, Σ' and Σ'', were set arbitrarily to 0 and 0.001 eV. Moreover, $W(E, \mathbf{k})$ is a weighting factor that depends on the point size of the DFT calculation to take the localization of each state $|E, \mathbf{k}\rangle$ on the bilayer surface into account, simulating the surface sensitivity of STM. The spectral function was calculated in an energy range between -1000 and 650 mV. The result is presented in Fig. 9.9.

From Spectral Function to JDOS Maps

The simulated FT-STS maps were calculated based on the CECs extracted from the spectral function. For the actual calculation the so called JDOS approximation was used (therefore, the final maps are called JDOS maps). For this purpose, the intensity at a certain coordinate $\mathbf{q}$ of a JDOS map was calculated as the sum over the product of the intensities at all points in $\mathbf{k}$-space separated by a vector $\mathbf{q}$:

$$\text{JDOS}(E, \mathbf{q}) = \sum_{\mathbf{k}_\parallel} A(E, \mathbf{k}_\parallel) \text{M}(E, \mathbf{k}_\parallel, \mathbf{k}_\parallel + \mathbf{q}) A(E, \mathbf{k}_\parallel + \mathbf{q}), \qquad (9.2)$$

where $A(E, \mathbf{k}_\parallel)$ and $A(E, \mathbf{k}_\parallel + \mathbf{q})$ depict the intensity of two states on the CEC(E) that are separated by $\mathbf{q}$, and $\text{M}(\mathbf{k}_\parallel, \mathbf{k}_\parallel + \mathbf{q})$ as the corresponding scattering matrix element. In general, the scattering matrix element is *a priori* unknown. It depends on the coupling of the initial and final electron states via a Coulomb potential and a spin-dependent scattering probability. In an attempt to take the spin-structure of the electron bands of the given system into account, we decided to assume a simple in-plane spin-polarization. This proceeding was motivated by the presence of the spin-polarized TES and the predicted Rashba-splitting of the bilayer bands[9]. Proper matrix elements were constructed by following Fermi's golden rule as an overlap of two spin states at $\mathbf{k}$ and $\mathbf{k}$'. The spin states can be written as $|\mathbf{S_k}\rangle = \frac{1}{\sqrt{2}}[1, \pm i\, exp(i\theta_k)]$. As long as the scattering impurity does not carry a magnetic moment, the impurity potential V can be derived from $\langle \mathbf{S_{k'}}|V|\mathbf{S_k}\rangle$, resulting in a multiplicative factor (that can still be energy dependent). The matrix elements are given by:

$$\text{M}(q) \propto |\langle \mathbf{S_{k'}}|\mathbf{S_k}\rangle|^2 = \frac{1}{2}(1 \pm cos\theta_q), \qquad (9.3)$$

where θ_q is the angle between $\mathbf{k}$ and $\mathbf{k}$', $\pm$ ensures the identity of the two band branches.

---

[9]Since the anisotropy of the splitting is very small, an out-of-plane component is neglected [202].
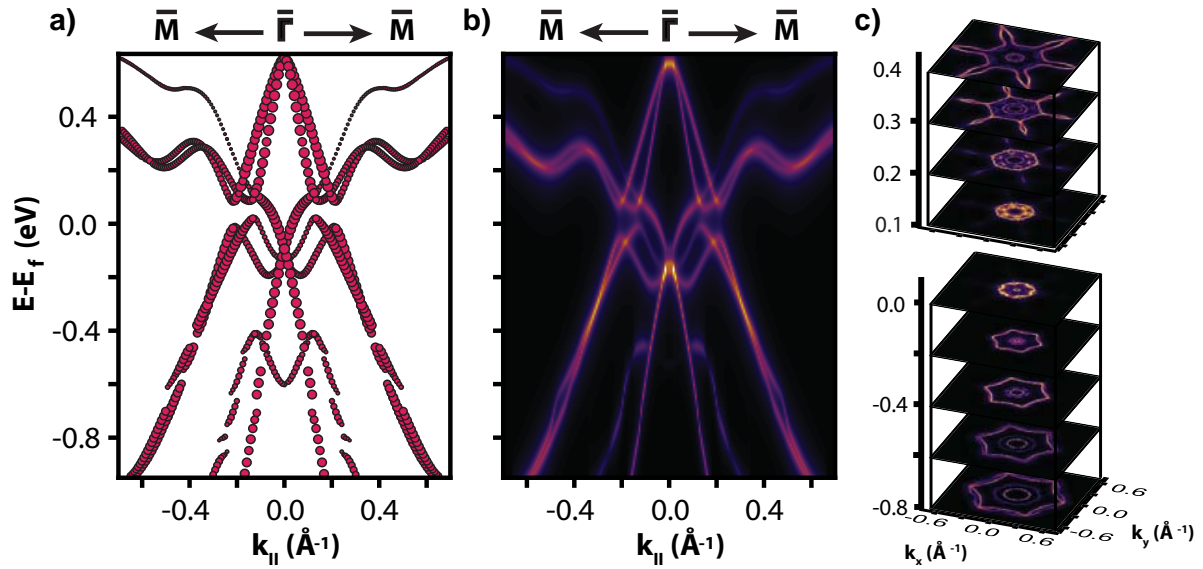
Figure 9.9.: From DFT to the spectral function of Bi/Bi$_2$Se$_3$: a) DFT calculation of Bi/Bi$_2$Se$_3$. The point size is proportional to the localization on the bilayer surface. **b)** The spectral function derived from (a). Its intensity is proportional to the DFT-point size. **c)** Stack of CECs taken from the spectral function at the energy indicated by the numbers on the left in eV.

Energy dependence is completely neglected. The matrix element depends on the angle between the spin orientation in **k** and **k**': With increasing angle the scattering probability is reduced. It reaches zero in case of opposite spin orientation. then the corresponding scattering channel does not make a contribution to the JDOS map.

In order to illustrate the JDOS approach, examples assuming simple CECs (circular, hexagonal) are given in Fig. 9.10. (a) and (d) show the CECs. (b) and (e) depict JDOS maps ignoring the spin-dependency during calculation, while the JDOS maps in (c) and (f) assume a spin-dependency as described above. Without spin-dependency, scattering between all states is possible. The JDOS pattern exhibits a sharp edge of great intensity following the contour of the corresponding CEC. The edge is dominated by backscattering (red arrows) and **q**-vectors of similar length (blue arrow). The finite intensity of the area within the edges stems from shorter scattering vectors. For a circular CEC the JDOS intensity distribution within the edge is isotropic. For a hexagonal CEC a six-fold star with increased intensity is visible. The star can be attributed to scattering along the arms of the hexagon (green arrow). For the described in-plane spin-polarization backscattering and all other scattering channels between states of opposite spin are ruled out. Therefore, in the resulting JDOS maps the edges of the features are now suppressed (red arrow).
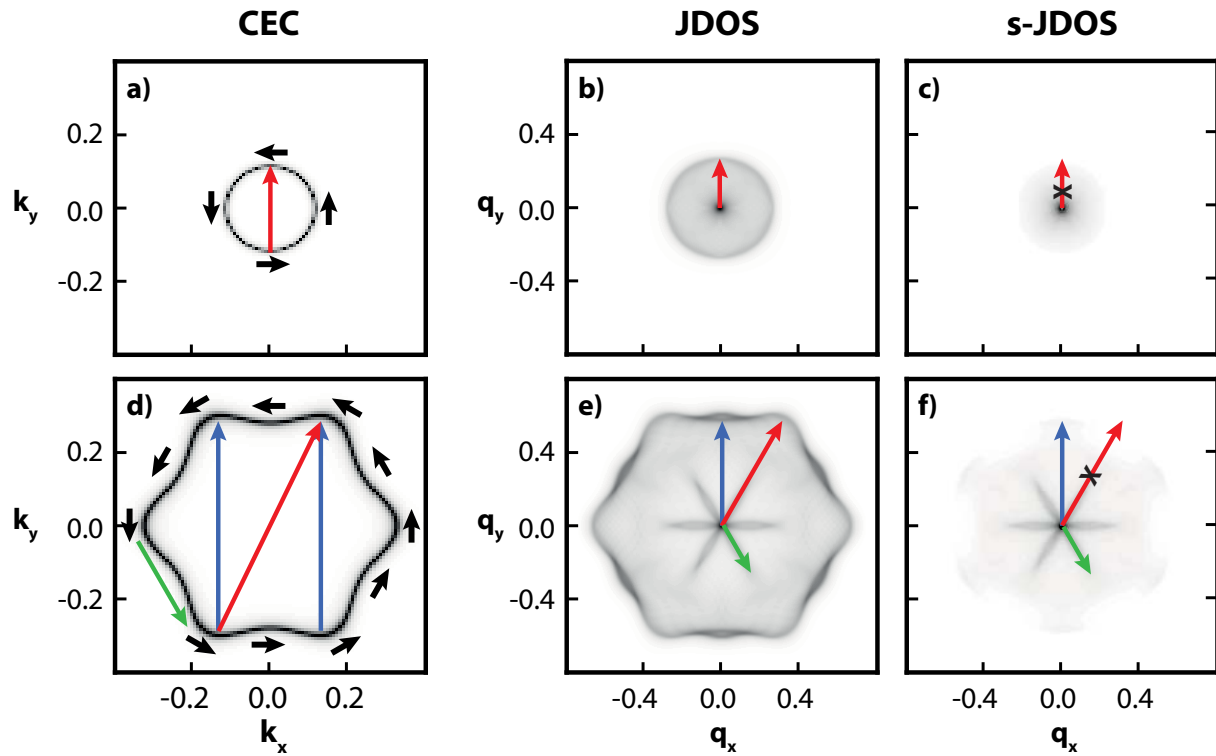
Figure 9.10.: JDOS simulation for simple CECs. a) and **d)** Schemes of a circular and hexagonal CEC. The black arrows denote the spin orientation. **b)** and **e)** Resulting JDOS maps ignoring the spin-polarization with $[\mathrm{M}(\mathbf{k}_{\parallel}, \mathbf{k}_{\parallel} + \mathbf{q}) = \mathbb{1}]$. **c)** and **f)** JDOS maps considering the spin-polarization with $[\mathrm{M}(\mathbf{k}_{\parallel}, \mathbf{k}_{\parallel} + \mathbf{q}) = \frac{1}{2}(1 \pm \cos\theta_q)]$.

The JDOS approximation is a phenomenological attempt to simulate FT-STSmaps. It can be used without knowing all the peculiarities, e.g. the spin-polarization of the system. However, even when an identity matrix is used, the method is good enough to identify measured features, since all **q**-vectors are taken into account. Then the presence or absence of **q**-vectors in the experimental data can be traced back to the spin-dependent matrix element. The matrix element can then be modeled in greater detail in order to increase the accuracy of the simulation.

Results of the JDOS Simulation of the Bi/Bi$_2$Se$_3$ Band Structure

The code for calculating JDOS maps was written in the IGOR software environment [203]. Each CEC consists of a quadratic grid of 150x150 pixels. Fig. 9.11 depicts CECs and the resulting JDOS maps for -800 mV and 350 mV as an example. (a) and (d) show the spin orientation chosen for the simulation, the actual orientation direction is unknown. The dominant **q**-vectors are marked by arrows. For -800 mV, the two outer hexagons in the CEC stem from the spin-split Bi-bilayer-VB, the middle circle stems from the Bi$_2$Se$_3$-VB and the inner circle from the TES. Hence, the light green arrow in (b) marks $180°$-scattering
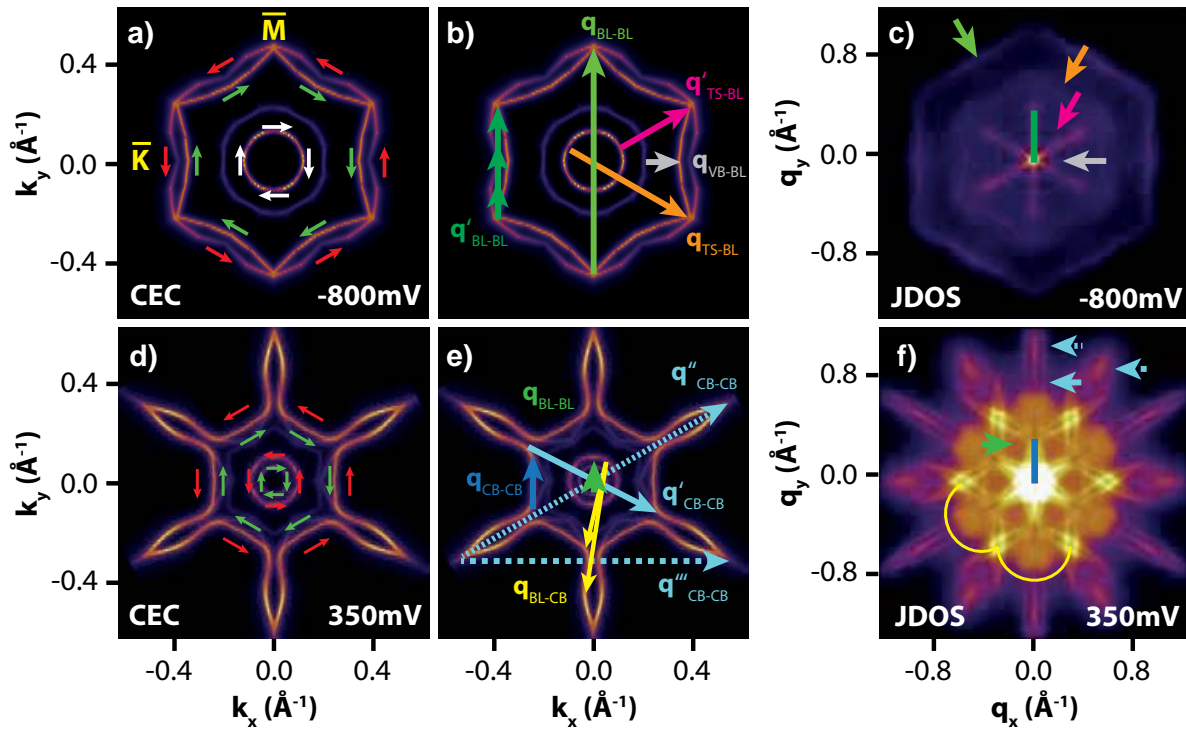
Figure 9.11.: From CEC to JDOS map for Bi/Bi$_2$Se$_3$ a) and **b)** CEC at -800 mV with the chosen spin-polarization and relevant **q**-vectors indicated by arrows. The larger circular feature is spin degenerate. **c)** Corresponding JDOS map. The features are marked with the same colors used for the vectors they originate from. **d)** to **f)** Same image sequence for 350 mV.

within the spin-split Bi-bilayer bands ($\mathbf{q}_{BL-BL}$). The form of the JDOS feature follows the form of the CEC of the bands (c). Dark green arrows mark scattering along the arms of the bilayer hexagon ($\mathbf{q}'_{BL-BL}$). The resulting feature exhibits a star-like form. Orange and pink mark the largest ($\mathbf{q}_{TS-BL}$) and smallest ($\mathbf{q}'_{TS-BL}$) possible scattering vectors between the bilayer bands and the TES. In the JDOS map, the area between the extrema is filled with intensity, indicating that multiple **q**-vectors with varying directions and momenta contribute to this feature. The area size depends on the arbitrarily chosen orientation of in-plane spin-polarization. If, e.g., the TES exhibied an opposite orientation, the area of the resulting hexagon would be larger, as the smallest contributing **q**-vector would decrease in length and the largest one would increase. However, this effect is quite weak as the Rashba splitting of the bilayer bands is not that strong.

A grey arrow marks scattering between the Bi$_2$Se$_3$-VB and the Bi-bilayer bands ($\mathbf{q}_{VB-BL}$). However, a resulting feature cannot be found in the JDOS map. The scattering between these bands is not suppressed, but its probability is much smaller than that of the other channels. Its intensity disappears within the intensity of the other features. This can be observed for scattering within the TES, too. Backscattering is suppressed, but all other **q**-vectors should contribute to the JDOS map. However, the resulting intensity is too small to define a visible feature, Fig. 9.10 (c).

At 350 mV, Fig. 9.10 (d-f), the outer structure of the CEC, a hexagon with star-shaped pockets at the edges, stems from the Bi_2Se_3-CBs. In the pockets, these bands are degenerate. Along the arms, the weaker band slipped closer to $\bar{\Gamma}$. Along $\bar{\Gamma}\bar{K}$ it is degenerate with another weak band, which is the TES. In the image center two stronger circles are visible stemming from the spin-split Bi-bilayer-VB.

Intraband scattering within the Bi_2Se_3-CB leads to four distinct features in the JDOS map. Scattering along the hexagon arms ($\mathbf{q}_{CB-CB}$) gives rise to a star with six arms orientated along $\bar{\Gamma}\bar{M}$. In the same orientation, there are features originating from scattering between opposite edges ($\mathbf{q}'_{CB-CB}$) and opposite pockets ($\mathbf{q}''_{CB-CB}$) of the Bi_2Se_3-CB. Scattering between next nearest pockets leads to features along $\bar{\Gamma}\bar{K}$ ($\mathbf{q}'''_{CB-CB}$).

Finally, interband scattering between the Bi-bilayer bands and the Bi_2Se_3-CBs ($\mathbf{q}_{BL-CB}$) leads to a flower-like area with the leaves again orientated along $\bar{\Gamma}\bar{M}$. Scattering between the Bi-bilayer-VBs ($\mathbf{q}_{BL-BL}$) should lead to a circular feature in the JDOS map, but its intensity is too weak to be identified.

9.3.3. Comparison of CEC, JDOS and FT-STS

With the procedure decribed above, JDOS maps were calculated for various bias voltages. By a comparison of FT-STS and JDOS maps, the observed features can be identified. Fig. 9.12 gives an overview of CEC , JDOS and FT-STS images at chosen energies. The identified features are marked with arrows. Features not visible in measured maps are marked with dotted arrows and crosses. All z-scales of FT-STS maps cover the same intensity interval. Maps of additional energies can be found in appendix B.7.

At -800 mV the broad hexagon from scattering between the bilayer band and the TES ($\mathbf{q}_{TS-BL}$ and $\mathbf{q}'_{TS-BL}$) is clearly visible in the FT-STS image. The outermost hexagon representing backscattering within the bilayer bands ($\mathbf{q}_{BL-BL}$) is missing, but the other bilayer scattering channel $\mathbf{q}'_{BL-BL}$, along the hexagon sides, is visible where it is in superposition with the before mentioned broad hexagon. While losing one feature in the FT-STS, another feature is enhanced: Around the singularity at $\bar{\Gamma}$ a circle of increased intensity is visible, which is assigned to $\mathbf{q}_{VB-BL}$ (grey arrow), the scattering channel between the bilayer- and Bi_2Se_3-VB. This will be strengthened by a comparison of the dispersion of simulated and measured $\mathbf{q}$-vectors in section 9.3.2.

At -350 mV this channel ($\mathbf{q}_{VB-BL}$) is not visible anymore, but the bilayer backscattering channel $\mathbf{q}_{BL-BL}$ is switched on. The broad hexagon ($\mathbf{q}_{TS-BL}$ and $\mathbf{q}'_{TS-BL}$) gets smaller and narrower, due to the negative band dispersion of the involved bands. All these features can be found at -150 mV, too. However, the broad hexagon and the bilayer backscattering are only visible where their features are in superposition.
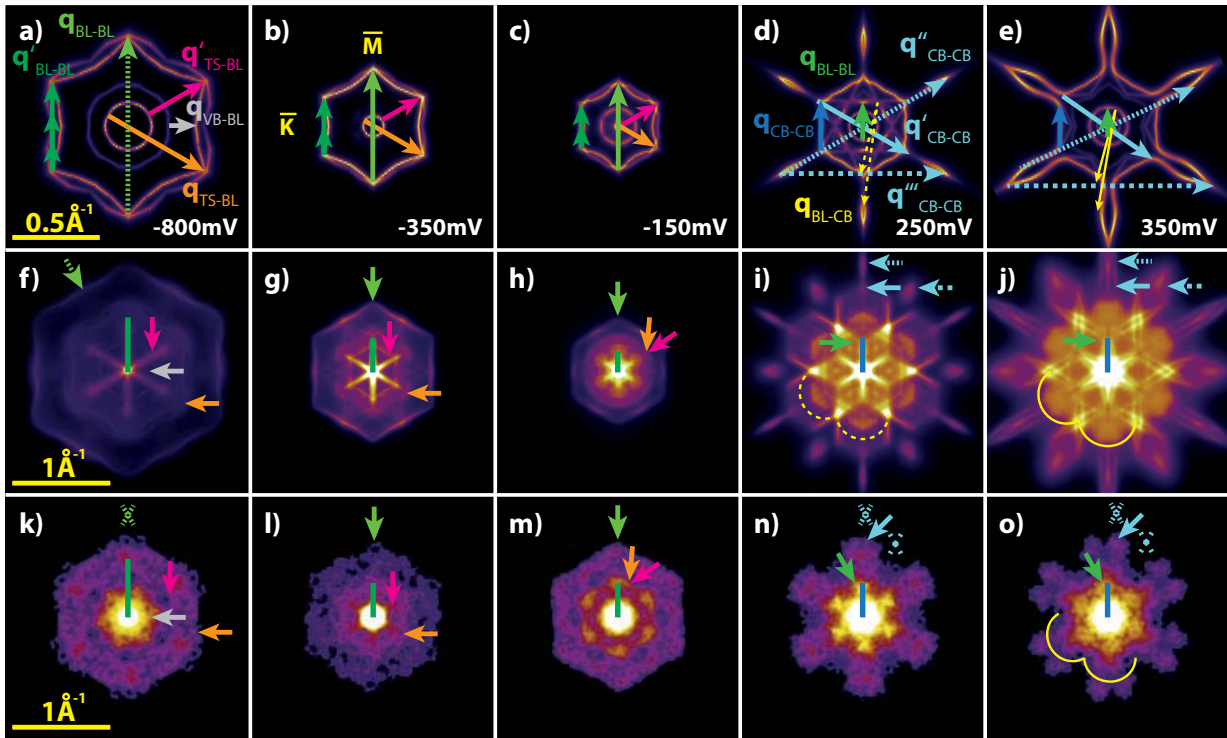
Figure 9.12.: Panel of chosen Bi/Bi$_2$Se$_3$ CECs and the corresponding JDOS and FT-STS maps. a)-e) CECs, **f)-j)** resulting JDOS and **k)-o)** measured FT-STS maps. Arrows and crosses mark **q**-vectors in the CEC and corresponding features in JDOS and FT-STS images. Vectors and features belonging together are coded with the same color. Marker of features/**q**-vectors not visible in the FT-STS map are dotted. Light-green, $\mathbf{q}_{BL-BL}$: Bi-bilayer backscattering. Dark-green, $\mathbf{q'}_{BL-BL}$: Bi-bilayer intraband scattering along the hexagon arm. Pink and orange, $\mathbf{q}_{TS-BL}/\mathbf{q'}_{TS-BL}$: Interband scattering between the Bi-bilayer band and the Dirac cone (same and opposite side). Grey, $\mathbf{q}_{VB-BL}$: Interband scattering between the Bi-bilayer- and Bi$_2$Se$_3$-VB, same side. Light-blue, $\mathbf{q'}_{CB-CB}/\mathbf{q''}_{CB-CB}/\mathbf{q'''}_{CB-CB}$: Bi$_2Se_3$-CB intraband scattering between pockets (pocket edges). Dark-blue, $\mathbf{q}_{CB-CB}$: Bi$_2$Se$_3$-CB intraband scattering along the hexagon arm.

At 250 mV, only two distinct features can be seen in the FT-STS map: Six spots close to $\bar{\Gamma}$ and a flower-like shape oriented in the same direction. The spots seem to be a superposition of a star stemming from scattering along the arms of the hexagonal Bi$_2$Se$_3$-CB ($\mathbf{q}_{CB-CB}$) and scattering between the bilayer bands ($\mathbf{q}_{BL-BL}$). As opposed to the expectation based on the simulation, $\mathbf{q}_{BL-BL}$ features are visible in the measured data. Starting as a full hexagon at 125 mV the feature gets smaller and loses intensity between the edges for higher energies. Latest at 200 mV the edges get disconnected and form six spots, see Fig. B.6. The second feature, the flower like-shape, can be assigned to backscattering of the edges of the Bi$_2$Se$_3$-CB hexagon ($\mathbf{q'}_{CB-CB}$). Scattering channels from the Bi$_2$Se$_3$ CB pockets, $\mathbf{q''}_{CB-CB}$ and $\mathbf{q'''}_{CB-CB}$, as well as scattering between bilayer bands and the Bi$_2$Se$_3$-CB ($\mathbf{q}_{BL-CB}$) are not visible in the FT-STS map.
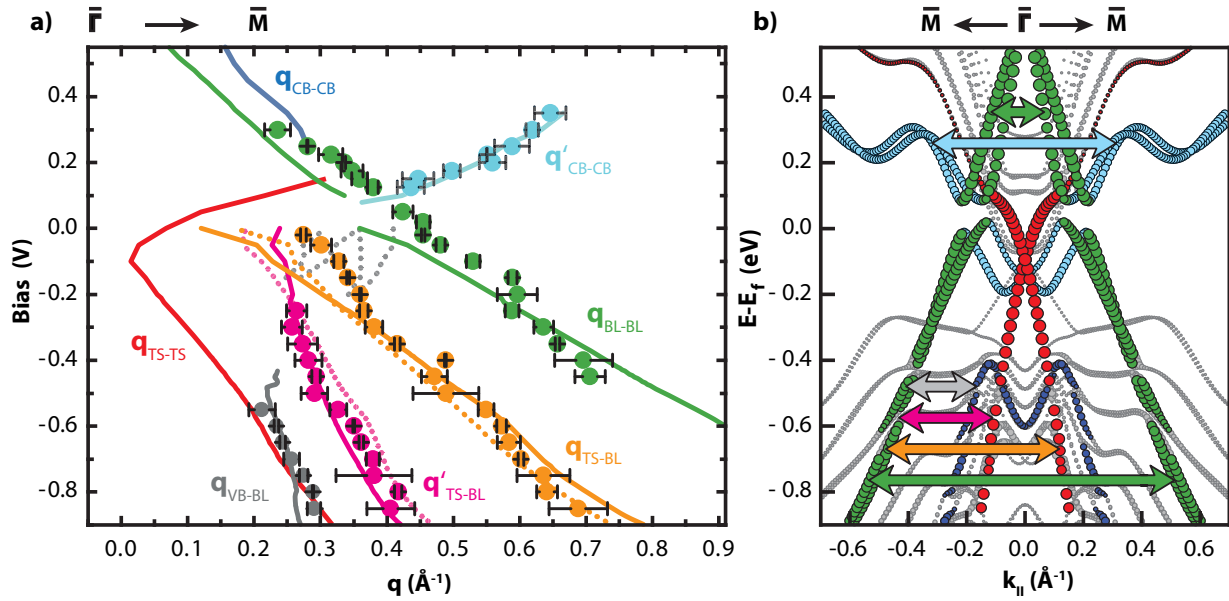
Figure 9.13.: Dispersion of q-vectors of the surface band structure of Bi/Bi$_2$Se$_3$ and identification of observed scattering channels a) Comparison of the dispersion of measured scattering vectors (dots) and of the JDOS simulation (lines/dotted lines) along $\bar{\Gamma}\bar{M}$. Different scattering channels are color coded: Green: Bi-bilayer intraband scattering. Light blue: Bi$_2$Se$_3$-CB intraband scattering. Grey: Interband scattering between the Bi-bilayer and the Bi$_2$Se$_3$-VB. Pink and orange: Interband scattering between the Bi-bilayer and TES (same and opposite side). Dotted and full lines describe scattering channels depending on the relative spin-orientation of the bilayer bands and the TES . Grey-dotted lines: Various interband scattering channels of the Bi$_2$Se$_3$-CB. Red line: Intraband scattering of the TES , forbidden due to backscattering. **b)** DFT calculated band structure along $\bar{\Gamma}\bar{M}$, including the observed scattering vectors **q** as arrows. Colors correspond to (a).

The identification of the flower is strengthened by the FT-STS map at 350 mV. The flower splits at the edges, just as one would expect from a look at the CEC. Here, the Bi$_2$Se$_3$-CB pockets get larger at higher energy and connect to the Bi$_2$Se$_3$-CB hexagon. Again, other features from scattering between the pockets ($\mathbf{q}''_{\text{CB-CB}}$ and $\mathbf{q}'''_{\text{CB-CB}}$) cannot be seen. While the six spots exhibit a much weaker intensity than before, another flower-shape feature occurs. This can be identified as one of the features not visible at lower energies, scattering between the bilayer bands and the Bi$_2$Se$_3$-CB ($\mathbf{q}_{\text{BL-CB}}$).

The dispersions of all scattering vectors along $\bar{\Gamma}\bar{M}$, as identified above, have been extracted from the FT-STS maps as well as the JDOS maps and are plotted in Fig. 9.13 (a) as dots and lines, respectively. To verify the identification, other theoretically possible **q**-vector dispersions are plotted for comparison. For an optimal visibility, only bands are plotted that are in the range of the experimental vectors. The agreement of experiment and theory, with respect to the **q**-vector length and the dispersion, is remarkable. Most of the features can be identified without doubt.

Below E_F, the Bi-bilayer bands play a dominant role. All $\mathbf{q}$-vectors found are linked to that band, either by scattering within the bilayer band ($\mathbf{q}_{\text{BL-BL}}$) or by interband scattering: with the Bi_2Se_3-VB ($\mathbf{q}_{\text{VB-BL}}$) or with the TES ($\mathbf{q}_{\text{TS-BL}}$ and $\mathbf{q}'_{\text{TS-BL}}$). Because of the Rashba-type spin-splitting of the Bi-bilayer bands, theory provides two possible dispersions (full and dotted lines) for $\mathbf{q}_{\text{TS-BL}}$ and $\mathbf{q}'_{\text{TS-BL}}$. In principle, one of the two dispersions is ruled out by spin-conservation. However, the difference in $\mathbf{q}$-vector length is too small to exclude one of the possibilities. Above E_F, intraband scattering of the bilayer bands can still be observed, but it is only accompanied by scattering involving the Bi_2Se_3-CB ($\mathbf{q}'_{\text{CB-CB}}$).

The presence of $\mathbf{q}$-vectors involving the TES, i.e. interband scattering with the Bi-bilayer bands ($\mathbf{q}_{\text{TS-BL}}$ and $\mathbf{q}'_{\text{TS-BL}}$), proves the localization of the TES at the surface of the bilayer. Hence, the influence of Bi_2Se_3 bulk bands should be reduced, resulting in a greater linearity of the TES. While this cannot be investigated directly, as no intraband scattering of the TES was observed, an analysis of the dispersion of the interband scattering bands $\mathbf{q}_{\text{TS-BL}}(E)$ and $\mathbf{q}'_{\text{TS-BL}}(E)$ answers this question. The linearity of these bands, together with the linearity of the bilayer backscattering band $\mathbf{q}_{\text{BL-BL}}(E)$, proves an overall linear dispersion of the TES for a large energy range, from -0.2 eV to at least -0.9 eV. This is within the energy range where Bi_2Se_3 bulk bands are present (below -0.4 eV). Therefore, the 2D TES of the $\text{Bi}/\text{Bi}_2\text{Se}_3$ system indeed exhibits an enhanced isolation from Bi_2Se_3 bulk bands.

Further Discussion

Besides the overall agreement of theory and experiment, there are some discrepancies and peculiarities that should be discussed in greater detail in the following:

1. The measured vectors identified as scattering between the bilayer bands and the Bi_2Se_3-VB ($\mathbf{q}_{\text{VB-BL}}$) are very close to theoretical values for backscattering within the TES ($\mathbf{q}_{\text{TS-TS}}$). The observation of such backscattering would question the topological protection of that state. However, the dispersion of the experimental $\mathbf{q}$-band matches better with the theoretical dispersion of scattering between the bilayer bands and the Bi_2Se_3-VB ($\mathbf{q}_{\text{VB-BL}}$).

2. Above -200 mV the experimental and theoretical values start to deviate for scattering between the bilayer bands and the TES ($\mathbf{q}_{\text{TS-BL}}$). -200 mV marks the onset of the Bi_2Se_3-CB. Therefore, various new scattering channels are possible and the observed feature might now stem from scattering with this band. The scattering channels that involve the Bi_2Se_3-CB and that are within the range of the experimental data are plotted as dotted grey lines. None of these match the experimental dispersion.

However, the visible feature might be a superposition of all these channels within that energy range. Unfortunately, the DFT calculations seem to fail quantitatively around E_F[10]. This might be caused by the approximation in the SLAB framework or might be due to a stronger or weaker interaction with the substrate. In any case, the participating bands cannot be identified exactly. However, there are two arguments against an involvement of the Bi$_2$Se$_3$-CB. First, the shapes of the observed features do not change or wash out, they get more pronounced and defined. Second, a similar deviation of the dispersion is also visible for scattering within the bilayer ($\mathbf{q}_{BL-BL}$). This deviation cannot be caused by a superposition of scattering vectors, as the distance between opposite bilayer bands is the largest in $\mathbf{k}$-space. No other scattering channel can provide features with such large $\mathbf{q}$-vectors. Also, a shift or change in the dispersion of the bilayer bands can be excluded by a comparison with ARPES data (see Fig. 9.5). Hence, the shift must have another origin than from the bare dispersion of the bands.

One possible explanation for the deviation is a systematic error in the measurement technique. The onset of the deviation at -200 mV occurrs together with the onset of the Bi$_2$Se$_3$-CB and an increase of the FT-STS signal quality: below -200 mV the features are less pronounced than above. The presence of this bulk band seems to push the surface states further into the vacuum, thereby increasing the strength of the features in the FT-STS map. Since the constant-current mode was used for the STS measurements, the higher conductance leads to a retraction of the tip, which might slightly reduce a possible tip induced band bending and might cause the band structure to shift up in energy. Tip induced band bending is indeed a common effect present on samples with a low LDOS at the surface (semiconductors, TIs...[32, 204]).

However, at -400 mV, the onset of the Bi$_2$Se$_3$-VB, no corresponding effect is observed. While the FT-STS quality increases in the presence of the bulk band, a jump cannot be observed. Of course, due to the larger number of states involved in tunneling, the influence of the tip's electric field might be reduced at this energy.

3. Another peculiarity is the vanishing of the bilayer backscattering band $\mathbf{q}_{BL-BL}(E)$ below -500 mV. Here, the onset of the Bi$_2$Se$_3$ -VB introduces new scattering channels to the system ($\mathbf{q}_{VB-BL}$). These are stronger than predicted and seem to suppress the intraband scattering of the bilayer[11].

---

[10]While JDOS and FT-STS maps match very well for almost all energies, they diverge close to the hybridization gap. E.g. compare maps at -100 mV, Figs. B.6 and B.7.

[11]However, $\mathbf{q}_{BL-BL}$ might not be completely suppressed. The vacuum density of states measured by STS is dominated by states with small $\mathbf{k}_{\parallel}$, which damps the QPI for large $\mathbf{q}$. The absence of $\mathbf{q}_{BL-BL}$ might contribute to a smaller scattering probability and reduced sensitivity of STS.

4. Above E_F, there is an energy range without features. This gap has about the same size and location as the hybridization gap predicted by theory and is consequently identified with it.

5. Finally, the experimental and theoretical values for one of the scattering channels of the Bi_2Se_3-CB, $\mathbf{q}'_{CB-CB}$, match very well. The absence of the other channels, $\mathbf{q}''_{CB-CB}$ and $\mathbf{q}'''_{CB-CB}$, might again be caused by the reduced sensitivity of STS for large $\mathbf{q}$-vectors. However, it is worth mentioning, that, when the Bi_2Se_3-CB hexagon and pockets are connected, the visible feature cuts off exactly where the dispersion of the band changes from positive to negative (when $\mathbf{q}'_{CB-CB}$ and $\mathbf{q}''_{CB-CB}$ meet). This cannot be explained with the model used for the simulation. But the spin-polarization of the simulated bands is only modeled by a simple Rashba approach. The real system might exhibit a more complicated behavior of the spins, where $\mathbf{q}''_{CB-CB}$ and $\mathbf{q}'''_{CB-CB}$ are ruled out, due to spin-conservation.

9.4. Summary and Outlook

The central hypothesis, that bismuth can be grown as a bilayer on Bi$_2$Se$_3$, has been proved successfully. Besides a simple proof of concept, a temperature dependent study was conducted to optimize the bilayer growth, concerning relaxation and point defects. The van-der-Waals gap between the bilayer and the substrate increased far more than assumed at the beginning, due to pseudomorphic growth. The large distance between bilayer and substrate results in a weaker interaction of the electron states. This can already be seen by the shape of the bilayer islands. These are more round than the triangular islands on substrates with a smaller van-der-Waals gap in between [41, 193].

DFT predicts a relocation of the TES from the substrate to the surface of the bilayer. The relocation is confirmed by an analysis of FT-STS maps that identified scattering vectors involving the TES. The dispersions of the bands involving the TES are measurable over a large energy range, pointing to an overall isolation of the TES from bulk bands. The linearity of the involved bands emphasize this point. However, the TES is not completely isolated. FT-STS detects scattering with the Bi-bilayer bands.

The presence of the TES is not the only change to the bilayer's electronic structure. A charge transfer from the bilayer to the substrate moves the bilayer bands up in energy by about ~ 0.6 eV. The resulting electric field leads to a Rashba-type splitting of the bands and to a band bending close to the surface, introducing quantum well states originating from bulk conduction and valence bands. These hybridize with the original bilayer bands. Consequently, a hybridization gap opens close to E_F along $\bar{\Gamma}\bar{\text{M}}$.

Such a hybridization gap has been found for Bi-bilayers on Bi$_2$Te$_2$Se, too [41]. Here, Kim *et al.* propose that the hybridization gap of the bilayer is hosting the 1D TES, since the original bilayer gap of the system is closed, due to the influence of the substrate. This argument is supported by an increased density of states at the edges of the sample, measured by STM, just in the energy range of the hybridization gap.

However, the 1D TES is supposed to rely on a gap opening in all directions, which is not the case for the hybridization gap of Bi/Bi$_2$Te$_2$Se . Hence, not only the energetic position, but the existence of 1D TES remains an open question. This is also the case for BiBi$_2$Te$_3$ [40], that, too, exhibits a closed bilayer gap and only a partially opened hybridization gap.

In contrast, according to DFT, the coupling of the Bi-bilayer to the Bi$_2$Se$_3$ substrate is small enough to preserve the original bilayer gap. Moreover, the band inversion of the bilayer bands remains intact. Hence, the Bi/Bi$_2$Se$_3$ is so far the only system investigated that should actually host 1D TES.

a) TI island with spin-polarized 1D TES channels

b) tip — STS intensity map measured with a non-spin-polarized tip

c) tip — STS intensity map measured with an in-plane spin-polarized tip
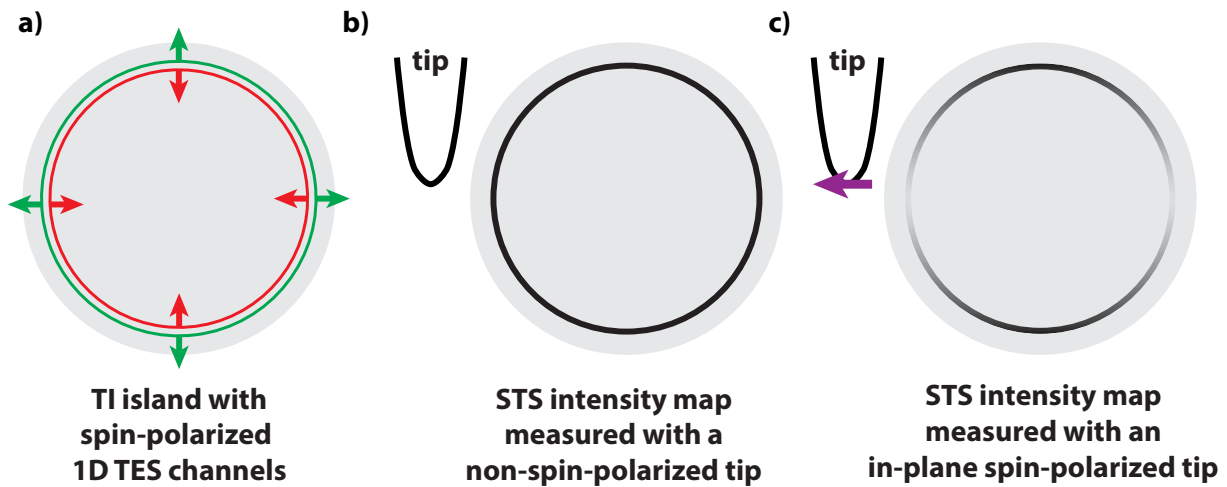
Figure 9.14.: Proposal for an SP-STM measurement of 1D TES. a) Island with 1D TES. Green and red denote 1D channels with opposite momentum. **b)** Edge state intensity expected for an STS map taken with a non-spin-polarized tip. The edge state exhibits a homogenous LDOS (black) with equal contributions from both channels. **c)** With an in-plane spin-polarized tip the intensity should vary. When the spin polarization of the tip is in parallel/anti-parallel configuration to the 1D TES, the parallel oriented TES contributes fully to the measured intensity, while the TES with anti-parallel spin orientation provides no contribution (grey). In perpendicular orientation, both TES contribute equally to the measured intensity, leading to an overall higher intensity than in parallel/anti-parallel configuration (black, see text).

As one can see, the existence of 1D TES of Bi-bilayers grown on different samples is discussed controversially. One problem with the experiments conducted so far is, that the topological nature of the edge states was determined by indirect evidence: the extension of the state away from the edge and the change of this extension depending on energy.

A direct proof is still missing. But it could be realized with a SP-STM measurement of such samples. With SP-STM it should be possible to probe the helical spin behavior of the 1D TES. For this purpose, STS maps of the edge have to be taken at energies where the TES exists. When taken with a non spin-polarized tip, the 1D TES leads to an increased homogenous intensity at the edges [205]. But taking into account simple spin selection rules, the intensity should vary when a tip with a finite in-plane spin-polarization is used. Here, the intensity depends on the relative orientation between the polarization of the tip and the polarization of the two TES channels, see Fig. 9.14.

When the tip polarization is in parallel orientation to one of the TES channels, the contribution of this channel to the measured intensity is maximized. While the tip polarization is in parallel orientation to one TES channel, it is in an anti-parallel orientation with the polarization of the second TES channel. Due to the orthogonal spin orientation of tip and TES channel, the contribution of this channel to the measured intensity is zero.

When the tip polarization is orientated perpendicular to the spin polarization of the TES channels, each channel contributes to the measured intensity with $1/\sqrt{2}$ of the maximum contribution of a single channel. The sum of these contributions is larger than the sum for the parallel/anti-parallel case, leading to an over all increased intensity.

Therefore, for an STS map taken at the right energy with an in-plane spin-polarized tip, the measured intensity at the bilayer edge should not only be increased, but vary with the orientation of the edge. Moreover, maxima and minima should depend on the actual in-plane spin-polarization of the tip: When the spin polarization of the tip is rotated in-plane, e.g. by a magnetic field, the extrema should rotate with the tip polarization. And the extrema should vanish, when the polarization of the tip is rotated out-of-plane.

Due to the preserved original band gap of Bi-bilayers grown on Bi_2Se_3, this system is the most promising, if not the only candidate for such an experiment. While the VT-STM was the ideal system for the presented growth study, the proposed experiment has to be conducted with a system capable of applying an in-plane magnetic field to the tip in order to enable a change of its magnetization.

The Role of FT-STS

The detailed study of the electronic structure of Bi/Bi_2Se_3 was only possible by utilizing the FT-STS technique. To my knowledge, the investigated system is the most complex one studied so far by FT-STS, counting the number of involved electron bands and the number of distinct scattering vectors [74, 150, 206–210]. A fundamental problem with such a complex system is the identification of the origin of the detected scattering vectors. To this end, the electronic structure of the system must be either measured by ARPES or predicted by theory. A comparison of possible scattering vectors (deduced from ARPES/theory) and actually measured scattering vectors (FT-STS) then allows to identify the origin of scattering vectors and provides information about the involved scattering matrix.

However, a complete identification of the observed FT-STS features was only possible by simulating the FT-STS maps with the JDOS approach. The simulation allowed to identify superpositions and to definitely verify the origin of the observed features.

The direct visual comparison of measured and simulated maps turned out to be very useful. Enhanced, damped or suppressed channels can be identified easily. However, the comparison can be taken one step further. By comparing the feature intensities quantitatively, an estimate of the scattering probability can be derived and will help identifying the factors influencing it.

While the present study was conducted using a VT-STM with a flow cryostat (and the quality of the data is remarkable for such a system), for such measurements an STM within a bath-cryostat is explicitly recommended. The noise-level of a bath-cryostat system is significantly lower and in general it is far more stable, see section 5.1.3. Moreover, the number of possible tip changes or crashes is reduced[12].

Even in case of VT-STM measurements, FT-STS maps have been proven to be an excellent tool to investigate complex band structures with defined bands (e.g. surface state bands). Typically, STM and ARPES are used in combination for a comprehensive insight into topographic (STM) and electronic (ARPES) features of a sample. FT-STS based investigations offer the advantage that electronic band structures can be investigated not only below but also above E_F, thereby providing additional information on the scattering probability between individual bands.

---

[12]This will enable the use of the constant-height mode for the tip, a mode that was not used in this study in order to prevent crashes.

10. Conclusion and Outlook

It was the intention of this thesis to explore the consequences of topological protection of the edge states of topological insulators in the presence of disorder; and to develop methods of manipulation that allow a tailoring of a given TI for a particular purpose. Three of the presented experiments deal with the influence of TRS preserving changes:

TRS Preserving Influences

For TlBiSe$_2$ it has been shown that the TES can be shifted into the bulk by surface disorder. It is not destroyed by a TRS preserving perturbation, unlike trivial surface states. This is a direct consequence of its topological origin. Among the intrinsic spin-polarization of the TES and the large band gap of some of the known TIs, including TlBiSe$_2$, it is this robustness, that makes TIs potential candidates for providing spin-polarized currents in commercial devices. A large band gap ensures that also at room temperature a current is just carried by the spin-polarized TES. And the robustness allows applications in ambient conditions, where surfaces get contaminated.

The most promising TIs right now are bismuth based chalcogenides, e.g. Bi$_2$Se$_3$ and Bi$_2$Te$_3$. These systems exhibit a large band gap and a single Dirac cone with an almost linear dispersion. Using the example of PbBi$_4$Te$_7$, it has been experimentally shown, that by adding group IV elements to the composition, the size of the bulk band gap, as well as the shape of the Dirac cone and the position of the Dirac point can be changed, while the topological nature of the system is conserved. Therefore, the stoichiometric variation provides one path of tailoring TIs. Depending on the type of composition and surface termination, also the localization of the TES can be influenced. E.g. for PbBi$_4$Te$_7$ with quintuple layer termination, the TES is located in the slab below the surface QL.

Another path of manipulation has been investigated by growing a Bi-bilayer on Bi$_2$Se$_3$. Here, the TES of the substrate is shifted to the new surface of the system. Therefore, it is more isolated from the bulk bands of the substrate. The Dirac cone exhibits a linear dispersion for an energy range of at least 0.7 eV.

Accomplishing these results was only possible by an analysis of $\mathbf{q}$-vectors based on FT-STS maps. Together with the method developed to simulate FT-STS maps, it was possible to investigate the interaction between single bands, learn about the involved scattering matrix elements and deduce the band dispersion.

The manipulation methods investigated in these three experiments allow a wide range of adjustments, as the TES responds to all applied changes. In fact, besides the protection of its bare existence, the TES is quite sensitive to any kind of enviromental changes. And it is striking that in all three experiments, the localization of the TES is somehow changed. This can be seen from a positive point of view, i.e. the great potential to tailor and protect the TES. On the other side, this may also have some negative consequences: In order to utilize the TI's potential to generate spin-polarized currents, the electrons have to be injected into a material working as a conductor. The TI and the conductor have to share an interface. However, introducing an electrode to the edge of a TI might disturb the surface to such an extent, that the TES shifts into the bulk. Then the electrode has no direct access to the TES anymore.

Especially for the promising systems Bi_2Se_3, Bi_2Te_3 and their related compounds, this interface issue is severe. Deposited metals typically cluster on the surface, e.g. Fe (see Fig.6.3) or Al (Fig.A.2). Consequently, electrodes based on these materials will lack an ordered structure. Establishing an interface with the most promising conductor of spin-polarized currents, i.e. graphene, might fail already with the attempt of introducing any kind of graphene sheet to the surface. The typical method to grow graphene, cracking of hydrocarbon gas stuck to the substrate surface, makes use of annealing temperatures higher than 700 K[1] [212]. However, the TIs described disintegrate already at much lower temperatures, e.g. Bi_2Se_3 at around 470 K (see Fig. A.1 h). It is therefore of great interest to find new subclasses of TIs exhibiting the same advantages as the described systems, such as a large band gap and a single topologically protected Dirac cone with linear dispersion, but forming well-defined interfaces with electrodes that do not perturb the TES too much. Furthermore, it should be thought of methods that reduce the TES mobility or even pin its localization.

Surface Doping and Its Consequences

Another general effect limiting the application of TIs is the band bending effect induced by surface doping. For Fe atoms deposited on Bi_2Se_3, this thesis has proven exclusion of this effect by incorporating the adatoms into the surface quintuple layer, while the magnetic moments of the Fe atoms are conserved. Hence, this method allows for investigating the interaction of surface magnetic impurities with the TES without any secondary effects disturbing the measurements.

---

[1]Alternative methods are thermal decomposition of carbide or segregation of carbon atoms from the bulk. However, the systems presented are neither carbides nor do they contain great amounts of carbon [211].

The absence of the band bending seems to be critical for this interaction. So far, the TRS breaking behavior of magnetic impurities was observed for bulk doped crystals [102, 150, 213, 214] but not for surface doped samples. This could be interpreted as a principal difference of the influence of bulk and surface doping over topological protection, which is in contradiction to theoretical predictions [215, 216].

In fact, due to a Ruderman-Kittel-Kasuya-Yosida (RKKY) interaction[2] between magnetic surface impurities, a magnetic coupling should already be established at much lower doping concentrations than needed for bulk doping[3]. This RKKY coupling has now been observed for a Bi_2Te_3 surface doped with Mn [219]. However, it was only verified for a small energy range and for very small amounts of deposited Mn (1 % of a monolayer). At 2 % Mn coverage, the effect vanished. This was explained by band bending induced effects: A stronger warping of the topologically protected Dirac cone that suppresses the texture of the coupling; and the shift of the bulk conduction band below the Fermi level, which changes the nature of electrons from 2D (TES electrons) to 3D (bulk electrons) and leads to a faster decay of coupling strengths between the magnetic impurities[4]. With an incorporation of the atoms into the surface, the effect should occur for larger energy ranges and higher densities of magnetic atoms. Such an experimental result would confirm the hypothesis, that magnetic interactions are influenced by the presence of band bending.

The Search for a Prototypical 2D Topological Insulator

The properties and the potential of 3D TIs get more and more explored by experiment. This is not the case for 2D TIs, since there are no systems available that are easy to handle or can act as model systems (large band gap, sharp localization of the TES). The Bi-bilayer promises some potential to take on this role, but the substrates used so far to grow the bilayer lead to a disappearance of the bilayer band gap. DFT calculations have shown that the gap remains open for Bi-bilayers grown on Bi_2Se_3. However, it was not possible to verify the conserved gap by the experimental techniques used in this thesis. ARPES cannot access the gap, it is located above Fermi level. And the intensities of QPI patterns at that energy were too weak to be analyzed. But an SP-STM measurement of the sample's edge at the corresponding energy could directly prove the existence of the 2D TES.

---

[2]Here, the magnetic exchange between impurities is mediated via substrate electrons.

[3]Also, the doping threshold to establish the RKKY interaction on TIs is predicted to be smaller than on other surfaces, e.g. Co atoms on Cu(111) [215, 217, 218]. The 2D nature of the TES electrons that mediate the interaction leads to a slower decay of the RKKY coupling strength as the electrons cannot dissipate into the bulk. This allows larger distances between magnetic impurities, nanometers instead of ångstroms. Therefore, a lower impurity density is needed to establish remanent magnetization.

[4]This means for 2 % coverage the average distance between Mn atoms is too large to establish a RKKY interaction, although this distance is smaller than for samples where only 1 % of Mn is deposited.

The New VT-STM and Its Qualities

The STM investigations described here were conducted with a new VT-STM, that combines fast introduction and exchange of samples with an optimized stability. It was this optimization that allowed a sample characterization not only with respect to step heights or lattice constants, but also concerning electronic properties, e.g. the interaction of electron bands. In fact, the band structure of the Bi-bilayer on Bi_2Se_3 and its interactions were the most complex system investigated so far by a $\mathbf{q}$-based analysis of QPI patterns.

This shows the potential of VT-STMs and STMs in general, also for spectroscopic investigations. While ARPES is the best tool to directly investigate the band structure of a given system, the interaction between bands cannot be investigated. In addition, a high-quality ARPES map depends on a minimum structure size and is limited to energies below the Fermi level. An STM based $\mathbf{q}$-vector analysis allows the investigation of smaller structures at energies below and above the Fermi level. It is the high spatial resolution that makes STS based methods the prime spectroscopic probes for nanostructures and their interactions, e.g. the RKKY interaction of magnetic impurities, Kondo resonances or the protected edge states of 2D topological insulators.

Part III.

Appendix

A. Additional Notes on Fe/Bi$_2$Se$_3$

Overview of Different Annealing Temperatures

Fig. A.1 gives an overview of Bi$_2$Se$_3$ surface topographies before and after Fe deposition, as well as after additional annealing. Only a few Se vacancies are visible on the bare Bi$_2$Se$_3$ surface right after cleaving the crystal (a). Deposited Fe is primarily distributed as single atoms (b). Note that the image quality in (b) is considerably enhanced, most likely due to the enhanced substrate density of states induced by surface doping.

Annealing to 240 K (c), forces less than 1 % Fe atoms to move into the substrate, substituting atoms of the first Bi layer (type A defects). Annealing to 260 K (d) leads to a slightly increased number of subsurface Fe atoms (type A) and clusters form on the surface. Exposure to 300 K (e), results in a drastic drop to $\approx$ 15 % of the density of Fe atoms on the surface compared to the initial coverage, with the same amount of subsurface Fe atoms. Most of these can be categorized as type A. Type B defects (Fe substituting atoms of the second Bi layer) occur in very small numbers. Also, the number of small clusters increased.
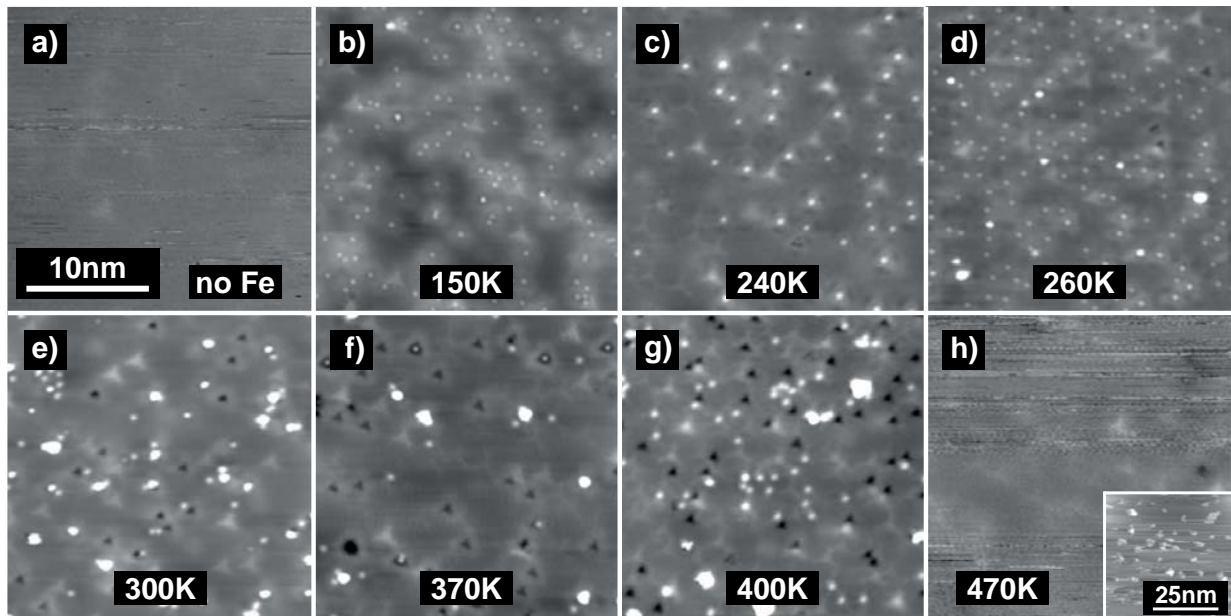
Figure A.1.: Overview of surfaces of Bi$_2$Se$_3$ after Fe deposition and annealing. a) Surface right after cleaveng the crystal. **b)** Surface after depositing 1 % Fe at $\leq$ 150 K. **c)-h)** Surfaces after annealing to given temperatures. The inset in (h) shows a larger area of the sample in the main image. On a large scale the surface is covered with patches of material that can only originate from the sample itself. All images were measured with U_{B}= 0.25 V, I= 200 pA.
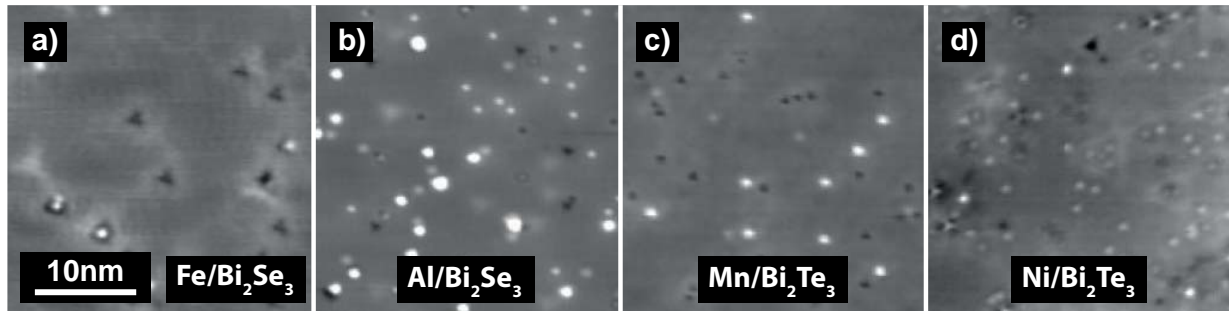
Figure A.2.: Surface doping with other materials. a) Fe/Bi$_2$Se$_3$ after annealing to 370 K. $U_B=$ 0.25 V, $I=$ 200 pA. **b)** Al on Bi$_2$Se$_3$ deposited at $\leq$ 150 K, then annealed to 260 K. $U_B=$ 1 V, $I=$ 50 pA. **c)** Mn on Bi$_2$Te$_3$, deposited at $\leq$ 150 K. $U_B=$ 1 V, $I=$ 20 pA. **d)** Ni on Bi$_2$Te$_3$, deposited at 12 K. This sample was measured and prepared in a bath cryostat system with a base temperature of 4.2 K. $U_B=$ 0.2 V, $I=$ 1 nA.

The percentage of adatoms and the overall percentage of subsurface Fe atoms remains the same after annealing to 370 K (f). However, the percentage of type B subsurface Fe atoms increases. The clusters are larger, but reduced in number. When annealed to 400 K (g) almost all subsurface Fe atoms seem to be of type B and the clusters are even larger. However, the tip stability is reduced too much to measure STM images on a larger scale. Still some Fe adatoms remain on the surface. After annealing to 470 K the surface shows a similar topography as in the freshly cleaved case (h). Also the tip exhibits the same instability. Clusters and adatoms cannot be found and Fe subsurface atoms are almost completely gone, too. In some regions the surface is covered with material unlike the clusters seen before (inset). The only possible source for this material is the sample itself. It can be concluded, that the crystal starts to disintegrate at $\geq$ 470 K.

Surface Doping of the Bi$_2$X$_3$ Family

Migration into the surface by annealing during or after deposition is not a unique feature of the Fe on Bi$_2$Se$_3$ system. During my Ph.D. time I tested different adatoms (Fe, Al, Mn, Ni) on different substrates (Bi$_2$Se$_3$, Bi$_2$Te$_3$). This section is meant to give a small summary of the observed doping to prove the general applicability of this technique to pseudobinary calchogenides without going into further details concerning specific adatom behavior (Since investigating the migration was not the primary goal of the experiments described in the following passages.).

Al deposited on Bi$_2$Se$_3$ behaves similar to Fe, see Fig. A.2 (b). At low temperatures the adatoms remain on the surface. When annealed, some adatoms diffuse into the surface and clusters can be found on top. As in the case of Fe, it cannot be clarified if these clusters are made of the deposited material or material from the substrate.

Mn deposited on Bi_2Te_3 (c) diffuses already into the substrate at a deposition temperature of ≤ 150 K. The depressions are triangular but have a smaller apparent depth than in the case of Fe. These were identified as Mn atoms on Bi sites for bulk doped Bi_2Te_3 [102]. The bulk diffused Al atoms exhibit a greater resemblance to their Mn counterparts than to the Fe subsurface atoms. Since for Mn and Fe the deposited atoms substitute Bi, this is assumed for Al, too.

Ni diffuses already into the Bi_2Te_3 substrate at 12 K (d). Also the mobility of the atoms remaining on the surface is increased. Some adatoms are located on top of in the bulk diffused Ni sites. This behavior was found for Fe only at annealing temperatures of 370 K and higher. Even though the mobility for Ni atoms seems quite high, no clusters were found on the surface. This could be an indication that the clusters in general are not formed by adatoms, but by substituted bismuth.

B. Additional Notes on Bi/Bi$_2$Se$_3$

Growth of Bismuth on Bi$_2$Se$_3$

First Bilayer - Large Temperature Range

Fig. B.1 gives an overview over bismuth films grown on Bi$_2$Se$_3$ with coverages of $\sim$50 %, $\sim$150 % and $\sim$250 % of a bilayer, each grown at different temperatures: 250 K, 300 K, 370 K and 450 K. Temperatures of 270 K - 450 K lead to rough films of percolating Bi with vacancy islands in between. Only at a growth temperature between 200 K and 270 K a smooth, closed film can be grown for the first layer. Moreover, at this temperature, the second and following layers are smooth but exhibit surface reconstructions. The first (and second) layer can be identified as Bi(111)-bilayers. The identification is based on lattice constants, evaporator calibration and electronic structure (see Fig. 9.1).

The nature of the films grown at 270 K-450 K is unknown. However, the number of possible structures can be narrowed down by a comparison of the area coverage with the amount of deposited material. The deposited material can be calculated from the evaporator parameters. In the following, the coverage is given in percentage of closed Bi(111)-bilayers. In case of bilayer growth the ratio between coverage and deposited material is 1:1, growth of (111)-monolayers would result in a ratio of 2:1, due to their half lateral atom density, and growth of {012}-films would result in a ratio of 1.25:1 (single-layer) or 0.6:1 (doublelayer). These ratios have been analyzed for growth at 250 K, 300 K and 450 K, Tab. B.1.

Temperature	Area coverage	Material deposition	Ratio
250 K	60 %	60 %	1:1
	155 %	150 %	1.05:1
300 K	50 %	40 %	1.25:1
	140 %	120 %	1.15:1
450 K	55 %	55 %	1:1
	145 %	160 %	0.9:1

Table B.1.: Growth of the 1st Bi layer at 200 K, 300 K and 450 K: Area coverages and material deposited (in percent) normalized to one (111)-bilayer.
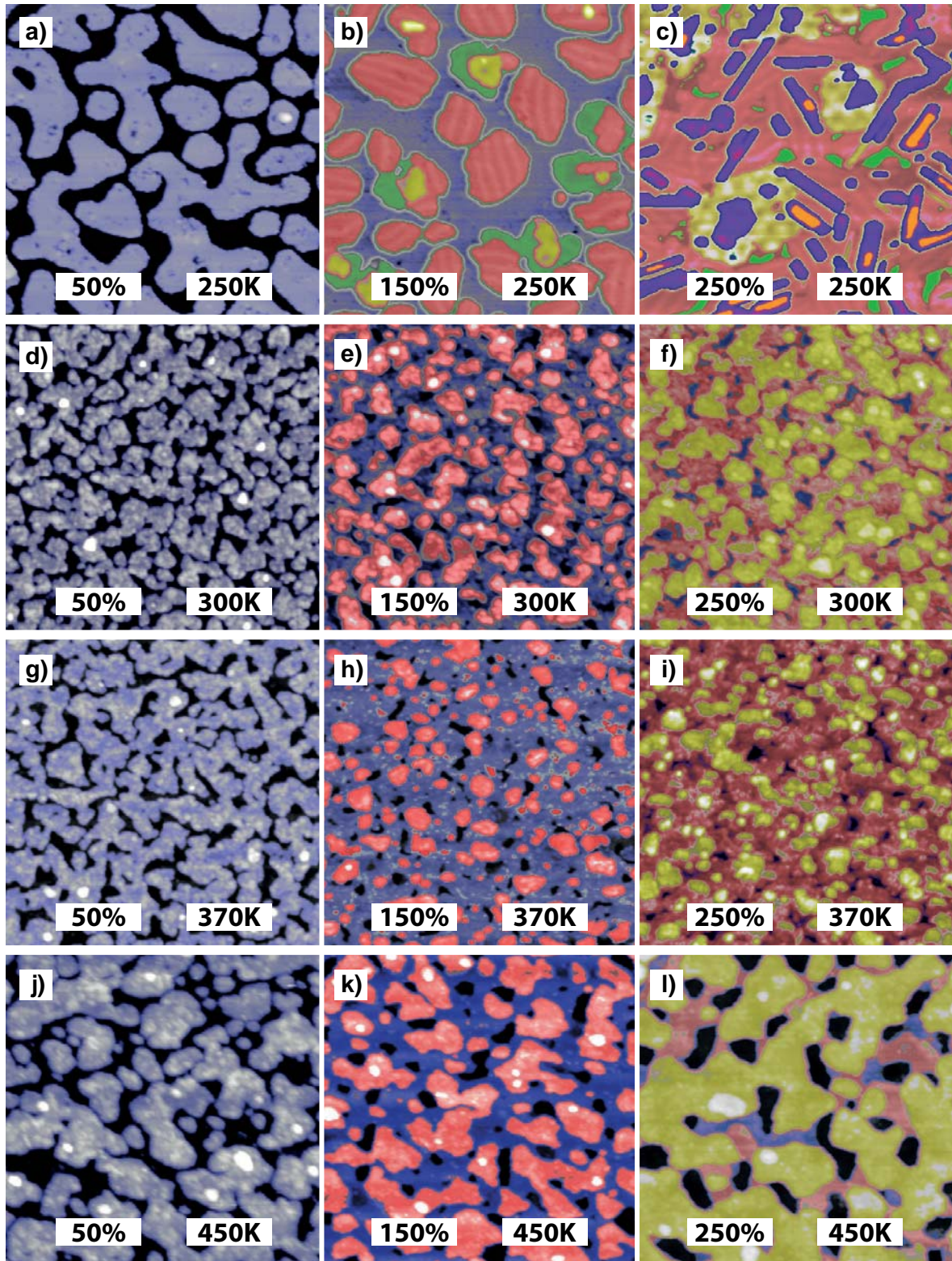
Figure B.1.: Temperature dependent growth of Bi on Bi$_2$Se$_3$. In the given examples only at 250 K defined layers can be grown. Coverages and temperatures as given in the images. The layers are color coded for increased visibility: From bottom to top: black, blue, green, red, yellow, purple, orange. Dark shades of color represent smaller height, bright shades represent greater height. For all images: U_B= 1 V, I= 20 pA, 100 nm x 100 nm.

Indeed, samples grown at 250 K and 450 K exhibit a ratio of (almost) 1:1. In contrast, films grown at 300 K deviate from a 1:1 ratio and tend towards the ratio of {012}-single layers. Interestingly, for samples grown at 300 K and 450 K the ratios for 50 % and 150 % coverage differ. This is the second indication for a phase change after the observed change of layer height described in the main part (Fig. 9.2). Based on this analysis, (111)-monolayers can be excluded as possible structures but not the {012}-phase films. The ratio change between different coverages might even indicate a structural change from (111)-bilayers to {012}-single-layers (450 K) or vice versa (300 K).

Second Bilayer

Upon closer examination, the one-to-two bilayer regime is dominated by islands with different heights, see Fig. B.2. At a coverage of less than 150 % of a bilayer, *low-level islands* with a height of 4.7 ± 0.1 Å dominate the surface, colored in green. Above a coverage of 150 % *high-level islands* with a height of 6.3 ± 0.1 Å dominate, colored in red. The nature of these islands can again be determined by a comparison of the amount of deposited material and the areal coverage of the islands.

Low-Level and High-Level Island Nature

Fig. B.2 presents topography images of three different preparations. In (a) 108 % of the material needed for one bilayer is used, in (b) 117 % and in (c) 150 %. For all three preparations the area covered by islands differs from the values expected from the amount of the deposited material. The deviation is even different for all depositions, see Tab. B.2.

Deposition via evaporator[†]	Coverage of 1st bilayer[‡]			Ratio low/high	Deposition via coverage
	Low	High	All		
108 %	8.7 %	3.0 %	11.7 %	2.9 : 1	107.3 %
117 %	18.8 %	7.6 %	26.4 %	2.5 : 1	117.0 %
150 %	12.5 %	41.2 %	55.5 %	0.3 : 1	148.3 %

Table B.2.: Comparison of the amount of deposited material and coverage of the 2nd Bi-bilayer islands. † The first column gives the amount of deposited material calculated from evaporator parameters in percentage needed for one bilayer. ‡ Second to fourth column give areal coverages of the first bilayer by low-level islands, high-level islands and the coverages in total. The fifth column gives the ratio of low-level to high-level island coverage. The sixth column gives the amount of deposited material calculated from coverage, assuming low-level islands are Bi(111)-monolayers and high-level islands are Bi(111)-bilayers. Now the depositions calculated from evaporator parameters and coverage match within a margin of 2 %.
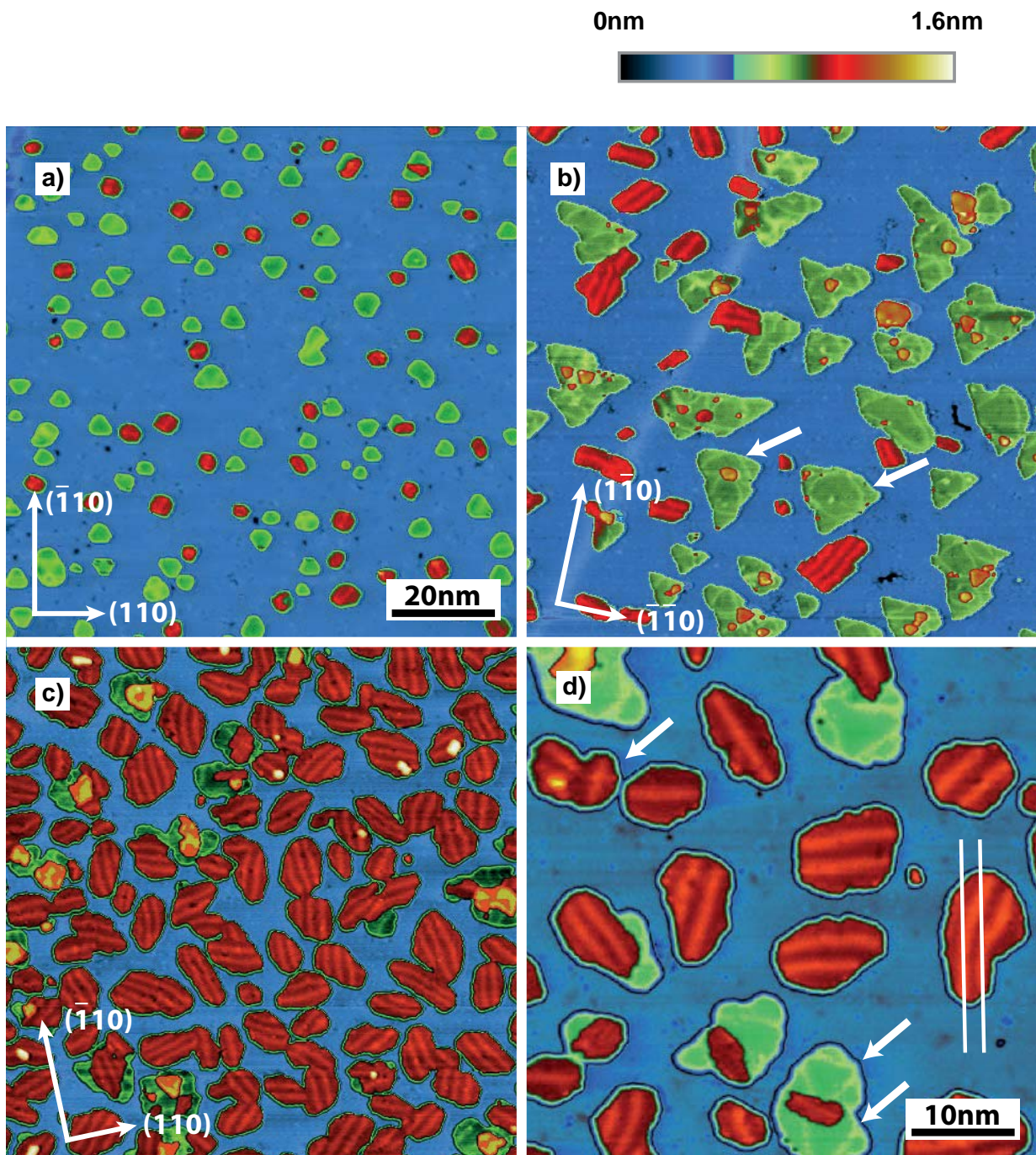
Figure B.2.: Growth of the second Bi-bilayer. a) 108 % of a bilayer, **b)** 120 % and **c)** 150 %. **d)** zoomed image at 150 %. The first bilayer is colored in blue, low-level islands in green, high-level islands in red, structures with a greater height in orange/yellow. Arrows in (b) point to islands with different surface patterns. The right island exhibits one (distorted) triangle. The left island exhibits two, since it consists of two islands grown together. Arrows in (d) point to conserved surface patterns. The lines highlight an orientation change that follows the shape of the island. All samples were grown at 250 K and measured with U_B: 1 V, I: 20 pA.

At 150 % deposition, 55 % of the first bilayer is covered with additional islands. Most of these are high-level islands (41.2 % coverage), low-level islands contribute additional 12.5 %. From the small deviation to the amount of deposited material one can assume that high-level islands are bilayers and the deviation is caused by low-level islands. These are then assumed to be Bi(111)-monolayers.

This hypothesis is underpinned by several points: The high-level-island-height is the same as the one of the first bilayer (~ 6.3 Å). Some islands consist of several high and low-level areas, indicating that high-level islands consist of a low-level layer and an additional layer. Finally, the difference between coverage and deposition of all investigated surfaces can be explained. If one assumes that low-level islands exhibit half the lateral atom density of bilayers, the deposition calculated via the coverage matches the deposition calculated via evaporator parameters within a margin of less than 2 %.

Discussion of Layer Heights

The growth of Bi(111)-monolayers (green islands) allows experimental insight into the internal layer distances of bilayers grown on Bi_2Se_3. The absolute values, as well as the ratio between interlayer distance (size of the van-der-Waals gap, here the height of the first monolayer, i.e. green island) and intralayer distance (the height of the second monolayer, i.e. height difference between red and green island), is changed drastically compared to bulk values and bilayers grown on Bi_2Te_3, see Tab B.3. For Bi on Bi_2Te_3 intra- and interlayer distances increase by about the same percentage (3.1 % and 3.4 %) compared to bulk values [40, 187].Their ratio is conserved. For Bi on Bi_2Se_3 the intralayer distance is increased by 6.9 % compared to bulk values, while the interlayer distance is increased by 100 %, resulting in an almost doubled ratio. This indicates a strong decoupling between bilayer(s) and the substrate[1]. Since the second bilayer exhibits the same overall height

| System | Heights | | | Ratio |
	Interlayer	Intralayer	Overall	
Bi(111)	2.35 Å	1.59 Å	3.94 Å	1.48:1
Bi/Bi_2Te_3	2.42 Å	1.64 Å	4.06 Å	1.48:1
Bi/Bi_2Se_3†	4.7 Å	1.7 Å	6.4 Å	2.76:1

Table B.3.: Comparison of inter- and intralayer distances of Bi(111)-bilayers in bulk crystal configuration and grown on Bi_2Te_3, as well as on Bi_2Se_3. Bulk and Bi/Bi_2Te_3 values were measured via LEED [40, 187], Bi/Bi_2Se_3 values were measured via STM at a bias voltage of 1 V. †: Values were taken from second bilayer islands.

---

[1]However, mono- and bilayers might have different electronic structures. Therefore the change in ratio might not (only) be caused by a change of the distances between the layers.

as the first bilayer, it is most likely that the ratio for layers within the first bilayer is the same as for the investigated second bilayer. This strong decoupling from the substrate would explain the rounder shape of Bi-islands on Bi_2Se_3 compared to the triangular ones on Bi_2Te_3: The influence of the hexagonal lattice of the substrate is reduced.

A Closer Look at Monolayer Islands

The monolayer islands (green) exhibit a triangular shape. At 108 %, Fig. B.2 (a), two orientations can be found with the tip either pointing along the $(\bar{1}10)$ or the $(1\bar{1}0)$ direction, indicating hcp/fcc growth of the islands. Islands pointing along $(\bar{1}10)$ dominate with a ratio of 4:1. At 120 % coverage, Fig. B.2 (b), only one type of orientation can be found. The larger islands exhibit a pattern of stripes forming a triangle on their surface rotated by 180° to the island orientation. Each island shows one triangle on its surface. The triangle is preserved when two islands grow together e.g. see the islands marked with white arrows in Fig B.2 (b) and (d).

A Closer Look at Bilayer Islands

The bilayer islands also exhibit a surface reconstruction resembling parallel stripes and show a rather rectangular shape. The stripes have a period of 4.6 ± 0.4 nm. They are mostly aligned along the long island axis and this orientation is conserved when the islands grow together, see white stripes in Fig. B.2 (d). The pattern is a topographical rather than an electronic feature. It is visible in all topography images at all measured bias voltages with a constant period, while STS images show different features, see Fig. B.3. Additionally, an electronic pattern would follow the edges of the structure and would not be conserved when islands grow together. Most likely, the observed stripes are a Moiré pattern induced by a linear lateral relaxation of the 2nd bilayer compared to the first one. Then the stripe periodicity is the common multiple of the lateral lattice constant of both bilayers. With that relation the lattice constant along the relaxed axis of the 2nd bilayer is calculated to be 4.4 ± 0.5 Å, about 5 % larger than the lattice constant of the first bilayer.

An analysis of the angular orientation of the stripe pattern finds at least two preferred directions for the linear relaxation, in the convention used here for 0° and 120°, Fig. B.3 (d). By a comparison with the orientation of the 1st bilayer, which is known from atomically resolved images, these directions are identical with the (110) and (100) high symmetry directions of the hexagonal lattice. If the high symmetry directions of the substrate are the preferred directions of relaxation, an increased probability should also be found for the (010) direction (60°). However, this is not the case. This deviation, and in general the

large number of other orientations found by the analysis, can be explained by the mismatch of the symmetry of the Moiré pattern (two-fold) and the lateral lattice structure of the substrate (three-fold). Relaxation forces the islands into a rectangular shape, away from a triangular shape that is typical for islands grown on a substrate exhibiting a hexagonal lattice. This competition between triangular and rectangular island-shape may lead to a greater variation of stripe orientation, as the orientation of the pattern not only influences the island shape but is also influenced by the shape vice versa. In that case, the statistical population, i.e. the number of investigated islands, was not sufficiently large enough to find a (distinct) peak for an orientation along the (010) direction (60°).

Summary of 2nd Bilayer Regime

In conclusion, in a low coverage regime, the growth on top of the first bilayer is dominated by monolayer Bi(111)-islands. This is the first reported growth of Bi(111) monolayers. With increased deposition, a second monolayer grows on top of these islands. As a result most islands are converted to bilayers already before 50 % of the surface is covered. On both types of islands the surface exhibits a surface reconstruction, which reduces the compressive strain of the first bilayer. Due to the two step growth, the inter- and intralayer distances can be estimated. The unusual height of the Bi-bilayers on Bi$_2$Se$_3$ is mainly caused by a doubling of the van-der-Waals gap, which is a unique property of this system.

Higher Coverage

With additional coverage two structures appear on top of the second bilayer: islands and chains, see Fig. B.4. The islands have an unusually small height of 2.3 Å, and the chains exhibit a height of 6.6 Å. On some of these chains an additional chain grows on top with a height of 2.9 Å. Just taking the structure height into account, the islands seem to consist of monolayers and the chains show bilayer height (with additional monolayer chains on top). Overall, there is no dominant feature in the regime around 250 % coverage. This changes when the sample is annealed.
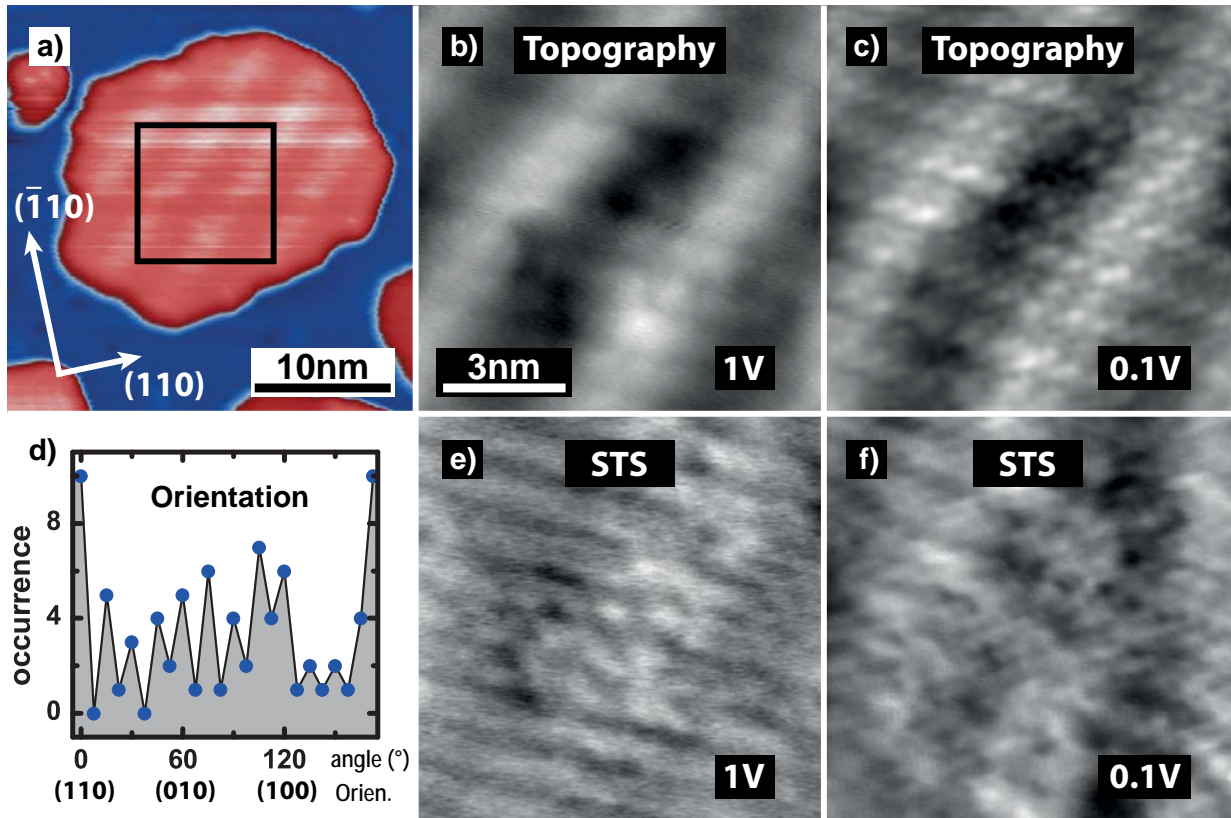
Figure B.3.: Topography, STS maps and stripe orientation of 2nd Bi-bilayer islands: a) Overview scan of a bilayer island (red) on top of the first Bi-bilayer (blue). The black box marks the area for (b), (c), (e) and (f). **b)** and **c)**: Topography at given bias voltages. **e)** and **f)** STS images at given bias voltages. All images were measured with $I = 20 \, \text{pA}$. STS maps were measured with a sensitivity of $5 \, \text{mV}$. **g)**: Histogram of the angular orientation of the stripes. For the histogram 102 islands were analyzed in total.

Higher Coverage and High-Temperature Annealing

The as-grown Bi(111)-bilayer islands (less than one bilayer coverage) were too small to produce a clear ARPES-signal. Instead the islands disturb the signal from the substrate underneath leading to broader bands. This is also the case for islands grown on top of the first bilayer. To increase the island size, all samples for ARPES measurements were annealed to 450 K before measurement. Fig. B.5 shows the influence of annealing on the ARPES signal as described in section B.

Therefore, the influence of additional annealing on the film morphology for several coverages was investigated by STM, see Fig. B.4. At 50 % bilayer deposition (a-c), the resulting islands exhibit a flat surface, in stark contrast to the rough surfaces of islands grown at 450 K. While the island size is increased, the height is lowered by about 0.7 Å to 5.5 Å, which matches the height of islands grown at 450 K. But the reduced height might not be due to a change of the bilayer structure, but could be due to a change of the electronic environment on the surface. This is covered with dirt. It is not possible to obtain an unperturbed STM image. The jumps between lines indicate loose atoms on the surface that now and then stick to the tip. The atoms originate most likely from the substrate, which is known to decompose at these temperatures[2].

At 150 % bilayer deposition (d-f), the first bilayer (blue) shows a rippled structure. The vanishing of monolayer islands (green) underlines the dominant role of bilayer growth (red) at this regime. Also the coverage of bilayer islands with an extra thin layer (yellow) is increased. Judging by its height the extra layer is most likely a monolayer. The height of the second bilayer is not changed.

Image quality and dominant structures (after annealing) alter drastically for the deposition of about (and more) than 180 % bilayer coverage. The images show no perturbations, indicating a clean surface. The added material seems to prevent decomposition of the substrate. After 180 % deposition and annealing to 450 K, the surface is terminated either by the first bilayer (blue) or by a second bilayer/thin layer-combination (yellow). Simple second bilayer islands (red) cannot be found anymore, even simple monolayer coverage (green) is preferred.

At 250 % coverage, the second bilayer is completely covered after annealing. The termination is dominated by the above mentioned thin layer (yellow) and an additional layer (purple). As in the case of the monolayer and bilayer islands presented in section B, the nature of these films can be determined by a comparison of area coverage with the amount of deposited material, see Tab. B.4.

---

[2]Also material evaporated from hot surfaces during the annealing process can stick to the surface. However,
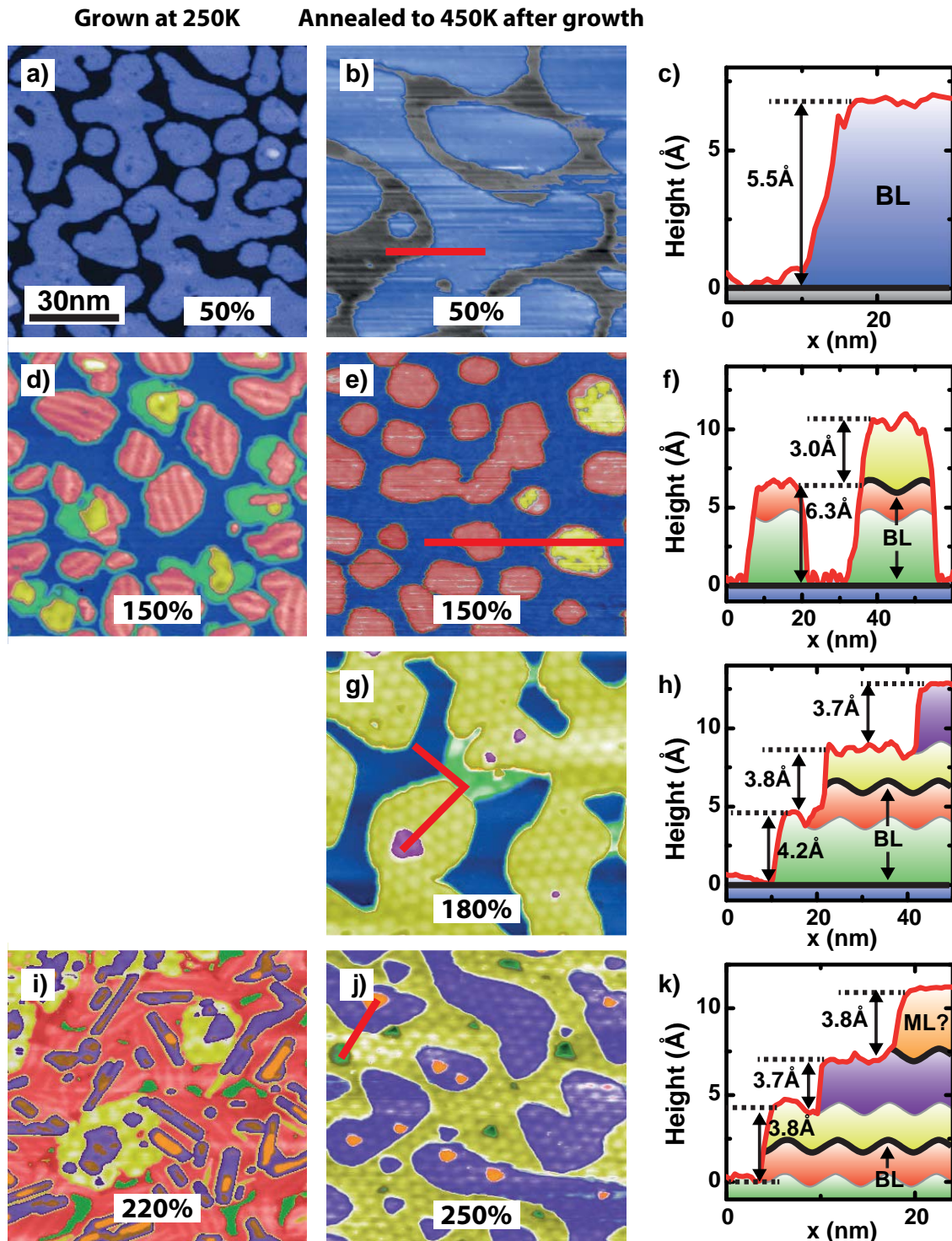
Figure B.4.: Bi-bilayers on Bi$_2$Se$_3$: Annealing after growth. Images to the left show the surface with different coverages grown at $250\,\text{K}$ without annealing. The number in the image gives the amount of deposited material in percentage of one bilayer. Images in between show the surface after annealing to $450\,\text{K}$. A red bar marks the position of a line profile. Diagrams to the right show the line profiles of the middle images. Layers are color coded: From bottom to top: black (substrate), blue, green, red, yellow, purple, orange. Dark shades of color represent lower, bright shades higher altitude. For all STM images: $U_B = 1\,\text{V}$, $I = 20\,\text{pA}$.

The calculated depositions match under the assumption that the two thin layers (yellow and purple) are monolayers. Both monolayers exhibit a strong, hexagonal Moiré-pattern, but with different lattice constants: 5.5 ± 0.3 nm[3] for the bottom ML (yellow) and 4.0 ± 0.2 nm for the top ML (purple).

The height of the second monolayer (purple), can be measured directly: 3.6 Å. The height of the first ML (yellow) is 2.3 Å for the non-annealed samples. For the annealed sample, the height can only be determined indirectly, since in this case the yellow ML is always on top of a bilayer (red). Together with the previously determined height of that bilayer, the height of the yellow ML can be calculated to be about 2 Å. The independent growth of these layers, as well as the different lattice constant of the Moiré-pattern suggest to treat them as single layers.

Summary

The growth of bismuth on Bi$_2$Se$_3$ is complex. Within certain parameters (growth temperature between 200 and 270 K) bismuth grows in the form of (111)-bilayer(s). The first bilayer grows pseudomorphically, with an unusually large van-der-Waals gap between bilayer and Bi$_2$Se$_3$, a smooth surface and an intact bilayer structure.

The large compressive strain, induced by a large mismatch of the lateral lattice constants (8.6 %), not only leads to this large van-der-Waals gap, but splits the bilayers grown on top more and more laterally, until independent monolayers have grown. These are the first bismuth (111)-monolayers reported so far.

	Areal coverage				Deposited material[†]	
BL (blue)	BL+ML (green)	2BL+ML (yellow)	2BL+2ML (purple)	all	via coverage	via eva.-rate
44.4 %	5.2 %	49.5 %	0.9 %	178 %	187 %	180 %
-	5.9 %	58.6 %	34.6 %	260 %	255 %	256 %

Table B.4.: Amount of deposited material calculated from evaporator parameters and area coverage concerning the second and third bilayer. † The amount of deposited material is given in percentage of bilayers. The area coverage was calculated under the assumption that layers labeled yellow and purple are monolayers. BL: bilayer, ML: monolayer.

---

this would introduce adatoms to all investigated surfaces, which is not the case.

[3]Close to the edge of the layers, the pattern is stretched or compressed as in the case of the wave pattern of the second bilayer.

Each layer demands a different temperature-treatment for optimal growth. While the growth temperature remains the same, the system has to be annealed to form ordered films, starting with the third (bi)-layer.

While epitaxial Bi-bilayer growth on Bi_2Se_3 is possible, the breaking of the bilayer into monolayers, the unusually large van-der-Waals gap, the large diversity of layer heights and surfaces, and the different temperatures needed during growth indicate the induced strain is so large, that already the structure of the second bilayer is compromised. It seems unlikely that the growth of a smooth Bi(111)-bilayer on a substrate with an even smaller lateral lattice constant is possible.

Influence of Annealing on the ARPES-Signal

The growth parameters optimized by STM for a smooth and closed bilayer growth were not usable for ARPES. A growth of exactly one bilayer was not possible. All samples that were checked with ARPES right after growth showed an extremely reduced signal quality. It was not possible to identify any signal of the bilayer VB.

A reason for the reduced signal quality might have been the calibration of the evaporator. It was not possible to calibrate it as precise as in the STM lab. A growth of exactly 100 % was not possible. Either the substrate was not completely covered with bilayer or the bilayer was covered with additional material. Both surfaces could lead to a perturbation of the ARPES signal

It has been shown that an annealing of the system can lead to larger islands without loosing the general structural integrity of the bilayer. This would then lead to an increased ARPES signal, see section B. Indeed, annealing the investigated samples improved the signal quality. Fig. B.5 (a-c) shows ARPES images of samples without annealing (a) and with annealing for 5 min at 420 K (b) and 450 K (c), respectively. Higher temperatures were not used to keep the substrate's integrity intact. The quality turned out to be the best for samples annealed to 450 K. Therefore, this temperature was used for all sample preparations for the ARPES measurements.

Fig. B.5 (d) shows the band structure of the system at different coverages. All previously identified bands occur at all coverages. Only the feature intensities are changing, which might be due to small differences in image acquisition rather than to the change in coverage.
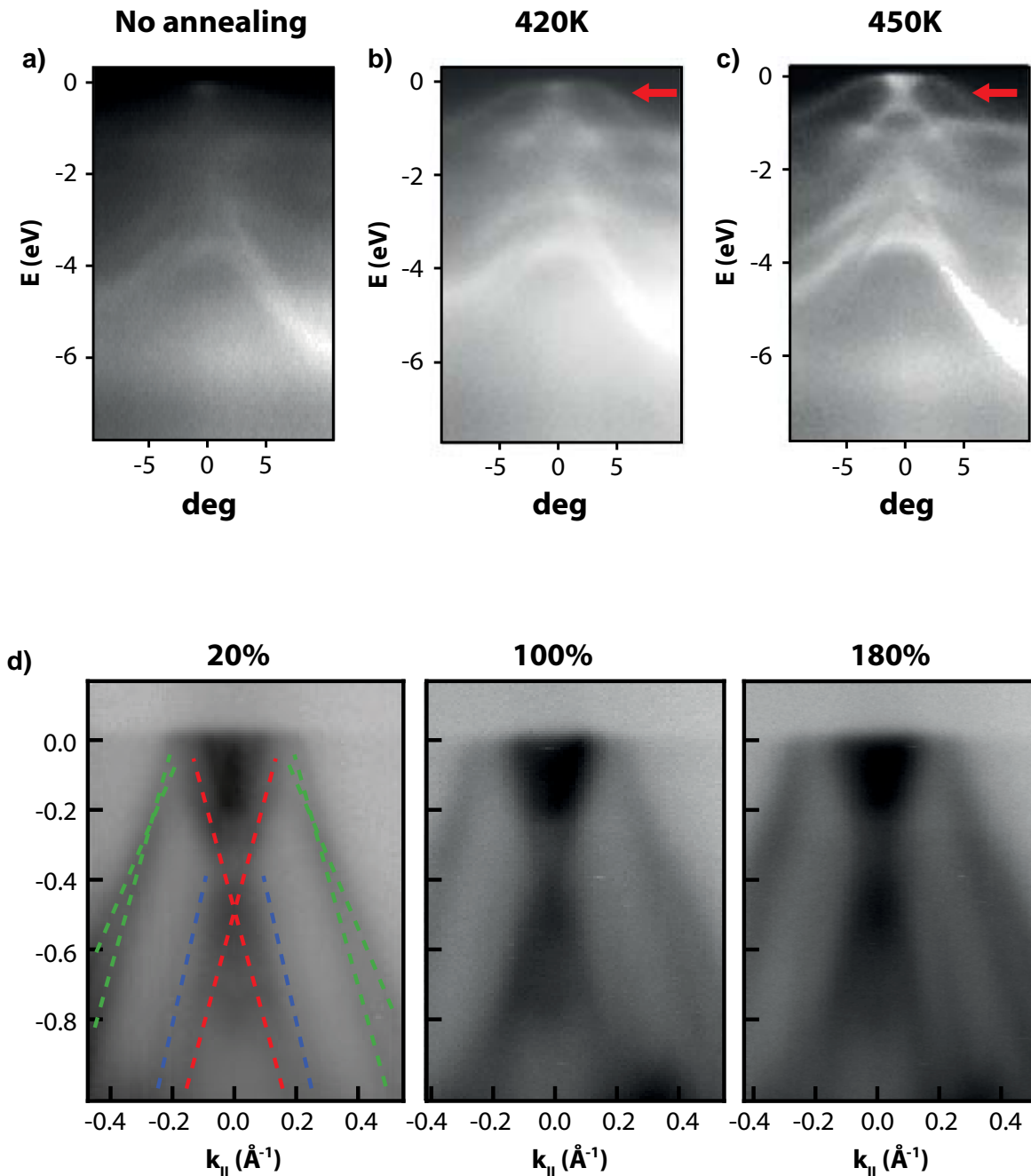
Figure B.5.: ARPES-signal depending on different annealing temperatures after growth and on different coverages of Bi-bilayers on Bi_2Se_3 : a) No annealing, **b)** 5 min at 420 K, **c)** 5 min at 450 K. All data were been taken with a photon energy of $E_{Ph} = 18$ eV and a path energy of $E_{Ph} = 10$ eV. A red arrow marks the emerging Bi-bilayer bands. **d)** Images taken from samples with different coverages. The nominal coverage is given above each image. All samples were annealed for 5 min at 450 K after deposition. All images were taken with a photon energy of $E_{Ph} = 10$ eV and a path energy of $E_{Ph} = 40$ eV.

CEC, JDOS, FT-STS Overview Figures

This section provides overview figures concerning the interaction of bands present at the surface of the Bi/Bi$_2$Se$_3$ system. Fig. B.6 gives an overview of FT-STS maps based on STM measurements. Fig. B.7 gives an overview of CECs taken from the calculated spectral function of the system (a-j) and JDOS images calculated from the CECs (k-t).
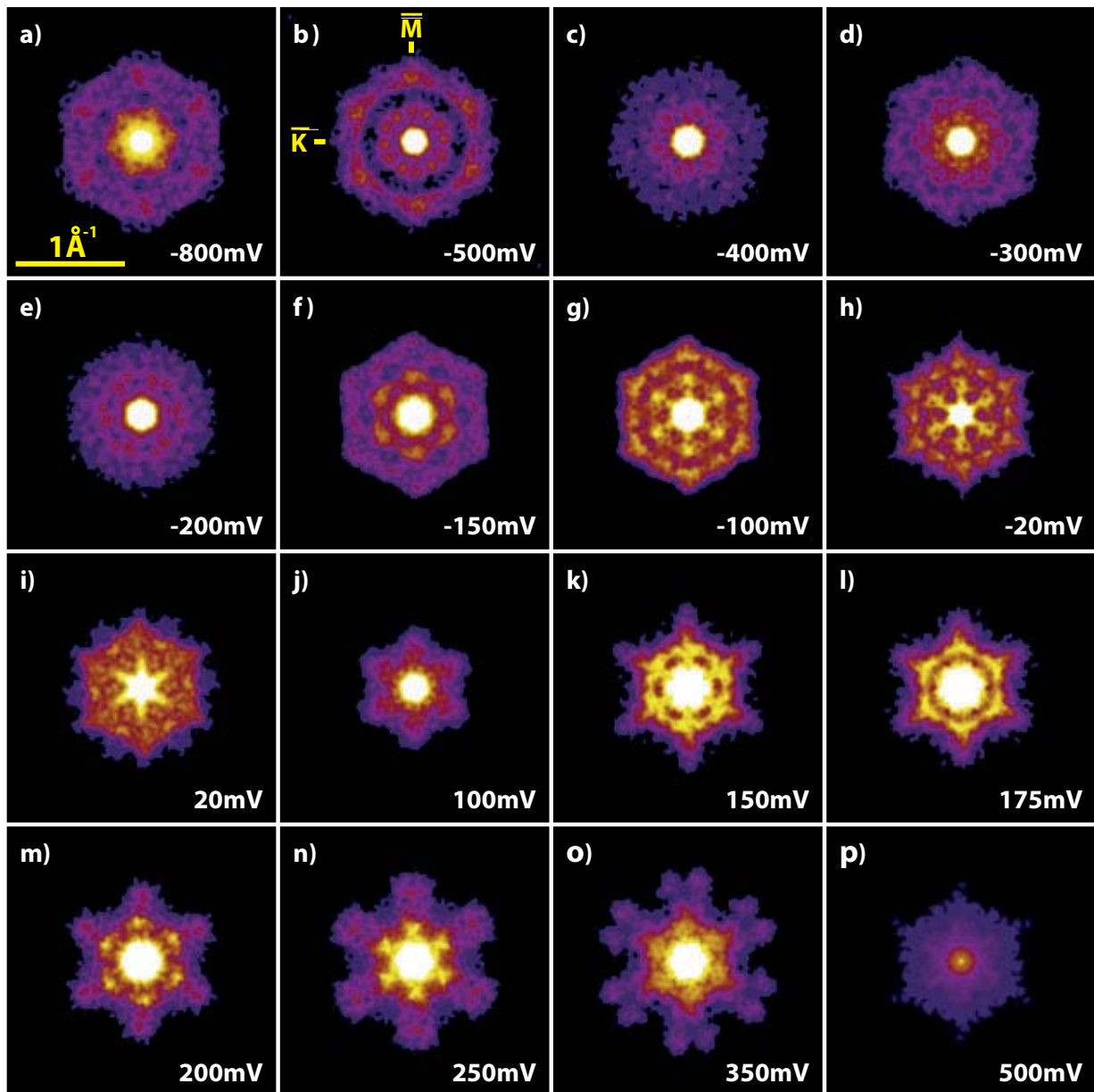
Figure B.6.: Overview of Bi/Bi$_2$Se$_3$ FT-STS maps. The original STS images were taken with $U_B = -50\,\mathrm{mV}$ and $I = 3\,\mathrm{nA}$. The used bias voltage and the image size is given in the images.

CECs
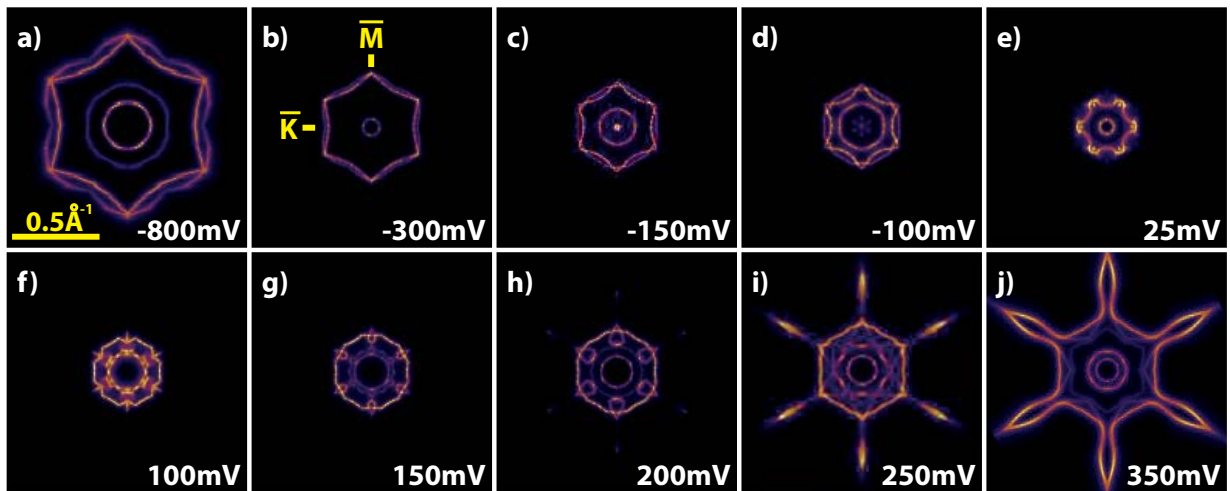
JDOS
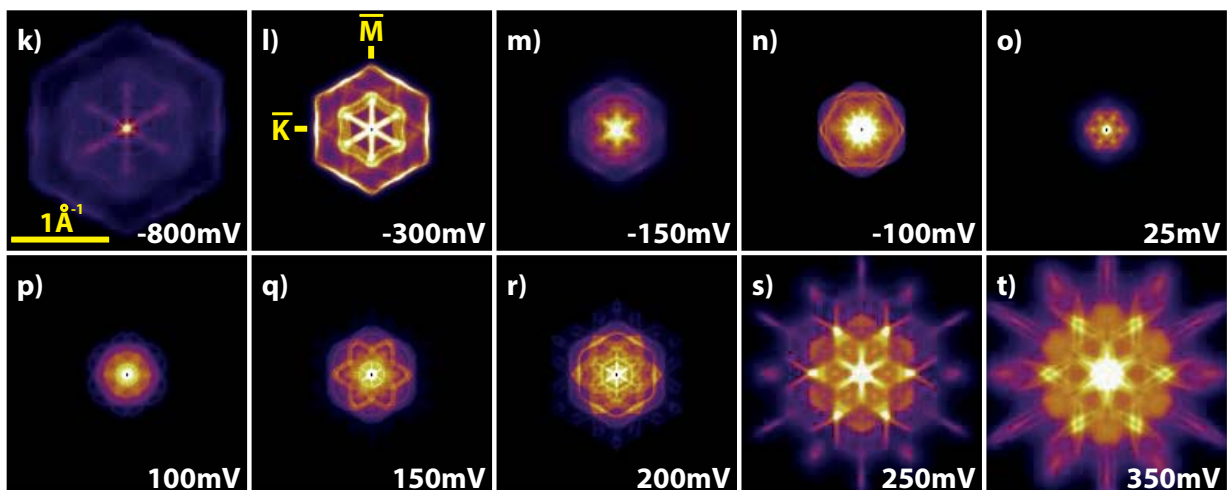
Figure B.7.: Overview of CECsand JDOS maps. The CECs were taken from the calculated spectral function of Bi/Bi_2Se_3. The JDOS maps were calculated from the CECs. The used bias voltage and the image size is given in the images.

Bibliography

[1] L. J. Edgar, *Method and apparatus for controlling electric currents*, Patent No. US1745175, US Patent Office (1930), cited on page(s): 1

[2] J. Bardeen and W. Brattain, *The Transistor, A Semi-Conductor Triode.* Physical Review **74**, 230 (1948), cited on page(s): 1

[3] *First HDD Drive*, URL: `http://www-03.ibm.com/ibm/history/exhibits/storage/storage\_350.html` (accessed October 2014), cited on page(s): 1

[4] *Intel 4004 Microprocessor*, URL: `http://www.intel.com/Assets/PDF/DataSheet/4004\_datasheet.pdf` (accessed October 2014), cited on page(s): 1

[5] *Apple A8X transistor count*, URL: `https://www.apple.com/ipad-air-2/performance` (accessed October 2014), cited on page(s): 1

[6] M. Hilbert and P. López, *The world's technological capacity to store, communicate, and compute information.* Science **332**, 60 (2011), cited on page(s): 1

[7] M. N. Baibich, J. M. Broto, A. Fert, F. N. Van Dau, and F. Petroff, *Giant Magnetoresistance of (001)Fe/(001)Cr Magnetic Superlattices.* Physical Review Letters **61**, 2472 (1988), cited on page(s): 1

[8] G. Binasch, P. Grünberg, F. Saurenbach, and W. Zinn, *Enhanced magnetoresistance in layered magnetic structures with antiferromagnetic interlayer exchange.* Physical Review B **39**, 4828 (1989), cited on page(s): 1

[9] C. Chappert, A. Fert, and F. N. Van Dau, *The emergence of spin electronics in data storage.* Nature materials **6**, 813 (2007), cited on page(s): 1

[10] M. Fuechsle, J. A. Miwa, S. Mahapatra, H. Ryu, S. Lee, O. Warschkow, L. C. L. Hollenberg, G. Klimeck, and M. Y. Simmons, *A single-atom transistor.* Nature nanotechnology **7**, 242 (2012), cited on page(s): 2

[11] S. A. Wolf, D. D. Awschalom, R. A. Buhrman, J. M. Daughton, S von Molnár, M. L. Roukes, A. Y. Chtchelkanova, and D. M. Treger, *Spintronics: a spin-based electronics vision for the future.* Science **294**, 1488 (2001), cited on page(s): 2, 44

[12] A. Brataas, A. D. Kent, and H. Ohno, *Current-induced torques in magnetic materials.* Nature materials **11**, 372 (2012), cited on page(s): 2

[13] G. D. Fuchs, G. Burkard, P. V. Klimov, and D. D. Awschalom, *A quantum memory intrinsic to single nitrogen vacancy centres in diamond.* Nature Physics **7**, 789 (2011), cited on page(s): 2

[14] M. Pavicic, *Companion to Quantum Computation and Communication*, Wiley-VCH (2013), ISBN: 3527408487, cited on page(s): 2

[15]   S. Datta and B. Das, *Electronic analog of the electro-optic modulator.* Applied Physics Letters **56**, 665 (1990), cited on page(s): 2

[16]   J. Jacob, G. Meier, S. Peters, T. Matsuyama, U. Merkt, A. W. Cummings, R. Akis, and D. K. Ferry, *Generation of highly spin-polarized currents in cascaded InAs spin filters.* Journal of Applied Physics **105**, 093714 (2009), cited on page(s): 2

[17]   J. Wunderlich, B.-G. Park, A. C. Irvine, L. P. Zârbo, E. Rozkotová, P. Nemec, V. Novák, J. Sinova, and T. Jungwirth, *Spin Hall effect transistor.* Science **330**, 1801 (2010), cited on page(s): 2

[18]   A. A. Khajetoorians, J. Wiebe, B. Chilian, and R. Wiesendanger, *Realizing all-spin-based logic operations atom by atom.* Science **332**, 1062 (2011), cited on page(s): 2

[19]   Y. Ando, *Topological Insulator Materials.* Journal of the Physical Society of Japan **82**, 102001 (2013), cited on page(s): 2

[20]   M. Hasan and C. Kane, *Colloquium: Topological insulators.* Reviews of Modern Physics **82**, 3045 (2010), cited on page(s): 2

[21]   X.-L. Qi and S.-C. Zhang, *Topological insulators and superconductors.* Reviews of Modern Physics **83**, 1057 (2011), cited on page(s): 2, 32

[22]   S.-Q. Shen, *Topological Insulators*, Springer (2012), ISBN: 978-3-642-32857-2, cited on page(s): 2, 32

[23]   S. Murakami, N. Nagaosa, and S.-C. Zhang, *Dissipationless quantum spin current at room temperature.* Science **301**, 1348 (2003), cited on page(s): 2, 31, 43

[24]   S. Murakami, N. Nagaosa, and S.-C. Zhang, *Spin-Hall Insulator.* Physical Review Letters **93**, 156804 (2004), cited on page(s): 2, 31, 43

[25]   L. Fu and C. Kane, *Topological insulators with inversion symmetry.* Physical Review B **76**, 045302 (2007), cited on page(s): 2

[26]   S. Murakami, *Phase transition between the quantum spin Hall and insulator phases in 3D: emergence of a topological gapless phase.* New Journal of Physics **9**, 356 (2007), cited on page(s): 2, 31, 43

[27]   M. König, S. Wiedmann, C. Brüne, A. Roth, H. Buhmann, L. W. Molenkamp, X.-L. Qi, and S.-C. Zhang, *Quantum spin hall insulator state in HgTe quantum wells.* Science **318**, 766 (2007), cited on page(s): 2

[28]   D Hsieh, Y Xia, D Qian, L Wray, J. H. Dil, F Meier, J Osterwalder, L Patthey, J. G. Checkelsky, N. P. Ong, A. V. Fedorov, H Lin, A Bansil, D Grauer, Y. S. Hor, R. J. Cava, and M. Z. Hasan, *A tunable topological insulator in the spin helical Dirac transport regime.* Nature **460**, 1101 (2009), cited on page(s): 2

[29]   Y. Xia, D. Qian, D. Hsieh, L. Wray, A. Pal, H. Lin, A. Bansil, D. Grauer, Y. S. Hor, R. J. Cava, and M. Z. Hasan, *Observation of a large-gap topological-insulator class with a single Dirac cone on the surface.* Nature Physics **5**, 398 (2009), cited on page(s): 2, 47, 50

[30] F. D. M. Haldane, *Model for a Quantum Hall Effect without Landau Levels: Condensed-Matter Realization of the Parity Anomaly*. Physical Review Letters **61**, 2015 (1988), cited on page(s): 3, 31, 45

[31] C.-Z. Chang, J. Zhang, X. Feng, J. Shen, Z. Zhang, M. Guo, K. Li, Y. Ou, P. Wei, L.-L. Wang, Z.-Q. Ji, Y. Feng, S. Ji, X. Chen, J. Jia, X. Dai, Z. Fang, S.-C. Zhang, K. He, Y. Wang, L. Lu, X.-C. Ma, and Q.-K. Xue, *Experimental observation of the quantum anomalous Hall effect in a magnetic topological insulator*. Science **340**, 167 (2013), cited on page(s): 3, 31, 45

[32] P. Cheng, C. Song, T. Zhang, Y. Zhang, Y. Wang, J.-F. Jia, J. Wang, Y. Wang, B.-F. Zhu, X. Chen, X. Ma, K. He, L. Wang, X. Dai, Z. Fang, X. Xie, X.-L. Qi, C.-X. Liu, S.-C. Zhang, and Q.-K. Xue, *Landau Quantization of Topological Surface States in Bi2Se3*. Physical Review Letters **105**, 076801 (2010), cited on page(s): 3

[33] X.-L. Qi, T. L. Hughes, and S.-C. Zhang, *Topological field theory of time-reversal invariant insulators*. Physical Review B **78**, 195424 (2008), cited on page(s): 3, 31, 46

[34] A. Essin, J. Moore, and D. Vanderbilt, *Magnetoelectric Polarizability and Axion Electrodynamics in Crystalline Insulators*. Physical Review Letters **102**, 146805 (2009), cited on page(s): 3, 31, 46

[35] X.-L. Qi, R. Li, J. Zang, and S.-C. Zhang, *Inducing a magnetic monopole with topological surface States*. Science **323**, 1184 (2009), cited on page(s): 3, 31, 46

[36] L. Fu and C. Kane, *Superconducting Proximity Effect and Majorana Fermions at the Surface of a Topological Insulator*. Physical Review Letters **100**, 096407 (2008), cited on page(s): 3, 31, 46

[37] *Search for "Topological Insulator" Publications*, URL: http : / / apps . webofknowledge.com/ (accessed October 2014), cited on page(s): 3

[38] Y. Koroteev, G. Bihlmayer, E. Chulkov, and S. Blügel, *First-principles investigation of structural and electronic properties of ultrathin Bi films*. Physical Review B **77**, 045428 (2008), cited on page(s): 4, 109

[39] M Wada, S Murakami, F Freimuth, and G Bihlmayer, *Localized edge states in two-dimensional topological insulators: Ultrathin Bi films*. Physical Review B **83**, 121310 (2011), cited on page(s): 4, 109, 110

[40] T. Hirahara, N. Fukui, T. Shirasawa, M. Yamada, M. Aitani, H. Miyazaki, M. Matsunami, S. Kimura, T. Takahashi, S. Hasegawa, and K. Kobayashi, *Atomic and Electronic Structure of Ultrathin Bi(111) Films Grown on Bi2Te3 (111) Substrates: Evidence for a Strain-Induced Topological Phase Transition*. Physical Review Letters **109**, 227401 (2012), cited on page(s): 4

[41] S. H. Kim, K.-H. Jin, J. Park, J. S. Kim, S.-h. Jhi, T.-h. Kim, and H. W. Yeom, *Edge and interfacial states in a two-dimensional topological insulator: Bi(111) bilayer on Bi2Te2Se*. Physical Review B **89**, 155436 (2014), cited on page(s): 4, 124, 140

[42] G. Binnig, H. Rohrer, C. Gerber, and E. Weibel, *Tunneling through a controllable vacuum gap.* Applied Physics Letters **40**, 178 (1982), cited on page(s): 9

[43] G Binnig and H. Rohrer, *Scanning tunneling microscopy.* Surface Science **126**, 236 (1983), cited on page(s): 9

[44] R. J. Hamers, *Atomic-Resolution Surface Spectroscopy with the Scanning Tunneling Microscope.* Annual Review of Physical Chemistry **40**, 531 (1989), cited on page(s): 9

[45] D. M. Eigler and E. K. Schweizer, *Positioning single atoms with a scanning tunnelling microscope.* Nature **344**, 524 (1990), cited on page(s): 9

[46] G. Binnig, H. Rohrer, C. Gerber, and E. Weibel, *7x7 Reconstruction on Si(111) Resolved in Real Space.* Physical Review Letters **50**, 120 (1983), cited on page(s): 9

[47] M. F. Crommie, C. P. Lutz, and D. M. Eigler, *Confinement of electrons to quantum corrals on a metal surface.* Science **262**, 218 (1993), cited on page(s): 9

[48] J. S. Foster, J. E. Frommer, and P. C. Arnett, *Molecular manipulation using a tunnelling microscope.* Nature **331**, 324 (1988), cited on page(s): 9

[49] I. Tilinin, M. Rose, J. Dunphy, M. Salmeron, and M. Van Hove, *Identification of adatoms on metal surfaces by STM: experiment and theory.* Surface Science **418**, 511 (1998), cited on page(s): 9

[50] R. J. Driscoll, M. G. Youngquist, and J. D. Baldeschwieler, *Atomic-scale imaging of DNA using scanning tunnelling microscopy.* Nature **346**, 294 (1990), cited on page(s): 9

[51] W Häberle, J. K. Hörber, F Ohnesorge, D. P. Smith, and G Binnig, *In situ investigations of single living cells infected by viruses.* Ultramicroscopy **42-44 (Pt**, 1161 (1992), cited on page(s): 9

[52] R. Wiesendanger, H. Güntherodt, G. Güntherodt, R. Gambino, and R. Ruf, *Observation of vacuum tunneling of spin-polarized electrons with the scanning tunneling microscope.* Physical Review Letters **65**, 247 (1990), cited on page(s): 9

[53] A Ichimiya, Y Tanaka, and K Ishiyama, *Quantitative measurements of thermal relaxation of isolated silicon hillocks and craters on the Si(111)-7 x 7 surface by scanning tunneling microscopy.* Physical review letters **76**, 4721 (1996), cited on page(s): 9

[54] S Krause, L Berbil-Bautista, G Herzog, M Bode, and R Wiesendanger, *Current-induced magnetization switching with a spin-polarized scanning tunneling microscope.* Science **317**, 1537 (2007), cited on page(s): 9

[55] S. Loth, M. Etzkorn, C. P. Lutz, D. M. Eigler, and A. J. Heinrich, *Measurement of Fast Electron Spin Relaxation Times with Atomic Resolution.* Science **329**, 1628 (2010), cited on page(s): 9

[56] R. Wiesandanger, *Scanning Probe Microscopy and Spectroscopy*, Cambridge University Press (1994), ISBN: 0521428475, cited on page(s): 9

[57] C. J. Chen, *Introduction to Scanning Tunneling Microscopy*, Oxford University Press (1993), ISBN: 0195071506, cited on page(s): 9

[58] D. J. Griffiths, *Introduction to Quantum Mechanics*, 2nd ed., Pearson Prentice Hall (2013), ISBN: 9781292024080, cited on page(s): 11, 13

[59] J. Bardeen, *Tunnelling from a Many-Particle Point of View.* Physical Review Letters **6**, 57 (1961), cited on page(s): 12

[60] I. Giaever, *Electron Tunneling Between Two Superconductors.* Physical Review Letters **5**, 464 (1960), cited on page(s): 13

[61] I. Giaever, *Energy Gap in Superconductors Measured by Electron Tunneling.* Physical Review Letters **5**, 147 (1960), cited on page(s): 13

[62] J. Tersoff and D. R. Hamann, *Theory and Application for the Scanning Tunneling Microscope.* Physical Review Letters **50**, 1998 (1983), cited on page(s): 14

[63] J. Tersoff and D. R. Hamann, *Theory of the scanning tunneling microscope.* Physical Review B **31**, 805 (1985), cited on page(s): 14

[64] H. A. Kramers, *Wellenmechanik und halbzahlige Quantisierung.* Zeitschrift für Physik **39**, 828 (1926), cited on page(s): 15

[65] G. Wentzel, *Eine Verallgemeinerung der Quantenbedingungen für die Zwecke der Wellenmechanik.* Zeitschrift für Physik **38**, 518 (1926), cited on page(s): 15

[66] L. Brillouin, *La Mécanique Ondulatoire de Schrödinger une Method Générale de Resolution par Approximations Successives.* Comptes Rendus des Seances de l'Académie des Sciences **183**, 24 (1926), cited on page(s): 15

[67] N. Lang, *Spectroscopy of single atoms in the scanning tunneling microscope.* Physical Review B **34**, 5947 (1986), cited on page(s): 15

[68] A. Wachowiak, *Aufbau einer 300mK Ultrahochvakuum Rastertunnelmikroskopie Anlage mit 14 Tesla Magnet und spinpolarisierte Rastertunnelmikroskopie an ferromagnetischen Fe-Inseln*, PhD Thesis, Hamburg University (2003), cited on page(s): 19, 20

[69] D. Haude, *Rastertunnelspektroskopie auf der InAs(110)-Oberfläche: Untersuchungen an drei-, zwei- und nulldimensionalen Elektronensystemen im Magnetfeld*, PhD thesis, Hamburg University (2001), cited on page(s): 19, 20

[70] A. J. Heinrich, J. A. Gupta, C. P. Lutz, and D. M. Eigler, *Single-atom spin-flip spectroscopy.* Science **306**, 466 (2004), cited on page(s): 20

[71] C.-l. Chiang, C. Xu, Z. Han, and W Ho, *Real-space imaging of molecular structure and chemical bonding by single-molecule inelastic tunneling probe.* Science **344**, 885 (2014), cited on page(s): 20

[72] R. Wiesendanger, *Spin mapping at the nanoscale and atomic scale.* Reviews of Modern Physics **81**, 1495 (2009), cited on page(s): 20

[73] M. Morgenstern, D. Haude, V. Gudmundsson, C. Wittneven, R. Dombrowski, C. Steinebach, and R. Wiesendanger, *Low temperature scanning tunneling spectroscopy on InAs(110).* Journal of Electron Spectroscopy and Related Phenomena **109**, 127 (2000), cited on page(s): 21

[74] M. F. Crommie, C. P. Lutz, and D. M. Eigler, *Imaging standing waves in a two-dimensional electron gas.* Nature **363**, 524 (1993), cited on page(s): 25, 108, 142

[75] F. Reinert and S. Hüfner, *Photoemission spectroscopy - From early days to recent applications.* New J. Phys. **7**, 97 (2005), cited on page(s): 25

[76] A. Damascelli, Z. Hussain, and Z.-X. Shen, *Angle-resolved photoemission studies of the cuprate superconductors.* Reviews of Modern Physics **75**, 473 (2003), cited on page(s): 27

[77] C. Nordling, E. Sokolowski, and K. Siegbahn, *Precision Method for Obtaining Absolute Values of Atomic Binding Energies.* Physical Review **105**, 1676 (1957), cited on page(s): 27

[78] G. Gobeli, F. Allen, and E. Kane, *Polarization Evidence for Momentum Conservation in Photoelectric Emission from Germanium and Silicon.* Physical Review Letters **12**, 94 (1964), cited on page(s): 28

[79] M. Traum, N. Smith, and F. Di Salvo, *Angular Dependence of Photoemission and Atomic Orbitals in the Layer Compound 1 T-TaSe2.* Physical Review Letters **32**, 1241 (1974), cited on page(s): 28

[80] N. V. Smith, M. M. Traum, and F. Di Salvo, *Mapping energy bands in layer compounds from the angular dependence of ultraviolet photoemission.* Solid State Communications **15**, 211 (1974), cited on page(s): 28

[81] K. Klitzing, G. Dorda, and M. Pepper, *New Method for High-Accuracy Determination of the Fine-Structure Constant Based on Quantized Hall Resistance.* Physical Review Letters **45**, 494 (1980), cited on page(s): 31

[82] K. von Klitzing, *The quantized Hall effect.* Reviews of Modern Physics **58**, 519 (1986), cited on page(s): 31

[83] L Landau, *On the theory of phase transitions.* Zh. Eksp. Teor. Fiz. **7**, 234 (1937), cited on page(s): 31

[84] P. W. Anderson, *Basic Notions Of Condensed Matter Physics*, Advanced b, Addison Wesley (1997), ISBN: 9780786741939, cited on page(s): 31

[85] D. Thouless, M Kohmoto, M. Nightingale, and M. den Nijs, *Quantized Hall Conductance in a Two-Dimensional Periodic Potential.* Physical Review Letters **49**, 405 (1982), cited on page(s): 31, 34

[86] X.-G. Wen, *Topological orders and edge excitations in fractional quantum Hall states.* Advances in Physics **44**, 405 (1995), cited on page(s): 31

[87] D. Pesin and A. H. MacDonald, *Spintronics and pseudospintronics in graphene and topological insulators.* Nature materials **11**, 409 (2012), cited on page(s): 31, 44

[88] Reisio, *Basketball*, URL: http://en.wikipedia.org/wiki/File:Basketball.png (accessed October 2014), cited on page(s): 33

[89] A. Klink, *Rubber Duck*, URL: http://en.wikipedia.org/wiki/File:Rubber_Duck.jpg\#filelinks (accessed October 2014), cited on page(s): 33

[90] WestportWiki, *Donut*, URL: `http://en.wikipedia.org/wiki/File:Chocolate\_Frosted\_Donuts\_(Coffee\_An),\_Westport,\_CT\_06880\_USA\_-\_Mar\_2013.jpg` (accessed October 2014), cited on page(s): 33

[91] H. Zhang, C.-X. Liu, X.-L. Qi, X. Dai, Z. Fang, and S.-C. Zhang, *Topological insulators in Bi2Se3, Bi2Te3 and Sb2Te3 with a single Dirac cone on the surface.* Nature Physics **5**, 438 (2009), cited on page(s): 34, 47, 48

[92] H. Kramers, *Théorie générale de la rotation paramagnétique dans les cristaux.* Proc. Amsterdam Acad. **33**, 959 (1930), cited on page(s): 36

[93] C. Wu, B. A. Bernevig, and S.-C. Zhang, *Helical Liquid and the Edge of Quantum Spin Hall Systems.* Physical Review Letters **96**, 106401 (2006), cited on page(s): 36, 37

[94] A. H. Castro Neto, F. Guinea, N. M. R. Peres, K. S. Novoselov, and A. K. Geim, *The electronic properties of graphene.* Reviews of Modern Physics **81**, 109 (2009), cited on page(s): 37

[95] X.-L. Qi and S.-C. Zhang, *The quantum spin Hall effect and topological insulators.* Physics Today **63**, 33 (2010), cited on page(s): 38

[96] P. W. Anderson, *Absence of Diffusion in Certain Random Lattices.* Physical Review **109**, 1492 (1958), cited on page(s): 38

[97] P. A. Lee, *Disordered electronic systems.* Reviews of Modern Physics **57**, 287 (1985), cited on page(s): 38

[98] T. Ando, T. Nakanishi, and R. Saito, *Berry's Phase and Absence of Back Scattering in Carbon Nanotubes.* Journal of the Physical Society of Japan **67**, 2857 (1998), cited on page(s): 38

[99] M. V. Berry, *Quantal Phase Factors Accompanying Adiabatic Changes.* Proceedings of the Royal Society A: Mathematical, Physical and Engineering Sciences **392**, 45 (1984), cited on page(s): 39

[100] L. A. Wray, S.-Y. Xu, Y. Xia, D. Hsieh, A. V. Fedorov, Y. S. Hor, R. J. Cava, A. Bansil, H. Lin, and M. Z. Hasan, *A topological insulator surface under strong Coulomb, magnetic and disorder perturbations.* Nature Physics **7**, 32 (2011), cited on page(s): 41

[101] J. Honolka, A. Khajetoorians, V. Sessi, T. Wehling, S. Stepanow, J.-L. Mi, B. Iversen, T. Schlenk, J. Wiebe, N. Brookes, A. Lichtenstein, P. Hofmann, K. Kern, and R. Wiesendanger, *In-Plane Magnetic Anisotropy of Fe Atoms on Bi2Se3(111).* Physical Review Letters **108**, 256811 (2012), cited on page(s): 41

[102] Y. S. Hor, P. Roushan, H. Beidenkopf, J. Seo, D. Qu, J. G. Checkelsky, L. a. Wray, D. Hsieh, Y. Xia, S.-Y. Xu, D. Qian, M. Z. Hasan, N. P. Ong, A. Yazdani, and R. J. Cava, *Development of ferromagnetism in the doped topological insulator Bi2xMnxTe3.* Physical Review B **81**, 195203 (2010), cited on page(s): 42, 147, 153

[103] J. Linder, T. Yokoyama, and A. Sudbø, *Anomalous finite size effects on surface states in the topological insulator Bi2Se3.* Physical Review B **80**, 205401 (2009), cited on page(s): 42

[104] K. He, Y. Zhang, C.-Z. Chang, C.-L. Song, L.-L. Wang, X. Chen, J.-F. Jia, Z. Fang, X. Dai, W.-Y. Shan, S.-Q. Shen, Q. Niu, X.-L. Qi, S.-C. Zhang, X.-C. Ma, and Q.-K. Xue, *Crossover of the three-dimensional topological insulator Bi2Se3 to the two-dimensional limit.* Nature Physics **6**, 584 (2010), cited on page(s): 42

[105] A. A. Taskin, S. Sasaki, K. Segawa, and Y. Ando, *Manifestation of Topological Protection in Transport Properties of Epitaxial Bi2Se3 Thin Films.* Physical Review Letters **109**, 066803 (2012), cited on page(s): 42

[106] G. Schubert, H. Fehske, L. Fritz, and M. Vojta, *Fate of topological-insulator surface states under strong disorder.* Physical Review B **85**, 201105 (2012), cited on page(s): 42

[107] H. Zhang, J.-H. Choi, Y. Xu, X. Wang, X. Zhai, B. Wang, C. Zeng, J.-H. Cho, Z. Zhang, and J. G. Hou, *Atomic Structure, Energetics, and Dynamics of Topological Solitons in Indium Chains on Si(111) Surfaces.* Physical Review Letters **106**, 026801 (2011), cited on page(s): 43

[108] H. W. Yeom and T.-H. Kim , cited on page(s): 43

[109] T.-H. Kim and H. W. Yeom, *Topological Solitons versus Nonsolitonic Phase Defects in a Quasi-One-Dimensional Charge-Density Wave.* Physical Review Letters **109**, 246802 (2012), cited on page(s): 43

[110] J. Moore and L Balents, *Topological invariants of time-reversal-invariant band structures.* Physical Review B **75**, 121306 (2007), cited on page(s): 44

[111] L. Fu, C. Kane, and E. Mele, *Topological Insulators in Three Dimensions.* Physical Review Letters **98**, 106803 (2007), cited on page(s): 44

[112] I. Žutić, J. Fabian, and S. Das Sarma, *Spintronics: Fundamentals and applications.* Reviews of Modern Physics **76**, 323 (2004), cited on page(s): 44

[113] S.-Y. Xu, Y Xia, L. a. Wray, S Jia, F Meier, J. H. Dil, J Osterwalder, B Slomski, A Bansil, H Lin, R. J. Cava, and M. Z. Hasan, *Topological phase transition and texture inversion in a tunable topological insulator.* Science **332**, 560 (2011), cited on page(s): 44, 106

[114] M Morgenstern, J Klijn, C. Meyer, and R Wiesendanger, *Real-Space Observation of Drift States in a Two-Dimensional Electron System at High Magnetic Fields.* Physical Review Letters **90**, 056804 (2003), cited on page(s): 45

[115] E. Majorana, *Teoria simmetrica dell'elettrone e del positrone.* Il Nuovo Cimento **14**, 171 (1937), cited on page(s): 46

[116] F. Wilczek, *Majorana returns.* Nature Physics **5**, 614 (2009), cited on page(s): 46

[117] V Mourik, K Zuo, S. M. Frolov, S. R. Plissard, E. P. a. M. Bakkers, and L. P. Kouwenhoven, *Signatures of Majorana fermions in hybrid superconductor-semiconductor nanowire devices.* Science **336**, 1003 (2012), cited on page(s): 46

[118] D Hsieh, D Qian, L Wray, Y Xia, Y. S. Hor, R. J. Cava, and M. Z. Hasan, *A topological Dirac insulator in a quantum spin Hall phase*. Nature **452**, 970 (2008), cited on page(s): 47, 108, 109

[119] D. Hsieh, Y. Xia, D. Qian, L. Wray, F. Meier, J. Dil, J. Osterwalder, L. Patthey, A. Fedorov, H. Lin, A. Bansil, D. Grauer, Y. Hor, R. Cava, and M. Hasan, *Observation of Time-Reversal-Protected Single-Dirac-Cone Topological-Insulator States in Bi2Te3 and Sb2Te3*. Physical Review Letters **103**, 146401 (2009), cited on page(s): 47

[120] G. Zhang, H. Qin, J. Teng, J. Guo, Q. Guo, X. Dai, Z. Fang, and K. Wu, *Quintuple-layer epitaxy of thin films of topological insulator Bi2Se3*. Applied Physics Letters **95**, 053114 (2009), cited on page(s): 48

[121] *The Landolt-Boernstein Database*, URL: http://www.springermaterials.com/docs/index.html (accessed October 2014), cited on page(s): 49

[122] Y. L. Chen, J. G. Analytis, J.-H. Chu, Z. K. Liu, S.-K. Mo, X. L. Qi, H. J. Zhang, D. H. Lu, X Dai, Z Fang, S. C. Zhang, I. R. Fisher, Z Hussain, and Z.-X. Shen, *Experimental realization of a three-dimensional topological insulator, Bi2Te3*. Science **325**, 178 (2009), cited on page(s): 48, 49

[123] W.-C. Lee, C. Wu, D. P. Arovas, and S.-C. Zhang, *Quasiparticle interference on the surface of the topological insulator Bi2Te3*. Physical Review B **80**, 245439 (2009), cited on page(s): 49

[124] T. Zhang, P. Cheng, X. Chen, J.-F. Jia, X. Ma, K. He, L. Wang, H. Zhang, X. Dai, Z. Fang, X. Xie, and Q.-K. Xue, *Experimental Demonstration of Topological Surface States Protected by Time-Reversal Symmetry*. Physical Review Letters **103**, 266803 (2009), cited on page(s): 49

[125] H. Beidenkopf, P. Roushan, J. Seo, L. Gorman, I. Drozdov, Y. S. Hor, R. J. Cava, and A. Yazdani, *Spatial fluctuations of helical Dirac fermions on the surface of topological insulators*. Nature Physics **7**, 939 (2011), cited on page(s): 49, 50, 68

[126] V. A. Greanya, W. C. Tonjes, R. Liu, C. G. Olson, D.-Y. Chung, and M. G. Kanatzidis, *Determination of the valence band dispersions for Bi2Se3 using angle resolved photoemission*. Journal of Applied Physics **92**, 6658 (2002), cited on page(s): 50

[127] S. Chizhevskay and L. Shelimova, *Electroactive and electroinactive dopants in Bi2Te3 and their interaction with antisite defects*. Inorg. Mater. (Transl. of Neorg. Mater.) **31**, 1083 (1995), cited on page(s): 50

[128] P Larson, V. A. Greanya, W. C. Tonjes, R. Liu, and S. D. Mahanti, *Electronic structure of Bi2 X 3 (X = S , Se , T) compounds : Comparison of theoretical calculations with photoemission studies*. Physical Review B **65**, 085108 (2002), cited on page(s): 50

[129] J Chen, C Jang, S Adam, M. S. Fuhrer, E. D. Williams, and M Ishigami, *Charged-impurity scattering in graphene*. Nature Physics **4**, 377 (2008), cited on page(s): 50

[130] M. Bianchi, D. Guan, S. Bao, J. Mi, B. B. Iversen, P. D. C. King, and P. Hofmann, *Coexistence of the topological state and a two-dimensional electron gas on the surface of Bi2Se3.* Nature communications **1**, 128 (2010), cited on page(s): 50

[131] M. S. Bahramy, P. D. C. King, A de la Torre, J Chang, M Shi, L Patthey, G Balakrishnan, P. Hofmann, R Arita, N Nagaosa, and F Baumberger, *Emergent quantum confinement at topological insulator surfaces.* Nature communications **3**, 1159 (2012), cited on page(s): 50, 77

[132] Z.-H. Zhu, G Levy, B Ludbrook, C. N. Veenstra, J. A. Rosen, R Comin, D Wong, P Dosanjh, A Ubaldini, P Syers, N. P. Butch, J Paglione, I. S. Elfimov, and A Damascelli, *Rashba Spin-Splitting Control at the Surface of the Topological Insulator Bi2Se3.* Physical Review Letters **107**, 186405 (2011), cited on page(s): 50

[133] P. King, R. Hatch, M. Bianchi, R. Ovsyannikov, C. Lupulescu, G. Landolt, B. Slomski, J. Dil, D. Guan, J. Mi, E. Rienks, J. Fink, A. Lindblad, S. Svensson, S. Bao, G. Balakrishnan, B. Iversen, J. Osterwalder, W. Eberhardt, F. Baumberger, and P. Hofmann, *Large Tunable Rashba Spin Splitting of a Two-Dimensional Electron Gas in Bi2Se3.* Physical Review Letters **107**, 096802 (2011), cited on page(s): 50, 77

[134] T. Valla, Z.-H. Pan, D. Gardner, Y. Lee, and S. Chu, *Photoemission Spectroscopy of Magnetic and Nonmagnetic Impurities on the Surface of the Bi2Se3 Topological Insulator.* Physical Review Letters **108**, 117601 (2012), cited on page(s): 50, 77

[135] H. M. Benia, C. Lin, K. Kern, and C. R. Ast, *Reactive Chemical Doping of the Bi2Se3 Topological Insulator.* Physical Review Letters **107**, 177602 (2011), cited on page(s): 50, 77, 122

[136] J. Wiebe, A. Wachowiak, F. Meier, D. Haude, T. Foster, M. Morgenstern, and R. Wiesendanger, *A 300 mK ultra-high vacuum scanning tunneling microscope for spin-resolved spectroscopy at high energy resolution.* Review of Scientific Instruments **75**, 4871 (2004), cited on page(s): 53, 60

[137] *Omicron VT-STM Technical Data*, URL: http://www.omicron.de/en/products/variable-temperature-spm/technical-data (accessed October 2014), cited on page(s): 53, 54

[138] T. Eelbo, *Construction of a new Ultra-High Vacuum Variable-Temperature Scanning Tunneling Microscope*, Diploma Thesis, Hamburg University (2008), cited on page(s): 54, 56

[139] S. H. Pan, *Piezoelectric motor*, Patent No. WO9319494 (A1), European Patent Office (1993), cited on page(s): 56

[140] *Material Property Data*, URL: www.matweb.com (accessed October 2014), cited on page(s): 58

[141] *EPO-TEK H77 Data Sheet*, URL: http://www.epotek.com/site/administrator/components/com_products/assets/files/Style_Uploads/H77.pdf (accessed October 2014), cited on page(s): 59

[142] A. F. Wells, *Structural Inorganic Chemistry*, 5th ed., Oxford University Press (1984), ISBN: 0199657637, cited on page(s): 61

[143] H. J. F. Jansen and A. J. Freeman, *Total-energy full-potential linearized augmented-plane-wave method for bulk solids: Electronic and structural properties of tungsten.* Physical Review B **30**, 561 (1984), cited on page(s): 61

[144] I. Horcas, R. Fernandez, J. M. Gomez-Rodriguez, J. Colchero, J. Gomez-Herrero, and A. M. Baro, *WSXM: A software for scanning probe microscopy and a tool for nanotechnology.* Review of Scientific Instruments **78**, 013705 (2007), cited on page(s): 63

[145] M. Scholz, J. Sánchez-Barriga, D. Marchenko, A. Varykhalov, A. Volykhov, L. Yashina, and O. Rader, *Tolerance of Topological Surface States towards Magnetic Moments: Fe on Bi2Se3.* Physical Review Letters **108**, 256810 (2012), cited on page(s): 67, 83, 122

[146] T. Schlenk, *Spin-Resolved and Inelastic Scanning Tunneling Spectroscopy of Magnetic Atoms and Clusters*, PhD thesis, Hamburg University (2013), cited on page(s): 69

[147] M. Bianchi, R. C. Hatch, Z. Li, P. Hofmann, F. Song, J. Mi, B. B. Iversen, Z. M. A. El-Fattah, P. Löptien, L. Zhou, A. A. Khajetoorians, J. Wiebe, R. Wiesendanger, and J. W. Wells, *Robust surface doping of Bi2Se3 by rubidium intercalation.* ACS nano **6**, 7009 (2012), cited on page(s): 70, 77

[148] J. Navrátil, J. Horák, T. Plecháček, S. Kamba, P. Lošt'ák, J. Dyck, W. Chen, and C. Uher, *Conduction band splitting and transport properties of Bi2Se3.* Journal of Solid State Chemistry **177**, 1704 (2004), cited on page(s): 70

[149] Y. Hor, A. Richardella, P. Roushan, Y. Xia, J. Checkelsky, A. Yazdani, M. Hasan, N. Ong, and R. Cava, *p-type Bi2Se3 for topological insulator and low-temperature thermoelectric applications.* Physical Review B **79**, 195208 (2009), cited on page(s): 70

[150] Y. Okada, C. Dhital, W. Zhou, E. D. Huemiller, H. Lin, S. Basak, A. Bansil, Y.-B. Huang, H. Ding, Z. Wang, S. D. Wilson, and V. Madhavan, *Direct Observation of Broken Time-Reversal Symmetry on the Surface of a Magnetically Doped Topological Insulator.* Physical Review Letters **106**, 206805 (2011), cited on page(s): 71

[151] C.-L. Song, Y.-P. Jiang, Y.-L. Wang, Z. Li, L. Wang, K. He, X. Chen, X.-C. Ma, and Q.-K. Xue, *Gating the charge state of single Fe dopants in the topological insulator Bi2Se3 with a scanning tunneling microscope.* Physical Review B **86**, 045441 (2012), cited on page(s): 71, 73

[152] D. West, Y. Sun, S. Zhang, T. Zhang, X. Ma, P. Cheng, Y. Zhang, X. Chen, J. Jia, and Q. Xue, *Identification of magnetic dopants on the surfaces of topological insulators: Experiment and theory for Fe on Bi2Te3(111).* Physical Review B **85**, 081305(R) (2012), cited on page(s): 71, 73, 76

[153] S. Hoffmann, C. Sø ndergaard, C. Schultz, Z. Li, and P. Hofmann, *An undulator-based spherical grating monochromator beamline for angle-resolved photoemission spectroscopy.* Nuclear Instruments and Methods in Physics Research Section A: Accelerators, Spectrometers, Detectors and Associated Equipment **523**, 441 (2004), cited on page(s): 77, 119

[154] M. Bianchi, R. Hatch, J. Mi, B. Iversen, and P. Hofmann, *Simultaneous Quantization of Bulk Conduction and Valence States through Adsorption of Nonmagnetic Impurities on Bi2Se3.* Physical Review Letters **107**, 086802 (2011), cited on page(s): 77, 78, 122

[155] G. Kresse and J. Hafner, *Ab initio molecular dynamics for liquid metals.* Physical Review B **47**, 558 (1993), cited on page(s): 80

[156] G Kresse, *Efficient iterative schemes for ab initio total-energy calculations using a plane-wave basis set.* Physical Review B **54**, 11169 (1996), cited on page(s): 80

[157] J. Perdew, K Burke, and M Ernzerhof, *Generalized Gradient Approximation Made Simple.* Physical review letters **77**, 3865 (1996), cited on page(s): 80, 121

[158] G Kresse, *From ultrasoft pseudopotentials to the projector augmented-wave method.* Physical Review B **59**, 1758 (1999), cited on page(s): 80

[159] D. C. Tsui, H. L. Stormer, and A. C. Gossard, *Two-Dimensional Magnetotransport in the Extreme Quantum Limit.* Physical Review Letters **48**, 1559 (1982), cited on page(s): 80

[160] M. Ye, K. Kuroda, Y. Takeda, Y. Saitoh, K. Okamoto, S.-Y. Zhu, K. Shirai, K. Miyamoto, M. Arita, M. Nakatake, T. Okuda, Y. Ueda, K. Shimada, H. Namatame, M. Taniguchi, and A. Kimura, *Perpendicular magnetic anisotropy with enhanced orbital moments of Fe adatoms on a topological surface of Bi2Se3.* Journal of physics. Condensed matter : an Institute of Physics journal **25**, 232201 (2013), cited on page(s): 83

[161] L. Shelimova, P. Konstantinov, O. Karpinsky, E. Avilov, M. Kretova, and V. Zemskov, *X-Ray diffraction study and electrical and thermal transport properties of the nGeTe*mBi2Te3 homologous series compounds.* Journal of Alloys and Compounds **329**, 50 (2001), cited on page(s): 85

[162] O. G. Karpinskii, L. E. Shelimova, M. A. Kretova, E. S. Avilov, and V. S. Zemskov, *X-ray Diffraction Study of Mixed-Layer Compounds in the Pseudobinary System SnTe-Bi2 Te3.* Inorganic Materials **39**, 305 (2003), cited on page(s): 85

[163] L. E. Shelimova, O. G. Karpinskii, T. E. Svechnikova, E. S. Avilov, M. a. Kretova, and V. S. Zemskov, *Synthesis and structure of layered compounds in the PbTe-Bi2Te3 and PbTe-Sb2Te3 systems.* Inorganic Materials **40**, 1264 (2004), cited on page(s): 85, 86, 91

[164] I. Petrov and R. Imanov, *Electron Diffraction Study of PbTe-Bi2Te3 Phases.* Kristallografiya **14**, 699 (1969), cited on page(s): 86

[165] S. V. Eremeev, G. Landolt, T. V. Menshchikova, B. Slomski, Y. M. Koroteev, Z. S. Aliev, M. B. Babanly, J. Henk, A. Ernst, L. Patthey, A. Eich, A. A. Khajetoorians, J. Hagemeister, O. Pietzsch, J. Wiebe, R. Wiesendanger, P. M. Echenique, S. S. Tsirkin, I. R. Amiraslanov, J. H. Dil, and E. V. Chulkov, *Atom-specific spin mapping and buried topological states in a homologous series of topological insulators.* Nature communications **3**, 635 (2012), cited on page(s): 89, 94

[166] R. C. Hatch, M. Bianchi, D. Guan, S. Bao, J. Mi, B. B. Iversen, L. Nilsson, L. Hornekæ r, and P. Hofmann, *Stability of the BiSe3(111) topological state: Electron-phonon and electron-defect scattering.* Physical Review B **83**, 241303 (2011), cited on page(s): 93

[167] S. V. Eremeev, Y. M. Koroteev, and E. V. Chulkov, *Ternary thallium-based semimetal chalcogenides Tl-V-VI2 as a new class of three-dimensional topological insulators.* JETP Letters **91**, 594 (2010), cited on page(s): 98, 99

[168] T. Sato, K. Segawa, H. Guo, K. Sugawara, S. Souma, T. Takahashi, and Y. Ando, *Direct Evidence for the Dirac-Cone Topological Surface States in the Ternary Chalcogenide TlBiSe2.* Physical Review Letters **105**, 136802 (2010), cited on page(s): 98, 106

[169] Y. L. Chen, Z. K. Liu, J. G. Analytis, J.-H. Chu, H. J. Zhang, B. H. Yan, S.-K. Mo, R. G. Moore, D. H. Lu, I. R. Fisher, S. C. Zhang, Z. Hussain, and Z.-X. Shen, *Single Dirac Cone Topological Surface State and Unusual Thermoelectric Property of Compounds from a New Topological Insulator Family.* Physical Review Letters **105**, 266401 (2010), cited on page(s): 98, 106

[170] O. Madelung, *Semiconductors: Data Handbook*, 3rd ed., Springer (2004), ISBN: 978-3-642-18865-7, cited on page(s): 98, 104

[171] K. Hoang and S. Mahanti, *Atomic and electronic structures of thallium-based III-V-VI2 ternary chalcogenides: Ab initio calculations.* Physical Review B **77**, 205107 (2008), cited on page(s): 98

[172] S. V. Eremeev, G. Bihlmayer, M. Vergniory, Y. M. Koroteev, T. V. Menshchikova, J. Henk, a. Ernst, and E. V. Chulkov, *Ab initio electronic structure of thallium-based topological insulators.* Physical Review B **83**, 205129 (2011), cited on page(s): 99, 106

[173] M Hoesch, T. Greber, V. Petrov, M. Muntwiler, M. Hengsberger, W. Auwärter, and J. Osterwalder, *Spin-polarized Fermi surface mapping.* Journal of Electron Spectroscopy and Related Phenomena **124**, 263 (2002), cited on page(s): 100

[174] F. J. Giessibl, *Atomic resolution on Si(111)-(7x7) by noncontact atomic force microscopy with a force sensor based on a quartz tuning fork.* Applied Physics Letters **76**, 1470 (2000), cited on page(s): 100

[175] T. R. Albrecht, P. Grütter, D. Horne, and D. Rugar, *Frequency modulation detection using high-Q cantilevers for enhanced force microscope sensitivity.* Journal of Applied Physics **69**, 668 (1991), cited on page(s): 100

[176] *Noncontact Atomic Force Microscopy,* Springer (2002), ISBN: 978-3-642-62772-9, cited on page(s): 103

[177] J. Lobo-Checa, M. Matena, K. Müller, J. H. Dil, F. Meier, L. H. Gade, T. A. Jung, and M. Stöhr, *Band formation from coupled quantum dots formed by a nanoporous network on a copper surface.* Science **325**, 300 (2009), cited on page(s): 105

[178] K. Kuroda, M. Ye, A. Kimura, S. Eremeev, E. Krasovskii, E. Chulkov, Y. Ueda, K. Miyamoto, T. Okuda, K. Shimada, H. Namatame, and M. Taniguchi, *Experimental Realization of a Three-Dimensional Topological Insulator Phase in Ternary Chalcogenide TlBiSe2.* Physical Review Letters **105**, 146801 (2010), cited on page(s): 106

[179] T. Sato, K. Segawa, K. Kosaka, S. Souma, K. Nakayama, K. Eto, T. Minami, Y. Ando, and T. Takahashi, *Unexpected mass acquisition of Dirac fermions at the quantum phase transition of a topological insulator.* Nature Physics **7**, 840 (2011), cited on page(s): 106

[180] S.-Y. Xu, M. Neupane, C. Liu, S. Jia, L. a. Wray, G. Landolt, B. Slomski, J. H. Dil, N. Alidoust, S. Basak, H. Lin, J. Osterwalder, A. Bansil, R. J. Cava, and M. Z. Hasan, *Anomalous spin-momentum locked two-dimensional states in the vicinity of a topological phase transition.* Arxiv , 1204.6518 (2012), cited on page(s): 106

[181] T. Hirahara, G. Bihlmayer, Y. Sakamoto, M. Yamada, H. Miyazaki, S.-i. Kimura, S. Blügel, and S. Hasegawa, *Interfacing 2D and 3D Topological Insulators: Bi(111) Bilayer on Bi2Te3.* Physical Review Letters **107**, 166801 (2011), cited on page(s): 107, 110, 124

[182] P. Roushan, J. Seo, C. V. Parker, Y. S. Hor, D Hsieh, D. Qian, A. Richardella, M. Z. Hasan, R. J. Cava, and A. Yazdani, *Topological surface states protected from backscattering by chiral spin texture.* Nature **460**, 1106 (2009), cited on page(s): 108

[183] S. Murakami, *Quantum Spin Hall Effect and Enhanced Magnetic Response by Spin-Orbit Coupling.* Physical Review Letters **97**, 236805 (2006), cited on page(s): 108

[184] I. Knez, R.-R. Du, and G. Sullivan, *Evidence for Helical Edge Modes in Inverted InAs/GaSb Quantum Wells.* Physical Review Letters **107**, 136603 (2011), cited on page(s): 108

[185] B. Zhou, H.-Z. Lu, R.-L. Chu, S.-Q. Shen, and Q. Niu, *Finite Size Effects on Helical Edge States in a Quantum Spin-Hall System.* Physical Review Letters **101**, 246807 (2008), cited on page(s): 109

[186] T. Seyller, A. Bostwick, K. V. Emtsev, K. Horn, L. Ley, J. L. McChesney, T. Ohta, J. D. Riley, E. Rotenberg, and F. Speck, *Epitaxial graphene: a new material.* physica status solidi (b) **245**, 1436 (2008), cited on page(s): 109

[187] H. Mönig, J. Sun, Y. Koroteev, G. Bihlmayer, J. Wells, E. Chulkov, K. Pohl, and P. Hofmann, *Structure of the (111) surface of bismuth: LEED analysis and first-principles calculations.* Physical Review B **72**, 085410 (2005), cited on page(s): 109, 115, 158

[188] *Non-Tetrahedrally Bonded Elements and Binary Compounds I*, Springer-Verlag (1998), ISBN: 3-540-64583-7, cited on page(s): 109, 115

[189] A. Kawasuso and S. Okada, *Reflection High Energy Positron Diffraction from a Si(111) Surface*. Physical Review Letters **81**, 2695 (1998), cited on page(s): 111

[190] T. Nagao, J. Sadowski, M. Saito, S. Yaginuma, Y. Fujikawa, T. Kogure, T. Ohno, Y. Hasegawa, S. Hasegawa, and T. Sakurai, *Nanofilm Allotrope and Phase Transformation of Ultrathin Bi Film on Si(111)-7x7*. Physical Review Letters **93**, 105501 (2004), cited on page(s): 111, 115

[191] C. Eder, *Thesis: Strukturelle Charakterisierung von epitaktisch gewachsenem Bismut auf Bismutselenid mittels Rastertunnelmikroskopie*, URL: `http://www.physnet.uni-hamburg.de/services/biblio/\_\_\_Bachelorarbeiten/Eder\_Cornelius\_2012.pdf`, Bachelor Thesis, University of Hamburg (2012), cited on page(s): 111

[192] T. Schlenk, M. Bianchi, M. Koleini, A. Eich, O. Pietzsch, T. O. Wehling, T. Frauenheim, A. Balatsky, J.-L. Mi, B. B. Iversen, J. Wiebe, A. A. Khajetoorians, P. Hofmann, and R. Wiesendanger, *Controllable Magnetic Doping of the Surface State of a Topological Insulator*. Phys. Rev. Lett. **110**, 126804 (2013), cited on page(s): 112

[193] F. Yang, L. Miao, Z. Wang, M.-y. Yao, F. Zhu, Y. Song, M.-x. Wang, J.-p. Xu, A. Fedorov, Z Sun, G. Zhang, C. Liu, F. Liu, D. Qian, C. Gao, and J.-f. Jia, *Spatial and Energy Distribution of Topological Edge States in Single Bi(111) Bilayer*. Physical Review Letters **109**, 016801 (2012), cited on page(s): 113

[194] C.-S Jiang, H. Yu, C.-K Shih, and P. Ebert, *Effect of the Si substrate structure on the growth of two-dimensional thin Ag films*. Surface Science **518**, 63 (2002), cited on page(s): 114

[195] *FLEUR: For a program description see*, URL: `http://www.flapw.de` (2013), cited on page(s): 121

[196] N. Fukui, T. Hirahara, T. Shirasawa, T. Takahashi, K. Kobayashi, and S. Hasegawa, *Surface relaxation of topological insulators: Influence on the electronic structure*. Physical Review B **85**, 115426 (2012), cited on page(s): 122

[197] M. Chen, J.-P. Peng, H.-M. Zhang, L.-L. Wang, K. He, X.-C. Ma, and Q.-K. Xue, *Molecular beam epitaxy of bilayer Bi(111) films on topological insulator Bi2Te3: A scanning tunneling microscopy study*. Applied Physics Letters **101**, 081603 (2012), cited on page(s): 122

[198] P. Löptien, L. Zhou, J. Wiebe, A. A. Khajetoorians, J. L. Mi, B. B. Iversen, P. Hofmann, and R. Wiesendanger, *Screening and atomic-scale engineering of the potential at a topological insulator surface*. Physical Review B **89**, 085401 (2014), cited on page(s): 122

[199] L. Miao, Z. F. Wang, W. Ming, M.-y. Yao, M. Wang, F. Yang, Y. R. Song, F. Zhu, A. V. Fedorov, Z Sun, C. L. Gao, C. Liu, Q.-K. Xue, C.-X. Liu, F. Liu, D. Qian, and J.-F. Jia, *Quasiparticle dynamics in reshaped helical Dirac cone of topological insulators.* Proceedings of the National Academy of Sciences of the United States of America **110**, 2758 (2013), cited on page(s): 124

[200] C. Hess, S. Sykora, T. Hänke, R. Schlegel, D. Baumann, V. B. Zabolotnyy, L. Harnagea, S. Wurmehl, J. van den Brink, and B. Büchner, *Interband Quasiparticle Scattering in Superconducting LiFeAs Reconciles Photoemission and Tunneling Measurements.* Physical Review Letters **110**, 017006 (2013), cited on page(s): 129

[201] D. Watson, *The natural neighbor series manuals and source codes.* Computers & Geosciences **25**, 463 (1999), cited on page(s): 129

[202] L El-Kareh, G Bihlmayer, A Buchter, H Bentmann, S Blügel, F Reinert, and M Bode, *A combined experimental and theoretical study of Rashba-split surface states on the sqrt(3) x sqrt(3) Pb/Ag(111) R30Â° surface.* New Journal of Physics **16**, 045017 (2014), cited on page(s): 130

[203] *Igor Pro (WaveMetrics Inc., Lake Oswego, OR, USA),* URL: http : / / www . wavemetrics.com (2013), cited on page(s): 132

[204] F. Marczinowski, J. Wiebe, F. Meier, K. Hashimoto, and R. Wiesendanger, *Effect of charge manipulation on scanning tunneling spectra of single Mn acceptors in InAs.* Physical Review B **77**, 115318 (2008), cited on page(s): 138

[205] I. K. Drozdov, A. Alexandradinata, S. Jeon, S. Nadj-Perge, H. Ji, R. J. Cava, B. Bernevig, and A. Yazdani, *One-dimensional topological edge states of bismuth bilayers.* Nature Physics , 664 (2014), cited on page(s): 141

[206] D Fujita, K Amemiya, T Yakabe, H Nejoh, T Sato, and M Iwatsuki, *Observation of two-dimensional Fermi contour of a reconstructed Au(111) surface using Fourier transform scanning tunneling microscopy.* Surface Science **423**, 160 (1999), cited on page(s): 142

[207] J. E. Hoffman, K McElroy, D.-H. Lee, K. M. Lang, H Eisaki, S Uchida, and J. C. Davis, *Imaging quasiparticle interference in Bi2Sr2CaCu2O8+delta.* Science **297**, 1148 (2002), cited on page(s): 142

[208] A. R. Schmidt, M. H. Hamidian, P Wahl, F Meier, A. V. Balatsky, J. D. Garrett, T. J. Williams, G. M. Luke, and J. C. Davis, *Imaging the Fano lattice to 'hidden order' transition in URu2Si2.* Nature **465**, 570 (2010), cited on page(s): 142

[209] M. P. Allan, A. W. Rost, A. P. Mackenzie, Y. Xie, J. C. Davis, K Kihou, C. H. Lee, A Iyo, H Eisaki, and T.-M. Chuang, *Anisotropic energy gaps of iron-based superconductivity from intraband quasiparticle interference in LiFeAs.* Science **336**, 563 (2012), cited on page(s): 142

[210] T. Hänke, S. Sykora, R. Schlegel, D. Baumann, L. Harnagea, S. Wurmehl, M. Daghofer, B. Büchner, J. van den Brink, and C. Hess, *Probing the Unconventional Superconducting State of LiFeAs by Quasiparticle Interference.* Physical Review Letters **108**, 127001 (2012), cited on page(s): 142

[211] X. Yu, C. Hwang, C. Jozwiak, A. Köhl, A. Schmid, and A. Lanzara, *New synthesis method for the growth of epitaxial graphene.* Journal of Electron Spectroscopy and Related Phenomena **184**, 100 (2011), cited on page(s): 146

[212] M. Gao, Y. Pan, L. Huang, H. Hu, L. Z. Zhang, H. M. Guo, S. X. Du, and H.-J. Gao, *Epitaxial growth and structural property of graphene on Pt(111).* Applied Physics Letters **98**, 033101 (2011), cited on page(s): 146

[213] Y. L. Chen, J.-H. Chu, J. G. Analytis, Z. K. Liu, K Igarashi, H.-H. Kuo, X. L. Qi, S. K. Mo, R. G. Moore, D. H. Lu, M Hashimoto, T Sasagawa, S. C. Zhang, I. R. Fisher, Z Hussain, and Z. X. Shen, *Massive Dirac fermion on the surface of a magnetically doped topological insulator.* Science **329**, 659 (2010), cited on page(s): 147

[214] S.-Y. Xu, M. Neupane, C. Liu, D. Zhang, A. Richardella, L. Andrew Wray, N. Alidoust, M. Leandersson, T. Balasubramanian, J. Sánchez-Barriga, O. Rader, G. Landolt, B. Slomski, J. Hugo Dil, J. Osterwalder, T.-R. Chang, H.-T. Jeng, H. Lin, A. Bansil, N. Samarth, and M. Zahid Hasan, *Hedgehog spin texture and Berry's phase tuning in a magnetic topological insulator.* Nature Physics **8**, 616 (2012), cited on page(s): 147

[215] Q. Liu, C.-X. Liu, C. Xu, X.-L. Qi, and S.-C. Zhang, *Magnetic Impurities on the Surface of a Topological Insulator.* Physical Review Letters **102**, 156603 (2009), cited on page(s): 147

[216] D. A. Abanin and D. A. Pesin, *Ordering of Magnetic Impurities and Tunable Electronic Properties of Topological Insulators.* Physical Review Letters **106**, 136802 (2011), cited on page(s): 147

[217] P Wahl, P Simon, L. Diekhöner, V. Stepanyuk, P Bruno, M. Schneider, and K Kern, *Exchange Interaction between Single Magnetic Adatoms.* Physical Review Letters **98**, 056601 (2007), cited on page(s): 147

[218] R. Biswas and A. Balatsky, *Impurity-induced states on the surface of three-dimensional topological insulators.* Physical Review B **81**, 233405 (2010), cited on page(s): 147

[219] P. Sessi, F. Reis, T. Bathon, K. a. Kokh, O. E. Tereshchenko, and M. Bode, *Signatures of Dirac fermion-mediated magnetic order.* Nature communications **5**, 5349 (2014), cited on page(s): 147

Publications, peer reviewed

[A1]   F. Pielmeier, G. Landolt, B. Slomski, S. Muff, J. Berwanger, A. Eich, A. A. Kha-jetoorians, Z. S. Wiebe J. Aliev, M. B. Babanly, R. Wiesendanger, J. Osterwalder, E. V. Chulkov, F. J. Giessibl, and J. H. Dil, *Response of the topological surface state to surface disorder in TlBiSe2* New Journal of Physics **17**, 023067 (2015)

[A2]   A Eich, M. Michiardi, G. Bihlmayer, X.-G. Zhu, J.-L. Mi, B. B. Iversen, R Wiesen-danger, P. Hofmann, A. A. Khajetoorians, and J Wiebe, *Intra- and interband elec-tron scattering in a hybrid topological insulator: Bismuth bilayer on Bi2Se3* Physical Review B **90**, 155414 (2014)

[A3]   A. Rusydi, A. Goos, S. Binder, A. Eich, K. Botril, P. Abbamonte, X. Yu, M. B. H. Breese, H. Eisaki, Y. Fujimaki, S. Uchida, N. Guerassimova, R. Treusch, J. Feldhaus, R. Reininger, M. V. Klein, and M. Rübhausen, *Electronic Screening-Enhanced Hole Pairing in Two-Leg Spin Ladders Studied by High-Resolution Resonant Inelastic X-Ray Scattering at Cu M Edges* Physical Review Letters **113**, 067001 (2014)

[A4]   T. Schlenk, M. Bianchi, M. Koleini, A. Eich, O. Pietzsch, T. O. Wehling, T. Frauen-heim, A. Balatsky, J.-L. Mi, B. B. Iversen, J. Wiebe, A. A. Khajetoorians, P. Hof-mann, and R. Wiesendanger, *Controllable Magnetic Doping of the Surface State of a Topological Insulator* Physical Review Letters **110**, 126804 (2013)

[A5]   S. V. Eremeev, G. Landolt, T. V. Menshchikova, B. Slomski, Y. M. Koroteev, Z. S. Aliev, M. B. Babanly, J. Henk, A. Ernst, L. Patthey, A. Eich, A. A. Khajetoorians, J. Hagemeister, O. Pietzsch, J. Wiebe, R. Wiesendanger, P. M. Echenique, S. S. Tsirkin, I. R. Amiraslanov, J. H. Dil, and E. V. Chulkov, *Atom-specific spin mapping and buried topological states in a homologous series of topological insulators* Nature communications **3**, 635 (2012)

[A6]   S. Herres-Pawlis, S. Binder, A. Eich, R. Haase, B. Schulz, G. Wellenreuther, G. Henkel, M. Rübhausen, and W. Meyer-Klaucke, *Stabilisation of a highly reactive bis(mu-oxo)dicopper(III) species at room temperature by electronic and steric con-straint of an unconventional nitrogen donor ligand* Chemistry **15**, 8678 (2009)

[A7]   L. Redecke, S. Binder, M. I. Y. Elmallah, R. Broadbent, C. Tilkorn, B. Schulz, P. May, A. Goos, A. Eich, M. Rübhausen, and C. Betzel, *UV-light-induced conversion and aggregation of prion proteins* Free radical biology and medicine **46**, 1353 (2009)

Publications in work

[B1]   M. Vondracek, M. Michiardi, J. Warmuth, L. Barreto, C. Piamonteze, A. Eich, A. A. Khajetoorians, J.-L. Mi, B. B. Iversen, P. Hofmann, J. Wiebe, J. Honolka, and R. Wiesendanger, *Combined XMCD and STS study of transition metal adatoms adsorbed on the surface of prototypical 3D topological insulators*, To be submitted (2015)

Conference Contributions

[C1] A. Eich, M. Michiardi, G. Bihlmayer, A. A. Khajetoorians, J. Wiebe, J.-L. Mi, B. B. Iversen, P. Hofmann, and R. Wiesendanger, *Experimantal characterization and simulation of quasi-particle interference on Bi/Bi2Se3*, Talk, APS March Meeting (2014)

[C2] M. Michiardi, A. Eich, G. Bihlmayer, A. A. Khajetoorians, J. Wiebe, J.-L. Mi, B. B. Iversen, P. Hofmann, and R. Wiesendanger, *Experimental characterization and simulation of quasi-particle-interference in the Bi-bilayer topological insulator*, Talk, DPG Spring Conference (2014)

[C3] J. Warmuth, M. Vondracek, M. Michiardi, L. Barreto, C. Piamonteze, A. Eich, A. A. Khajetoorians, J.-L. Mi, B. B. Iversen, P. Hofmann, J. Wiebe, J. Honolka, and R. Wiesendanger, *Combined XMCD and STS study of transition metal adatoms adsorbed on the surface of prototypical 3D topological insulators*, Poster, DPG Spring Conference (2014)

[C4] A. Eich, T. Schlenk, M. Bianchi, M. Koleini, O. Pietzsch, T. O. Wehling, T. Frauenheim, A. Balatsky, J.-L. Mi, B. B. Iversen, J. Wiebe, A. A. Khajetoorians, P. Hofmann, and R. Wiesendanger, *Controllable magnetic doping of the surface state of a topological insulator*, Talk, DPG Spring Conference (2013)

[C5] A. Eich, J. Honolka, A. A. Khajetoorians, V. Sessi, M. Koleini, T. O. Wehling, S. Stepanow, J.-L. Mi, B. B. Iversen, A. Balatsky, T. Schlenk, J. Wiebe, O. Pietzsch, N. Brookes, A. I. Lichtenstein, P. Hofmann, M. Bianchi, K. Kern, and R. Wiesendanger, *Properties of magnetically doped topological insulator Fe/Bi2Se3*, Poster, SPS'12 and SPSTM-4 (2012)

[C6] J. Wiebe, J. Honolka, A. A. Khajetoorians, V. Sessi, M. Koleini, T. O. Wehling, S. Stepanow, J.-L. Mi, B. B. Iversen, T. Schlenk, A. Eich, O. Pietzsch, N. Brookes, A. I. Lichtenstein, P. Hofmann, M. Bianchi, K. Kern, and R. Wiesendanger, *In-plane magnetic anisotropy of Fe atoms on Bi2Se3(111)*, Poster, CECAM Workshop Topological Materials (2012)

[C7]   A. Eich, S. V. Eremeev, G. Landolt, T. V. Menshchikova, B. Slomski, Y. M. Koroteev, Z. S. Aliev, M. B. Babanly, J. Henk, A. Ernst, L. Patthey, A. A. Khajetoorians, J. Hagemeister, O. Pietzsch, J. Wiebe, R. Wiesendanger, P. M. Echenique, S. S. Tsirkin, I. R. Amiraslanov, J. H. Dil, and E. V. Chulkov, *STM studies on the ternary topological insulator PbBi4Te7*, Poster, DPG Spring Conference (2012)

[C8]   A. Eich, S. V. Eremeev, G. Landolt, T. V. Menshchikova, B. Slomski, Y. M. Koroteev, Z. S. Aliev, M. B. Babanly, J. Henk, A. Ernst, L. Patthey, A. A. Khajetoorians, J. Hagemeister, O. Pietzsch, J. Wiebe, R. Wiesendanger, P. M. Echenique, S. S. Tsirkin, I. R. Amiraslanov, J. H. Dil, and E. V. Chulkov, *STM studies on the ternary topological insulator PbBi4Te7*, Poster, 493. Heraeus Seminar (2011)

Abbrevations

Acknowledgments

At the end of this book I want to take the chance to say thank you to all my supervisors, colleagues and staff members that supported me during my Ph.D. time.

In particular I want to thank Prof. Dr. Roland Wiesendanger for the opportunity to gain my doctor's degree in his group. The conditions he provided allowed me to perform research at the highest level and to present my work at conferences around the world.

I am grateful for the support of my supervisors. I thank Dr. Oswald Pietzsch for his advice during the construction of my microscope and during my first two years of measuring. My thanks go to Prof. Dr. Alexander A. Khajetoorians for proposing an endless number of projects I could work on and for the little tricks he taught me on how to squeeze the best results out of an STM (except the last one). And I thank Dr. Jens Wiebe, especially for proofreading this monster thesis.

Many thanks go to my fellow colleagues Dr. Tobias Schlenk, Matteo Michiardi and Jonas Warmuth with whom I had the privilege to work together on several projects, as well as to Dr. Thomas Eelbo, Dr. Mike Gyamfi and Dr. Stefan Meckler for their advice during the construction of my microscope. Working with you guys was not only constructive (literally), it was a delight.

I thank Rolf-Dieter Benecke, Horst Biedermann and their teams from the mechanical and electronic workshops for their support during the construction of my microscope. Furthermore, I thank Jörg Völkel and Dieter Klatt for the steady supply with liquid helium, even in times when the liquefier was broken and there was officially no liquid helium left.

Last but not least I thank the Konrad-Adenauer-Stiftung for the financial support as well as for the opportunity to meet and discuss with so many other young scientists from so many different fields of research.